GlobAlbedo

Author: GlobAlbedo Consortium

TITLE: GlobAlbedo Algorithm Theoretical Basis Document

Version 3.1

Document Number: GlobAlbedo_Albedo_ATBD_V3_1 Date 06/06/2012

Distribution:

ESA	O. Leonard	X
	S. Pinnock	X
University College London	J-P. Muller	X
	T. Kennedy	X
	P. Lewis	X
Swansea	P. North	X
Free University of Berlin	J. Fisher	X
	R. Preusker	X
Brockmann Consult	C. Brockmann	X
	U. Krämer	X
	O. Danne	X
	N. Fomferra	X

Author: _____ Date: _____

Manager/Project Office _____ Date: _____

PA: _____ Date: _____

CHANGE RECORD

ISSUE	DATE	PAGES CHANGED	COMMENTS
A	18/07/10	All new	Draft
1	09/09/10	All sections	First Issue
2	09/11/10	All sections	Response to RIDs raised by Simon Pinnock (7/10/2010)
2.1	26/11/10	Equation 15 p.43	New formulation in equation 9 now propagated through to Nsky terms.
2.2	16/02/11	Equn 19b	Added in information for Chi squared in eqn 19b and in the accumulator text.
3.0	07/04/11	All sections	Major revision, including prototype results
3.1	06/06/2012	All	Global ToC added, fAPAR material added

CONTRIBUTORS

Author Names	Organisation
G. López, J.-P. Muller, D. Potts, N. Shane	UCL MSSL
P. Lewis	UCL Geography
C. Brockmann, O. Danne, O. Krueger	Brockmann Consult
A. Heckel, P. North	Swansea University
L. Guanter	Freie Universität Berlin

CONTENTS

1 Introduction

1.1 Purpose and Scope of Document

The purpose of this document is to provide the background and theoretical justification for the algorithm employed to estimate albedo in the ESA GlobAlbedo product. The primary features of the product are:

- It is a 15 year product covering the years 1995-2010;
- It is a gap-free core 1 km resolution (also 5 arc-minutes (≈10km) and 30 arc-minutes (≈50km)) gridded product over the Earth land surface;
- It provides estimates of albedo in 3 broad wavebands (visible, shortwave infrared and total shortwave: 0.3-0.7μm, 0.7-3μm, 0.3-3μm);
- It is derived primarily from estimates of surface directional spectral reflectance from 3 (streams of) European satellite sensor data ((A)ATSR and related, SPOT Vegetation, and MERIS);
- It incorporates uncertainties in the observations (and other elements of an optimal estimation framework) so that an uncertainty can be attributed to the final albedo product;

1.2 Context

Land surface albedo is the proportion of incident radiation over some waveband that is reflected from a surface. As such, it is one of the most important 'parameters' characterising the Earth's radiative regime due to its impact on the climatic and biospheric processes. Knowledge of albedo is of critical importance to land surface monitoring and modelling, particularly in regard to considerations of climate and the biosphere. When albedo is used in models, it has often been specified simply as a parameter, i.e. a fixed number for some given land cover type. However, many years of monitoring have shown that it can vary very significantly both spatially and temporally. That said, being an angular and spectral integral, it is relatively conservative inter-annually, other than due to factors such as snow and possibly fire and dramatic land cover change. As particularly high changes in albedo occur due to the presence of absence of snow, modellers tend to consider these two cases separately: a snow free albedo and one with snow included.

The definition of albedo, A, is straightforward: it is the ratio of total upwelling to total downwelling radiation (without further qualification, over the entire solar radiation (shortwave) regime, practically around 350-2500 nm). Its definition limits it to the bounds (0,1) in the absence of emission effects. Its value lies primarily in its role in energy budget considerations within climate or weather prediction models, in that the proportion of (shortwave) radiation absorbed by the surface (and converted to heat energy or used in biochemical processes such as photosynthesis) is $1-A$. As an example of the critical role of albedo in the Earth system, Ridgwell et al., (2009) consider a geo-engineering solution as a technological solution for reducing global warming in which they suppose bio-

engineering to supply a +0.04 change in maximum canopy albedo (a 15-20% increase in albedo) across prescribed cropland areas. By examining this scenario in a GCM, they predict global annual average surface air temperatures to be around 0.1°C lower than with no change, with more extreme regional variations such as a 1°C cooling during summer months throughout North America and Eurasia. Another way of interpreting these results is that a 15 or 20% positive bias in estimates of crop albedo can have a large (especially regional) impact on GCM predictions of surface temperatures. We note that GCOS (2006) and Schaaf et al. (2009) suggest a relative accuracy of 5% (or 0.005, whichever is larger). The relative accuracy required in the SoW are: BHR: 10% (or 0.005 absolute, whichever is larger); DHR: 20% (or 0.01, whichever is larger). The target accuracy requirements identified by and agreed with the GlobAlbedo users in GlobAlbedo_RB_D01_v2_0 (2010) are: Albedo >0.15, 20% and for Albedo <0.15, 0.015, i.e. 10% relative accuracy (or 0.015, whichever is larger).

Earth surface albedo is generally split into two spectral components: visible (VIS) and near infrared (NIR). The main reason for this is that visible albedo is of primary importance in consideration of photosynthesis in vegetation canopies: the radiation absorbed in this region over vegetation canopies, $1-A_{VIS}$, is in essence partitioned between that absorbed by the canopy (*fAPAR* – the faction of absorbed *PAR*, where *PAR* is 'photosynthetically-active radiation', a misnomer since it is the vegetation that is active in this sense, not the radiation) and that absorbed by soil or non-photosynthetically active components of the canopy. In this argument, we assume *PAR* and the visible waveband to be equivalent. Then we can note that $fAPAR \le 1-A_{VIS}$, i.e. $1-A_{VIS}$ provides an upper bound estimate of $fAPAR$. Another reason for splitting the shortwave albedo into (at least two) spectral components is that the proportion of solar radiation in these wavebands varies with atmospheric conditions (the main factors being aerosols at shorter wavelengths and water vapour at longer wavelengths). This comment gives an immediate insight into some issues that arise in the estimation of albedo: as it depends of atmospheric state (at the very least the proportion of downwelling radiation in VIS and NIR bands) it is not an intrinsic property of the Earth surface. Instead, we can say that it is a function of some intrinsic characterisation of the surface and the illumination conditions (spectral and angular). It is for this reason that we separate 'optimal parameter estimation' from 'albedo estimation' in consideration of the problem. In attempting to arrive at a useful *intrinsic* surface product *related to* albedo, GCOS (2004) specify 'black-sky albedo' (directional-hemispherical reflectance) as the product required for climate change purposes. This is essentially equivalent to the albedo in the absence of diffuse illumination. It is still however a function, rather than a fixed parameter, as it can vary significantly with solar zenith angle. It is therefore usually computed for a specific time (such as local solar noon) to provide a consistent framework. An obvious issue to arise from that though is that since the sun angle at local solar noon changes throughout the year, this normalized 'black-sky albedo' would apparently change over time, even if the surface underwent no change.

A more flexible description of albedo can be provided by a data product that provides estimates of intrinsic surface properties that, with an appropriate radiative transfer model, allow the estimation of spectral directional reflectance (the spectral BRDF). This term, the spectral BRDF, $BRDF_\lambda$ is the fundamental description of surface reflectance, being the ratio of reflected spectral radiance ($Wm^{-2}sr^{-1}nm^{-1}$) exiting around a direction vector Ω

(relative to a surface normal vector) to the spectral irradiance ($Wm^{-2}nm^{-1}$) incident on the surface from direction Ω' at some wavelength λ. More practically, we define the BRF, the bidirectional reflectance factor $R_\Lambda(\Omega,\Omega')$ (unitless), the ratio of the BRDF to that of a perfect Lambertian reflectors under the same illumination conditions, over a waveband Λ.

2 Applicable and Reference documents

2.1 Applicable documents

2.2 Reference Documents

Barnsley, M. J., A. H. Strahler, K. P. Morris and J-P. Muller. 1994. Sampling the surface bidirectional reflectance distribution function (BRDF): 1. Evaluation of current and future satellite sensors. Remote Sensing Reviews. 8(4):271-311.

EOEP-DUEP-EOPS-SW-09-0001 SoW Statement of Work for DUE-GlobAlbedo Project, Version 1.0, April 2009

ESA (2009) DUE GlobAlbedo Project, Statement of Work, EOEP-DUEP-EOPS-SW-09-0001, Issue 1, Revision 0, 6 April 2009.

Gao, F., X. Li, A. H. Strahler, and C. B. Schaaf, "Evaluation of the Li-transit kernel for BRDF modeling," *Remote Sens. Rev.*, vol. 19, pp. 205–224, 2000.

GCOS. 2006: satellite- based products for climate. supplemental details to the satellite-based component of the "Implementation plan for the Global observing system for Climate in support of the UnFCCC", GCOS-107 (WMo/Td no. 1338). 90p.

GCOS. 2004: Implementation plan for the Global observing system for Climate in support of the UnFCCC. Report GCOS – 92 (WMO/TD No. 1219). 136p.

Geiger, B.; Carrer, D.; Franchisteguy, L.; Roujean, J.-L.; Meurey, C.; , "Land Surface Albedo Derived on a Daily Basis From Meteosat Second Generation Observations," *Geoscience and Remote Sensing, IEEE Transactions on* , vol.46, no.11, pp.3841-3856, Nov. 2008

GlobAlbedo (2010) Technical Specifications Document: GlobAlbedo_TS_D02_V2_0 Date 17/06/10

Hagolle, O., A. Lobo, P. Maisongrande, F. Cabot, B. Duchemin, and A. de Pereyra, "Quality assessment and improvement of temporally composited products of remotely sensed imagery by combination of VEGETATION 1 & 2 images," *Remote Sens. Environ.*, vol. 94, no. 2, pp. 172–186, Jan. 2001.

Hansen, P.C., Nagy, J,G., O'Leary, D.P.O. (2006) Deblurring Images: matrices, spectra and filtering, SIAM series on Fundamentals of Algorithms, Society for Industrial and Applied Mathematics. ISBN 0-89871-618-7.

Hu, B., W. Lucht, and A.H. Strahler, The Interrelationship of Atmospheric Correction of Reflectances and Surface BRDF Retrieval : A Sensitivity Study, *IEEE Trans. Geosci. Remote Sensing* **37** (2) : 724-738 (1999)

Huber, P. J., 1973, Robust regression: Asymptotics, conjectures, and Monte Carlo: Ann. Statist., **1**, 799-821.

Justice, C., E. Vermote, J. Townshend, R. Defries, D. Roy, D. Hall, V. Salomonson, J. Privette, G. Riggs, A. Strahler , W. Lucht, R. Myneni, Y. knyazi, S. Running, R. Nemani, Z. Wan, A. Huete, W. van Leeuwen, R. Wolfe, L. Giglio, JJ-P. Muller , P. Lewis and M. Barnsley (1998) The Moderate Resolution Imaging Spectroradiometer (MODIS): Land Remote Sensing for Global Change Research. *IEEE Trans. Geosci. and Rem. Sens.* 36(4), 1228-1249.

Klein, A. G., & Stroeve, J. (2002). Development and validation of a snow albedo algorithm for the MODIS instrument. Annals of Glaciology, 34, 45−52.

Lewis, P., & Barnsley, M. (1994). Influence of the sky radiance distribution on various formulations of the Earth surface albedo. Proceedings of the Colloque International Mesures Physiques et Signatures en Teledetection (pp. 707−716). Val d'Isere: France.

Lewis, P. (1995), The Utility of Linear Kernel-Driven BRDF Models in Global BRDF and Albedo Studies. Proc IGARSS'95, Firenze, Italy.Volume 2,10-14 July 1995 Page(s):1186 - 1188 vol.2

Li, X., F. Gao, L. Chen, and A. H. Strahler, “Derivation and validation of a new kernel for kernel-driven BRDF models,” in *Remote Sensing for Earth Science, Ocean and Sea Ice Applications*, 1999, vol. 3868, SPIE Proc. Series, pp. 368–379

Li, X., F. Gao, J. Wang, and A. Strahler, “A priori knowledge accumulation and its application to linear BRDF model inversion,” *J. Geophys. Res.*, vol. 106, no. D11, pp. 11 925–11 935, 2001.

Liang, S., Narrowband to broadband conversions of land surface albedo I Algorithms, Remote Sensing of Environment 76, 213-238, 2000

Liang, S. and P. Lewis (1996), A Parametric Radiative Transfer Model for Sky Radiance Distribution. *J. Quant. Spectrosc. Radiat.eTransfer*, 55(2), 181-189.

Liang, S., Stroeve, J., & Box, J. E. (2005). Mapping daily snow/ice shortwave broadband albedo from Moderate Resolution Imaging Spectroradiometer (MODIS): The improved direct retrieval algorithm and validation with Greenland in situ measurement. Journal of Geophysical Research, 110, D10109.

Lucht, W., C. B. Schaaf, and A. H. Strahler, An algorithm for the retrieval of albedo from space using semiempirical BRDF models, IEEE Trans. Geosci. Remote Sensing, 38, 977-998, 2000.

Lucht, W., and P. Lewis, Theoretical noise sensitivity of BRDF and albedo retrieval from the EOS-MODIS and MISR sensors with respect to angular sampling, Int. J. Remote Sensing, 21, 81-98, 2000.

Lyapustin, A., Y. Wang, J. Martonchik, J.L. Privette, B. Holben, I. Slutsker, A. Sinyuk, and A. Smirnov, (2006), Local analysis of MISR surface BRF and albedo over GSFC and Mongu AERONET sites, IEEE Trans. Geosci. Rem. Sens., 44, 1707-1718.

Maignan, F., F.-M. Bréon and R. Lacaze, Bidirectional reflectance of Earth targets: Evaluation of analytical models using a large set of spaceborne measurements with emphasis on the hot spot, *Remote Sensing of Environment* 90 (2004), pp. 210–220.

Moody, E. G., M. D. King, C. B. Schaaf, and S. Platnick, MODIS-Derived Spatially Complete Surface Albedo Products: Spatial and Temporal Pixel Distribution and Zonal Averages, Journal of Applied Meteorology and Climatology, 47,2879-2894,2008.

Moody, E. G., M. D. King, C. B. Schaaf, D. K. Hall Northern Hemisphere five-year average (2000-2004) spectral albedos of surfaces in the presence of snow: Statistics computed from Terra MODIS land productsRemote Sensing of Environment 111 (2007) 337-345

Nilson, T., and A. Kuusk, A reflectance model for the homogeneous plant canopy and its inversion, Remote Sensing of Environment, 27,157-167, 1989.

Pinker, R. T. and I. Laszlo, Modelling surface solar irradiance for satellite applications on a global scale, Journal of Applied Meteorology, 31,194-211, 1992.

Pinty, B., T. Lavergne, R. E. Dickinson, J.-L. Widlowski, N. Gobron, and M. M. Verstraete (2006), Simplifying the interaction of land surfaces with radiation for relating remote sensing products to climate models, *J. Geophys. Res.*, 111, D02116, doi:10.1029/2005JD005952.

Pinty, B., T. Lavergne, M. Voßbeck, T. Kaminski, O. Aussedat, R. Giering, N. Gobron, M. Taberner, M. M. Verstraete, and J.-L. Widlowski (2007), Retrieving surface parameters for climate models from Moderate Resolution Imaging Spectroradiometer (MODIS)-Multiangle Imaging Spectroradiometer (MISR) albedo products, *J. Geophys. Res.*, 112, D10116, doi:10.1029/2006JD008105.

Pinty, B., Jung, M., Kaminski, T., Lavergne, T., Mund, M., Plummer, S., Thomas, E., Widlowski, J.L., 2011a. Evaluation of the JRC-TIP 0.01° products over a mid-latitude deciduous forest site. Remote Sens. Environ. 115, 3567-3581.

Pinty, B., Andredakis, I., Clerici, M., Kaminski, T., Taberner, M., Verstraete, M. M., et al. (2010a). Exploiting the MODIS albedos with the Two-stream Inversion Package (JRC-TIP) Part I: effective Leaf Area Index, Vegetation and Soil properties. Journal of Geophysical Research, 116.

Pinty, B., Clerici, M., Andredakis, I., Kaminski, T., Taberner, M., Verstraete, M. M., et al. (2010b). Exploiting the MODIS albedos with the Two-stream Inversion Package JRC-TIP) Part II: Fractions of transmitted and absorbed fluxes in the vegetation and soil layers. Journal of Geophysical Research, 116.

Pinty, B., Taberner, M., Haemmerle, V.R., Paradise, S.R., Vermote, E., Verstraete, M.M., Gobron, N., Widlowski, J.-L., 2011b. Global-Scale Comparison of MISR and MODIS Land Surface Albedos. J Climate 24, 732-749.

Pokrovsky, I.O., O.M.Pokrovsky,and J.-L.Roujean, “Development of an operational procedure to estimate surface albedo from the SEVIRI/MSG observing system in using POLDER BRDF measurements,” *Remote Sens. Environ.*, vol. 87, no. 2/3, pp. 198–242, Oct. 2003.

Qin, J., G. Yan , S. Liu , S. Liang , H. Zhang , J. Wang and X. Li "Application of ensemble kalman filter to geophysical parameters retrieval in remote sensing: A case study of kernel-driven BRDF model inversion", *Sci. China Ser. D, Earth Sci.*, vol. 49, pp. 632 2006.

Quaife T. and P. Lewis (2010) Temporal constraints on linear BRF model parameters IEEE Transactions on Geoscience and Remote Sensing, doi:10.1109/TGRS.2009.2038901

Rebelo, L. P. Lewis, and D. Roy, "A temporal-BRDF model-based approach to change detection," in *Proc. IEEE IGARSS*, 2004, vol. 3, pp. 2103–2106.

Ridgwell, A., J. S. Singarayer, A. M. Hetherington and P.J. Valdes, (2009), Tackling Regional Climate Change By Leaf Albedo Bio-geoengineering, Current Biology 19, 146–150, DOI 10.1016/j.cub.2008.12.025

Román, M. O., C. B. Schaaf, P. Lewis, F. Gao, G. P. Anderson, J. L. Privette, A. H. Strahler, C. E. Woodcock, M. Barnsley, Assessing the coupling between surface albedo derived from MODIS and the fraction of diffuse skylight over spatially-characterized landscapes, Remote Sensing of Environment, 114, 738-760,2010.

Roujean, J.L., M. Leroy and P.Y. Deschamps, A Bidirectional Reflectance Model of the Earth's Surface for the Correction of Remote Sensing Data, *J. Geophys. Res.*, **97** (D18) : 20455-20468 (1992)

Samain, O. B. Geiger, and J. Roujean, "Spectral normalization and fusion of optical sensors for the retrieval of BRDF and albedo: Application to VEGETATION, MODIS, and MERIS data sets," *IEEE Trans. Geosci. Remote Sens.*, vol. 44, no. 11, pp. 3166–3179, Nov. 2006.

Samain, O., Jean-Louis Roujean, Bernhard Geiger, Use of a Kalman filter for the retrieval of surface BRDF coefficients with a time-evolving model based on the ECOCLIMAP land cover classification, Remote Sensing of Environment, Volume 112, Issue 4, Remote Sensing Data Assimilation Special Issue, 15 April 2008, Pages 1337-1346.

Schaaf, C. B., A. H. Strahler, F. Gao, W. Lucht, X. Li, X. Zhang, Y. Jin, E. Tsvetsinskaya, J.-P. Muller, P. Lewis, M. Barnsley, G. Roberts, C. Doll, S. Liang, and J. L. Privette, (2002) First operational BRDF, albedo nadir reflectance products from MODIS, *Remote Sensing of Environment*, 83, 135-148.

Schaaf, C.B., J. Cihlar, A. Belward, E. Dutton, and M. Verstraete, Albedo and Reflectance Anisotropy, ECV-T8: GTOS Assessment of the status of the development of standards for the Terrestrial Essential Climate Variables, ed., R. Sessa, FAO, Rome, May 2009.

Stroeve, J., Box, J., Gao, F., Liang, S., Nolin, A., & Schaaf, C. (2005). Accuracy assessment of the MODIS 16-day snow albedo product: Comparisons with Greenland in situ measurements. Remote Sensing of the Environment, 94, 46−60.

Twomey, S. (1977) Introduction to the mathematics of inversion in remote sensing and indirect measurement, Elsevier. ISBN 0-486-69451-8.

Vermote, E. F., D. Tanré, J.L. Deuzé, M. Herman, J.J. Morcrette, Second Simulation of the Satellite Signal in the Solar Spectrum, 6S : An Overview, *IEEE Transactions On Geoscience And Remote Sensing* **35** (3) : 675-686 (1997)

Vermote, E. C. Justice, and F. Breon, "Towards a generalized approach for correction of the BRDF effect in MODIS directional reflectances," *IEEE Trans. Geosci. Remote Sens.*, vol. 47, no. 3, pp. 898–908, Mar. 2009.

Wanner, W., X. Li, and A. H. Strahler, 1995, On the derivation of kernels for kernel-driven models of bidirectional reflectance, J. Geophys. Res., 100(D10), 21,077-21,089.

Wanner , W., A. Strahler , B. Hu, P. Lewis , J-P. Muller X. Li , C. Schaaf , M. Barnsley, (1997), Global retrieval of Bidirectional reflectance and albedo over land from EOS MODIS and MISR Data: Theory and Algorithms.*Journal of Geophysical Research,* Vol. 102 , pp. 17,143 - 17,162

Walthall, C. L., J. M. Norman, J. M. Welles, G. Campbell, and B. L. Blad. Simple equation to approximate the bidirectional reflectance from vegetation canopies and bare soil surfaces. Appl. Opt., 24,383-387, 1985.

Wang, Y., Alexei I. Lyapustin, Jeffrey L. Privette, Robert B. Cook, Suresh K. SanthanaVannan, Eric F. Vermote, Crystal L. Schaaf, Assessment of biases in MODIS surface reflectance due to Lambertian approximation, Remote Sensing of Environment, Volume 114, Issue 11, 15 November 2010, Pages 2791-2801, ISSN 0034-4257, DOI: 10.1016/j.rse.2010.06.013.

WWW1. https://lpdaac.usgs.gov/lpdaac/products/modis_products_table/brdf_albedo_quality/16_day_l3_global_500m/v5/combined, accessed 05 January 2010

Zibordi, G and Voss, K.J. (1989) Geometrical and spectral distribution of sky radiance – comparison between simulations and field measurements, Remote Sensing of Environment, 27(3), 343-358.

2.3 Definitions and Abbreviations

2.3.1 Definitions

2.3.2 Spectral and directional quantities

Item	Definition
θ	zenith angle (radians)
ϕ	azimuth angle (radians)
Ω	solar geometry vector
Ω	viewing geometry vector
Ω	incident geometry vector
λ	wavelength (nm unless otherwise specified)
Λ	waveband Λ of width Δλ

2.3.3 Atmospheric quantities

Item	Definition
$L_\lambda(\Omega_v,\Omega_s,V)$	At satellite radiance (in direction Ω_v, illuminated from direction Ω_s).
$L_\lambda\downarrow(\Omega_i)$	Downwelling spectral radiance (at the ground) in direction Ω_i.
$L_{0\lambda}\downarrow(\Omega_i)$	Downwelling spectral radiance at the bottom of the atmosphere over a totally absorbing lower boundary.
$L_{0\lambda Iso}\downarrow(\Omega_i)$	$L_{0\lambda}\downarrow(\Omega_i)$ under assumptions of isotropic diffuse illumination.
$L_{0\lambda}(\Omega_i)$	Downwelling diffusely transmitted radiance at the bottom of the atmosphere for a totally absorbing lower boundary.
$\eta_\lambda(\mu_s)$	Integral of $L_{0\lambda}(\Omega_i)$ over sky illumination hemisphere.
$L_{sky\lambda}(\Omega_i)$	Downwelling sky radiance under Lambertian surface assumptions.
$E_{s\lambda}$	Exoatmospheric solar irradiance.
$\bar{\rho}_\lambda$	Spherical albedo of the atmosphere for upward travelling radiation.

$t_\lambda(-\mu_s)$	Downwelling direct transmittance of the atmosphere along the path from the Sun to the ground.
t_i	Effective transmission functions for atmospheric influence (*i*=0…3).
$T_\lambda(-\mu_s)$	Downwelling diffuse transmittance of the atmosphere along the path from the Sun to the ground.
$\gamma_\lambda(-\mu_s)$	Total transmittance of the atmosphere along the path from the Sun to the ground.
$\gamma_\lambda(\mu_v)$	Total transmittance of the atmosphere along the path from the ground to the sensor.
D_λ	Proportion of diffuse illumination (at the bottom of the atmosphere).
$D_{0\lambda}$	Proportion of diffuse illumination (at the bottom of the atmosphere) for a totally absorbing lower boundary.
$D_{0\lambda\downarrow}$	Proportion of diffuse illumination (at the bottom of the atmosphere) for a totally absorbing lower boundary; equivalent to $T_\lambda(-\mu_s)/\gamma_\lambda(-\mu_s)$
$D_{0\lambda\uparrow}$	Proportion of diffuse illumination (at the top of the atmosphere) for a totally absorbing lower boundary; equivalent to $T_\lambda(\mu_v)/\gamma_\lambda(\mu_v)$
M_λ	Degree of multiple scattering enhancement.
$N_{sky\lambda}(\Omega_i)$	Normalised sky radiance distribution under an absorbing lower boundary.
V	Horizontal visibility.
$\beta_{Rayleigh}$	Rayleigh scattering extinction coefficient at sea level.
τ	Aerosol optical depth (AOD) at 550 nm.
Δ_Λ	An ancillary term used in compensating for BRDF effects in surface-atmosphere coupling.

2.3.4 Reflectance-based quantities

Item	**Definition**

R_λ	Lambertian-equivalent surface reflectance (surface reflectance retrieved from atmospheric correction, with surface Lambertian assumption)
R'_Λ	Local average Lambertian surface reflectance.
$R_{L\Lambda}$	Lambertian equivalent reflectance with multiple interaction enhancement.
$R_{atm,\Lambda}(\Omega_v,\Omega_s)$	Atmospheric intrinsic reflectance (path reflectance)
$BRDF_\lambda$	Spectral bidirectional reflectance distribution function (*BRDF*).
$R_\lambda(\Omega_v,\Omega_s)$	Spectral bidirectional reflectance factor (BRF).
$R^*_\lambda(\Omega_v,\Omega_s)$	Apparent spectral bidirectional reflectance factor (BRF).
$\overline{R}_\Lambda(\Omega_v)$	Directional hemispherical reflectance (black sky albedo)
$\overline{R'}_\Lambda(\Omega_v)$	N_{sky} weighted directional hemispherical reflectance
$\overline{\overline{R}}_\Lambda$	bihemispherical reflectance (white sky albedo).
$\overline{\overline{R'}}_\Lambda$	N_{sky} weighted bihemispherical reflectance.
$\overline{\overline{R''}}_\Lambda$	Local average bihemispherical reflectance.
$f_{X,\Lambda}$	RossThick – LiSparse Reciprocal (RTLSR) BRF kernel model parameter *X*. Note that these are also referred to by an index when convenient, so that $f_{iso} = f_0$, $f_{vol} = f_1$, $f_{geo} = f_2$. This variation in notation also applies to any kernels.
$K_X(\Omega_v,\Omega_s)$	RTLSR BRF model kernel *X*.
$\overline{K}_X(\Omega_v)$	Directional hemispherical integral of $K_X(\Omega_v,\Omega_s)$ for direction Ω_v.
$\overline{\overline{K}}_X$	Bihemispherical integral of $K_X(\Omega_v,\Omega_s)$.
$\overline{\overline{K'}}_{X\,\lambda}$	N_{sky} weighted bihemispherical integral of

	$K_X(\Omega_v,\Omega_s)$.
$K_{x,\lambda}(\Omega_s)$	Weighted sum of $\overline{\overline{K}}_X$ and $\overline{\overline{K'}}_{X\,\lambda}$ for given atmospheric conditions.
$\overline{\overline{\delta K}}_{x,\lambda}$	The departure of $\overline{\overline{K'}}_{X\,\Lambda}$ with respect to $\overline{\overline{K}}_X$.

2.3.5 Albedo-related quantities

Item	Definition
$\overline{R}_\Lambda(\Omega_s)$	Directional hemispherical integral of reflectance (black sky albedo).
$\overline{\overline{R}}_\Lambda$	Bihemispherical integral of reflectance (white sky albedo).
$\overline{\overline{R'}}_\Lambda$	N_{sky} weighted bihemispherical integral of reflectance.
A	Surface albedo (over all wavelengths)
$A_\Lambda(\vartheta_s)$	Surface albedo (full expression) over waveband Λ.
$A_{\Lambda Iso}(\Omega_s)$	Surface albedo over waveband Λ under assumptions of direct and isotropic diffuse illumination.

2.4 Abbreviations

(A)ATSR(-2)	(Advanced) Along-Track Scanning Radiometer (-2)
BRDF	Bidirectional Reflectance Distribution Function (units sr^{-1})
NIR	Near Infrared
VIS	Visible
SW	Shortwave
fAPAR	Fraction of Absorbed PAR
PAR	Photosynthetically Active Radiation
GCM	Global Climate Model
IDL	Interactive Data Language (Research Systems Inc.)

3 Mathematical and Physical Background

3.1 Mathematical Description of albedo

Surface albedo (see section 3 for symbol definitions) can be stated:

$$A_{\Lambda}\left(\vartheta_s\right)=\frac{\int_0^{2\pi}d\phi_v\int_0^{2\pi}d\phi_i\int_{\Lambda_{\min}}^{\Lambda_{\max}}d\lambda\int_0^{2\pi}d\mu_v\int_0^{1}R_{\lambda}\left(\Omega_v,\Omega_s\right)L_{\lambda}\downarrow\left(\Omega_i\right)\mu_i\mu_v d\mu_i}{\pi\int_0^{2\pi}d\phi_i\int_{\Lambda_{\min}}^{\Lambda_{\max}}d\lambda\int_0^{1}L_{\lambda}\downarrow\left(\Omega_i\right)\mu_i d\mu_i} \qquad \textbf{1}$$

The numerator in the equation above is carried out over all downwelling (i.e. incident, subscript *i*) and upwelling angles ('viewing', subscript *v*) (over hemispheres) and over all wavelengths in the waveband. Note that in equation 1, $\mu_X=\cos\vartheta_X$. The downwelling spectral radiance at the ground is $L_{\lambda}\downarrow\left(\Omega_i\right)$ in direction Ω_i, being due to both direct and diffuse transmission of downwelling radiation in the atmosphere and enhancements due to multiple scattering between the surface and the atmosphere. Statement of the problem is simplified by considering first the case with no enhancement (i.e. a totally absorbing lower boundary), giving $L_{0\lambda}\downarrow\left(\Omega_i\right)$. In this case, we may simply split the downwelling spectral radiance into a diffuse term $L_{0\lambda}\left(\Omega_i\right)$, a 'sky radiance' function over Ω_i, and a direct term that is only defined in the direct solar beam:

$$L_{0\lambda}\downarrow\left(\Omega_i\right)=L_{0\lambda}\left(\Omega_i\right)+\frac{\mu_s E_{s\lambda}t_{\lambda}\left(-\mu_s\right)}{\pi} \qquad \textbf{2a}$$

We define the integral of sky radiance:

$$\eta_{\lambda}\downarrow\left(\mu_s\right)=\frac{1}{\pi}\int_0^{2\pi}d\phi_i\int_0^{1}L_{0\lambda}\left(\Omega_i\right)\mu_i d\mu_i=\frac{\mu_s E_{s\lambda}T_{\lambda}\left(-\mu_s\right)}{\pi} \qquad \textbf{2b}$$

and note from 2a,b that for isotropic diffuse illumination:

$$L_{0\lambda}\downarrow(\Omega_i)=\frac{\mu_s E_{s,\lambda}\gamma_\lambda(-\mu_s)}{\pi}$$

where $\gamma_\lambda(-\mu_s)=t_\lambda(-\mu_s)+T_\lambda(-\mu_s)$ is the total downward transmission. More generally, we can consider a normalised sky radiance function:

$$N_{sky\lambda}(\Omega_i)=\frac{L_{0\lambda}(\Omega_i)}{\eta_\lambda\downarrow(\mu_s)}$$

so that:

$$L_{0\lambda}\downarrow(\Omega_i)=\frac{\mu_s E_{s\lambda}}{\pi}\left[T_\lambda(-\mu_s)N_{sky\lambda}(\Omega_i)+t_\lambda(-\mu_s)\right]$$

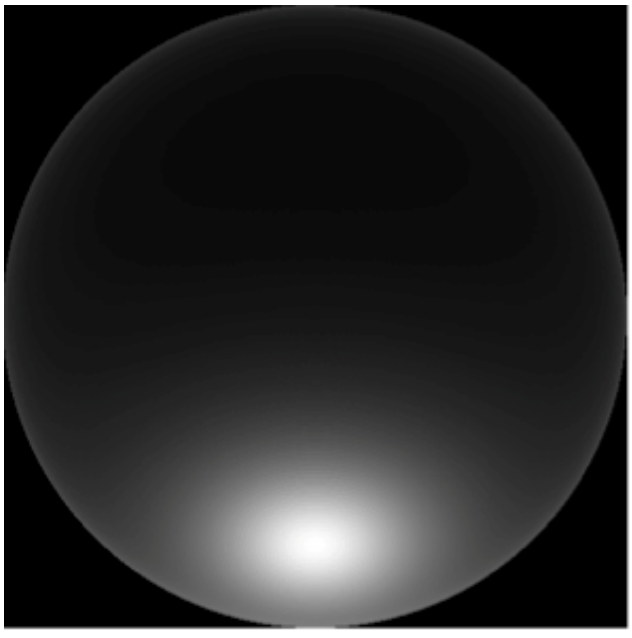

(a) N_{sky} 650 nm (scaled 0.000 to 6.71)

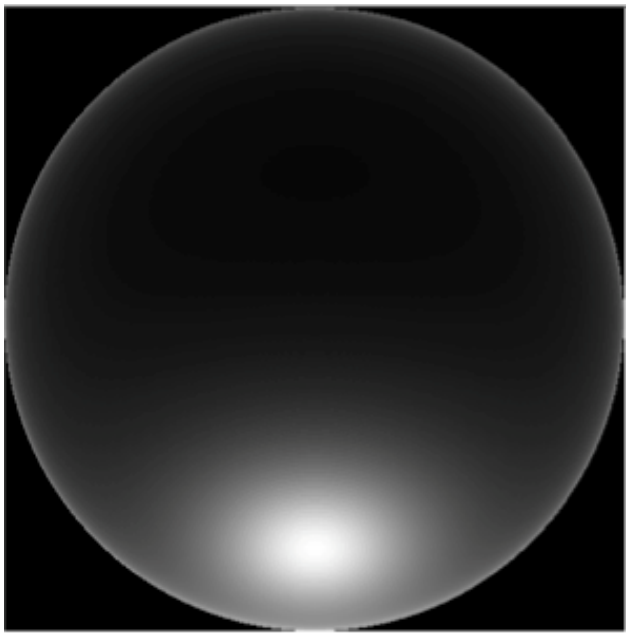

(a) N_{sky} 859 nm (scaled 0.000 to 6.33)

Figure 3-1. Polar plot of normalised sky radiance for a solar zenith angle of 45°.

Figure 3-1 shows polar plots of $N_{sky\lambda}(\Omega_i)$ generated with the sky radiance model of Zibordi and Voss (1989) (see also Liang and Lewis, 1996) for an optical thickness of 0.106 at 550

nm. For this low optical thickness, there are no major differences between the normalized sky radiance at red and NIR wavelengths, although they will likely depart further for lower visibility (higher AOT).

If we define the proportion of diffuse illumination for a totally absorbing lower boundary $D_{0\lambda}$:

$$D_{0\lambda} = \frac{T_\lambda(-\mu_s)}{T_\lambda(-\mu_s) + t_\lambda(-\mu_s)}$$

then

$$L_{0\lambda}\downarrow(\Omega_i) = \frac{\mu_s E_{s,\lambda}\gamma_\lambda(-\mu_s)}{\pi}\left[1 + D_\lambda(-\mu_s)\left(N_{sky\lambda}(\Omega_i) - 1\right)\right]$$

so that, in effect, the term $D_\lambda(-\mu_s)\left(N_{sky\lambda}(\Omega_i) - 1\right)$ acts as an enhancement to the isotropic illumination case.

Multiple scattering between the ground and atmosphere can be effected through a Neumann Series providing an enhancement.

$$M_\lambda = \frac{1}{1 - \bar{\bar{R}}_\lambda \bar{\bar{\rho}}_\lambda}$$

where $\bar{\bar{\rho}}_\lambda$ is the atmospheric spherical albedo and $\bar{\bar{R}}_\lambda$ is the bihemispherical integral of the surface reflectance. For this component, we ignore directionality in both the atmospheric and surface signal, as it only occurs for second order plus scattering between the surface and atmosphere and the radiation can be assumed to be diffused. This is the same approximation made in the 6s radiative transfer code. It follows from above that:

$$\frac{\pi L_{0\lambda}\downarrow(\Omega_i)}{\mu_s E_{s\lambda}\gamma_\lambda(-\mu_s)} = \left[(1 - D_{0\lambda}) + D_{0\lambda}N_{sky\lambda}(\Omega_i)\right]\left[1 + \bar{\bar{R}}_\lambda \bar{\bar{\rho}}_\lambda M_\lambda\right]$$

We now define some utility functions that are integrals of surface reflectance. The directional-hemispherical integral of reflectance (the 'black sky albedo') over some waveband is:

$$\overline{R}_{\Lambda}\left(\Omega_i\right)=\frac{1}{\pi}\int_{\Lambda_{\min}}^{\Lambda_{\max}}d\lambda\int_{0}^{2\pi}d\phi_v\int_{0}^{1}R_{\lambda}\left(\Omega_v,\Omega_i\right)\mu_v d\mu_v$$

The bihemispherical integral of reflectance over a waveband $\overline{\overline{R}}_{\lambda}$ is:

$$\overline{\overline{R}}_{\Lambda}=\frac{1}{\pi}\int_{\Lambda_{\min}}^{\Lambda_{\max}}d\lambda\int_{0}^{2\pi}d\phi_i\int_{0}^{1}\overline{R}_{\lambda}\left(\Omega_i\right)\mu_i d\mu_i$$

and an $N_{sky\lambda}$-weighted integral:

$$\overline{\overline{R}}'_{\Lambda}=\frac{1}{\pi}\int_{\Lambda_{\min}}^{\Lambda_{\max}}d\lambda\int_{0}^{2\pi}d\phi_i\int_{0}^{1}\overline{R}_{\lambda}\left(\Omega_i\right)N_{sky\lambda}\left(\Omega_i\right)\mu_i d\mu_i$$

If all terms are assumed constant over a waveband:

$$\begin{aligned}\frac{\int_{\Lambda_{\max}}^{\Lambda_{\max}}d\lambda\int_{0}^{2\pi}d\phi_i\int_{0}^{1}L_{0\lambda}\downarrow\left(\Omega_i\right)\mu_i d\mu_i}{\mu_s E_{s\lambda}\gamma_{\lambda}\left(-\mu_s\right)} &= 1+\left(1-D_{0\Lambda}\right)\overline{\overline{R}}_{\Lambda}\overline{\overline{\rho}}_{\Lambda}M_{\Lambda}+D_{0\Lambda}\overline{\overline{R}}'_{\Lambda}\overline{\overline{\rho}}_{\Lambda}M_{\Lambda}\\ &= M_{\Lambda}\left(1+D_{0\Lambda}\overline{\overline{\rho}}_{\Lambda}\left(\overline{\overline{R}}'_{\Lambda}-\overline{\overline{R}}_{\Lambda}\right)\right)\\ &\approx M_{\Lambda}\end{aligned}$$

We can also write:

$$\frac{\int_{\Lambda_{\max}}^{\Lambda_{\max}}d\lambda\int_{0}^{2\pi}d\phi_v\int_{0}^{2\pi}d\phi_i\int_{0}^{1}d\mu_v\int_{0}^{1}R_{\lambda}\left(\Omega_v,\Omega_i\right)L_{\lambda}\downarrow\left(\Omega_i\right)\mu_v\mu_i d\mu_i}{\mu_s E_{s\lambda}\gamma_{\Lambda}\left(-\mu_s\right)}=\left[\left(1-D_{0\Lambda}\right)\overline{\overline{R}}_{\Lambda}+D_{0\Lambda}\overline{\overline{R}}'_{\Lambda}\right]M_{\Lambda}$$

so that we can write albedo as:

$$A_\Lambda\left(\Omega_s\right)=\frac{\left(1-D_{0\Lambda}\right)\overline{R}_\Lambda\left(\Omega_s\right)+D_{0\Lambda}\overline{\overline{R'}}_\Lambda}{1-D_{0\Lambda}\overline{\overline{\rho}}_\Lambda\left(\overline{\overline{R}}_\Lambda-\overline{\overline{R'}}_\Lambda\right)}$$

which is particularly interesting because although the multiple scattering enhancement has an impact on absolute values of downwelling and upwelling radiance, it is greatly reduced when considering albedo as it depends on the difference $\overline{\overline{R}}_\Lambda-\overline{\overline{R'}}_\Lambda$ rather than the absolute value $\overline{\overline{R}}_\Lambda$ and is further diminished by the proportion of diffuse illumination $D_{0\Lambda}$.

We can approximate this expression for albedo then as:

$$A_\Lambda\left(\vartheta_s\right)=\left(1-D_{0\Lambda}\right)\overline{R}_\Lambda\left(\Omega_s\right)+D_{0\Lambda}\overline{\overline{R'}}_\Lambda$$

i.e. we can approximate albedo as a weighted sum of directional-hemispherical integral of reflectance $\overline{R}_\Lambda\left(\Omega_s\right)$ (black sky albedo) and a weighted bihemispherical integral[1] $\overline{\overline{R'}}_\Lambda$.

3.2 Mathematical description of atmospheric correction

Although this document does not directly deal with atmospheric correction (see relevant sections of the ATBD), it is necessary to consider how samples of reflectance that have undergone this process fit into the general definitions of albedo and related quantities.

The apparent reflectance $R^*_\Lambda\left(\Omega_v,\Omega_s,V\right)$ of the surface (i.e. that including atmospheric effects) over some waveband is related to the satellite measurement of radiance over that waveband $L_\Lambda\left(\Omega_v,\Omega_s,V\right)$, for some given atmospheric state V by:

$$L_\Lambda\left(\Omega_v,\Omega_s,V\right)=\frac{\mu_s E_{s,\lambda}}{\pi}R^*_\Lambda\left(\Omega_v,\Omega_s,V\right)$$

First, we note that if the surface is assumed Lambertian, the apparent reflectance can be given by:

[1] If the term 'blue sky albedo' had not already been appropriated for other purposes (the actual albedo, under specific illumination conditions expressed in equation 1 or the various approximations above) then this would seem an appropriate term for this integral $\overline{\overline{R'}}_\Lambda$ … it is the integral of black sky albedo over a normalised sky radiance function.

$$R^*_\Lambda(\Omega_v,\Omega_s) = R_{atm,\Lambda}(\Omega_v,\Omega_s) + \gamma_\lambda(-\mu_s)\gamma_\lambda(\mu_v)\frac{R_\Lambda}{1-\bar{\bar{\rho}}_\lambda R'_\Lambda} \quad \textbf{3}$$

This is the formula most generally used to estimate surface reflectance from satellite data. The term R'_Λ is in effect a local average Lambertian surface reflectance that accounts for so-called 'environment radiance' effects, i.e. multiple scattering between the atmosphere and both the ground area being represented within a particular pixel and the surrounding area. In the absence of further information, this is often approximated by R_Λ. Indeed, in the pre-processing of surface reflectance products within GlobAlbedo, this is the case, so we can write:

$$R^*_\Lambda(\Omega_v,\Omega_s) = R_{atm,\Lambda}(\Omega_v,\Omega_s) + \gamma_\lambda(-\mu_s)\gamma_\lambda(\mu_v)\frac{R_\Lambda}{1-\bar{\bar{\rho}}_\lambda R_\Lambda} \quad \textbf{4}$$

The target variable here is the Lambertian surface reflectance R_Λ, which is an attempt to characterise the intrinsic surface property BRF $R_\lambda(\Omega_v,\Omega_s)$. Equation 3 (or 4) will provide a different estimate of R_Λ as the viewing and illumination geometries vary, but this is not quite the same as $R_\lambda(\Omega_v,\Omega_s)$.

A fuller version of equation 3 that incorporates BRDF effects can be given after Vermote et al. (1997) as:

$$R^*_\Lambda(\Omega_v,\Omega_s) = R_{atm,\Lambda}(\Omega_v,\Omega_s) + \gamma_\Lambda(-\mu_s)\gamma_\Lambda(\mu_v)\left[\frac{\bar{\bar{\rho}}_\Lambda \bar{\bar{R}}''^2_\Lambda}{1-\bar{\bar{\rho}}_\Lambda \bar{\bar{R}}''_\Lambda} + R'_\Lambda(\Omega_v,\Omega_s)\right] \quad \textbf{5}$$

where

$$\begin{aligned} R'_\Lambda(\Omega_v,\Omega_s) \;=\; & \left(1-D_{0\Lambda\downarrow}\right)\left(1-D_{0\Lambda\uparrow}\right)R_\Lambda(\Omega_v,\Omega_s) + \left(1-D_{0\Lambda\downarrow}\right)D_{0\Lambda\uparrow}\,\overline{R'}_\Lambda(\vartheta_s) \\ & + D_{0\Lambda\downarrow}\left(1-D_{0\Lambda\uparrow}\right)\overline{R'}_\Lambda(\vartheta_v) + D_{0\Lambda\downarrow}D_{0\Lambda\uparrow}\,\bar{\bar{R}}_\Lambda \end{aligned} \quad \textbf{6}$$

and

$$\overline{R'}_{\Lambda}(\vartheta_v) = \frac{1}{\pi}\int_{\Lambda_{\min}}^{\Lambda_{\max}} d\lambda \int_0^{2\pi} d\phi_i \int_0^1 R_\lambda(\Omega_v,\Omega_i) N_{sky\lambda}(\Omega_i)\mu_i d\mu_i$$

$$\overline{R'}_{\Lambda}(\vartheta_s) = \frac{1}{\pi}\int_{\Lambda_{\min}}^{\Lambda_{\max}} d\lambda \int_0^{2\pi} d\phi_v \int_0^1 R_\lambda(\Omega_v,\Omega_s) N_{sky\lambda}(\Omega_v)\mu_v d\mu_v \quad (7)$$

is the directional-hemispherical reflectance in direction Ω_v (and Ω_s) weighted by the normalised sky radiance distribution. After Lyapustin et al. (2006) we could also describe these normalised sky radiance distribution terms as downwelling and upwelling normalised path radiance. Strictly, since $N_{sky\lambda}(\Omega_i)$ refers to a downwelling term and $N_{sky\lambda}(\Omega_v)$ an upwelling term, they are only equivalent functions for a homogeneous atmosphere. Since their only real role is as a normalised term weighting in an integral of reflectance, this distinction should not generally be of great importance.

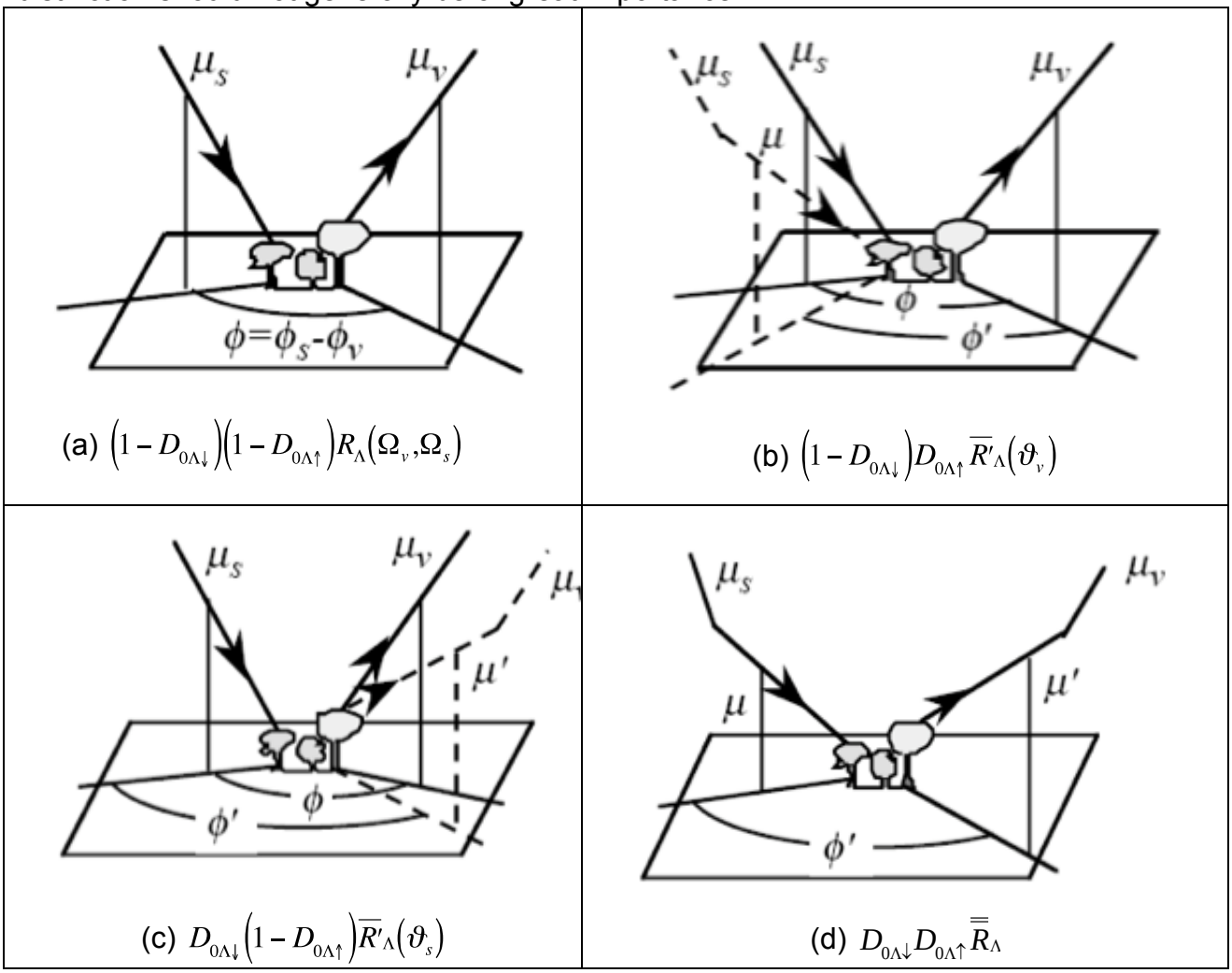

Figure 3-2. Atmospheric interaction mechanisms (from Vermote et al. 2006[2])

[2] http://6s.ltdri.org/6S_code2_thiner_stuff/6s_ltdri_org_manual.htm

Figure 2 demonstrates the linear interaction mechanisms in equation 6. The first involves direct transmission on the upward and downward path and interacts with the BRF. The second is an integral over the diffuse sky radiance field and a direct transmission in the viewing direction. The third is the complement of this for the solar direction. The forth is approximated by the proportion of downwelling and upwelling diffuse radiation and the bihemispherical integral of reflectance. We can think of these as linear interaction terms as they interact with the surface only once. The multiple interaction (non-linear in surface reflectance) term in equation 5 involves scattering back and forth between the surface and atmosphere.

Note that in the above, all terms are assumed constant over the waveband. This is to allow expressions to be written to relate to satellite measurements over a finite waveband and is a good approximation for narrow wavebands. Following for the assumptions made in the surface reflectance products (i.e. ignoring the local spatial averaging or environment radiance in the multiple interactions between surface and atmosphere), we can consider $\overline{\overline{R'}}_\Lambda \approx \overline{\overline{R}}_\Lambda$. In arriving at equation 5, Vermote et al. (1997) assume that all second-order plus interactions between the surface and atmosphere are completely diffused. Lyapustin and Knyazikhin (2001) find that for second order plus interactions between the surface and atmosphere, the rate of change of radiance with scattering order is very close to constant. As a simplification of this concept, the treatment of multiple interactions by Vermote et al. (1997) is found to be accurate to within several tenths of a percent for low reflectance or low BRDF anisotropy, but Lyapustin and Knyazikhin (2001) claim the errors to be non-negligible for higher surface reflectance and/or higher anisotropies. In such a case, they suggest that numerical codes should be used to calculate the first three orders of scattering, and the ratio of the second and third orders used to estimate the maximum eigenvalue term (effectively the product $\overline{\overline{\rho}}_\Lambda \overline{\overline{R}}_\Lambda$) for improved estimates of multiple scattering for these cases.

With the approximation above for no impact of environment reflectance, we note that equation 5 can be written:

$$R^*_\Lambda(\Omega_v,\Omega_s) = R_{atm,\Lambda}(\Omega_v,\Omega_s) + \gamma_\Lambda(-\mu_s)\gamma_\Lambda(\mu_v)\left[R'_\Lambda(\Omega_v,\Omega_s) + \frac{\overline{\overline{\rho}}_\Lambda \overline{\overline{R}}^2_\Lambda}{1-\overline{\overline{\rho}}_\Lambda \overline{\overline{R}}_\Lambda}\right] \quad \textbf{8}$$

It has been noted (Hu et al., 1999) that the impact of ignoring the BRDF effects can lead to relative errors of between 2 and 7 percent in reflectance (average values for red and NIR) for a non-turbid atmosphere and up to 15% for higher optical thickness. Errors in the parameters of the model can be significantly higher than that, i.e. the ability to describe the BRDF shape from data derived from assuming a Lambertian surface is rather compromised.

Whilst the Lambertian approximation has been widely used in atmospheric correction for land surface remote sensing, there is growing concern that the errors in reflectance

associated with this approximation may be quite significant. Wang et al. (2010) note that the impact of the Lambertian assumption in atmospheric correction assumption is (for a typical 'upward bowl-shaped BRF) to under-estimate BRF at high zenith angles and over-estimate at low angles. i.e. to dampen the apparent BRF. When propagated through integrals for albedo estimations, Wang et al. show the albedo estimate to be reduced by 0.004 in the near infrared, 0.005 in the red, and 0.008 in the green MODIS bands. The accommodation of this dampening effect is essentially what equation 9 provides. Hu et al. also note that a single iteration of approximations to the angular integral terms reduces errors to around 1 percent, even an optical thickness of 0.4. One other aspect that Hu et al. examine is the impact of assuming the atmospheric diffuse fields to be isotropic (i.e. ignoring $N_{sky\lambda}$). Although their analysis is brief, it seems to conclude that if $N_{sky\lambda}$ is ignored, final errors in the BRF of around 1 percent can occur, even with iterative treatment of the angular integrals. This does not in itself make a strong case for including $N_{sky\lambda}$.

Lyapustin et al. (2006) give a slightly different formulation for atmospheric influences to that of Vermote et al. (1997), although the core concepts are the same as presented here. Of particular note from the work of Lyapustin et al. is the use of a 1-D Green's function of the atmosphere in calculating the diffusely-transmitted surface-reflected radiance at the top of the atmosphere.

In looking to treat the BRDF effects, we can begin by equating equations 4 and 8 to derive a relationship between the primed bidirectional reflectance term $R'_\Lambda\left(\Omega_v,\Omega_s\right)$ and the Lambertian equivalent reflectance R_Λ:

$$R'_\Lambda\left(\Omega_v,\Omega_s\right)+\frac{\bar{\bar{\rho}}_\Lambda \bar{\bar{R}}^2_\Lambda}{1-\bar{\bar{\rho}}_\Lambda \bar{\bar{R}}_\Lambda}=R_\Lambda+\frac{\bar{\bar{\rho}}_\Lambda R^2_\Lambda}{1-\bar{\bar{\rho}}_\Lambda R_\Lambda}$$

We can write this as:

$$R'_\Lambda\left(\Omega_v,\Omega_s\right)=R_\Lambda+\delta$$

where δ is:

$$\delta=\frac{\bar{\bar{\rho}}_\Lambda R^2_\Lambda}{1-\bar{\bar{\rho}}_\Lambda R_\Lambda}-\frac{\bar{\bar{\rho}}_\Lambda \bar{\bar{R}}^2_\Lambda}{1-\bar{\bar{\rho}}_\Lambda \bar{\bar{R}}_\Lambda}$$

which will tend to be small and which we can approximate as:

$$\delta = \left(\overline{\overline{R}}_\Lambda - R_\Lambda\right)\Delta_\Lambda + O\left[\left(\overline{\overline{R}}_\Lambda - R_\Lambda\right)\right]^2$$

where

$$\Delta_\Lambda = \left[1 - \frac{1}{\left(1 - \overline{\overline{\rho}}_\Lambda R_\Lambda\right)^2}\right]$$

This function is plotted in figure 3. For $\overline{\overline{\rho}}_\Lambda R_\Lambda < 0.2$ it ranges from 0 to close to -0.6. As $\overline{\overline{\rho}}_\Lambda R_\Lambda \to 1,\ \Delta_\Lambda \to -\infty$. We can now approximate the Lambertian equivalent reflectance by:

$$R_\Lambda \approx \frac{R'_\Lambda\left(\Omega_v,\Omega_s\right) - \Delta_\Lambda \overline{\overline{R}}_\Lambda}{\left(1 - \Delta_\Lambda\right)}$$

Accepting this approximation, we can expand the $R'_\Lambda\left(\Omega_v,\Omega_s\right)$ term from equation 6:

$$\begin{aligned} R_\Lambda = \Big[&\left(1 - D_{0\Lambda\downarrow}\right)\left(1 - D_{0\Lambda\uparrow}\right)R_\Lambda\left(\Omega_v,\Omega_s\right) + \left(1 - D_{0\Lambda\downarrow}\right)D_{0\Lambda\uparrow}\overline{R}'_\Lambda\left(\Omega_s\right) \\ &+ D_{0\Lambda\downarrow}\left(1 - D_{0\Lambda\uparrow}\right)\overline{R}'_\Lambda\left(\Omega_v\right) + \left(D_{0\Lambda\downarrow}D_{0\Lambda\uparrow} - \Delta_\Lambda\right)\overline{\overline{R}}_\Lambda\Big] \Big/ \left(1 - \Delta_\Lambda\right) \end{aligned} \quad \textbf{9}$$

Interestingly, as $\overline{\overline{\rho}}_\Lambda R_\Lambda \to 1$ and $\Delta_\Lambda \to -\infty, R_\Lambda \to \overline{\overline{R}}_\Lambda$, so as $\overline{\overline{\rho}}_\Lambda R_\Lambda$ increases, we lose the ability to determine the directional effects in the surface reflectance from a measurement. Also, if we write:

$$R_\Lambda\left(\Omega_v,\Omega_s\right) = f_{iso} + R_{\Lambda+}\left(\Omega_v,\Omega_s\right)$$

then $\overline{R}'_\Lambda\left(\Omega_s\right) = f_{iso} + \overline{R}'_{\Lambda+}\left(\Omega_s\right)$, $\overline{R}'_{\Lambda+}\left(\Omega_s\right)$ being the N_{sky}–weighted integral of $R_{\Lambda+}\left(\Omega_v,\Omega_s\right)$, and similarly for other integrals. Then:

$$R_\Lambda = f_{iso}\left(1-\Delta_\Lambda\right)/\left(1-\Delta_\Lambda\right)+\left[\left(1-D_{0\Lambda\downarrow}\right)\left(1-D_{0\Lambda\uparrow}\right)R_{\Lambda+}\left(\Omega_v,\Omega_s\right)+\left(1-D_{0\Lambda\downarrow}\right)D_{0\Lambda\uparrow}\overline{R'}_{\Lambda+}\left(\Omega_s\right)\right.$$
$$\left.+D_{0\Lambda\downarrow}\left(1-D_{0\Lambda\uparrow}\right)\overline{R'}_{\Lambda+}\left(\Omega_v\right)+\left(D_{0\Lambda\downarrow}D_{0\Lambda\uparrow}-\Delta_\Lambda\right)\overline{\overline{R}}_{\Lambda+}\right]/\left(1-\Delta_\Lambda\right)$$
$$=f_{iso}+\left[\left(1-D_{0\Lambda\downarrow}\right)\left(1-D_{0\Lambda\uparrow}\right)R_{\Lambda+}\left(\Omega_v,\Omega_s\right)+\left(1-D_{0\Lambda\downarrow}\right)D_{0\Lambda\uparrow}\overline{R'}_{\Lambda+}\left(\Omega_s\right)\right.$$
$$\left.+D_{0\Lambda\downarrow}\left(1-D_{0\Lambda\uparrow}\right)\overline{R'}_{\Lambda+}\left(\Omega_v\right)+\left(D_{0\Lambda\downarrow}D_{0\Lambda\uparrow}-\Delta_\Lambda\right)\overline{\overline{R}}_{\Lambda+}\right]/\left(1-\Delta_\Lambda\right)$$

i.e. if we decompose a reflectance model $R_\Lambda\left(\Omega_v,\Omega_s\right)$ into an isotropic component f_{iso} and a directional component $R_{\Lambda+}\left(\Omega_v,\Omega_s\right)$ then the isotropic component is maintained as simply an offset to the weighted directional components, even when this approximation is used. This is a useful property resulting from the linearity of the expressions. One obvious implication is that if the surface *is* Lambertian, i.e. $R_{\Lambda+}\left(\Omega_v,\Omega_s\right)=0$, then we obtain the correct interpretation $R_\Lambda = f_{iso}$. Another point of interest is that if we were to define the offset term $f_{iso}=\overline{\overline{R}}_\Lambda$, then $\overline{\overline{R}}_{\Lambda+}=0$ and it follows that:

$$R_\Lambda = \overline{\overline{R}}_\Lambda + \frac{\left[\left(1-D_{0\Lambda\downarrow}\right)\left(1-D_{0\Lambda\uparrow}\right)R_{\Lambda+}\left(\Omega_v,\Omega_s\right)+\left(1-D_{0\Lambda\downarrow}\right)D_{0\Lambda\uparrow}\overline{R'}_{\Lambda+}\left(\Omega_s\right)+D_{0\Lambda\downarrow}\left(1-D_{0\Lambda\uparrow}\right)\overline{R'}_{\Lambda+}\left(\Omega_v\right)\right]}{\left(1-\Delta_\Lambda\right)}$$

which is in many ways a more elegant expression of the atmospheric-surface coupling.

We re-iterate at this point the comments of Lyapustin and Knyazikhin (2001) that under high anisotropy, high reflectance and (effectively) high $\overline{\overline{\rho}}_\Lambda$ (very turbid atmospheres) the approximation in equation 8 are likely to become significant, inducing at least errors of greater than a few tenths of a percent (Vermote et al., 1997).

That said, equation 9, derived from the 'full' coupling expression in equation 8, assuming only that second order plus impacts of $\overline{\overline{R}}_\Lambda - R_\Lambda$ are negligible has two very attractive properties, namely: (i) it is a linear combination of reflectance integrals; (ii) it allows the non-Lambertian effects in surface-atmosphere coupling to be treated effectively as a post-processing step to atmospheric correction, i.e. we can first proceed with an atmospheric correction routine that assumes the surface to be Lambertian (i.e. calculate R_Λ) with *no* prior knowledge of the surface BRF (or even its shape, as required in the 6s code), and incorporate the non-Lambertian interactions as part of the BRDF modelling scheme.

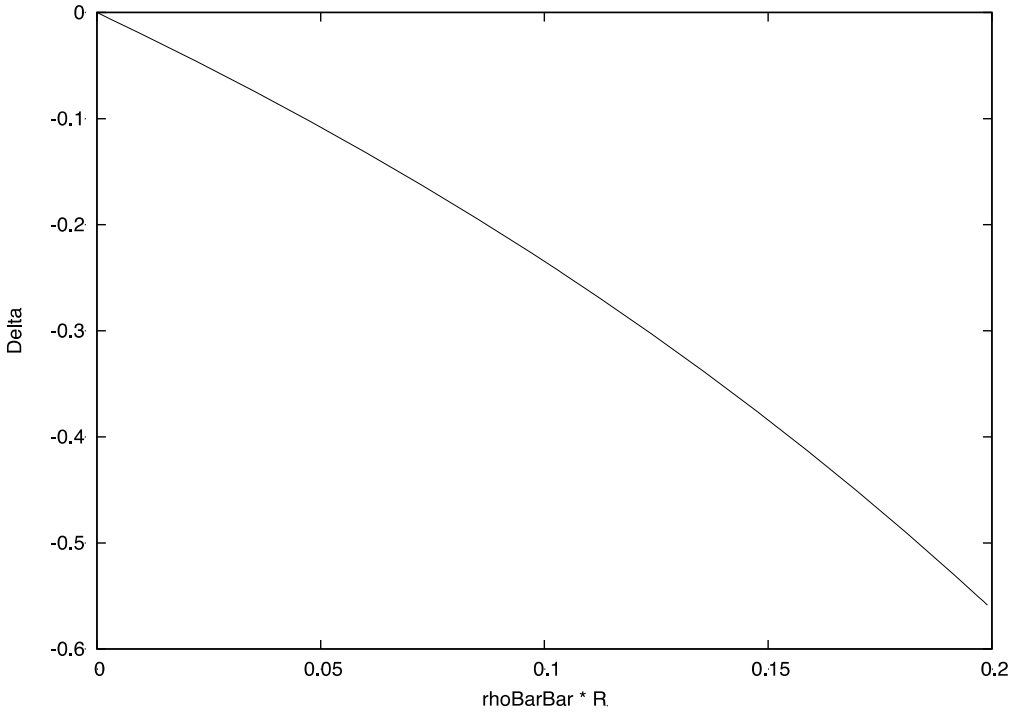

Figure 3-3. Δ_Λ **as a function of** $\overline{\overline{\rho}}_\Lambda R_\Lambda$

We have now defined a method which allows Lambertian-equivalent reflectance to be interpreted as a weighted sum of reflectance integrals. This is more elegant that previous approaches by Vermote et al. (1997), Hu et al. (1999) and Wang et al. (2010) in that their methods require iteration to achieve what should be (if the approximations hold) the same result.

The Δ_Λ term and the transmission terms $D_{0\Lambda\downarrow}$and $D_{0\Lambda\uparrow}$are estimated during the pre-processing step, and $N_{sky\lambda}$ (equation 7) can also be derived. Equation 9 contains four reflectance-related elements, all of which are normalised by $\left(1-\Delta_\Lambda\right)$: the first is the bidirectional term: the BRF $R_\Lambda\left(\Omega_v,\Omega_s\right)$, weighted by the proportion of direct illumination in the downwelling and upwelling directions. This treats radiation that is not scattered out of the direct path on the way down and up through the atmosphere. The second term is the directional-hemispherical integral of reflectance for the given solar illumination vector, i.e. radiation not scattered out of the direct path on the way down through the atmosphere, but scattered over 2π sr at the surface and diffusely transmitted through the atmosphere. The prime in the term $\overline{R'_\Lambda}\left(\Omega_s\right)$ is used to indicate that this upward diffuse transmission varies with angle, so the integral is weighted by the nomalised version of this term. The proportionate contribution of this term is a weighting by the proportion of downwelling

direct and upwelling diffuse illumination. The complementary third term is a directional-hemispherical integral weighted by the directional distribution of downwelling (sky) radiance and scattered into the viewing vector. As noted above, the weighting function would be the same for both upward and downward transmission if the atmosphere were symmetrical in the vertical direction. The final term involves the bihemispherical integral of reflectance, which is an integral over all viewing and illumination directions, weighted by the appropriate directional transmission functions. If the surface is assumed Lambertian, all reflectance terms are equal and the various products of downwelling and upwelling diffuse/directional components sum to unity.

We can use the 6s code (outputting some interim variables) to test the approximation developed above (against the full model of equation 8). We know from above that the highest errors will occur when anisotropy is high ($O\left[\left(\bar{\bar{R}}_\Lambda - R_\Lambda\right)\right]^2$ may become important), especially for higher off-nadir angles), and when the product $\bar{\bar{\rho}}_\Lambda R_\Lambda$ is high (Δ_Λ high). This implies worst case scenarios with high zenith angles, high atmospheric optical thickness (AOT), bright surfaces, variable/anisotropic BRDF functions, and shorter wavelengths. To demonstrate the operation of the linear correction term under these circumstances, we produce simulations of TOA reflectance with 6s, using AOT (550 nm) of (0.9, 0.6, 0.3) (high to moderate) in the solar principal plane (-70 to 70 degrees) for a solar zenith angle of 45 degrees, for MODIS band 3 (470 nm). The surface reflectance function is specified using the RossThick (volumetric kernel) LiSparse (geometric kernel) kernels (see below for details). Specific model parameters are given with the simulations below, for two datasets with 'bright' and 'moderate' surface reflectance.

Although we present the mathematics and physical concepts behind these linear kernel models below, it is of value here to investigate the influence of the coupling achieved in equation 9 on these kernels. For the present, it is sufficient to accept that a linear model of surface reflectance can be phrased $R_\Lambda\left(\Omega_v,\Omega_s\right) = f_{iso\Lambda} + f_{vol\Lambda}K_{vol}\left(\Omega_v,\Omega_s\right) + f_{geo\Lambda}K_{geo}\left(\Omega_v,\Omega_s\right)$. The kernels are plotted (continuous line) in figure 4 (a and b for $K_{vol}\left(\Omega_v,\Omega_s\right)$ and $K_{geo}\left(\Omega_v,\Omega_s\right)$ respectively) for the viewing/illumination angles described above. The Δ_Λ terms are shown for simulations with model parameters $\left\{f_{iso\Lambda}, f_{vol\Lambda}, f_{geo\Lambda}\right\} = \left\{0.4,0.4,0.0\right\}$ and $\left\{0.7,0.0,0.2\right\}$ respectively for (a) and (b), which are bright, highly anisotropic surfaces. In the figures, the lines with symbols correspond to an AOT of 0.9 and those without an AOT of 0.3 (high, and moderate AOT, respectively). The lines labelled 'modified kernel (Delta assumed zero)' show the modification of the kernels according to equation 9 with $\Delta_\Lambda = 0$. These express the impact of the weighted integral terms in equation 9 and are effectively dampened versions of the kernels. Note from above that there is no modification to the isotropic term. The dampening effect is much greater for AOT 0.9 than for AOT 0.3 (remember, this is a 'worst case' scenario, in the blue band), with the kernel becoming almost flat and, significantly, changing shape with increasing AOT.

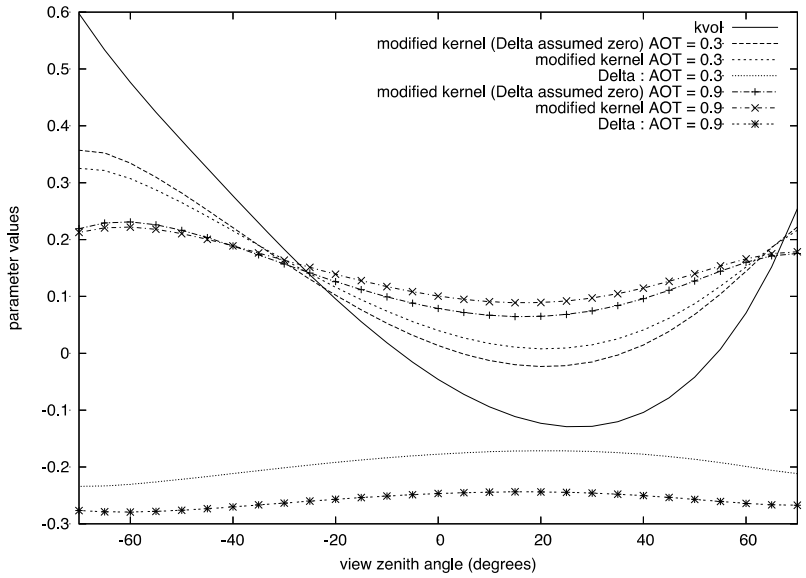

(a) Volumetric kernel terms

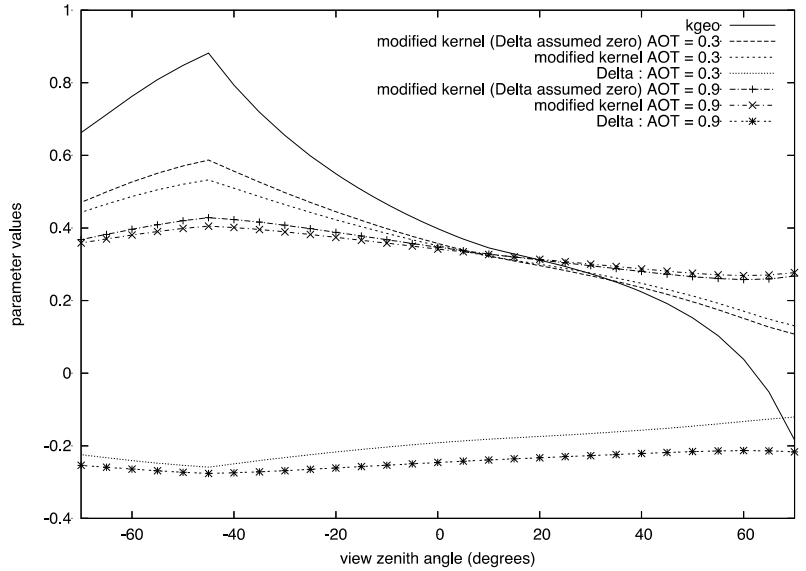

(b) Geometric kernel terms

Figure 3-4 BRF Kernels under varying atmospheric conditions and assumptions

The lines labelled 'modified kernel' include the impact of the Δ_Λ term in equation 9. As expected, these are only slight modifications from not including it, although they always show a decrease in the magnitude of the kernel. The significance of the change in magnitude of the kernels is that, if Lambertian-equivalent data are used to estimate the BRDF model parameters, the magnitude of the BRDF effects (the value of the non-isotropic kernels) will be under-estimated. This may be quite significant, as shown in tables 4-1 and 4-2 below. These tables show the results of estimating (2 term) model parameters from the Lambertian equivalent reflectance, using the various forms of kernels shown above (namely: the bidirectional kernel (i.e. accepting the Lambertian assumption); the coupling equation 9, with $\Delta_\Lambda = 0$; and the full equation 9). The RMSE obtained when estimating the model parameters is also shown for these three scenarios.

	True	Lambertian	$\Delta_\Lambda = 0$	Full
$f_{iso\Lambda}$	0.400	0.433	0.412	0.401
$f_{vol\Lambda}$	0.400	0.188	0.333	0.398
RMSE	1.000	0.971	1.000	1.000

Table 4-3-1 (i) Bright, volumetric: AOT = 0.3

	True	Lambertian	$\Delta_\Lambda = 0$	Full
$f_{iso\Lambda}$	0.700	0.534	0.654	0.703
$f_{geo\Lambda}$	0.200	0.086	0.168	0.201
RMSE	1.000	0.984	1.000	1.000

Table 4-1 (ii) Bright, geometric: AOT = 0.3

	True	Lambertian	$\Delta_\Lambda = 0$	Full
$f_{iso\Lambda}$	0.200	0.214	0.203	0.200
$f_{vol\Lambda}$	0.200	0.103	0.183	0.199
RMSE	1.000	0.972	1.000	1.000

Table 4-1 (iii) Moderate, volumetric: AOT = 0.3

	True	Lambertian	$\Delta_\Lambda = 0$	Full
$f_{iso\Lambda}$	0.350	0.272	0.338	0.351
$f_{geo\Lambda}$	0.100	0.047	0.092	0.100
RMSE	1.000	0.984	1.000	1.000

Table 4-1 (iv) Moderate, geometric: AOT = 0.3

	True	Lambertian	$\Delta_\Lambda = 0$	Full
$f_{iso\Lambda}$	0.400	0.451	0.416	0.401
$f_{vol\Lambda}$	0.400	0.079	0.317	0.397
RMSE	1.000	0.902	1.000	1.000

Table 4-3-2 (i) Bright, volumetric: AOT = 0.9

	True	Lambertian	$\Delta_\Lambda = 0$	Full
$f_{iso\Lambda}$	0.700	0.468	0.646	0.702
$f_{geo\Lambda}$	0.200	0.032	0.161	0.201
RMSE	1.000	0.909	1.000	1.000

Table 4-2 (ii) Bright, geometric: AOT = 0.9

	True	Lambertian	$\Delta_\Lambda = 0$	Full
$f_{iso\Lambda}$	0.200	0.224	0.204	0.200
$f_{vol\Lambda}$	0.200	0.044	0.179	0.199
RMSE	1.000	0.902	1.000	1.000

Table 4-2 (iii) Moderate, volumetric: AOT = 0.9

	True	Lambertian	$\Delta_\Lambda = 0$	Full
$f_{iso\Lambda}$	0.350	0.237	0.336	0.351
$f_{geo\Lambda}$	0.100	0.018	0.090	0.100
RMSE	1.000	0.984	1.000	1.000

Table 4-2 (iv) Moderate, geometric: AOT = 0.9

Clearly, accepting the Lambertian assumption can cause significant error in the parameter estimation, this error being greater for brighter surfaces and for higher AOT. The error in the isotropic parameter is significantly less than that in the 'shape' kernel, but even this can have up to around 25% relative error. It appears that the isotropic parameter is over-estimated for the volumetric scenarios and under-estimated for the geometric case. More significant, as expected from the discussion above, the volumetric and geometric kernel parameters can be severely under-estimated, by up to around 80% for AOT 0.9 or around 50% for AOT 0.3. The RMSE is generally quite high (>0.9), so the 'correct' kernel type can still explain the vast majority of the variation in the Lambertian-equivalent signal. The RMSE in the isotropic parameter is 21% relative error and 69% for the non-isotropic term for the Lambertian case.

Using equation 9, even when assuming $\Delta_\Lambda = 0$ gives a vary large improvement on this, the errors in both parameters being typically less than 10% relative, but in a few cases it may be as large as 20%. The RMSE (relative) for the isotropic term is 4.49% and 14.58% for the non-isotropic term. When the full expression is used, these relative errors are reduced to 0.25% and 0.49% respectively. It should be re-iterated that these tests are carried out under deliberately difficult conditions, and therefore the results using the full correction would seem to be a quite remarkable achievement with a linear (single pass) model.

Here, we confirm findings from other papers that using a Lambertian assumption can lead to rather high errors in BRF. We observe the impact to be a reduction in BRF magnitude relative to the bihemispherical reflectance. In all cases examined here, the true BRF is around twice the departure of the Lambertian equivalent BRF from the bihemsipherical reflectance. The point of cross-over between the various reflectance curves is observed to often be quite close to nadir, but this is not always the case. The impact of a Lambertian assumption on BRF retrieved from atmospheric correction tends to be less for low zenith angles, although this somewhat depends on this cross-over point. For sensors with view angles restricted to close to nadir, the impact may often be quite small, but this is likely less true for bright targets: it is probably not possible then to estimate the BRF of bright targets from a single view angle, unless the shape of the BRF is assumed known. This is not a new finding, but one we can stress from these results.

We find that a simple linear correction scheme is extremely effective in correcting the majority of non-Lambertian impacts. It has been observed by Hu et al. (1999) and Wang et al. (2010) that despite the Lambertian assumption causing potentially large errors in BRF, the errors in angular integrals of BRF (i.e. those we require for albedo estimation) are very much reduced, i.e. the positive and negative biases errors will broadly cancel each other out. We have not (yet) specifically investigated this point, but this is likely due to the error in the isotropic component using the Lambertian assumption being significantly lower than the other parameters. Since the weighting of the isotropic term is high relative to the other kernels in the linear models used here for albedo-related integrals of reflectance, it is most likely that (other things such as angular sampling regimes not being considered) processing data with the Lambertian assumption would give a good estimate of the bihemispherical reflectance. What should be examined in detail is the impact of the errors in the angular kernel parameters on the variation in directional-hemispherical reflectance with solar zenith angle, as this is likely dampened.

As will be seen later, modelling the (Lambertian equivalent) observations via equation 9 rather than treating them simply as direct estimates of $R_\Lambda\left(\Omega_v,\Omega_s\right)$ (as in all other schemes) allows for a very simple one-pass treatment of the diffuse illumination effects using linear kernel models. This is a novel aspect of the algorithm presented here.

In summary, we have derived a forumaltion that can describe the ‘Lambertian equivalent reflectance’, the term provided by simple atmospheric correction schemes such as those used here, as a linear function of weighted integrals of surface BRF (equation 9). This means that instead of assuming that the atmospheric scheme directly provides BRF, we can treat the dampening effects of the Lambertian assumption directly by modelling their impacts as part of any further BRF modelling.

3.3 Modelling of spectral directional reflectance and associated integrals

In the sections above, we have provided equations that relate estimates of Lambertian equivalent spectral reflectance to spectral BRF and related integrals, and also those relating these latter terms to albedo. The equations are essentially linear in nature, other than the multiple interactions between the surface and atmosphere that are of low magnitude in most cases (other than very high surface reflectance such as snow at visible wavelengths combined with a turbid atmosphere (i.e. high atmospheric reflectance)). The problem then can be stated as needing an estimate of the parameters controlling some model of spectral BRF. This could be achieved from sample observations of spectral BRF, or, via equation 8, Lambertian equivalent spectral reflectance.

There are many models that could be considered for this task, but since we do not require any physical interpretation of the model parameters a fully physical model is not necessary here. Rather, we can use the simplest form of model that is capable of well describing the spectral BRF of all (or as many as possible) surface types. A further consideration is that the model should be rapid to calculate and fit straightforwardly into an optimal estimation framework. These criteria suggest the use of 'parametric' or so-called 'semi-empirical' BRF models, such as the kernel-based models or RPV family. We might also loosely term these approaches to modeling 'additive' and 'multiplicative' kernel methods. Both approaches fulfill the fundamental requirement that they should be general in their application (i.e. capable of describing the angular variation of reflectance for a wide variety of cover types). Multiplicative formulations, exemplified by the RPV and MRPV models (Lavergne et al., 2006), are semi-analytical expression in which parameters are either exponent or straight multiplicative terms. The models tend to be near-linear under a log transform which can facilitate (linear) inversion, although due to the generally simple analytical form of the models, partial derivative expressions can easily be formulated to permit non-linear regression. Additive models, exemplified by the Ross-Li model combinations used in generation of the MODIS and MSG BRDF/albedo product streams (e.g. Schaaf et al., 2002) are essentially phrased as proportionate mixtures of archetype scattering behaviours (isotropic, volumetric and shadowing). It is generally found that there is little difference in any angular integral products using these two methods (Lucht and Lewis, 2000; Lyapustin et al., 2006), although each may have particular advantages and disadvantages under particular scenarios.

One particular advantage of the additive kernel models is their linear form. This has several implications, including ease of inversion and error propagation, linear spatial scaling of model parameters, the ability to pre-calculate angular integrals of the kernels (Lewis, 1995), and also, as we will show, insensitivity of the ordering of the two steps involved in albedo inference noted above. This latter quality will prove particularly important for GlobAlbedo applications, and so all examples below will proceed within a framework of additive kernels. Further, the practicalities of equation 8 further suggest that a model that is linear in form would be of value.

For these various reasons we therefore opt for linear kernel-driven models in this product. Within this family of models, there are several options. The most obvious choice is to use the same set of kernel models as the MODIS BRDF/albedo product, as this would afford opportunities to directly compare GlobAlbedo and MODIS albedo at the model parameter level. Indeed, the same kernel set is used operationally for the SEVIRI albedo product,

and can therefore be seen as an 'accepted' fundamental set that we may call Isotropic, RossThick and LiSparseModisReciprocal. kernels Options that should be considered are: (i) the hotspot enhancement model of Maignan et al. (2004); and (ii) the LiTransit model of Li et al. (1999).

A linear model of this family can be written:

$$R_\lambda(\Omega,\Omega') = f_{iso\lambda} + f_{vol\lambda}k_{vol}(\Omega,\Omega') + f_{geo\lambda}k_{geo}(\Omega,\Omega') \quad \textbf{10}$$

where the model parameters $f_{x\lambda}$[3], $x = \{iso, vol, geo\}$ are defined as a function of wavelength. The angular kernels $k_x(\Omega,\Omega')$ (for *x=iso*, $k_x(\Omega,\Omega') \equiv 1$) are functions of viewing and illumination angle only.

The concept behind the kernel models is 'semi-empirical' in that they start from physically-based principles and are then combined in an empirical manner. Two main versions of the volumetric kernels exist: RossThick and RossThin, being based on slightly different approximations in the linearization process (optically thick, and optically thin media, respectively). The 'theoretical' basis for these models is a solution for first order scattering from a medium of infinitesimal scatterers (leaves) over a soil background. The leaves are assumed uniformly distributed, with a spherical angular distribution, and of equal reflectance and transmittance $s/2$. The soil is assumed Lambertian, of reflectance ρ_0. These assumptions give (Roujean et al., 1992; Wanner et al., 1995):

$$R_{vol} = \frac{4s}{3\pi}\frac{(\pi/2-\xi)\cos\xi + \sin\xi}{\mu_i + \mu_v}\left(1-e^{-X}\right) + \rho_0 e^{-X}$$

with

$$X = \frac{LAI}{2}\left(\frac{\mu_i + \mu_v}{\mu_i \mu_v}\right)$$

where $\cos\xi = \cos\vartheta_i\cos\vartheta_v + \sin\vartheta_i\cos\vartheta_v\cos\phi$ is the cosine of the phase angle (for relative azimuth ϕ). All angles are in radians. If *LAI* is assumed high, $e^{-X} \approx e^{-LAIB}$ where *B* is assumed constant, equal to an average of the zenith angle function $\langle(\sec\vartheta_i + \sec\vartheta_v)/2\rangle$. This step is a linearization of the model so it can be expressed:

[3] Note that when convenient in formulae below, we refer to these parameters by an index, so that $f_{iso} = f_0, f_{vol} = f_1, f_{geo} = f_2$, similarly the kernels.

$$R_{vol} = c_{1\lambda} k_{vol}(\Omega,\Omega') + c_{2\lambda}$$

with

$$\begin{aligned} k_{vol}(\Omega,\Omega') &= \frac{(\pi/2 - \xi)\cos\xi + \sin\xi}{\mu_i + \mu_v} - \frac{\pi}{4} \\ c_{1\lambda} &= \frac{4s}{3\pi}\left(1 - e^{-LAIB}\right) \\ c_{2\lambda} &= \frac{s}{3} + \left(\rho_0 - \frac{s}{3}\right)e^{-LAIB} \end{aligned}$$

Note that the angular kernel $k_{vol}(\Omega,\Omega')$ is designed to equal zero at nadir viewing and illumination (following Roujean et al., 1992). Implementation of this kernel is aided by taking absolute values of view zenith angles whilst adding π to the relative azimuth where the view zenith was negative. Relative azimuth angles of zero, with the same viewing and illumination zenith angles, define the hot spot direction.

Breon et al. (2002) (see also Maignan et al., 2004) criticize the Ross kernel models because although they are created to mimic first order scattering, they ignore enhanced reflectance in the backscatter (hot spot direction). They suggest a 'hot spot' model for these kernels, which for RossThick[4] gives:

$$k'_{vol}(\Omega,\Omega') = \frac{(\pi/2 - \xi)\cos\xi + \sin\xi}{\mu_i + \mu_v}\left(1 + \frac{1}{1 + \xi/\xi_0}\right)$$

where the parameter ξ_0 controls the angular width of the hot spot feature. For low phase angles $(\xi \approx 0)$, the enhancement factor is equal to 2. At $\xi = \xi_0$ the enhancement factor is 1.5, and for $\xi >> \xi_0$ it tends to unity. There are two main arguments for the inclusion of this modification: (i) the hot spot is a real feature of first order volumetric scattering that is otherwise ignored; (ii) Observations from POLDER over a wide range of cover types (Breon et al. 2002) suggest that the parameter ξ_0 might reasonably be fixed to a value equating to 1.5°. The arguments for not including this term are: (i) most of the sensors we are dealing with very seldom have sampling near to the hot spot; (ii) any missing hot spot effects will likely be compensated for by the geometric kernel (see below); (iii) multiple

[4] Note that the normalisation term is left out here.

scattering is assumed isotropic in these models (see below) but any failings in this assumption are likely to be compensated for in the volumetric kernel. Including a strong hot spot effect based on considerations of first order scattering might therefore over-emphasise the feature, especially when poorly constrained by sampling; (iv) The hot spot feature at the angular widths of interest here has little impact on angular integrals (although it does have an impact on angular normalisation); (v) the MODIS processing chain does not use this modification, so if we include it here we will not be working with the same kernel set as that sensor. In fact, none of these reasons for not using this enhancement are very strong, but the latter, the fact that the kernel parameters would not be consistent with MODIS, has a practical impact for the optimal estimation framework used here, so we will not include this term.

Several options exist for the geometric kernel. The first to be explicitly formulated for this form of modelling is that due to Roujean et al. (1992). A family of kernels was defined as part of the 'ambrals' model for MODIS processing (Wanner et al., 1995). As with the Roujean geometric kernel, they are derived from considerations of the variation in the proportion of sunlit and shaded areas of a pixel viewed, as a function of the viewing and illumination geometries. The so-called Li kernels (in ambrals) are derived from consideration of these terms for a set of spheroids on a flat plane. An import term in all such considerations is the horizontal distance between the Sun and view directions. LiSparse is a model of the proportion of sunlit canopy (protrusion) and ground (K_C and K_G) with mutual shadowing effects ignored. The crown spheroids have vertical length 2B and horizontal width 2R and are centred at distance H above the ground. The crown and ground are assumed to have the same brightness term, *C*, so:

$$R_{geo} = C\left(K_C + K_G\right)$$

where:

$$K_C = \left(1 - \exp\left\{-\frac{\chi}{\mu_v'}\right\}\right)\frac{\left(1+\cos\xi'\right)}{2}$$

$$K_G = \exp\left\{-\chi\left[\frac{1}{\mu_v'} + \frac{1}{\mu_i'}\right]\left[1 - t + \cos t \sin t\right]\right\}$$

$$\cos t = \frac{H}{B}\frac{\sqrt{\Delta^2\left(\Omega,\Omega_s\right) + \left(\tan\vartheta_i' \tan\vartheta_v' \sin\phi\right)^2}}{1/\mu_i' + 1/\mu_v'}$$

Since $\cos t$ may lie outside of the bounds [-1,1] it needs to be limited to is range.

All primed zenith angles are defined by the function:

$$\vartheta' = \tan^{-1}\left(\frac{B}{R}\tan\vartheta\right)$$

Here, χ is the canopy cover (nadir view). As we can see, even under these simplifying assumptions, the (first order) reflectance depends (other than an overall brightness term *C*) on three parameters: canopy cover, spheroid aspect ratio, and spheroid relative height above the ground.

In the sparse approximation, χ is assumed small, so $e^X \approx 1+X$, which gives:

$$k_{geo-sparse}(\Omega,\Omega') = B + \frac{1}{2}\frac{(1+\cos\xi')}{\mu_v'}$$

$$B = \left[\frac{(t-\cos t\sin t)}{\pi} - 1\right]\left(\frac{1}{\mu_i'}+\frac{1}{\mu_v'}\right)$$

For the dense approximation, a concept of mutual shadowing is incorporated and the exponential term is assumed small. This gives rise to:

$$k_{geo-dense}(\Omega,\Omega') = \frac{(1+\cos\xi')}{-\mu_v' B} - 2$$

Soon after the publication of Wanner et al. (1995) it was recognised that there would be some disadvantages to these kernels not being reciprocitous, so slight modifications were made, giving:

$$k_{geo-sparse-recip}(\Omega,\Omega') = B + \frac{1}{2}\frac{(1+\cos\xi')}{\mu_v'\mu_i'}$$

$$k_{geo-dense-recip}(\Omega,\Omega') = \frac{(1+\cos\xi')}{-\mu_v'\mu_i' B} - 2$$

For MODIS processing, the parameter H/B is fixed to 2.0 and B/R to 1.0 for the Sparse kernel and originally 2.0 and 2.5 respectively for the Dense kernel. Here, as in the current MODIS product, we use only the LiSparseReciprocal kernel (with H/B = 2.0 and B/R = 1.0).

A criticism levelled at the Li kernels (Li et al., 1999; Gao et al., 2000) is the rather rapid rate of change of the sparse kernels as a function of angle for high zenith angles. This leads to a new compromise kernel, LiTransit for which:

$$k_{LiTransit} = \begin{cases} k_{sparse} & B \le 2 \\ \frac{2}{B} k_{sparse} & B > 2 \end{cases}$$

This kernel modification should seriously be considered for GlobAlbedo, but for the moment, we choose not to employ it to allow backward compatibility with the MODIS product.

Figure 3-5 and 9 show examples of the main kernel types for a range of solar zenith angles. Figure 3-5 shows the non-reciprocal version of the Li kernels. The reason for this is that those are then comparable to the figures in the original paper by Wanner et al. (1995), so a comparison of these figures and those from that paper serve to validate the kernel model implementation[5].

It also shows the Li kernels with the hot spot modification noted above. Figure 9 shows the 'standard' versions of the kernels.

Lewis (1995) describes some of the implications of using linear models for albedo estimation. Of particular relevance here is that:

$$\int d\Omega \int R_\lambda(\Omega,\Omega') g(\Omega,\Omega') d\Omega' = f_{iso\lambda} + f_{vol\lambda} K_{vol}(\Omega,\Omega') + f_{geo\lambda} K_{geo}(\Omega,\Omega') \qquad \textbf{11}$$

where

[5] A publicly-available test version of the kernel code is implemented by Prof. P. Lewis in python and is available for download from: http://www.geog.ucl.ac.uk/~plewis/globAlbedo/Kernels.py. As an example download http://www.geog.ucl.ac.uk/~plewis/globAlbedo/tester.py and run this by typing:

```
computer% python tester.py
```

This will then produce plots comparable with the kernels defined in Wanner et al. (1995), and by changing the options, any of this family of kernels.

$$K_x(\Omega,\Omega') = \int d\Omega \int k_x(\Omega,\Omega') g(\Omega,\Omega') d\Omega'$$

for any $g(\Omega,\Omega')$, i.e. the separation of angular and spectral terms in equation 10 facilitates dealing with angular integrals in any equations involving BRF. This applies both to the estimation of albedo and to the relationship between Lambertian equivalent reflectance and BRF.

Thus, we can write the 'black sky albedo' as:

$$\overline{R}_\lambda(\Omega_i) = f_{iso\lambda} + f_{vol\lambda}\overline{K}_{vol}(\Omega_i) + f_{geo\lambda}\overline{K}_{geo}(\Omega_i)$$

with

$$\overline{K}_x(\Omega_i) = \frac{1}{\pi}\int_0^{2\pi} d\phi_v \int_0^1 K_x(\Omega_v,\Omega_i)\mu_v d\mu_v$$

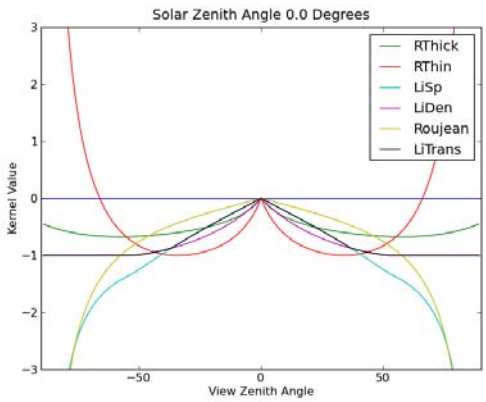

(a) SZA 0°

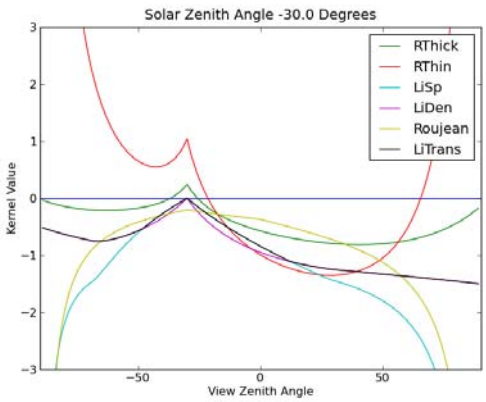

(b) SZA 30°

Figure 3-5. Linear Kernels (Principal plane) -- non-reciprocal Li and Ross HS

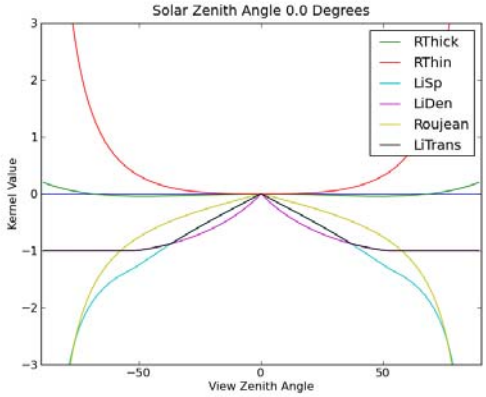

(a) SZA 0°

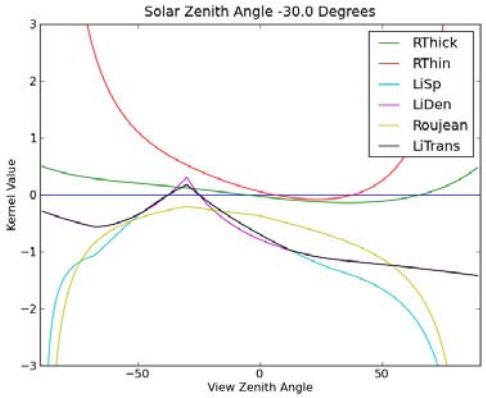

(b) SZA 30°

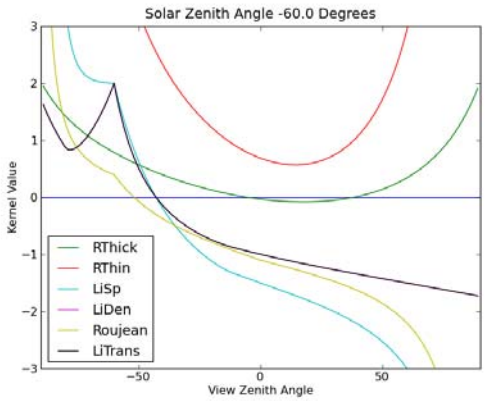

(c) SZA 60°

Figure 3-6. Linear Kernels (Principal plane) – Reciprocal Li

The bihemispherical integral of reflectance ('white sky albedo') becomes:

$$\overline{\overline{R}}_\lambda = f_{iso\lambda} + f_{vol\lambda}\overline{\overline{K}}_{vol} + f_{geo\lambda}\overline{\overline{K}}_{geo}$$

$$\overline{\overline{K}}_x = \frac{1}{\pi}\int_0^{2\pi} d\phi_i \int_0^1 \overline{K}_x(\Omega_i)\mu_i d\mu_i$$

And similarly, the $N_{sky\lambda}$-weighted integral:

$$\overline{\overline{R'}}_\lambda = f_{iso\lambda} + f_{vol\lambda}\overline{\overline{K'}}_x + f_{geo\lambda}\overline{\overline{K'}}_x$$

$$\overline{\overline{K'}}_x = \frac{1}{\pi}\int_0^{2\pi} d\phi_i \int_0^1 \overline{K}_{x\lambda}(\Omega_i)N_{sky\lambda}(\Omega_i)\mu_i d\mu_i$$

so that the spectral albedo can be written:

$$A_\lambda(\Omega_s) = \frac{f_{iso\lambda} + f_{vol\lambda}K_{vol,\lambda}(\Omega_s) + f_{geo\lambda}K_{geo,\lambda}(\Omega_s)}{1 - D_{0\lambda}\overline{\overline{\rho}}_\lambda\left(f_{vol\lambda}\overline{\overline{\delta K}}_{vol,\lambda} + f_{geo\lambda}\overline{\overline{\delta K}}_{geo,\lambda}\right)} \quad \textbf{12}$$

where

$$\overline{\overline{\delta K}}_{x,\lambda} = \overline{\overline{K}}_x - \overline{\overline{K'}}_{x,\lambda}$$

$$K_{x,\lambda}(\Omega_s) = (1 - D_{0\lambda})\overline{K}_x(\Omega_s) + D_{0\lambda}\overline{\overline{K'}}_x$$

Note that $K_{x,\lambda}(\Omega_s)$ is a function of wavelength, through its dependence on the proportion of diffuse illumination and also through any spectral dependency in $N_{sky\lambda}$.

Equation 12 gives albedo in terms of the kernel model parameters and functions (integrals and weighted integrals) of the kernels. All integrals can be pre-computed and approximated by analytical functions (as supplied with the MODIS BRDF/albedo product

for non-weighted components) or stored as look up tables (as a function of solar/viewing zenith angle and atmospheric state).

Equation 11 also has consequences for our treatment of Lambertian equivalent observations (c.f. equations 8 and 9). In particular, ignoring for the moment integrals over waveband, our model for Lambertian equivalent reflectance becomes simply:

$$R_\lambda = f_{iso\lambda} + f_{vol\lambda} K'_{vol}(\Omega,\Omega') + f_{geo\lambda} K'_{geo}(\Omega,\Omega') \qquad \textbf{13}$$

where

$$K'_x = t_0 k_x(\Omega_v,\Omega_s) + t_1 \overline{K'}_x(\Omega_s) + t_2 \overline{K'}_x(\Omega_v) + t_3 \overline{\overline{K}}_x \qquad \textbf{14}$$

$$\begin{aligned} t_{0x} &= (1-D_{0\lambda\downarrow})(1-D_{0\lambda\uparrow}) \\ t_{1x} &= (1-D_{0\lambda\downarrow})D_{0\lambda\uparrow} \\ t_{2x} &= D_{0\lambda\downarrow}(1-D_{0\lambda\uparrow}) \\ t_{3x} &= D_{0\lambda\downarrow}D_{0\lambda\uparrow} \end{aligned} \qquad \textbf{15a}$$

Incorporating the non-linear correction effects in equation 9 and considering these as average impacts over a waveband Λ:

$$\begin{aligned} t_{0x} &= (1-D_{0\Lambda\downarrow})(1-D_{0\Lambda\uparrow})/(1-\Delta_\Lambda) \\ t_{1x} &= (1-D_{0\Lambda\downarrow})D_{0\Lambda\uparrow}/(1-\Delta_\Lambda) \\ t_{2x} &= D_{0\Lambda\downarrow}(1-D_{0\Lambda\uparrow})/(1-\Delta_\Lambda) \\ t_{3x} &= (D_{0\Lambda\downarrow}D_{0\Lambda\uparrow}-\Delta_\Lambda)/(1-\Delta_\Lambda) \end{aligned} \qquad \textbf{15b}$$

Equation 14 (& 15a or 15b if the non-linear effects are included) defines modified versions of the kernels to be used in modelling the Lambertian equivalent reflectance. This means that if parameter estimation proceeds using these definitions rather than simply those in equation 10, the impact of the angular integrals on reflectance (including the directional distribution of sky radiance) is automatically taken into account. This is a powerful concept, since it potentially avoids the need for iteration to account for BRDF effects in atmospheric correction. Practically then, any scheme designed to provide optimal estimates of the model parameters from satellite observations can proceed with atmospheric correction based on Lambertian surface assumptions, so long as these

modified kernels are used rather than the original definitions. Since all of the modifications to the kernels rely on estimates of atmospheric parameters, it makes sense for these modified kernels (equation 14) to be output as part of the atmospheric correction scheme. Note also that in defining a general scheme of processing, if data which have been 'fully' atmospherically corrected happen to be used as input data, this is simply achieved by setting the diffuse *D* terms to zero.

3.4 Modelling albedo

Equation 12 above provides the recommended formula to estimate albedo. For this estimate, detailed knowledge of the atmospheric state is required to provide weighted angular integrals and the atmospheric spherical albedo for multiple interaction effects. Since the numerator of equation 12 will tend to be quite small, except for strongly anisotropic bright surfaces (e.g. snow), we can more generally consider albedo to be adequately represented by its linear approximation (i.e. ignoring the denominator), so we can write broadband albedo $A_\Lambda(\vartheta_s)$ as:

$$A_\Lambda(\vartheta_s) = f_{iso\Lambda} + f_{vol\Lambda}K_{vol\Lambda}(\vartheta_s) + f_{geo\Lambda}K_{geo\Lambda}(\vartheta_s) \quad \textbf{16a}$$

where, as before

$$K_{x\Lambda}(\vartheta_s) = (1 - D_{0\Lambda})\overline{K}_x(\vartheta_s) + D_{0\Lambda}\overline{\overline{K'}}_x \quad \textbf{16b}$$

The term $\overline{K}_x(\vartheta_s)$ is simply the directional-hemispherical integral of reflectance (black sky albedo). The term $\overline{\overline{K'}}_x$ is more complicated, being the N_{sky} weighted bihemispherical integral of $K_X(\Omega_v,\Omega_s)$. This term depends on atmospheric properties and would need to be defined in a LUT for each kernel as a function of solar zenith angle and atmospheric properties. The same is true of the proportion of diffuse radiation $D_{0\Lambda}$. In calculating albedo in a satellite albedo product then, we have to choose some set of values for the atmospheric terms. Since atmospheric measurements will not always be available (e.g. when there are no observations) and will in any case vary spatially and over a compositing period, some fixed values should be used. Clearly, albedo varies significantly with solar zenith angle for most cover types, so a reference solar zenith is also usually decided upon for product output, generally local solar noon.

From the assumed fixed atmospheric properties and reference solar zenith angle, we can calculate $\overline{\overline{K'}}_x$, $D_{0\Lambda}$ and $\overline{K}_x(\vartheta_s)$ (along with the terms in the numerator of equation 12 if required) to output a standard albedo product[6].

[6] Technically, these terms will also depend on the altitude of the site being observed, but this can be ignored for the standard albedo product.

Many users will not simply want a 'reference' albedo at some standard sun angle and atmosphere but will want to apply either equation 12 or equation 16 themselves to data. In such as case, the users need to calculate all of the relevant atmospheric terms and weighted angular integrals.

For cases when the atmospheric optical thickness is low and the solar zenith angle not too high (Lewis and Barnsley, 1994), and also the brightness and anisotropy of the ground not too great (otherwise the denominator of equation 12 will have more of an impact) it is appropriate to use a simpler formulation for estimating albedo, i.e. equation 16 with:

$$K_{x\Lambda}(\vartheta_s) = (1 - D_{0\Lambda})\overline{K}_x(\vartheta_s) + D_{0\Lambda}\overline{\overline{K}}_x$$

i.e. using the unweighted bihemispherical integrals of the kernels. Provided the user can estimate the proportion of diffuse illumination, albedo can then be very simply estimated by using fixed values of $\overline{\overline{K}}_x$, the 'white sky' integrals.

The difference between the 'white sky' kernel value for this simplified 'isotropic illumination' and the 'full' N_{sky}-weighted expression is shown in figure 10. The 'full' expression is much more sensitive to aerosol loading than the isotropic approximation as this not only alters the proportion of diffuse illumination, but also the directional distribution of the downwelling radiance (or its normalised equivalent N_{sky}).

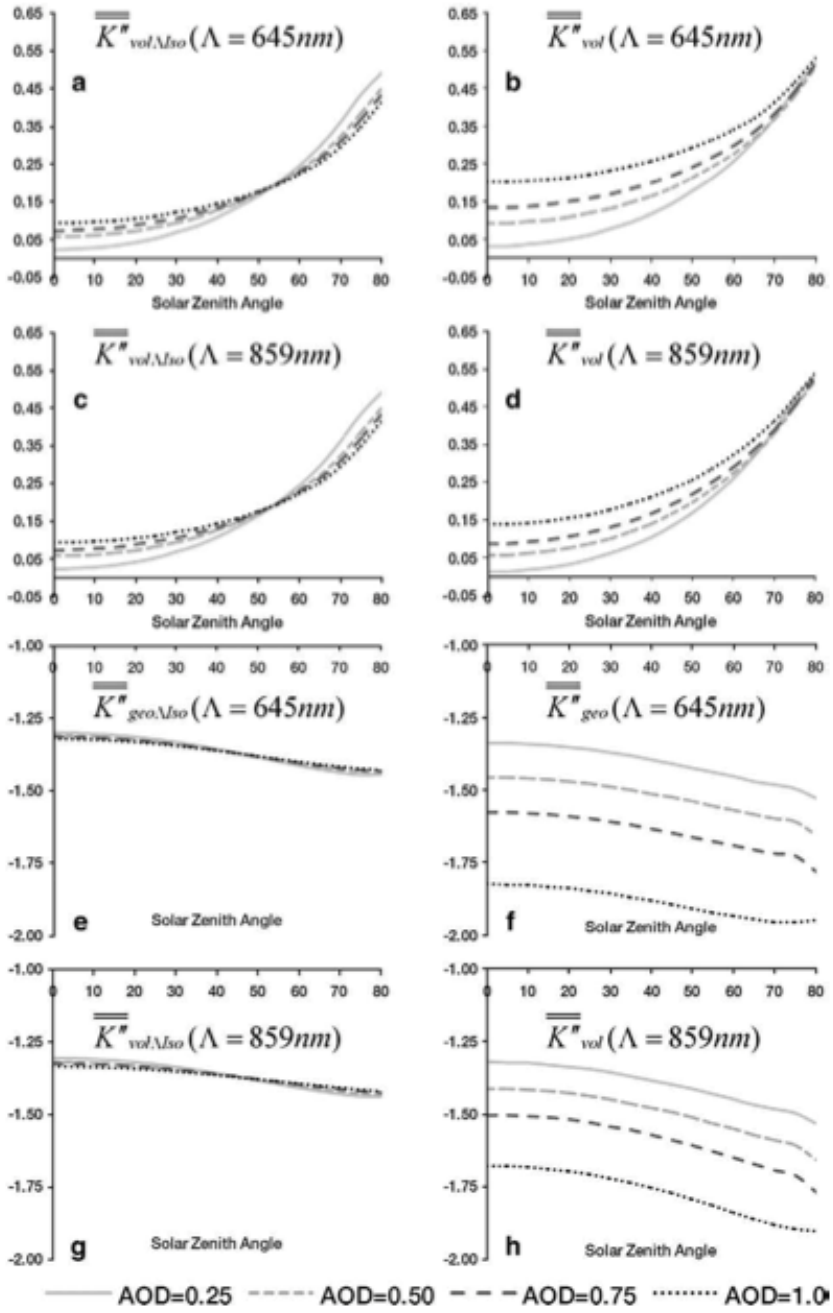

Figure 3-7. Angular integrals of kernels for varying aerosol optical depth (AOD) and solar zenith angles for MODIS red and NIR bands. The left column shows terms $K_{x\Lambda}(\vartheta_s)$ assuming isotropic illumination for the diffuse component. The results in the right column are for N_{sky}-weighting of the terms. From Roman et al. (2010).

Unweighted angular integrals of the kernels are given in Lucht et al., (2000) as polynomial functions and fixed values for $\overline{\overline{K}}_x$. The directional-hemispherical integral of reflectance as a

function of solar zenith angle ϑ_s can be approximated for most practical purposes by the following for kernel *x*:

$$\overline{K_x}(\vartheta_s) = g_{0,x} + g_{1,x}\vartheta_s^2 + g_{2,x}\vartheta_s^3$$

with the polynomial coefficients given by:

Term	Isotropic (iso)	Ross-Thick (vol)	Li-Sparse (geo)
g_0	1.0	-0.007574	-1.284909
g_1	0.0	-0.070887	-0.166314
g_2	0.0	0.307588	0.041840
$\overline{\overline{K}}_x$	1.0	0.189184	-1.377622

Table 3-3 Polynomial coefficients for black- and white-sky albedo

These coefficients fit nearly perfectly up to solar zenith angles of 80^o (Figure 11).

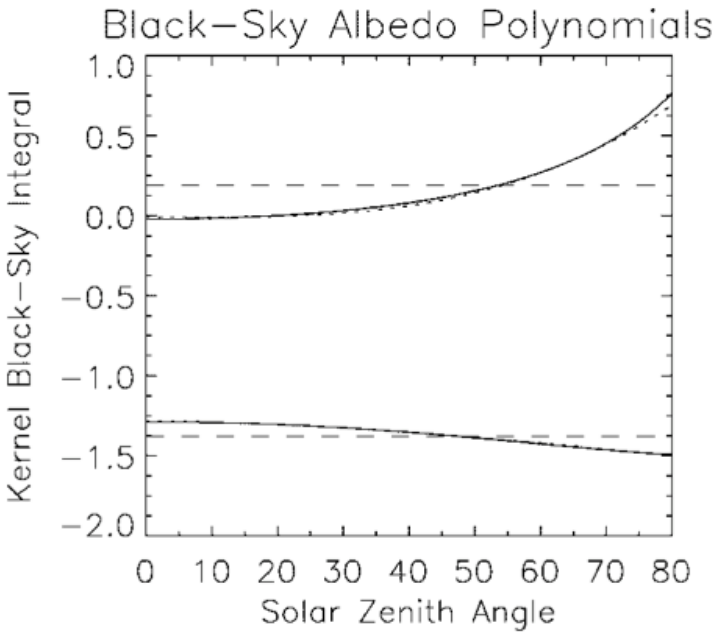

Figure 3-8. (From Lucht et al., 2000) Polynomial representation of black sky albedo as a function of solar zenith angle. Values shown for RossThick and of the LiSparse-R kernel (solid lines) and their polynomial representations (dotted lines).

Also shown is the value of the white-sky albedo as a constant for each kernel (dashed lines).

3.5 Spectral considerations

The task here can now be considered as providing an optimal estimate of the kernel model parameters from some set of satellite observations (from MERIS, (A)ATSR(-2) and VEGETATION sensors). One route to this would be to process the estimates of spectral BRF (or rather Lambertian equivalent reflectance) from each sensor independently to (narrow band) spectral parameter estimates and to then combine these. Since the spectral sampling of each instrument is different, this is not a straightforward task however. Further, whilst spectral albedo at the (typically) narrow wavebands of the satellite sensors may be of value for some applications, they are not a required component of the GlobAlbedo product.

The narrow-to-broadband conversion of the Lambertian equivalent reflectance is performed by the GlobAlbedo spectral directional reflectance/broadband directional reflectance (SDR/BBDR) processor. A detailed description of this procedure is provided in the GlobAlbedo SDR/BBDR ATBD. Two key aspects of the narrow-to-broadband conversion procedure in GlobAlbedo must be remarked here though:

a) Narrowband reflectance is converted to broadband in three spectral intervals by means of a linear weighting process. This preserves the linear nature of the GlobAlbedo processing chain, the advantages of which have been described earlier in this document. The methodology proposed by Liang (2000) has been reproduced in order to calculate the conversion coefficients for the spectral reflectance data derived from the three instruments in GlobAlbedo in a consistent manner, and also for the broadband conversion of the D and N_{sky} parameters used to performe angular integrals (e.g. equations 6 and 7).

b) Broadband conversion is performed on directional reflectance rather than on albedo data, i.e. spectral integration is performed before angular integration. This is a unique feature of the GlobAlbedo processing chain with respect to other albedo retrieval schemes, such as that of MODIS. Interchanging the angular and spectral integrals of surface reflectance is enabled by the linear nature of the GlobAlbedo processing chain. In addition, converting all observations to broadband has other advantages: the scheme works easily with data from any sensor (e.g. data from forthcoming missions such as PROBA-V or Sentinel-3 could be incorporated simply by converting all such data into BB reflectance estimates); there is reduced complexity of the processing chain; optimal use is made of available samples (e.g. single observations not sufficient to estimate model parameters, but can be used here). Also, some issues arise from this. In particular, in order to enable the combination of the R, D and N_{sky} parameters in broadband space, it must be assumed that the integral of the product is the same as the product of integrals. Such a condition is fulfilled by those variables due to it can be assumed that they are not correlated in either spectral or angular dimensions.

3.6 Parameter estimation

3.6.1 Unconstrained parameter estimation

This stage of processing assumes that we have as 'data' input a gridded product of BBDR data for the three wavebands considered, along with associated uncertainty information.

Thus, for some pixel over location *L*, we have vectors (of dimension 1x3) of observation-derived ('observation') of (Lambertian equivalent) reflectance $R_{L,t}$ for some set of times $T_{start} \le t \le T_{end}$. Each observation has its associated uncertainty matrix $C_{O,L,t}$ of dimension 3x3, and a (9x3) vector of modified kernel terms $K'_{L,t}$ (defined in equations 14 and 15) for each of the three kernels, for each of the three broadband:

$$K'_{L,t} = \begin{bmatrix} K'_{0,0,L,t} & K'_{1,0,L,t} & K'_{2,0,L,t} & 0 & 0 & 0 & 0 & 0 & 0 \\ 0 & 0 & 0 & K'_{0,1,L,t} & K'_{1,1,L,t} & K'_{2,1,L,t} & 0 & 0 & 0 \\ 0 & 0 & 0 & 0 & 0 & 0 & K'_{0,2,L,t} & K'_{1,2,L,t} & K'_{2,2,L,t} \end{bmatrix}$$

where $K'_{b,x,L,t}$ is the modified kernel for waveband *b* and kernel *x*. Thus, our model of (Lambertian equivalent) reflectance, $\hat{R}_{L,t}$ is:

$$\hat{R}_{L,t} = K'_{L,t} F_{L,t}$$

where $F_{L,t}$ is the (1x9) vector of model parameters. The estimation of this vector $F_{L,t}$ is the target of our optimal estimation framework. If there were very many samples of $R_{L,t}$ for each *L* and *t* (over a wide range of viewing and illumination angles), then we could attempt an unconstrained estimation of $F_{L,t}$ from the observations $R_{L,t}$. However, from satellite data, we are restricted in angular sampling by the sun and view angles at particular sensor overpasses, and further limited for optical data by missing samples due to cloud (or cloud shadow). Such an unconstrained estimation is usually phased as a minimisation of a cost function J_O with an L^2 norm:

$$J_{O,L} = \sum_{i=0}^{i=N} \left(\hat{R}_{L,i} - R_{L,i}\right)^T C_{O,L,i}^{-1} \left(\hat{R}_{L,i} - R_{L,i}\right) \qquad \textbf{17}$$

for a set of *N* observations over the time period of interest. For a linear model, such as we have here, we have an analytical solution to the estimation (dropping the location subscript for convenience):

$$\left[\sum_{i=0}^{i=N} K_i'^T C_{O,i}^{-1} K_i'\right] F_t = \left[\sum_{i=0}^{i=N} K_i'^T C_{O,i}^{-1} R_i\right] \quad \textbf{18}$$

This can be phrased in vector-matrix form as:

$$M_{O,t} F_t = O_t \quad \textbf{19a}$$

where $M_{O,t}$ is a 9x9 matrix and O_t a 1x9 vector.

A measure of the goodness of fit of the model to the observation set is χ^2:

$$\chi^2 = J_{O,L} = \sum_{i=0}^{i=N} \left(\hat{R}_{L,i} - R_{L,i}\right)^T C_{O,Li}^{-1} \left(\hat{R}_{L,i} - R_{L,i}\right)$$

which can be expanded to:

$$\chi^2 = \sum_{i=0}^{i=N} \hat{R}_{L,i}{}^T C_{O,Li}^{-1} \hat{R}_{L,i} + \sum_{i=0}^{i=N} R_{L,i}{}^T C_{O,Li}^{-1} R_{L,i} - 2\sum_{i=0}^{i=N} \hat{R}_{L,i}{}^T C_{O,Li}^{-1} R_{L,i}$$

and

$$\chi^2 = F_t^T \left[\sum_{i=0}^{i=N} K_i'^T C_{O,i}^{-1} K_i'\right] F_t + F_t^T \left[\sum_{i=0}^{i=N} K_i'^T C_{O,i}^{-1} R_i\right] - 2\left[\sum_{i=0}^{i=N} R_i{}^T C_{O,i}^{-1} R_i\right] \quad \textbf{19b}$$

From 19b then, we see that since we already have access to the first and second terms on the RHS, we need only keep track of the third term $\sum_{i=0}^{i=N} R_i{}^T C_{O,Li}^{-1} R_i$ in addition to be able to efficiently calculate the χ^2.

3.6.2 Uncertainty and angular sampling

An estimate of the model parameters at time *t*, F_t, is obtained from equation 18 using a linear solver. The uncertainty in the estimates of parameters is given by (Lucht and Lewis, 2000):

$$\sigma_U^2 = U^T M_{O,t}^{-1} U$$

19c

where U is a 1x9 vector expressing a linear combination of model parameters. Thus, setting $U^T = \{1,0,0,0,0,0,0,0,0\}$ gives the uncertainty in the first element of F_t.

There are two problems with this solution however: (i) the angular sampling available tends to mean that the estimate of the model parameters is only poorly determined. In many cases, *N* can be rather small and the problem may even be under-determined; (ii) as stated, equations 17 and 18 assume that the model parameters are constant over the time period of the observations. This introduces a smoothing to the parameters.

The MODIS BRDF/albedo product (Schaaf et al., 2002) uses equation 18 to solve for model parameter estimates with $C_{O,ti}^{-1}$ as an identity matrix (i.e. assuming observation uncertainties unknown or constant). In this case σ_U^{-1} expresses the weight of determination of the linear parameter combination, a measure of how well-resolved it is for a given angular sampling configuration. Figure 12 shows some examples of the impact of angular sampling on the linear model parameters. The weight of determination is considered here as a 'noise amplification factor' as it provides the uncertainty relative to the observation uncertainty. All angular configurations assume no cloud impacts. Provided there are sufficient observations, cloud impacts can be considered as a $1/\sqrt{N}$ modification to this term. Sampling windows of 16 days are considered here. In panel (a), the nadir reflectance at mean solar zenith angle is considered (so-called NBAR). This is seen to be quite a stable measure, as it is effectively an interpolation over the set of observations. Similarly, the black sky albedo (directional-hemispherical reflectance) at mean solar zenith angle is effectively an interpolated estimate and is well-constrained. The uncertainties in these terms is seen to decrease with increasing latitude due to orbital convergence. Terms which may be outside of the convex hull of angular sampling, 'extrapolation terms' of course have higher uncertainties: the nadir reflectance and nadir illumination angle (the isotropic parameter) and the black sky albedo at nadir illumination have significantly higher uncertainties, and these uncertainties tend to increase with increasing latitude as the solar zenith angle of the observations at the overpass time is rather distant to this nadir configuration. This means that the isotropic parameter may not always be a stable term to estimate, but reflectance values or integrals nearer to the domain of the actual angular sampling will be more stable. Panel (e) considers the bihemispherical integral of reflectance (white sky albedo). This has generally higher uncertainty than most other terms, though of a similar order of magnitude to the isotropic parameter. The decrease with increasing latitude is due to the greater number of observations and range of solar zenith angles at higher latitudes. Panel (f) shows that estimates of black sky albedo as a function of solar zenith angle are heavily conditioned by the angular sampling regime. Estimates at high solar zenith angles are generally unreliable.

Figure 13 shows the weight of determination of the linear kernel model parameters (other than the isotropic term shown above). The uncertainty in the Ross-Thick parameter in particular can be rather high, but this decreases with number of samples (i.e. with

increasing latitude) and range of solar zenith angles. The uncertainty of the Li-Sparse parameter is of a similar order of magnitude to the isotropic term, although as the absolute value of this parameter is generally much smaller than the isotropic term, the relative uncertainty can be high. Figure 14 compares some of the terms in figure 12 with those obtained from using the MRVP model. The dashed lines represent results from the linear kernels and the solid and dotted lines those from MRPV. The results are very similar for both, indicating that uncertainty in these terms is largely a matter of angular sampling, rather than the particular model used. That said, the two models are of course different, and so may produce rather different results in extrapolation (i.e. outside of the domain of the angular samples).

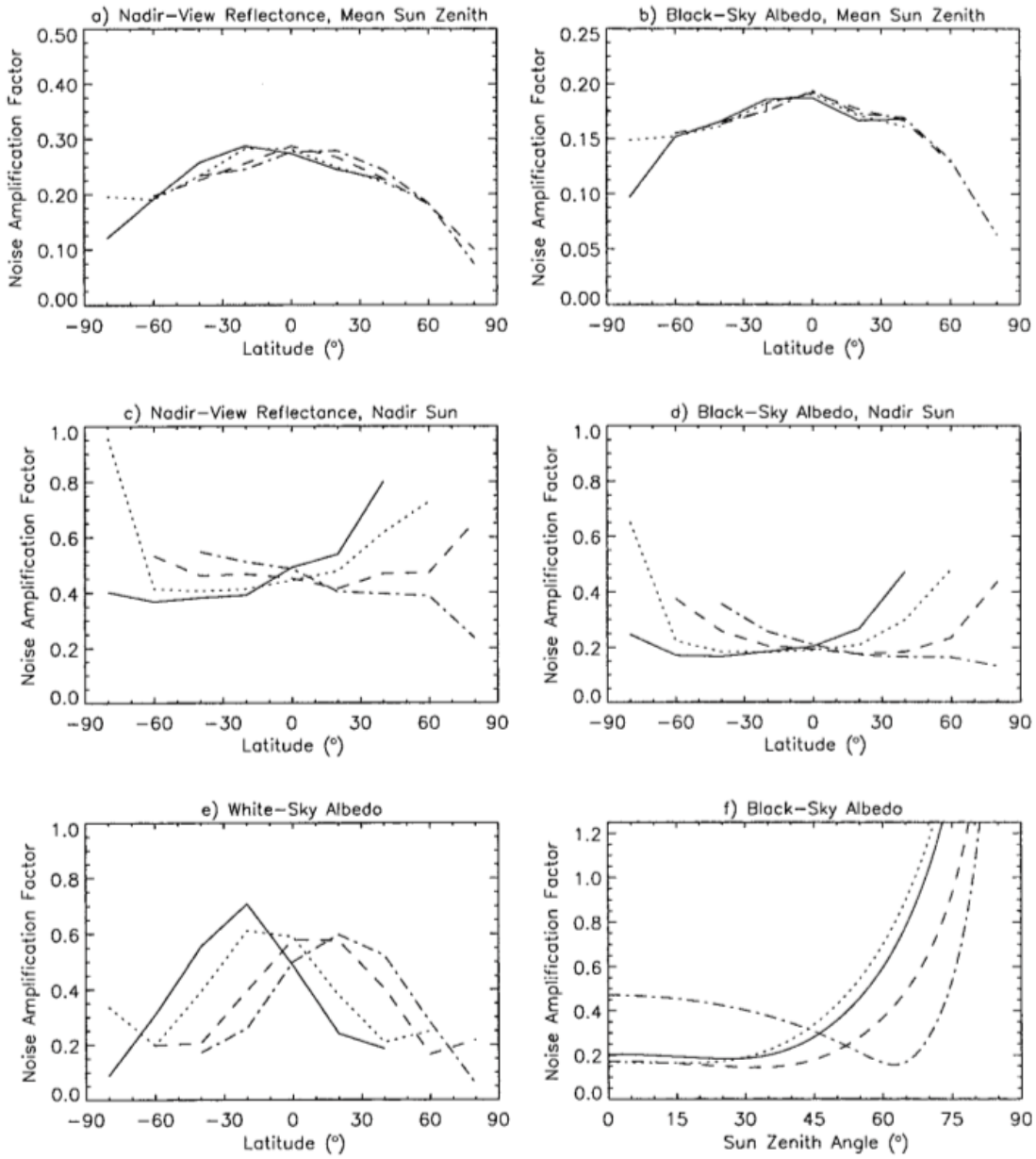

Figure 3-9. From Lucht and Lewis (2000). Noise sensitivity of the RossThick-LiSparse BRDF model. Weights of determination (noise amplication factors) are shown as a function of latitude for different 16-day time periods throughout the first half of the year, the time progressing through solid, dotted, dashed and dashed-dotted curves (days of year 0, 48, 96 and 144). Panel (f) shows the noise sensitivity of black-sky albedo extrapolation as a function of sun zenith angle for sample latitudes -60^{O}, -40^{O}, 0^{O} and 40^{O} latitude (solid, dotted, dashed, dashed-dotted curves), for sampling during the first 16-day period of the year. The terms 'mean sun zenith' and 'nadir sun' refer to evaluations at the mean sun zenith angle at which the observations were made at each respective latitude and for the case of a solar zenith angle extrapolated to nadir.

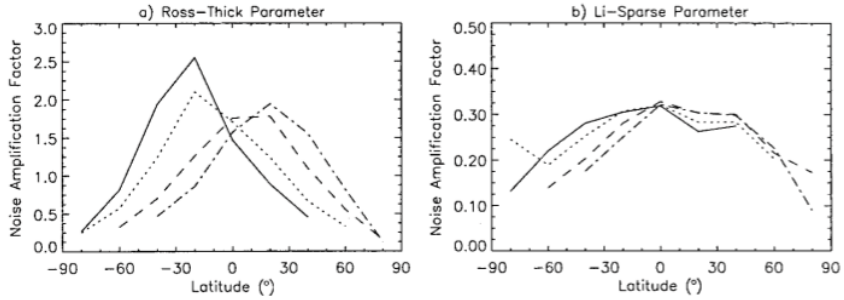

Figure 3-10. From Lucht and Lewis (2000). Impact of angular sampling on estimates of the linear model parameters. Lines have same meanings as in figure 12.

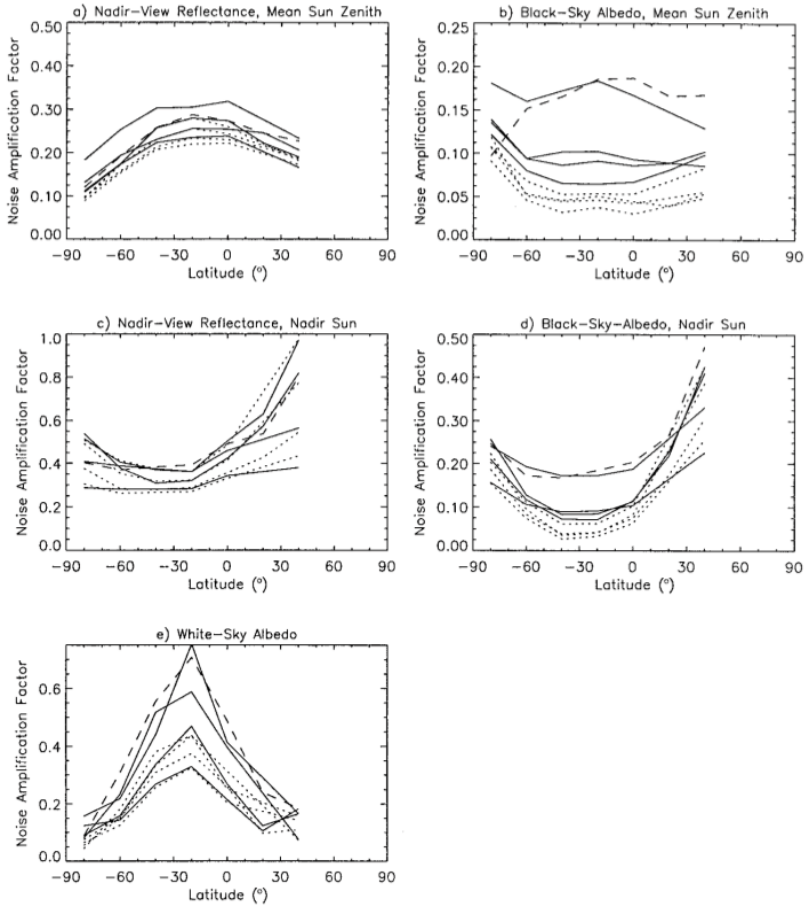

Figure 3-11. From Lucht and Lewis (2000). Noise sensitivity of the modified RPV BRDF model.

Inferred equivalent weights of determination (noise amplification factors) are shown as a function of latitude for the first 16-day period of the year and for the red (solid curves) and

near-infrared band (dotted curves) of four different land cover types. Also shown are the weights of determination for the RossThick-LiSparse BRDF model (dashed curves).

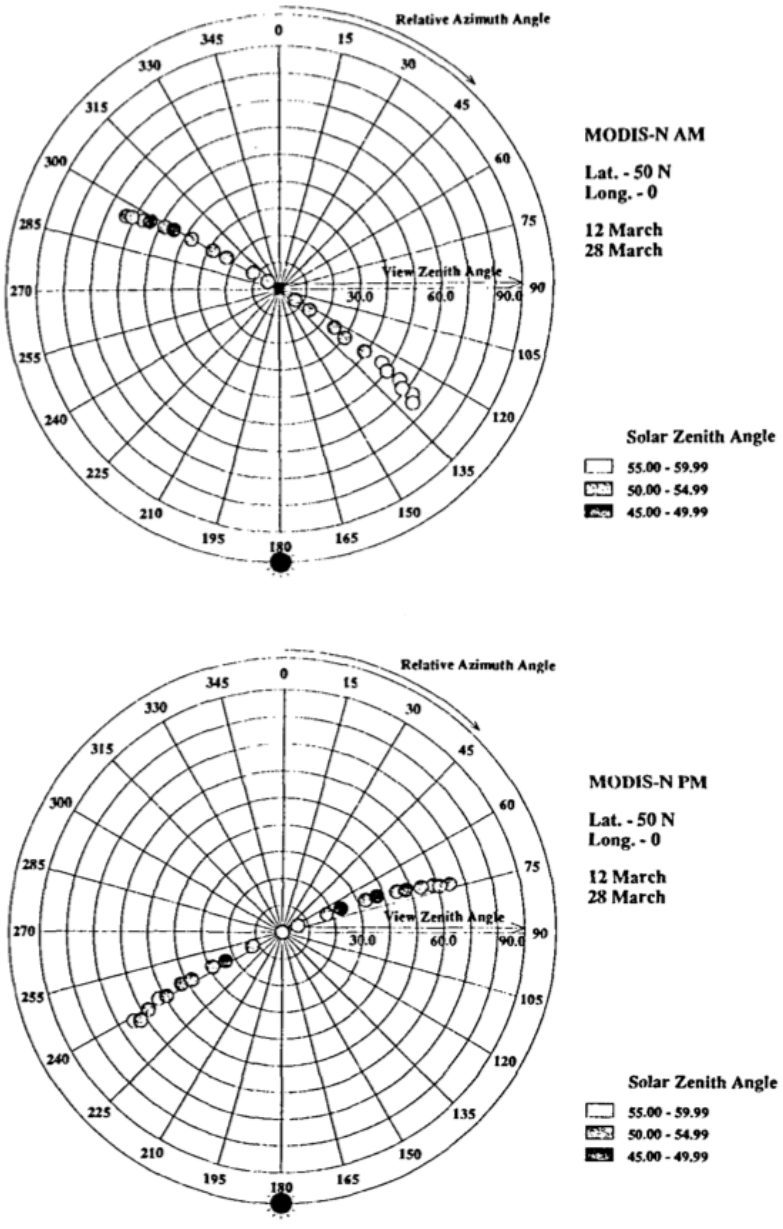

Figure 3-12. From Barnsley et al. 1994. Angular sampling of MODIS instruments (labelled MODIS-N) for the two platforms (Terra and Aqua). Concentric rings denote 10° increments of view zenith angle, ranging from 0° (i.e. nadir) at the center of the plot to 90° at the edge. Radial lines denote 15° increments of view azimuth angle,

where 0° = north and 180° = south. N.B. The width of the 'envelope' lines has been exaggerated for diagrammatic purposes.

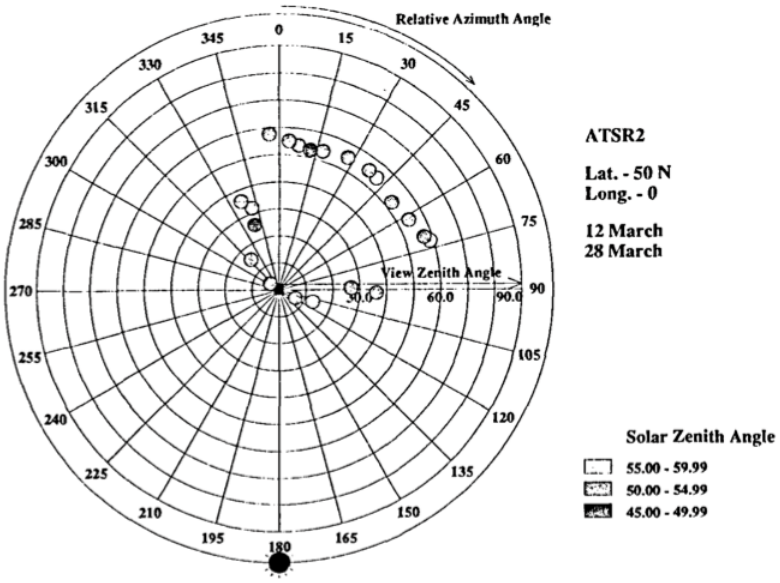

Figure 3-13. From Barnsley et al. 1994. Angular sampling of ATSR-2 instrument. Concentric rings denote 10° increments of view zenith angle, ranging from 0° (i.e. nadir) at the center of the plot to 90° at the edge. Radial lines denote 15° increments of view azimuth angle, where 0° = north and 180° = south. N.B. The width of the 'envelope' lines has been exaggerated for diagrammatic purposes.

This discussion has demonstrated that angular sampling plays a crucial role in providing reliable estimates of albedo model parameters. For the sensors under consideration here, VEGETATION has rather similar angular sampling to MODIS, and so will provide results similar to those above (though of course, from 2002 two MODIS instruments are used for the MODIS BRDF/albedo product, so the sampling number is increased). The general pattern of sampling from a wide field of view sensor such as MODIS or VEGETATION is demonstrated in figure 15. Variation in view zenith angle is achieved from cross-track sampling, leading to a slightly curved line in the polar plot. The relative azimuth of the sampling varies with latitude and time of year. The highest information content data is generally achieved through sampling in the solar principal plane. In the example in figure 15, the sampling is almost entirely cross principal plane, which is sub-optimal sampling. This relative azimuth angle and the number of samples are the main factors that impact the weight of determination shown above.

Figure 16 shows typical angular sampling possible from the ATSR-2 configuration (similarly AATSR) instrument. The pattern of angular sampling is clearly rather different to that in figure 15. There are essentially two clusters of samples, arising from the nadir and

off-nadir views of the sensor. The relative azimuth of the off-nadir samples rotates as a function of time of year and latitude. The coverage of the viewing hemisphere is rather limited, so estimates of model parameters and angular integrals will have higher uncertainties that that for VEGETATION or MODIS. MERIS angular sampling (not shown here) is similar to the near-nadir samples of figure 16, with a slightly more limited angular range.

For a product based on VEGETATION, MERIS and (A)ATSR, there is a concern that the angular sampling may not be sufficient for robust parameter estimation (the problem is ill-posed). This will be a particular problem for processing years when only ATSR-2 data are available, but is of general concern in solving for albedo estimates from sparse angular samples from satellite observations. In such a case, various constraints to the problem must be considered.

3.6.3 Temporal smoothness constraint

One of the most common approaches to dealing with ill-posed inverse problems is to apply regularisation. This is discussed in detail in e.g. Twomey (1977) or Hansen et al. (2006). In effect, this involves using one or more constraints to the cost function in equation 16. In practice, regularisation constraints are often applied to inverse problems, although they may not always be explicitly stated. The 'unconstrained' inversion of the model given above gathers samples over a 16 day window, and assumes that the parameters are constant over that time period. This is in itself a form of regularisation: the resulting model parameters will be a 'smoothed' version of the 'true' time-varying parameters.

A typical explicit example of regularisation is a first difference constraint (i.e. the parameter value tomorrow will be the same as today, to a certain degree of tolerance). This can be phrased as a model:

$$F_{t+1} - F_t = 0$$

with an uncertainty matrix C_M connecting these. Note that the parameter vector F must now be extended to include parameter values for each day, t. We will call this (1x(9x*N*)) vector simply F. A first order differential operator on is Δ, so the discrete differential of F is ΔF. With this constraint, we are able to provide estimates of the parameters at any desired time resolution (though 1 day would be a typical time step). The constraint can be included in the cost function:

$$J = \left(\hat{R} - R\right)^T C_O^{-1}\left(\hat{R} - R\right) + \left(\Delta F\right)^T C_M^{-1}\left(\Delta F\right) \qquad \textbf{20}$$

where now we have a full C_O matrix of $(3xN)^2$ and full C_M matrix of $(9xN)^2$. The minimisation of this cost function is obtained via:

$$\left[K'^{T}C_{O}^{-1}K' + \Delta^{T}C_{M}^{-1}\Delta\right]F = \left[K'^{T}C_{O}^{-1}R\right] \quad \textbf{21}$$

This approach was used by Quaife and Lewis (2010) to add a smoothness constraint to kernel-driven model parameter estimation. If C_M is considered constant, it can be represented by a scalar σ_M^2. This term then is the uncertainty in the constraint, i.e. the uncertainty in enforcing the parameter at time *t+1* to be the same as at time *t*, though we might also note that it is a Lagrange multiplier for the constraint. This form of first order difference constraint is directly equivalent to using a zero-order process model (i.e. the model is that $F_{t+1} = F_t$) in a Kalman smoother (Quaife and Lewis, 2010). The only practical difference between the approaches is that the result for all terms can be obtained at once through matrix manipulation in equation 20, whereas the Kalman smoother solves the problem sequentially (in two sweeps of the data)[7]. The term σ_M^2 in the context of the Kalman smoother is of course the uncertainty in the model prediction after one time step. The lower the value of σ_M^2, the more smooth the parameters will be, so, σ_M^2 is also thought of as a roughness parameter.

Both Kalman filters (essentially a one-directional variant of the smoother) and this direct Lagrangian approach have been applied to regularisation of linear kernel models (Qin et al., 2006; Samain et al., 2008; Quaife and Lewis, 2010). As noted, the approaches are practically identical. The difficulty in using such approaches is in defining the roughness parameter. It is not obvious, for instance, that this should be the same for all model parameters. There are many approaches to estimating this term. Samain et al. (2008) provide an estimate of the model noise covariance (related to the σ_M^2 here) as a function of land cover class, using data from previous unconstrained parameter estimations. Quaife et al. (2010) assume that the noise statistics of the observations are well-characterised and derive a roughness parameter estimate that matches this. Other approaches include generalised cross validation. Whilst any such approach may be valid and provide a good estimate of the temporal model uncertainty, it is very difficult to arrive at a solution that will be applicable globally. Thus, whilst we believe that a smoothness constraint using equation 20 may be one of the best theoretical ways to proceed with the globAlbedo product, we prefer not to implement this in the current version.

Instead, we apply a concept that we can more easily fit in with current experience of linear kernel parameter estimation. We can note that the optimal parameter estimate can be written (Quaife, 2009):

$$F = \left[K'^{T}C_{O}^{-1}K' + \Delta^{T}C_{M}^{-1}\Delta\right]^{-1}\left[K'^{T}C_{O}^{-1}\right]R = UR \quad \textbf{22}$$

[7] The approaches may also differ in the boundary conditions used (see Hansen et al., 2006 for a discussion of this).

where $U = \left[K'^T C_O^{-1} K' + \Delta^T C_M^{-1} \Delta\right]^{-1} \left[K'^T C_O^{-1}\right]$, i.e. we view the optimal estimation problem simply as a filtering problem: the optimal estimate of some element of F_t is simply the dot product of the appropriate line of U with the observations R. This can of course be phrased as a convolution problem. Thinking about the problem in this way, it should be obvious to the reader how a Kalman 'filter' can be equivalent to this constrained optimisation problem: the job of the filter (or smoother) is effectively to provide the appropriate terms in U so that the summation of these weights with the observations provides the correct estimate of F_t. In a Kalman filter, this is achieved sequentially, rather than involving manipulation of a large matrix as in 21.

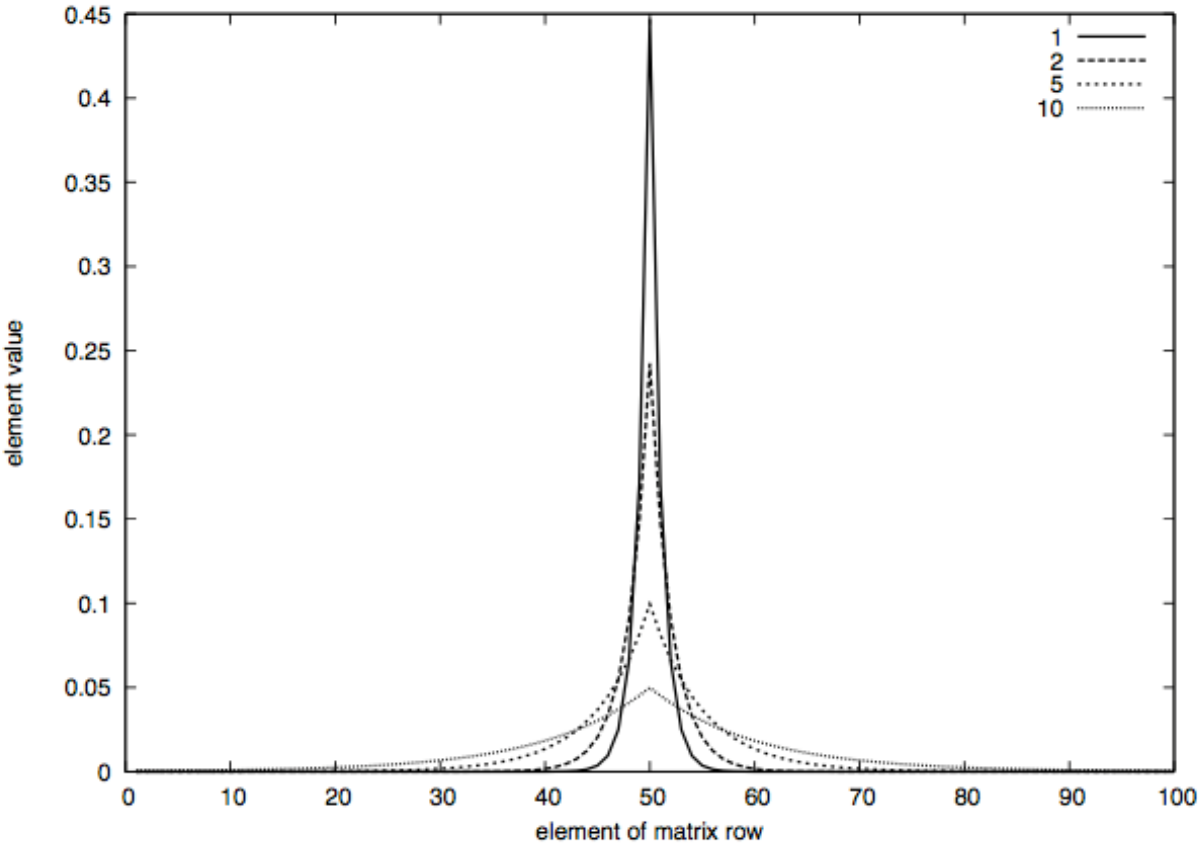

Figure 3-14. From Quaife (2009): Inverse differential operator for varying values of γ

It is of interest then to consider what these filters look like. In the case of equation 21, it is quite a complex weighting term, being a function of temporal and angular sampling. We can gain insight into the filters by considering a single parameter version of this model, i.e. $KF_t = R$ with K as an identity matrix I. Simplifying the observation variance-covariance matrix to $I\sigma_O^2$ and the constraint term to $I\sigma_M^2$ gives:

$$U = \left[1 + \frac{\sigma_O^2}{\sigma_M^2} \Delta^T \Delta\right]^{-1}$$

Setting $\gamma^2 = \sigma_O^2 / \sigma_M^2$, we have $U = \left[1 + \gamma^2 \Delta^T \Delta\right]^{-1}$. Quaife (2009) shows that for a large number of observations, the elements of U in the centre of the matrix (figure 17) correspond to a Laplace distribution[8] (for a first order differential constraint). This function, also known as a double exponential distribution, is the distribution of differences between two independent variates with identical exponential distributions and is written (as a continuous function):

$$U_i = \frac{1}{2\gamma} e^{-\frac{|i-t|}{\gamma}}$$

for time slot *t.* For the discrete case, the normalisation term will be slightly different and should make the sum of the filter terms unity.

It is clear that the impact of regularisation of this form is very similar to applying a smoothing operator to C_O^{-1}, i.e. for an estimate of parameters in the centre of the time series, we can use a weighted contribution from observations before and after that point. For the simple function $F_t = R$ the approaches are identical. Thus, we can approximate equation 20 with a modification of equation 17 to obtain the solution at a particular time *t*, F_t:

$$\left[\sum_{i=0}^{i=N} w(i,t) K_i'^T C_{O,i}^{-1} K_i'\right] F_t = \left[\sum_{i=0}^{i=N} w(i,t) K_i'^T C_{O,i}^{-1} R_i\right]$$

where:

$$w(i,t) = \frac{e^{-\frac{|i-t|}{\gamma}}}{\sum_{i=0}^{i=N} e^{-\frac{|i-t|}{\gamma}}}$$

We now have a simple temporal weighting function that will closely mimic the impact of a fuller regularisation such as by a Kalman smoother with a zero-order process model. We still have the problem of determining γ though. Even in the simple filtering case considered, it is clear that this should be a function of both the observation uncertainty and the (zero order process) model/constraint uncertainty and so should vary in both time and space. A pragmatic solution for estimating and appropriate γ is to accept that the satellite albedo products that we are used to dealing with (and which will be compared with this

[8] http://mathworld.wolfram.com/LaplaceDistribution.html

product) often have a time window of around 16 days. This is equivalent to a weighting function of zero outside this period, and 1/*N* within it. We can relate our new weighting terms to this by, for example, setting $w(i,t)$ so that it has a value of 0.5 of the maximum value at ± 8 days, so $\gamma = -8/\ln[0.5] = 11.5$.

A similar approach is used by Geiger et al. (2008) in deriving kernel model estimates from Meteosat Second Generation (MSG) data. In that case, the weighting function is set to zero for $i > t$ as their algorithm is intended for near realtime processing (i.e. cannot make use of 'future' observations). They use a characteristic time length of 5 days, rather than the 11.5 we propose here, but MSG have a great many more viewing opportunities per day than the sensors considered here.

Another reason for settling on the Laplace distribution as a useful temporal weighting function is that being an exponential, it can readily be implemented sequentially. Geiger et al. (2008) demonstrated that a recursive algorithm could be developed with a similar weighting term (see below), although that used only one-sided weighting. Here, we develop a similar approach that allows for two-sided weighting.

We can write the weighted summation as:

$$\frac{1}{W}\sum_{i=0}^{i=N} a_i e^{-\frac{|i-t|}{\gamma}} = \frac{1}{W}\sum_{i=0}^{i=t-1} a_i e^{-\frac{t-i}{\gamma}} + \frac{1}{W}a_i + \frac{1}{W}\sum_{i=t+1}^{i=N} a_i e^{-\frac{i-t}{\gamma}}$$

where W is the weighting normalisation term:

$$W = \sum_{i=0}^{i=N} e^{-\frac{t-i}{\gamma}} + 1 + \sum_{i=0}^{i=N} e^{-\frac{i-t}{\gamma}}$$

The first term on the r.h.s. of the summation above can be written:

$$\sum_{i=0}^{i=t-1} a_i e^{-\frac{t-i}{\gamma}} = \sum_{i=0}^{i=t} a_i E_i$$

where $E_i = e^{-\frac{t-i}{\gamma}}$ and we note that $E_{i+1} = e^{-\frac{t-i-1}{\gamma}} = E_i e^{\frac{1}{\gamma}}$ so:

$$\frac{1}{W}\sum_{i=0}^{i=N} a_i e^{-\frac{|i-t|}{\gamma}} = \frac{1}{W}\left[\left(a_0 e^{\frac{-t}{\gamma}} + a_1 e^{\frac{-t+1}{\gamma}} + \cdots a_{t-1} e^{\frac{-1}{\gamma}} + a_t\right) + \left(a_{t+1} e^{\frac{-1}{\gamma}} + a_{t+2} e^{\frac{-2}{\gamma}} + \cdots a_N e^{\frac{-(N-t)}{\gamma}}\right)\right]$$

We have the (timewise) negative samples: $S^- = \left(a_0 e^{\frac{-t}{\gamma}} + a_1 e^{\frac{-t+1}{\gamma}} + \cdots a_{t-1} e^{\frac{-1}{\gamma}} + a_t \right)$ and the positive samples: $S^+ = \left(a_{t+1} e^{\frac{-1}{\gamma}} + a_{t+2} e^{\frac{-2}{\gamma}} + \cdots a_N e^{\frac{-(N-t)}{\gamma}} \right)$. If we wish to perform the summation at t=t+1 then, we need simply multiply S^- by $e^{\frac{-1}{\gamma}}$ and add on the new a_{t+1} value:

$$S^-_{t+1} = S^-_{t+1} e^{\frac{-1}{\gamma}} + a_{t+1} = \left(a_0 e^{\frac{-t-1}{\gamma}} + a_1 e^{\frac{-t}{\gamma}} + \cdots a_{t-1} e^{\frac{-2}{\gamma}} + a_t e^{\frac{-1}{\gamma}} + a_{t+1} \right)$$

Then for S^+_{t+1} we might do the opposite: multiply by $e^{\frac{1}{\gamma}}$ and subtract a_{t+1}:

$$S^+_{t+1} = S^+ e^{\frac{1}{\gamma}} - a_{t+1} = \left(+a_{t+2} e^{\frac{-1}{\gamma}} + a_{t+3} e^{\frac{-2}{\gamma}} + \cdots a_N e^{\frac{-(N-t)+1}{\gamma}} \right)$$

Thus, so long as we store both the negative and positive summations at any point in time we wish to estimate the parameter values at, we can calculate the new summations for the next time step estimate directly from these, without recourse to performing new summations. This is a great efficiency saving, as otherwise, if a long time series were used in the regularisation, the data for these would have to be loaded and summed for each new estimation point. The potential downside of the approach is that it may be subject to rounding errors on the positive term in a computer implementation. This issue could be removed if the weighted summations were stored at each time point in time, at a cost of storing all summation terms.

If new samples are to be added to the observation set as time progresses, this can be achieved by modifying the positive accumulator:

$$S^+_{t+1} = S^+ e^{\frac{1}{\gamma}} - a_{t+1} + a_{N+1} e^{\frac{-((N+1)-(t+1))}{\gamma}} = \left(+a_{t+2} e^{\frac{-1}{\gamma}} + a_{t+3} e^{\frac{-2}{\gamma}} + \cdots a_N e^{\frac{-(N-t)+1}{\gamma}} + a_{N+1} e^{\frac{-(N-t)}{\gamma}} \right)$$

There is probably little point in removing values from the negative accumulator, as their weights will rapidly reduce to zero.

3.6.4 Negative aspects of regularisation and how to deal with them

Smoothing, or regularisation does not come without its own problems. As noted above, the smoothness parameter γ needs to be estimated, but the methods noted above are all aimed at estimating a single 'hyper parameter' for a time series. In reality, the most appropriate value of such terms will vary in both time and space. The impact of an under-estimate of a roughness parameter (i.e. over-estimate of smoothness) will be greatest at

times of rapid change, such as snow fall or melt, harvesting, or wildfire. In these cases, using a generic term will always smooth over the sudden change. The impact of this is somewhat mitigated by the temporal resolution of the product being 8 days, but with a γ of 11.5 when the post-change signal is to be characterised, samples 11.5 days prior to this will still have a relative weighting of 0.5 (i.e quite a strong influence). This could be treated by reducing the value of γ in these cases, but that would require change detection as part of the processing chain.

More effective general methods involve further weighting the time series. In some cases a derivative of the parameters is used as a weighting term. Thus, where the derivative is high, the value of γ is automatically reduced.

The two main methods for achieving re-weighting to allow for sudden changes are: (i) changing the norm of the function to be optimised from L^2 to L^1; (ii) using a Huber Norm. A third method is proposed to fit in with the filtering/weighting approach being used here.

3.6.4.1 Using an L^1 Norm

In using an L^1 norm for the smoothness constraint term, equation 19 is changed to:

$$J = \left(\hat{R} - R\right)^T C_O^{-1}\left(\hat{R} - R\right) + \left[(\Delta F)^T C_M^{-1}(\Delta F)\right]^{\frac{1}{2}}$$

In this case, the derivative of the second term on the r.h.s. becomes:

$$\frac{\partial J_\Delta}{\partial F} = \frac{1}{2}\frac{2\Delta^T C_M^{-1}(\Delta F)}{\left[(\Delta F)^T C_M^{-1}(\Delta F)\right]^{\frac{1}{2}}}$$

so the solution is found from (in place of equation 20):

$$\left[K'^T C_O^{-1} K' + W_1 \Delta^T C_M^{-1} \Delta\right] F = \left[K'^T C_O^{-1} R\right] \qquad \textbf{23}$$

where

$$W_1 = \frac{1}{2\left[(\Delta F)^T C_M^{-1}(\Delta F)\right]^{\frac{1}{2}}}$$

This problem is now however non-linear and cannot be solved simply with linear inversion methods. In practice, the implementation of the L^1 norm by multiplying C_M by $2\left[(\Delta F)^T C_M^{-1}(\Delta F)\right]^{\frac{1}{2}}$ can be achieved by iteration: first the problem is solved for an L^2 Norm, then $2\left[(\Delta F)^T C_M^{-1}(\Delta F)\right]^{\frac{1}{2}}$ is calculated and used to resolve for the parameters. The approach is attractive in that it requires no additional parameters beyond the norm (1 here). The impact of changing the norm in this way is that when changes in parameter values are rapid, this larger value is penalised much less with this norm than with the L_2. Practically, this allows some sudden changes to be realised in the parameters (Hansen et al., 2006).

3.6.4.2 Using a Huber Norm

The Huber norm is a blended weighting function that uses the L^2 norm for small residuals and the L^1 norm for large values. It is widely used in robust regression analyses. This will have a very similar effect to changing to the L^1 norm overall, but the properties and error propagation of the original problem are better maintained by keeping the L^2 norm for small residuals. The norm is defined via the function:

$$M_\alpha(r) = \begin{cases} \dfrac{r^2}{2} & ,0 \le |r| \le \alpha \\ |r| - \dfrac{\alpha}{2} & ,\alpha < |r| \end{cases}$$

where α is the residual threshold value between the two norms. Again, this weighting makes the problem non-linear, so we lose some of the advantages of using linear methods throughout the rest of this approach. With the Huber Norm, experimentation would be required to determine an appropriate value of α.

3.6.4.3 A filter-based method

In section 4.6.3 we propose using a weighting term on the observations in place of more complex regularisation. The efficient algorithm that results involves splitting samples into (timewise) negative and positive contributions. It is suggested that this approach mimics the main impacts of a smoother such as a Kalman smoother. Applying each set of contributions separately then (i.e. solving using only the negative contributions and using only the positive contributions) provides two independent estimates of the parameter at a given time. This essentially mimics using a Kalman filter in the forward and backward direction.

There are several ways this two-way processing could be used. Perhaps most obviously, the parameter estimates from the positive and negative processing could be directly compared, relative to the uncertainty in their estimation and step parameter changes identified. In such a case, processing could proceed from that point forward in time using only the positive values, and vice-versa for negative time steps. Alternatively, the discrepancy, relative to the uncertainty, could be used to weight the two contributions, so

that if it is low, the final estimate of the parameters is an equal weighting of both positive and negative terms, and if it is high, positive terms are more strongly weighted for forward processing and negative terms more strongly weighted for processing backward in time.

As yet, there has not been time to fully explore these approaches, so none of them are implemented in the current version of the algorithm. Instead, users of the product should be aware that the smoothing described above will occur in the presence of strong step changes, and that the impact can be gauged through knowledge of the weighting function used.

3.6.5 Prior knowledge constraint

Although regularisation or parameter weighting should improve our ability to obtain robust parameter (thence albedo) estimates from sparse angular samples over fixed window approaches, there will be occasions when there are only very few or even no samples available. In such cases, most algorithms adopt some 'backup approach' that is applied when these poor sampling conditions are identified. In the case of the MODIS BRDF/albedo product (Schaaf et al., 2002), a 'magnitude inversion' is attempted if between one and six observations are present[9]. This involves fitting an archetype BRDF 'shape' (i.e. set of model parameters) to what samples are present, and scaling the term accordingly. This is based on the observation that BRDF shape tends to not change rapidly in time, although its magnitude may do. The archetype shapes are defined for different land covers and applied according to the land cover type identified for a particular pixel.

This is an example of 'prior knowledge' being used to constrain the solution, but in the case of the MODIS product, there is a sharp transition between when it applied and when it is not. The transitions are defined by rules, and associate each parameter estimate with a particular QA value – see below for more details.

Geiger et al. (2008) apply constraints based on (uncorrelated) prior information, in terms of the prior means and prior variance. Similar approaches are considered by Li et al. (2001), Hagolle et al. (2001) and Pokrovsky et al. (2003).

In the approach of Geiger et al. (2008) the prior mean estimates come from a previous processing step, with the uncertainty inflated. This is stated to be mathematically equivalent to applying a decreasing weighting to the parameters over time, i.e. it is a form of regularisation, similar in many ways to a Kalman filter with a zero-order process model. Since the filter is applied only to historical samples, the parameter values remain unchanged in the absence of new samples, but the uncertainty in those estimates increases. As stated above, the main approach of Geiger et al. is for near real time processing, so this is an appropriate approach. An interesting output of the product described by Geiger et al. is the output of the time since last observation. In the context of this approach, this could be re-phrased as the minimum time (forward or backwards) to an observation. This use of 'priors' then is essentially the same as the temporal regularisation described above.

[9] There is also a condition on the weight of determination.

A second aspect of the approach of Geiger et al. (described in appendix A of that paper) is that a 'regularisation' term is applied to equation 17, which can be phrased as:

$$\left[\sum_{i=0}^{N} K'^{T} C_{O,i}^{-1} K' + C_p^{-1}\right] F_t = \left[\sum_{i=0}^{N} K'^{T} C_{O,i}^{-1} R + C_p^{-1} K_p\right] \quad \textbf{24}$$

This is implemented to avoid numerical problems when the number of samples is very low. They set the term K_p to $[0,0.03,0.3]^T$ and the diagonal of C_p to $[0,0.05^2,0.5^2]$. We can recognise this as a prior constraint on the parameters (hence the use here of subscript *p*). This is equivalent to adding a new cost term to equation 16 which is then minimised in combination with the other cost terms:

$$J_{p,t} = \left(F_t - F_{p,t}\right)^T C_{p,t}^{-1} \left(F_t - F_{p,t}\right) \quad \textbf{25}$$

In the case of Geiger et al., a constant global prior term is used, with a large uncertainty, as a very weak constraint on the solution. They apply no prior knowledge to the isotropic parameter. In practice, this will be similar to using the archetype kernel values of the MODIS approach (letting one parameter float free, even in the case of a single observation). It has the advantage however that an uncertainty value is returned, even in the case of a single observation.

If better prior estimates of the model parameters were available, they could be used to constrain the solution where the information content of the data (not just number of samples) is low. This is readily achieved through the use of appropriate parameters in equations 24 and 25. This idea is further explored in the following section.

4 Prior Estimation

4.1 The requirement for priors

It is very likely that the information content of the sensors proposed for use in GlobAlbedo have significantly less information content (in their ability to constrain estimates of albedo) that the data used in some other products, notably the MODIS BRDF/albedo product. This is mainly because of spectral sampling issues (particularly for MERIS), angular sampling (particularly MERIS and (A)ATSR/ATSR-2), and viewing opportunities (comparing those of VEGETATION with 2 MODIS sensors). The best scientific dataset then would most likely be obtained from a combination of data from all of these sensors, including MODIS, provided there were no significant calibration biases between the instruments. This is however not feasible within this project, and there is a further desire to generate a product that is not dependent on non-European data (e.g. to safeguard future production). Therefore non-European data will only be used here in the generation of one-off ancillary datasets for this product. In particular, MODIS data will be used to provide a prior estimate of model parameters F_p and associated uncertainty information C_p^{-1}.

There are many significant advantages to using a 'prior' in the processing. In particular, as noted in the previous section, it can provide a form of regularisation which allows a solution to be calculated even when sampling is weak. This is important as it obviates the need for a 'backup algorithm': there is instead a smooth, statistically-based blending of information from the prior estimate and the new observations, the quality of which can be assessed through a consistent uncertainty measure.

In the case of a small number of observations (when the estimate is strongly reliant on the prior estimate) the uncertainty should be relatively high, i.e. we should only use an external prior as this as a relatively weak constraint. A strong prior constraint would mean that the resulting product would be very dependent on the quality of the prior as a good estimate of model parameters, and therefore sensitive to any errors or biases they contain. It would also make it sensitive to the particular way in which the MODIS product is calculated (e.g. 16 day moving window).

That said, there are now more than 10 years of global MODIS BRDF/albedo data, at 500 m spatial resolution, every 8 days. There is clearly a lot to learn from these data, and one way to do that is to develop a spatially and temporally complete prior parameter estimate from them.

Moody et al. (2008) analysed 5 years of the MODIS BRDF/albedo product (collection 4) to develop a snow-free aggregate albedo climatology. Part of their assessment is an attempt to gauge the accuracy of a phenological interpolation method being developed, but even within that context, it is clear from their results that the inter-annual variability of bi-hemispherical reflectance ('white sky albedo' – a measure closely related to albedo) is surprisingly low. This is illustrated in figures 8 and 9 in their paper (figures 18 and 19 here). Their results also suggest that in the near infrared, the departure of ('white sky') albedo from the climatology is less than 0.05 for the vast majority of circumstances. Clearly these results must be put into context particularly as they apply only to a single five-year period (2000-2004) and we cannot claim that inter-annual variability of albedo is unimportant, but it does suggest that, in developing any algorithm to characterise albedo, a good first estimate of snow-free abledo can be obtained from a climatology.

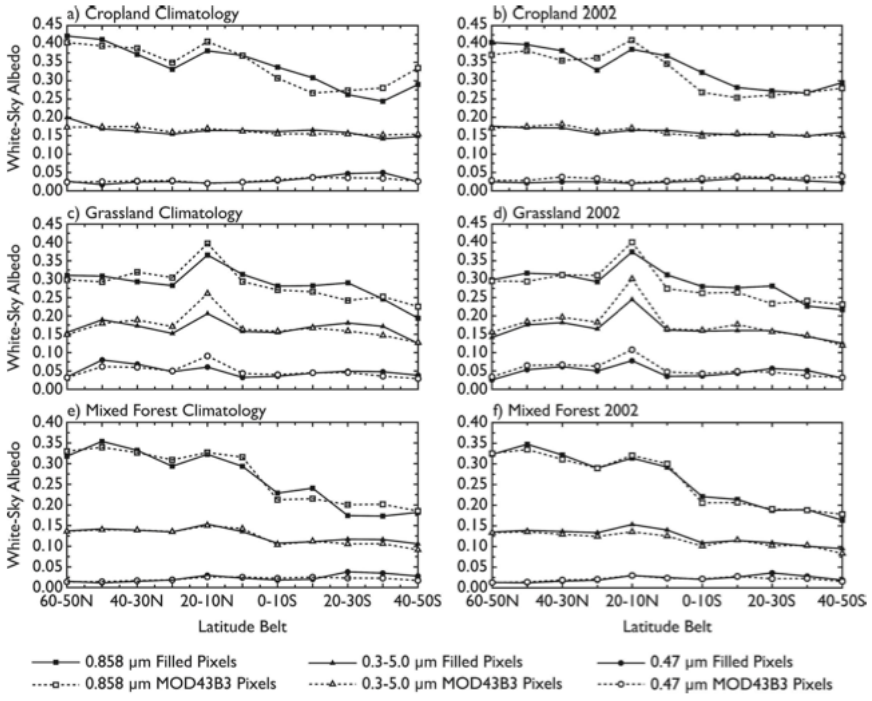

FIG. 8. Mean diffuse bihemispherical (white sky) albedo values computed by 10° latitude belts for three bands (0.47- and 0.86-μm narrowband and the 0.3–5.0-μm shortwave broadband) during the 16-day period of 12–27 Jul (data-day 193). Trends are computed for three ecosystem classes: (a), (b) cropland, (c), (d) grassland, and (e), (f) mixed forest from (left) the 5-yr aggregate climatology and (right) the 2002 single-year albedo data.

Figure 4-1. Zonal average MODIS albedo climatology and data for 2002 (from Moody et al., 2008)

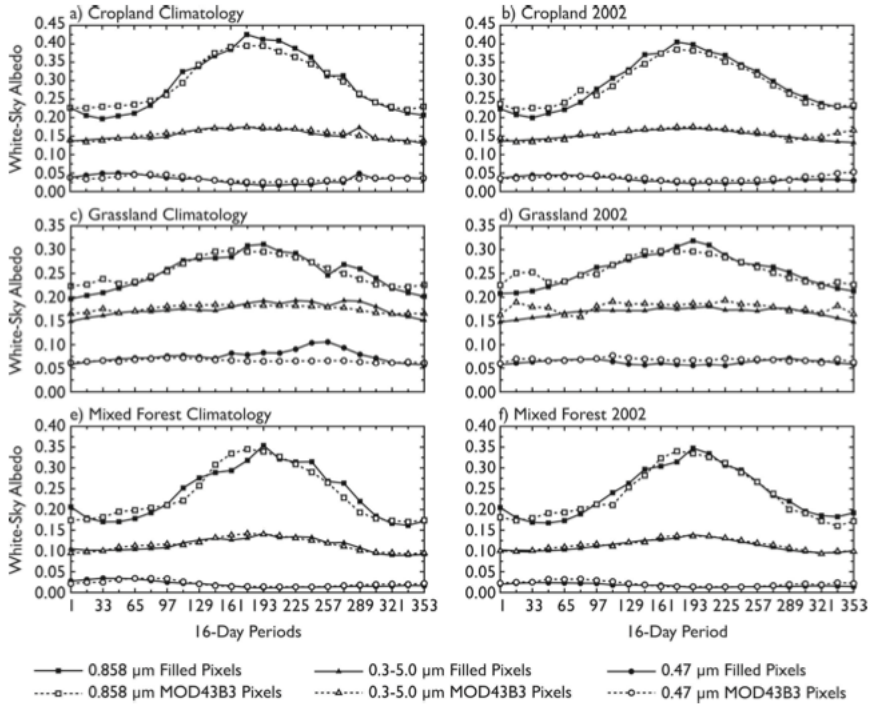

FIG. 9. As in Fig. 8, but for each 16-day period over the 50°–40°N latitude belt.

Figure 4-2. MODIS albedo climatology and data for 2002 (from Moody et al., 2008)

Given that the impact of snow on albedo is so great, we choose to develop two sets of prior information. These are: (i) snow free (i.e. processing of all MODIS data which is not flagged as 'snow'); (ii) snow (i.e. processing of all MODIS data which is flagged as 'snow'). A third, that we might term 'with snow' (processing of all data, whether snow free or not) might be worthwhile developing, as discussed below, although it will not be processed in this implementation of the globAlbedo product.

The use of these different priors will be expanded on in the algorithm description, but it is essentially so that input data that is given a high confidence of being snow-affected makes use of the 'snow' prior in its processing (and only makes use of 'snow' pixels in estimating the model parameters) and the 'no snow' prior is used for processing data that are identified as not being snow-affected. In practice, snow detection relies on thresholds in algorithms, and the measure would be better considered as a 'snow confidence' measure. If this were well understood and could be guaranteed to be a probability measure, this might be translated into a weighting term for the application of the two priors. However, such a characterisation is beyond the scope of this study. One approach then might be to produce three 'versions' of the globAlbedo product: one for snow-free conditions only (fed with high confidence snow free data); one for snow only, and one that is processed whether there is snow or not (but which flags the product as mostly coming from snow or no snow pixels). This latter product is similar to other albedo datasets produced, and should in many ways be the primary dataset we develop. However, if only a 'snow' and 'no snow' set of products are developed, and full uncertainty information is associated with both, then the 'with snow' product can be developed by combining these two datasets. We will therefore concentrate on the development of only the 'snow free' and 'snow' products. Each of these will carry information on the time to the closest 'snow free' and 'snow' sample, respectively, to allow a 'snow' flag to be carried through to a combined product.

It is worth noting at this point that there are questions about the appropriateness of the kernel models to be used here for modelling the BRF of snow. In particular, snow often has a large forward scattering peak which cannot be mimicked by these kernels. Stroeve et al. (2005) compared the (collection 4) MODIS albedo product with *in situ* measurements over the Greenland ice sheet. They conclude the that average root mean squared error between ground measurements and MODIS estimates was 0.04 (using only high quality MODIS estimates) which is only slightly larger than the uncertainty of the *in situ* measurements. For high snow albedo (>0.7) the agreement was good, but for lower values there was an apparent bias of around 0.05. Figure 20 represents a summary of these results, although interestingly, it compares ground measurements to both black sky and white sky albedo estimates. The fact that these (squares and triangles in the figure) are so close suggests that the weights of the non-isotropic kernel parameters are rather low. It may be then that the kernels are effectively giving an isotropic equivalent (effectively a mean of all observations in the case of the MODIS product) and that the directionality is largely ignored. A point emphasised by Stroeve et al. is that around 50% of the satellite observations obtained during the sunlit season at the latitude of Greenland are obtained at solar zenith angles beyond 70 degrees. At these angles, both treatment of atmospheric effects and surface modelling become rather difficult and uncertainties in both are likely to be high. There have been several other attempts to estimate snow albedo

from satellite data (e.g. Klein and Stroeve, 2002; Stroeve and Nolin, 2002; Liang et al., 2005) but none of these appear to perform significantly better than the MODIS kernel approach.

Other than issues with the kernels used to model snow, there is a case to be made that narrow-to-broadband coefficients especially tailored to snow will reduce errors in snow albedo, due to the completely different spectral behaviour of snow compared to most other (e.g. soil and vegetation) land surface types.

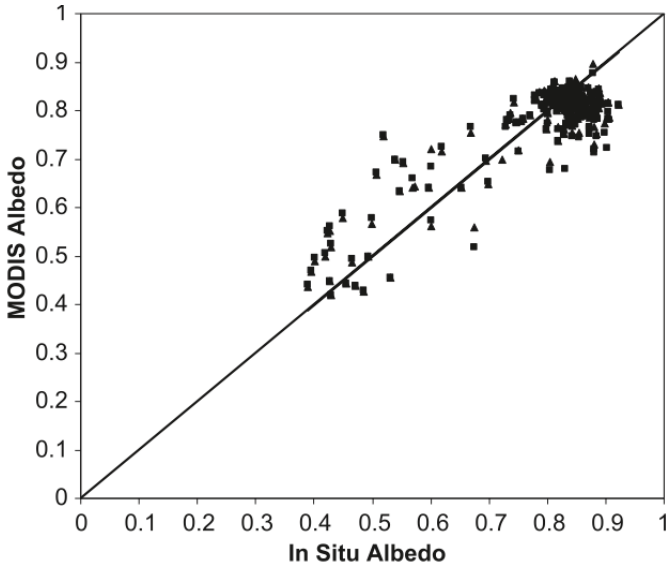

Figure 4-3. Comparison between clear-sky MODIS 16-day albedo and 16-day in situ albedo for both the Black sky albedo and white sky albedo, combined for all Greenland stations (from Stroeve et al., 2005).

4.2 Generations and use of prior

The key to the development of a widely useful albedo dataset is to make the best use of available information and to carefully treat uncertainties at all stages of processing. This latter point is best dealt with in a Bayesian/optimal estimation framework that we have developed above. This same framework should be used for any 'back-up' algorithms or gap filling.

If we suppose the existence of a background 'filler' albedo dataset (which could be derived for instance as a 16 day product of the mean albedo for any location over a long time period), defined by an expectation of the model parameters F_p, and we attach an uncertainty to this background albedo C_p^{-1}, then we can obtain the posterior mean (estimated) F_t from equation 24.

If we only want the background ('prior') estimate to act as a gap-filling term, the uncertainty in the background estimate expressed through the matrix C_p^{-1} needs to be sufficiently high that high-quality observations and angular sampling are essentially

unaffected by F_p but when the information content of the observations is low (or there are no samples), the solution defaults to F_p with associated uncertainty through C_p^{-1}.

The provision of a reasonable estimate of the background F_p is important for the utility of the product, and this is probably best achieved from existing datasets such as the MODIS albedo product (unless very weak priors are to be used, as in Geiger et al. 2008). Since the desire here is for a product independent of non-European sensors, the prior could be replaced once processing is completed by a new version of F_p from the full time series of the GlobAlbedo product. Indeed, if it were possible to store all S^- and S^+ terms in the algorithm described in section 4.6.3, the parameter estimate could be rapidly re-run with different versions of the prior estimate[10].

4.2.1 Input Data

The MODIS Collection V005 BRDF-Albedo model parameters product[11] (Lucht et al.,2000; Schaaf et al., 2002, 2008) is used to develop the prior parameter estimates. Specifically, MDC43A1[12] (BRDF-Albedo Model Parameters 16-Day L3 Global 500m) and MCD43A2[13] (BRDF-Albedo Quality 16-Day L3 Global 500m) are used. These data are freely available for download, although because the whole archive was required, special delivery of the product was arranged with NASA.

The product uses multiple observations from gridded atmospherically-corrected surface reflectance BRF over a 16-day time period, producing a product every 8 days. As well a generating BRDF/albedo products for the 7 MODIS land bands, results are also generated for the following broad wavebands: visible (0.3-0.7μm) - *VIS* , near-IR (0.7-5.0 μm) – *NIR* and total shortwave (0.7-5.0 μm) – *SW.*

The algorithm uses a reciprocal version of the semiempirical RossThick-LiSparse Reciprocal (RTLSR) kernel-driven BRF model (Lucht et al., 1999; Roujean et al.,1992; Wanner et al., 1995, 1997), the theory of which is presented above.

Gridded surface reflectance data are flagged as clear or contaminated (e.g. cloud). Clear observations are accumulated over a 16 day window, applying equation 17 to parameter estimation if the weight of determination is sufficiently good and there are sufficient (>=7)

[10] This is not considered practical at this stage however.

[11] http://modis-land.gsfc.nasa.gov/brdf.htm

[12] https://lpdaac.usgs.gov/lpdaac/products/modis_products_table/brdf_albedo_model_parameters/16_day_l3_global_500m/mcd43a1

[13] https://lpdaac.usgs.gov/lpdaac/products/modis_products_table/brdf_albedo_quality/16_day_l3_global_500m/mcd43a2

observations available. Only model fits with RMSE <0.1 and weights of determination <2.5 are considered candidates for model inversion. A filtering step is applied to remove outliers, based on a weighting of the residuals. If the majority of observations are flagged as 'snow free' the resulting parameters are flagged 'snow free', *vice-versa* if the majority are flagged 'snow'. If insufficient observations are available for a 'full' inversion, the results are given a poorer QA flag (see below).

All of the existing archive of the MODIS products described were used in processing, but for testing and demonstration, we have selected four example tiles with different environmental conditions. These range from almost permanent snow conditions in Siberia, tile h22v022 and seasonal snow in central Europe, tile h18v04 to tropical conditions in tile h19v08. Tile h25v06 (N. India, Himalayas) has very strong topographic impacts and significant snow cover. Figure 21 shows the locations of these 'test' tiles.

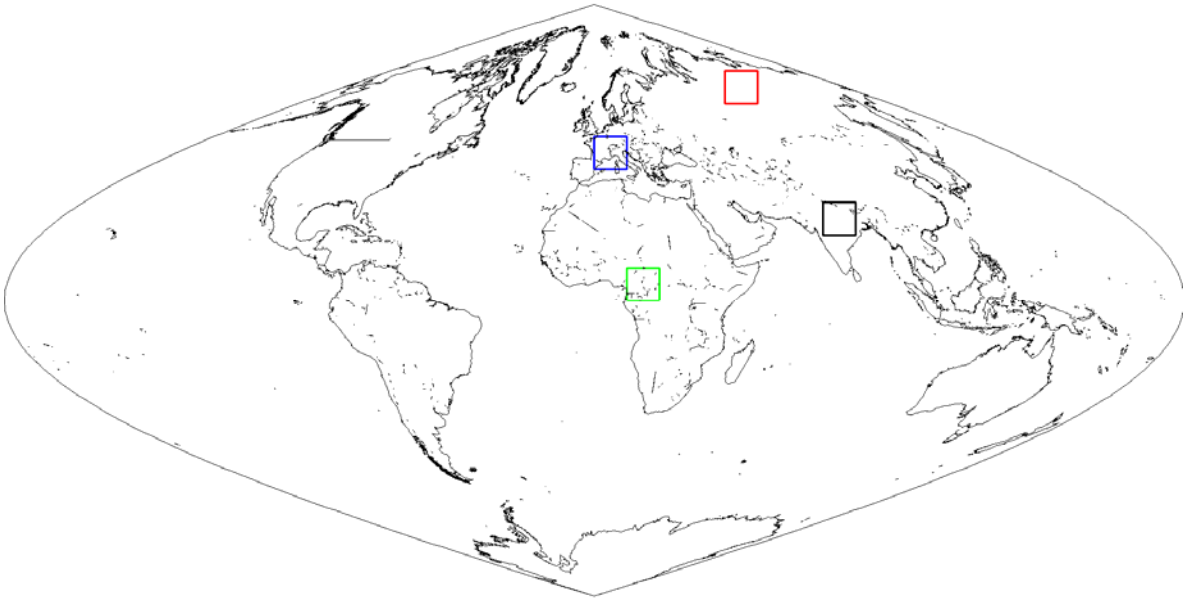

Figure 4-4. MODIS tiles, in blue: h18v04, green: h19v08, red: h22v02, black: h25v06

4.3 Estimating mean and uncertainty in priors: theory

Any optimal merging of data requires estimates of the uncertainties associated with the various data sources. Often this information is not directly available. The particular dataset of interest here is the MODIS BDRF/Albedo product (MCD43). Albedo is described for some waveband via spatial datasets of three model parameters f_{iso}, f_{vol} and f_{geo}, available from the NASA product MCD43A1 at 500m spatial resolution at 8-day intervals from early 2000 to the present (i.e. around 10 years of data).

The uncertainty in albedo is a function of the angular sampling achieved by the MODIS instruments and uncertainties in the input BRF data (due to errors in the compensation of

atmospheric effects, footprint/gridding issues etc.). Whilst the former can be described by standard statistical methods and described as a function of the weight of determination (WoD) (Lucht and Lewis, 2000), the latter is not routinely characterised for MODIS data. Further, if insufficient samples (<=7) are deemed available over the (16 day) period of observation, the linear BRF model cannot be inverted without further constraint and a 'backup algorithm' is brought to bear on the problem. In this case, a constrained model is used in the inversion (the so-called 'magnitude inversion). For these various reasons there is no routine assessment of the uncertainty associated with the BRF model parameters. Instead, to give the user a guide to reliability of the data, the product MCD43A2 provides Quality Assurance (QA) information associated with each pixel and time period of inversion. This is described in detail in WWW1. For each of the seven MODIS wavebands, QA is categorised into five levels (**Table 4-1. MODIS QA descriptors (source WWW1)**

.

Code	Meaning
0	best quality, full inversion (WoDs, RMSE majority good)
1	good quality, full inversion
2	Magnitude inversion (numobs >=7)
3	Magnitude inversion (numobs >=3&<7)
4	Fill value

Table 4-1. MODIS QA descriptors (source WWW1)

Thus, other than the 'fill value' (which we can interpret as 'no data') there are four categories of QA information that would be expected to have decreasing reliability with increasing code values.

In this analysis, we require an estimate of the mean and uncertainty in the BRF model parameters (for three broad wavebands) as a background estimate for GlobAlbedo processing. The uncertainty should be a relatively conservative estimate for this purpose (i.e. we should be minded to over-estimate uncertainty rather than under-estimate it, to avoid under-weighting new observations in the GlobAlbedo processing chain). The problem can be split into two components: (i) estimating the uncertainty associated with the best quality inversions (QA code 0); (ii) characterising the uncertainty of data with QA codes 1 to 3 relative to data with QA code 1. As noted above, we have access to around 10 years of data to achieve this. To calculate a mean from all observations (QA codes 0 to 3), we need access to the relative uncertainty of QA codes 1 to 3 to data with QA 0. For ease of implementation, we require a simple descriptor of relative uncertainty.

We assume that the mean and uncertainty for a given pixel for category QA code 0 can be estimated from samples over the ten years of observations, with a minimum of four samples and denote the mean $\overline{f}_{QA0,k}(i,j)$ and variance $\sigma^2_{QA0}(f_k,i,j)$ for some location i,j for parameter f_k. Of course this includes not only the uncertainty in the parameter but also

any *real* variation in the parameter over the time period. It is therefore liable to be an over-estimate of uncertainty.

We then estimate f_k for other QA codes from its mean value for pixel i,j over the ten-year time period, where a minimum of three samples exists and call this $\bar{f}_{QAc,k}(i,j)$ for QA codes $c=\{1,2,3\}$. We initially process only snow-free observations, as these are likely to give a more reliable estimate of uncertainty than those including some snow.

We assume $\overline{f}_{QA0,k}(i,j)$ represents f_k at (i,j) and characterise the departure from this for $\bar{f}_{QAc,k}$, relative to $\sigma^2_{QA0}(f_k,i,j)$:

$$\sigma^2_{QAc0,k}=\frac{1}{N}\sum_{i,j}\left(\frac{\bar{f}_{QAc,k}(i,j)-\bar{f}_{QA0,k}(i,j)}{\sigma_{QA0}(f_k,i,j)}\right)^2$$

where N is the number of samples over (i,j) (with 4 or more samples of QA 0 and 3 or more samples of QA *c*).

We then define a set of weighting terms W_{10}, W_{20} and W_{30} for each category of QA relative to *QA0* where:

$$W_{c0}=\frac{1}{\sigma_{QAc0,k}}$$

These weights can then be used in calculating estimates of the mean value for each parameter for each pixel $\overline{f}_k(i,j)$, using data from all QA categories:

$$\overline{f}_k(i,j)=\frac{1}{N_{(i,j)}}\sum_{c=0}^{c=3}\sum_{yQAc}W_{c0}f_{QAc,k}(i,j)$$

defining $W_{00}=1$. The summation over $yQAc$ is over all samples for pixel (i,j) that fall into category *QAc*. The normalisation term $N_{(i,j)}$ is:

$$N_{(i,j)}=\sum_{c=0}^{c=3}\sum_{yQAc}W_{c0}$$

4.4 Estimating mean and uncertainty in priors: practice

The first problem here is to take a set of model parameters of varying quality (described simply by Quality Assurance (QA) flags) and provide an updated estimate of the parameters at a particular place and time, along with estimates of parameter uncertainties and covariance. If we consider a parameter x_1 calculated in MCD43, an improved estimate of this parameter, $\bar{x}_1$ can be calculated from some set of 'observations' of x_1 by:

$$\bar{x}_1 = \sum_{i=1}^{i=n} \frac{x_{1,i}}{\sigma_{1,i}^2} \Bigg/ \sum_{i=1}^{i=n} \frac{1}{\sigma_{1,i}^2} \qquad \textbf{26}$$

where $x_{1,i}$ is the i^{th} sample (of a set of n) of x_1 and $\sigma_{1,i}$ is the mean squared error associated with that observation. We can define a relative weight $w_i = \sigma_{1,QA1}^2 / \sigma_{1,i}^2$ which is the error associated with the highest quality observation (QA1) relative to that with the observation. We assume this relative weighting to be the same for all parameters. Then:

$$\bar{x}_1 = \sum_{i=1}^{i=n} w_i x_{1,i} \Bigg/ \sum_{i=1}^{i=n} w_i \qquad \textbf{27}$$

This means that we do not need to know the absolute uncertainty associated with an observation, just its relative uncertainty. This is potentially very powerful as we have only QA information to assign uncertainties. The problem is reduced to one of defining the weighting terms associated with each QA state, w_{QAi}, so that:

$$\bar{x}_1 = \sum_{i=1}^{i=n} w_{QAi} x_{1,i} \Bigg/ \sum_{i=1}^{i=n} w_{QAi} \qquad \textbf{28}$$

In fact, the datasets we are analysing here are censored. This is because the model parameters are constrained to be non-negative. In this case, the expected value cannot be described simply as the mean. Since the censoring is likely to apply to only a small proportion of the parameter distribution, a median is an improved estimate of the mean of the unconstrained parameter distribution. Thus, we should probably estimate $\bar{x}_1$ as a weighted median, although that is not done here for ease of processing.

The value of w_{QAi} will be unity for QA1. It is not straightforward to define the other w_{QAi} terms however, particularly as the QA values cover quite wide ranges of circumstances. Since increasing QA state indicates a likely decrease in quality, we can suggest that w_{QAN} should monotonically decrease with increasing N. We can therefore proceed by assigning some arbitrary values that fit in this pattern and examine the impact of these choices. A

reasonable initial estimate of w_{QAN} would be $w_{QAN} = 0.618^{(N-1)}$, 0.618 being the Golden Mean, giving: $w_{QA1} = 1,\ w_{QA2} = 0.618,\ w_{QA3} = 0.382,\ w_{QA4} = 0.236.$

If we are interested in calculating an albedo climatology (i.e. a mean field), we could use equation 28 to estimate the weighted mean parameter values for each pixel at time period *d* over all samples that exist for the decade of observations. This is potentially very useful information (see Moody et al. 2007, 2008 and the discussion above).

We can further provide an estimate of the uncertainty in each model parameter. This is best phrased in matrix form, representing the uncertainty due to variances in the model parameters and covariances between them. Since the primary aim of this gap-filled product development is to provide a prior estimate of model parameters, it would be advantageous if the uncertainty estimate were conservative in nature (i.e. liable to be an over-estimate of uncertainty, rather than an under-estimate). We can therefore first consider the variance/covariance of the parameters over the sampling period:

$$\sigma_{1,2}^2 = \sum_{i=1}^{i=n}\left[w_{QAi}\left(x_{1,i} - \bar{x}_1\right)\left(x_{2,i} - \bar{x}_2\right)\right] \Big/ \sum_{i=1}^{i=n} w_{QAi}$$

where $\sigma_{1,2}^2$ is the covariance between parameters x_1 and x_2 (or variance if considered for the same parameter). For small sample sizes (as is the case here) this should be corrected for bias:

$$\sigma'^2_{1,2} = \frac{\sum_{i=1}^{i=n} w_{QAi} \sum_{i=1}^{i=n}\left[w_{QAi}\left(x_{1,i} - \bar{x}_1\right)\left(x_{2,i} - \bar{x}_2\right)\right]}{\left(\sum_{i=1}^{i=n} w_{QAi}\right)^2 - \sum_{i=1}^{i=n} w_{QAi}^2}$$

These terms will include both parameter uncertainty and any inter-annual variation, and so provide upper bound estimates, as required. The uncertainty associated with the estimate of the expected value and their co-variation, $s_{1,2}^2$ (the standard error) is:

$$s_{1,2}^2 = \sigma'^2_{1,2} \Big/ \sum_{i=1}^{i=n} w_{QAi}$$

In examining the estimate of the priors, we experimented (below) with a temporal weighting function. The concept is based on the idea that an optimal estimate of the prior for a given year can be given by a weighted average over time. The weighting function applied was $p_2^{|y-y0|}$ where p_2 is a smoothness parameter, *y* is the calendar year of any

particular sample, and y_0 is the 'focus' year. Setting p_2=1 gives a standard climatology, but decreasing values of p_2 give a shaper focussed weighting function (meaning that more of the information for the mean estimate comes from the focus year).

It is not immediately obvious whether a climatology product (p_2=1) should be used as a prior or whether a more focussed estimate is better[14]. Theoretically, the latter should provide a better constraint on the inversion, but a danger is that too much information from the MODIS estimates will be transferred to the GlobAlbedo product which is supposed to be generated from independent measurements. Since we really only want to use the prior as a weak constraint, a climatology might be a better approach. This has the additional advantage of needing only a single estimate, rather than products for every year. An important aspect of the prior processing is to give estimates of the uncertainty in the calculations of expected values of the model parameters (as a full variance / covariance matrix). Whilst this can theoretically be estimated from the sample data, the number of samples is likely quite small (<10) so we must consider the reliability of any such estimate. If we downweight temporally-distant samples (i.e. use p_2=1) the reliability of the uncertainty estimates may also be impacted.

It is necessary to assess the impact of a global smoothing (p_2) term, which might be applied independent of seasonality or temporal constraints. This is done in the following three subsections (5.4.1-5.4.3) by analysing, as a function of p_2: (1) the variation in the mean; (2) the variation of the standard error estimates; (3) the variation of the correlation coefficients. Results from smoothness parameter values from 0.5 to 0.9 (where 0.5 is strongly focussed on the target year) are compared with results from smoothness 1.0 (climatology). The analyses seek to determine whether there is any significant difference between estimates of these terms as a function of the smoothness parameter, and also whether the derived terms are consistent with what would be expected and what is required for a weak prior.

In section 5.4.4 we seek to test the reliability of the estimated model parameters by a cross validation exercise.

4.4.1 Analysis of estimated mean in priors

An analysis of the impact of the smoothness parameters in the weighted mean from f_0, f_1 and f_2 parameters for prior generation was performed for the test tiles. Scatterplots are shown below comparing different broadband albedo weighted mean parameters generated using smoothing parameter 1.0, always in the X axis and smoothing parameter 0.5 in Y axis. The day of year (DOY) refers to the starting 16-day period. The year of analysis is 2005. Tables describing the statistics of the relationships are also presented.

[14] A requirement from ESA for this product is that, if a prior is to be used, it should only be a climatology (so that it is not dependent on (new) non-European data), but the impact of a climatology prior as opposed to a focussed prior is still a worthwhile subject of investigation, and so conducted here.

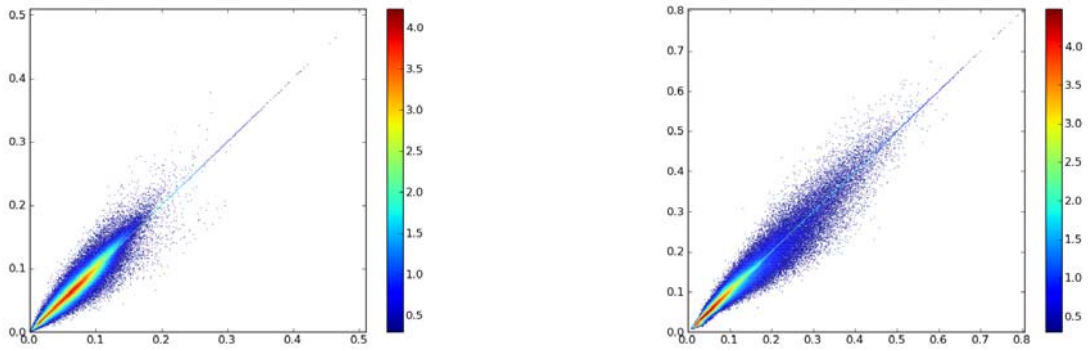

Figure 4-5. On the left, mean f_0 h18v04 DoY 001 1.0 vs 0.5, on the right, mean f_0 h18v04 DoY 145 1.0 vs 0.5

Smoothness parameter	R^2		Slope		Intercept	
DOY	***001***	***145***	***001***	***145***	***001***	***145***
0.5	0.970	0.976	0.992	0.992	0.000	0.001
0.6	0.981	0.985	0.993	0.993	0.000	0.001
0.7	0.989	0.991	0.995	0.994	0.000	0.001
0.8	0.995	0.996	0.997	0.996	0.000	0.000
0.9	0.999	0.999	0.999	0.998	0.000	0.000

Table 4-2. Statistics of model parameters (2005) predicted using different smoothness parameters, tile h18v04 DOY 001 and 145.

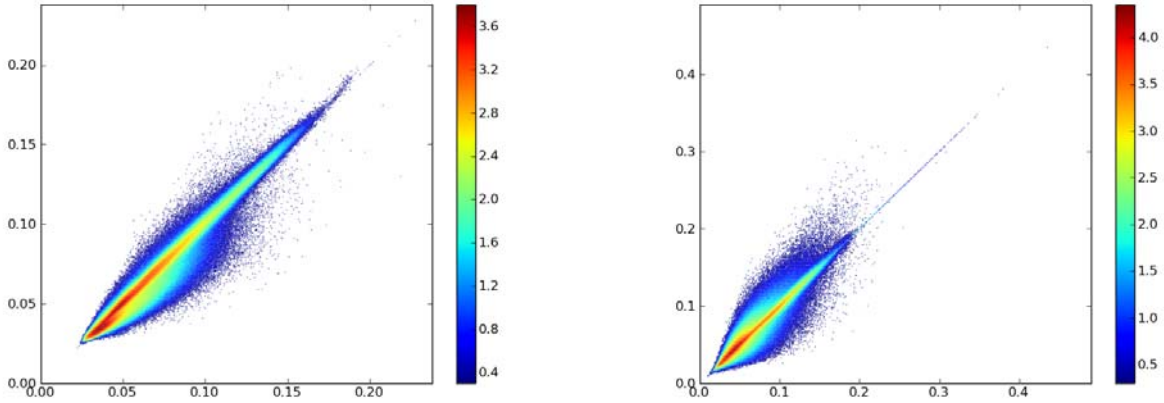

Figure 4-6. On the left, mean f_0 h19v08 DoY 001 1.0 vs 0.5, on the right, mean f_0 h19v08 DOY 145 1.0 vs 0.5

Smoothness parameter	R^2		Slope		Intercept	
DOY	***001***	***145***	***001***	***145***	***001***	***145***
0.5	0.968	0.943	1.007	0.986	-0.001	0.001
0.6	0.980	0.965	1.004	0.989	-0.001	0.001
0.7	0.989	0.981	1.001	0.991	-0.001	0.001
0.8	0.995	0.992	1.001	0.994	0.000	0.000
0.9	0.999	0.998	1.000	0.997	0.000	0.000

Table 4-3. Statistics of f_0 mean, with different smoothness parameters, tile h19v08 DoY 001 and 145

For tile h22v02, snow conditions were predominant in the scene on DOY 001, leaving only a few pixels for data analysis, so a scatterplot was only calculated for DOY 145.

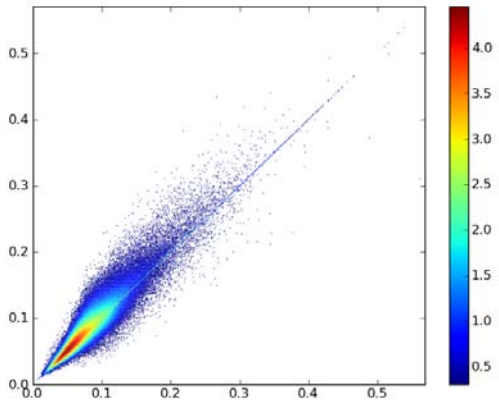

Figure 4-7. Mean f_0 h22v02 DOY 145 1.0 vs 0.5

Smoothness parameter	R^2	Slope	Intercept
0.5	0.921	1.040	-0.001
0.6	0.951	1.032	-0.001
0.7	0.974	1.024	-0.000
0.8	0.989	1.016	-0.000
0.9	0.998	1.008	-0.000

Table 4-4. Statistics of f_0 mean, with different smoothness parameters, tile h22v02 DoY 145

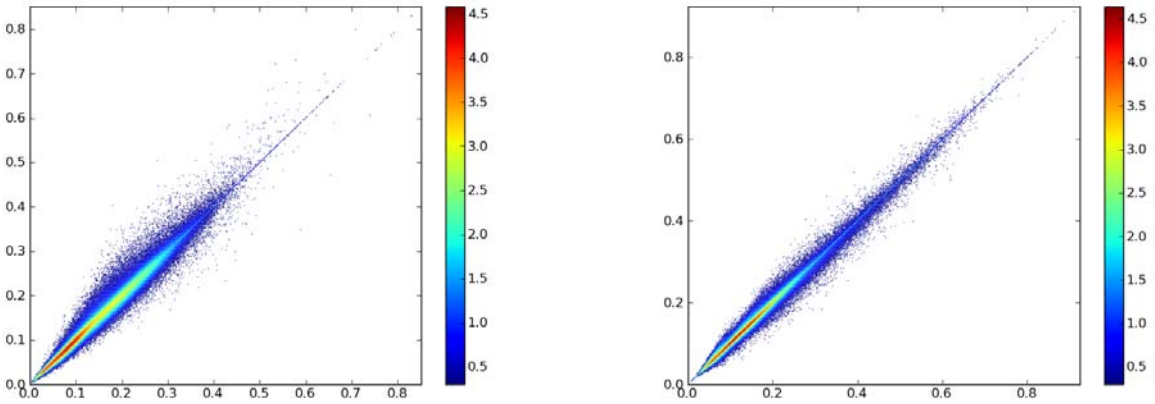

Figure 4-8. On the left, mean f_0 h25v06 DOY 001 1.0 vs 0.5, on the right, mean f_0 h25v06 DOY 145 1.0 vs 0.5

Smoothness parameter	R^2		Slope		Intercept	
DOY	***001***	***145***	***001***	***145***	***001***	***145***
0.5	0.990	0.995	1.004	0.998	-0.001	0.000
0.6	0.993	0.997	1.004	0.998	-0.001	0.000
0.7	0.996	0.998	1.003	0.999	-0.001	0.000
0.8	0.988	0.999	1.002	0.999	-0.000	0.000
0.9	1.000	1.000	1.001	1.000	-0.000	0.000

Table 4-5. Statistics of f_0 mean, with different smoothness parameters, tile h25v06 DoY 001 and 145

For all test tiles, the relationship between predictions of model parameters in the year 2005 using a climatology and predictions calculated from a weighted average, focussed on the year 2005 is extremely strong. There is negligible apparent bias in the estimates over these tiles. R^2 was always very high; the smallest value being 0.921 in tile h22v02 DOY 145, comparing smoothness parameters 0.5 and 1.0. From this, we conclude that changing the smoothness parameter has a very small impact overall on the weighted mean for all model parameters.

4.4.2 Analysis of standard deviations in estimated priors

In order to investigate the impact of different smoothness parameters in the standard error (SE) of the priors, a comparison of different prior SE generated with different smoothness parameters, ranging 0.5 to 1.0 was performed, the following scatterplots show in the X axis the SE from the VIS broadband for parameters, f_0, f_1 and f_2 calculated with smoothness parameter 1.0, in the Y axis the SE using 0.5 smoothness parameter. The day of year (DOY) again refers to the starting 16-day period. The year of analysis is 2005.

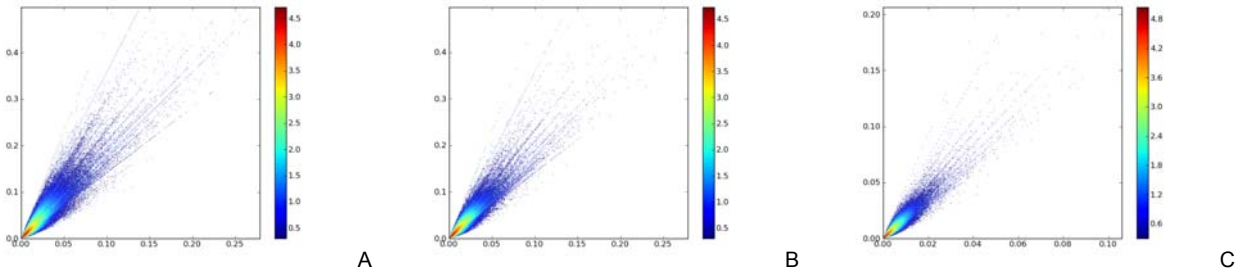

A B C

Figure 4-9. Scatterplots of standard error from smoothness parameter 1.0 in X axis and 0.5 in Y axis, A - VIS parameter f_0, B - VIS parameter f_1, C - VIS parameter f_2, Tile h18v04 DoY 001

SE	R^2			Slope			Intercept		
	f_0	f_1	f_2	f_0	f_1	f_2	f_0	f_1	f_2
0.5	0.882	0.889	0.889	1.965	1.890	1.891	0.000	0.000	0.000
0.6	0.931	0.935	0.936	1.685	1.635	1.639	0.000	0.000	0.000
0.7	0.964	0.966	0.967	1.462	1.430	1.436	0.000	0.000	0.000
0.8	0.985	0.986	0.987	1.280	1.261	1.266	0.000	0.000	0.000
0.9	0.997	0.997	0.997	1.128	1.120	1.122	0.000	0.000	0.000

Table 4-6. SE statistics from parameters f_0 , f_1 and f_2 tile h18v04 DOY 001

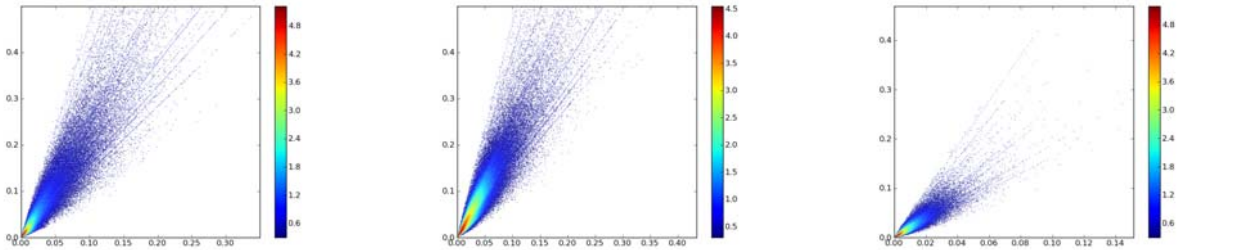

A B C

Figure 4-10. SE scatterplots from smoothness parameter 1.0 in X axis and 0.5 in Y axis, A - VIS parameter f_0, B - VIS parameter f_1, C - VIS parameter f_2, Tile h18v04 DOY 145

SE	R^2			Slope			Intercept		
	f_0	f_1	f_2	f_0	f_1	f_2	f_0	f_1	f_2
0.5	0.898	0.893	0.849	2.119	2.088	2.206	-0.001	-0.001	-0.001
0.6	0.939	0.937	0.915	1.822	1.797	1.832	-0.001	-0.001	0.000
0.7	0.968	0.967	0.958	1.564	1.548	1.551	0.000	0.000	0.000
0.8	0.987	0.987	0.983	1.342	1.333	1.330	0.000	0.000	0.000
0.9	0.997	0.997	0.996	1.155	1.152	1.149	0.000	0.000	0.000

Table 4-7. SE statistics from parameters f_0 , f_1 and f_2 tile h18v04 DOY 145

Figures 26 and 27 illustrate typical plots of the SE estimated for different smoothness parameters. As would be expected, the R^2 of the SE relationships increased with decreasing smoothness (increasing roughness) for all tiles examined, i.e. the relationship was weaker. If we assume the climatology-based uncertainty estimates to be the most reliable (being less sensitive to local variations), this might suggest that the SE estimates from the more focussed versions of processing are somewhat more unreliable. This is difficult to assess however, as the SE measure includes real variation as well as noise. In the climatology, the real variation is averaged out, but in the focussed versions it will have a stronger influence.

Of more significant note is that the bias for all relationships is negligible and that the slope apparently varies consistently and is close (though not identical) for all tiles. This scaling factor is approximately 2 for a smoothing factor of 0.5. This implies that the estimate of variance in the model parameters can readily be calculated from a climatology, since we can approximately re-estimate the terms for more focussed smoothing by a relative

scaling term. The quality of this prediction decreases with increasing scale factor (decreasing smoothness).

4.4.3 Analysis of model parameters correlation in estimated priors

To further assess the likely utility of the second order statistics estimated above, we calculated the correlation coefficients between every broadband (VIS, NIR and SW) every albedo model parameter (f_0, f_1 and f_2), and compared these estimates for varying smoothness parameters. If the correlation coefficients were to show any unexpected behaviour or vary significantly as a function of the smoothness parameter, then we would need to question the reliability of these estimates.

For the 3 bands, with 3 parameters, we obtain N(N-1)/2 (off-diagonal) correlation terms. i.e. 36 different correlation coefficients per degree of smoothness. Below, we present: (1) example images of the f_0 model parameters in the 3 bands, as a false colour composite (FCC); (2) example images of correlation coefficients between parameters f_0 between the VIS and NIR bands; (3) example scatterplots of correlation coefficients calculated with different smoothness parameters going from 0.5, in the Y axis to 1.0, in the X axis. In the image examples, high positive values of correlation coefficients are coloured green and high negative values red. The bounds of these colour labels is illustrated in an accompanying scatterplot in each case.

Examination of the scatterplots shows that the correlation information is mostly very similar for different values of the smoothness parameter: where high correlation is indicated from one smoothness parameter, it tends to be also indicated at other values of smoothness. We can conclude that this information then is consistent as a function of the smoothness parameter.

However, examination of the spatial plots of correlation coefficient shows them to be highly variable spatially, and not in any clear way related to surface features such as land cover variations. Further (not shown here), they are not very consistent as a function of time, with large swings between highly positive correlations and high negative values. Indeed, the vast majority of pixels apparently have a very high magnitude of correlation (either positive of negative). This could be an expression of true correlation between the parameters, but the fact that it is very high, and that it is spatially noisy and temporally unstable lead us to conclude that it is more likely just a poor estimate. We therefore conclude that correlation information calculated in the estimation of priors is likely not reliable and will therefore not make use of it in determining the prior distributions.

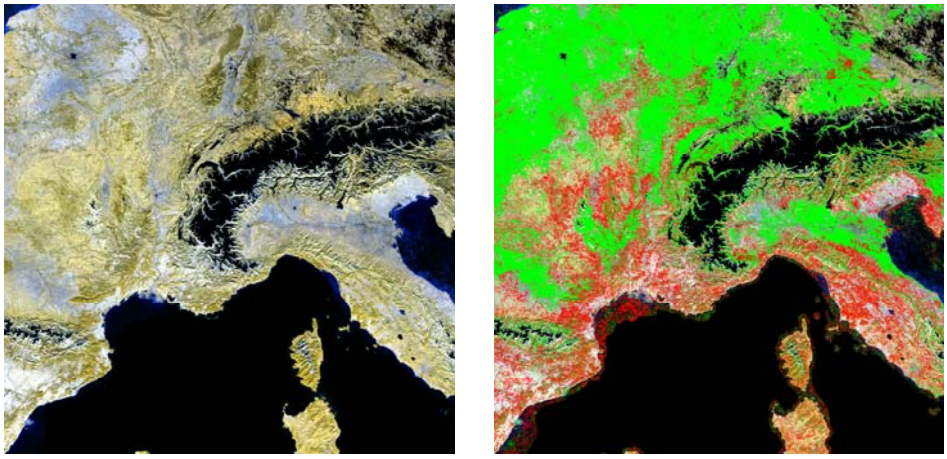

A B

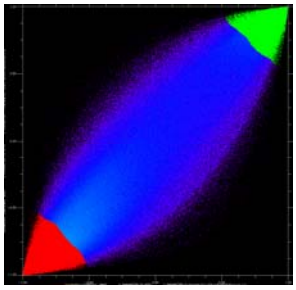

C

Figure 4-11. Tile h18v04: A) FCC mean f_0 (NIR,SW,VIS: RGB), DOY 001; B) in red strong negative correlation, in green strong positive correlation of VIS parameter f_0 and NIR parameter f_0 from smoothness parameter 0.5 and 1.0; C) correlation coefficients of VIS parameter f_0 in the x-axis and NIR parameter f_0 in the y-axis from smoothness parameter 0.5 and 1.0

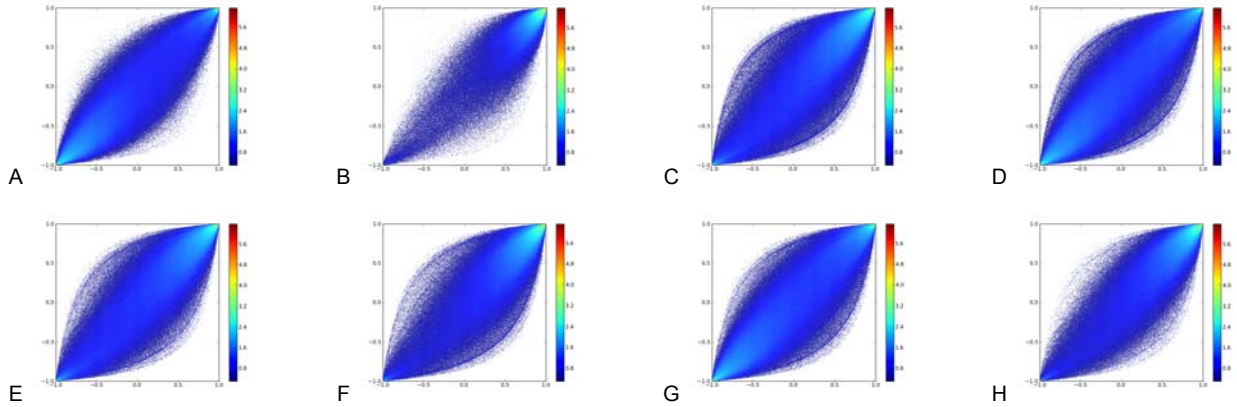

A B C D

E F G H

Figure 4-12. Tile h08v04 DoY 001, correlation coefficients for smoothing parameters 0.5 (y axis) and 1.0 (x axis) of VIS broadband albedo parameter f_0 with A: VIS f_1, B:

VIS f_2, C: NIR f_0, D: NIR f_1, E: NIR f_2, F: SW f_0, G: SW f_1 and, SW f_2

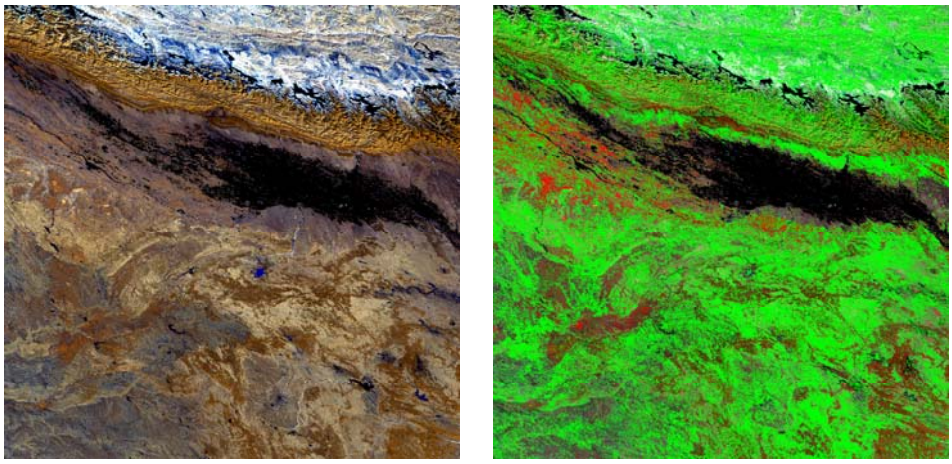

A B

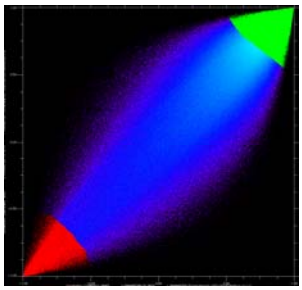

C

Figure 4-13. Tile h25v06: A) FCC mean f_0 (NIR,SW,VIS: RGB), DOY 001; B) in red strong negative correlation, in green strong positive correlation of VIS parameter f_0 and NIR parameter f_0 from smoothness parameter 0.5 and 1.0; C) correlation coefficients of VIS parameter f_0 in the x-axis and NIR parameter f_0 in the y-axis from smoothness parameter 0.5 and 1.0

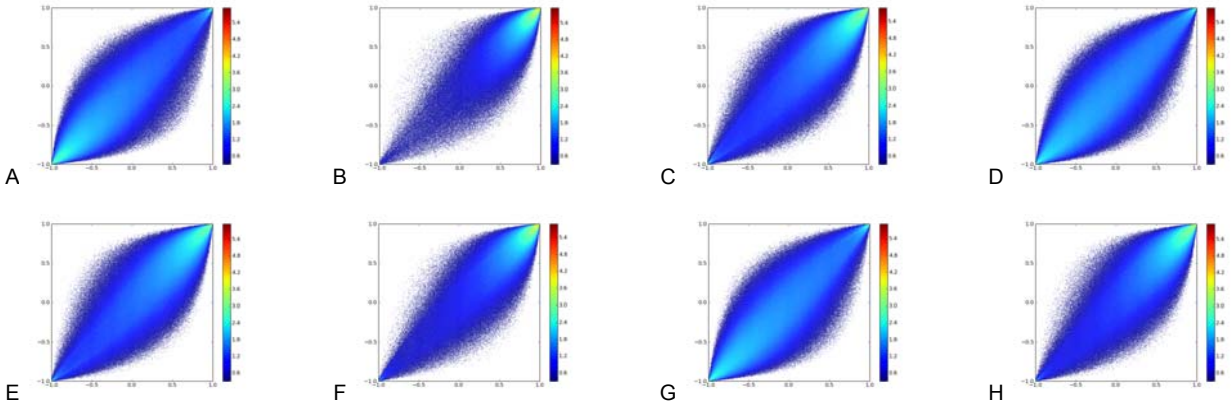

Figure 4-14. Tile h08v04 doy 001, correlation coefficients for smoothing parameters 0.5 (y axis) and 1.0 (x axis) of VIS broadband albedo parameter f_0 with A: VIS f_1, B: VIS f_2, C: NIR f_0, D: NIR f_1, E: NIR f_2, F: SW f_0, G: SW f_1 and, SW f_2

4.4.4 Cross-validation exercise

The purpose of this experiment is to assess the reliability (robustness) of the 'prior' estimate of model parameters. The sub-sections above have examined its stability and general behaviour as a function of the smoothness parameter.

For this cross-validation exercise we extract only QA0 values of the model parameters for the year 2005 as a reference dataset. We then attempt to estimate this value (where at least three samples are available) from datasets excluding the year 2005, using the methods described above (this is the 'prior'). We then have two independent estimates of the model parameters to compare. If they are close, we can conclude that the 'prior' (the test dataset) estimate of the model parameters is robust (i.e. it can predict the independently estimate of the parameters). There is no uncertainty information available for the reference (2005) dataset, but the 'prior' estimate includes a full uncertainty matrix. Given concerns regarding the reliability of estimated correlation information expressed above, we estimate the goodness of fit between the reference and test datasets both making use of the full uncertainty information and using only the leading diagonal of that matrix (i.e. ignoring correlation coefficients).

The goodness of fit (agreement) between the reference and test dataset is defined through a term ε. This is a measure of the squared difference between x, which is a vector containing the weighted means using a non-2005 estimate of 2005 (test data) and $\bar{x}$ which is a vector with the weighted means obtained from the 2005 dataset (reference) from 'high quality retrievals', weighted by the apparent uncertainty in x. Epsilon was calculated for every smoothness parameter and every 16-day rolling composite time period from 2005.

$$\varepsilon^2 = \frac{1}{2}((x-\bar{x})^T C^{-1}(x-\bar{x}))$$

To examine ε, we assess various characteristics of its spatial distribution (for each tile) as a function of DOY over 2005. Examples are shown in sub-plots A and B of figures 32-35 below. Specifically, they show the mode (peak of histogram) (A) and median (B) value of ε over each tile, for varying values of the smoothness parameter. These statistics are used as the distribution of ε is non-Normal. Sub-plots C show the relationship between the median ε for smoothness values 0.5 to 0.9 compared to that of the climatology (smoothness parameter 1.0). Figure 32 shows results for tile h18v04 with full correlation information and figure 33 that with only the parameter variance information used. Figures 34 and 35 show similar information for tile h25v06. Each set of figures is accompanied by a table giving the mean value of ε over all time and space samples (the mean over time of the mean over space) and the mean of the median values (the mean over time of the median over space). These are measures characteristic of ε as a whole for a particular tile, as a function of smoothness parameter.

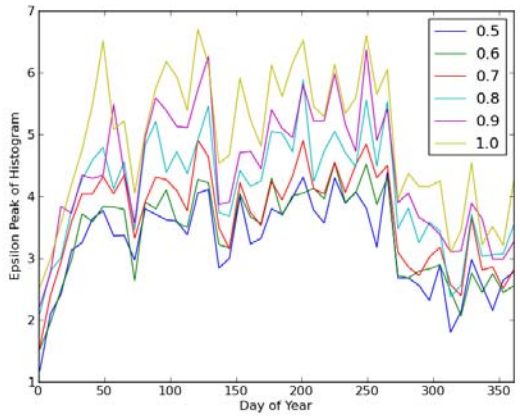

A

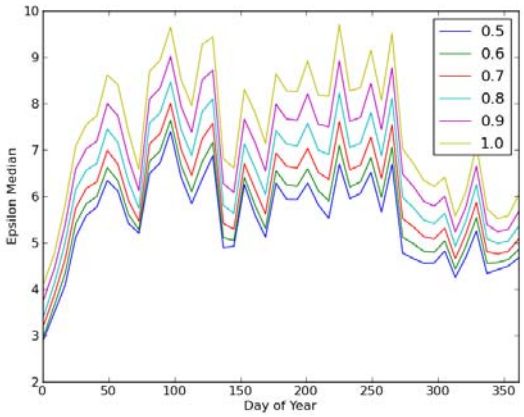

B

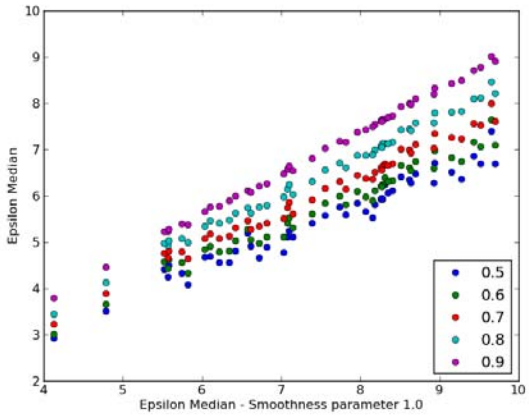

C

Figure 4-15. Temporal profile of epsilon A: peak of histogram, B: median and C: scatter plot of epsilon median for different smoothness parameters; Tile h18v04, with correlation information

Smoothness parameter	Mean of modes	Mean of medians
0.5	3.236	5.476
0.6	3.394	5.723
0.7	3.684	6.060
0.8	4.130	6.471
0.9	4.448	6.954
1.0	4.942	7.500

Table 4-8. Statistics of epsilon for tile h18v04 using correlation information.

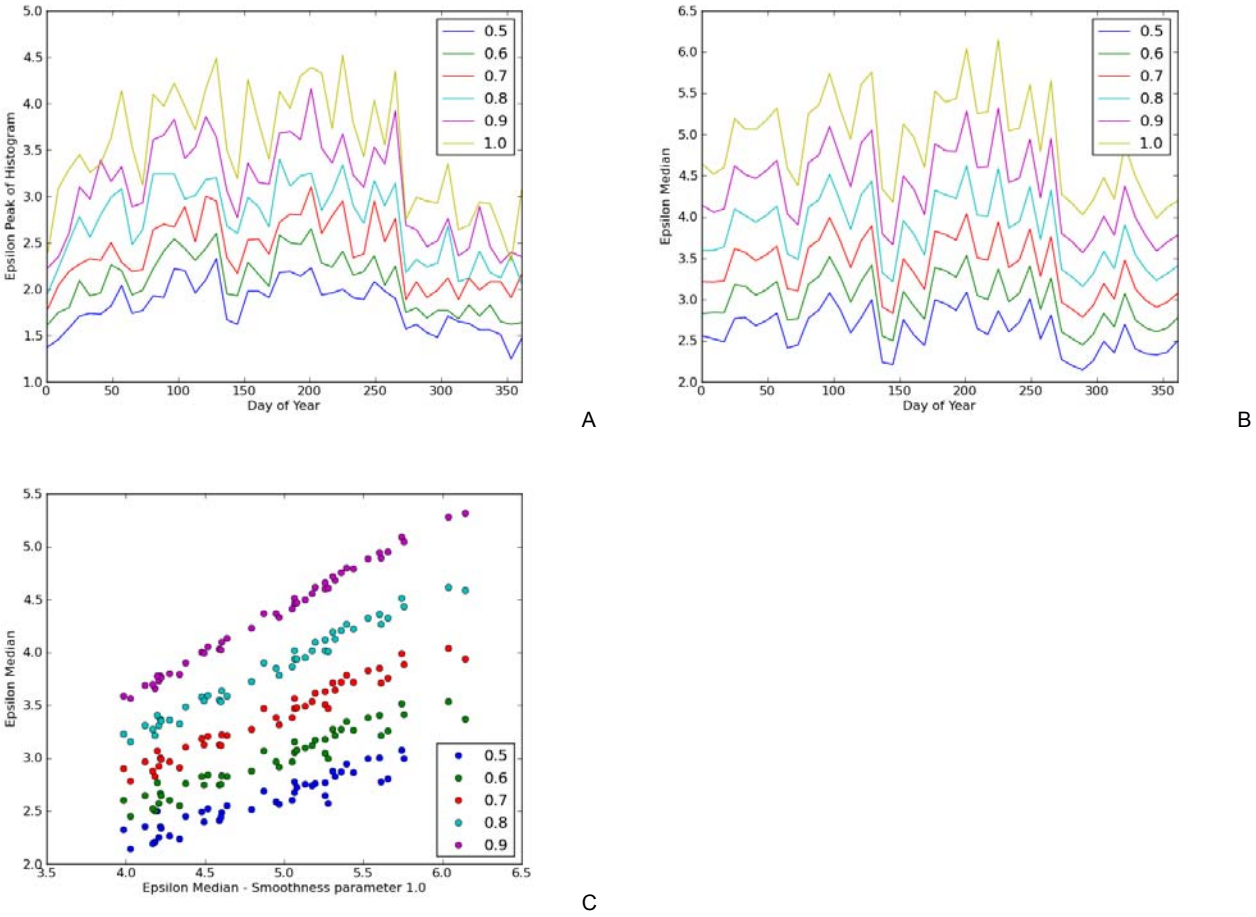

Figure 4-16. Temporal profile of epsilon A: peak of histogram, B: median and C: scatterplot of epsilon median from smoothness parameter 1.0 and 0.5 to 0.9; Tile h18v04, without correlation information

Smoothness parameter	Mean of modes	Mean of medians
0.5	1.820	2.618
0.6	2.081	2.982
0.7	2.399	3.388
0.8	2.739	3.839
0.9	3.109	4.349
1.0	3.537	4.917

Table 4-9. Statistics of epsilon for tile h18v04 not using correlation information.

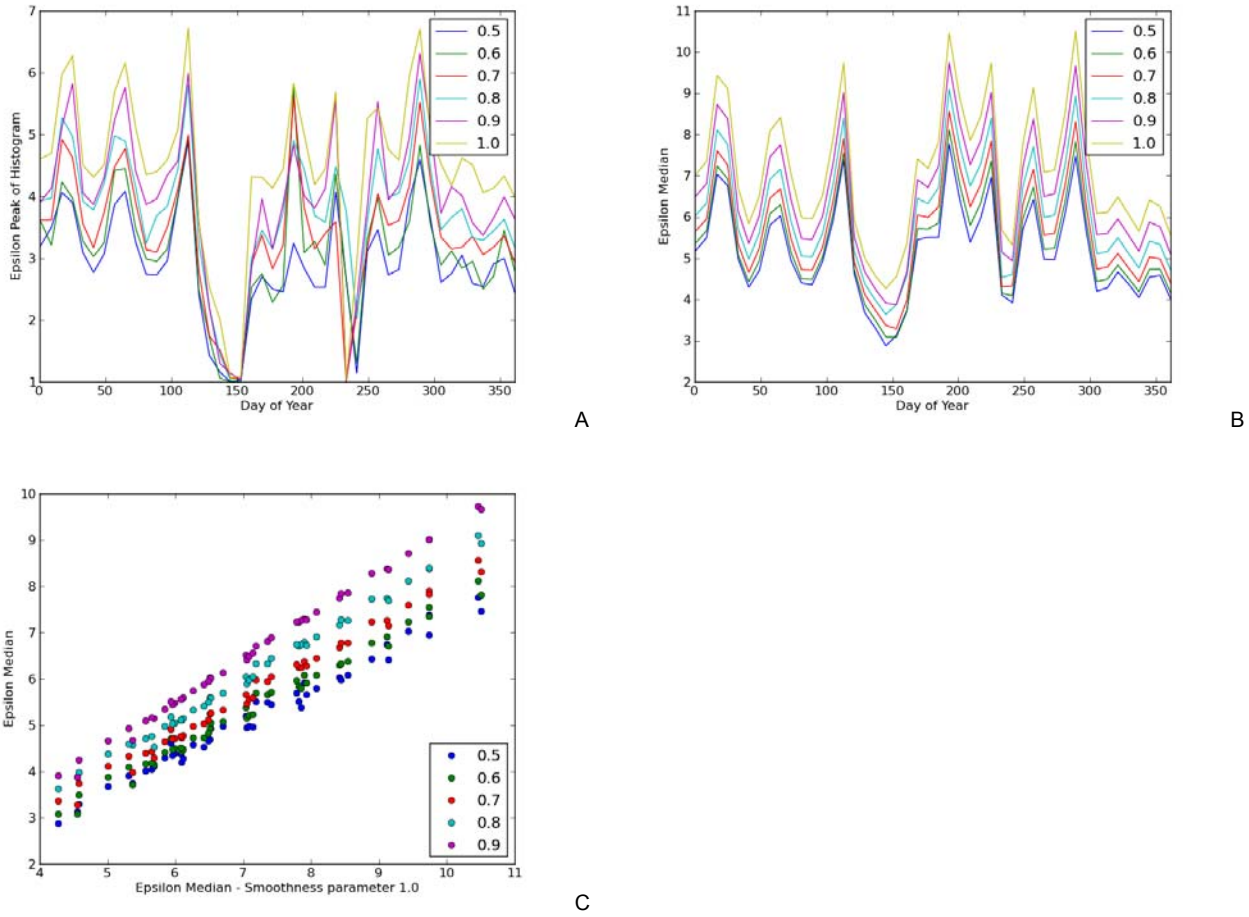

Figure 4-17. Temporal profile of epsilon A: peak of histogram, B: median and C: scatterplot of epsilon median from smoothness parameter 1.0 and 0.5 to 0.9; Tile h25v06, epsilon statistics with correlation information

Smoothness parameter	Mean of modes	Mean of medians
0.5	2.920	5.144
0.6	3.139	5.350
0.7	3.398	5.665
0.8	3.768	6.075
0.9	3.957	6.541
1.0	4.469	7.105

Table 4-10. Statistics of epsilon for tile h25v06 using correlation information.

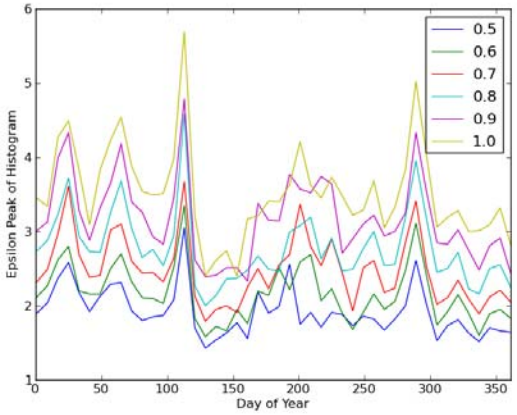

A

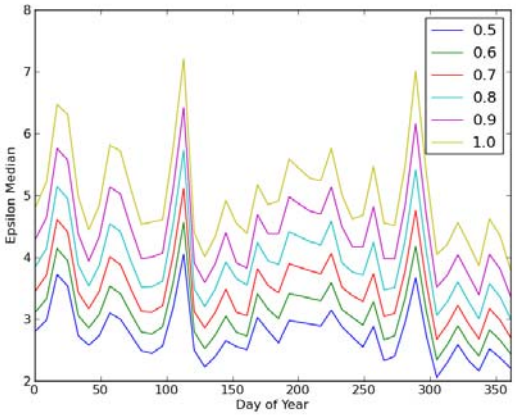

B

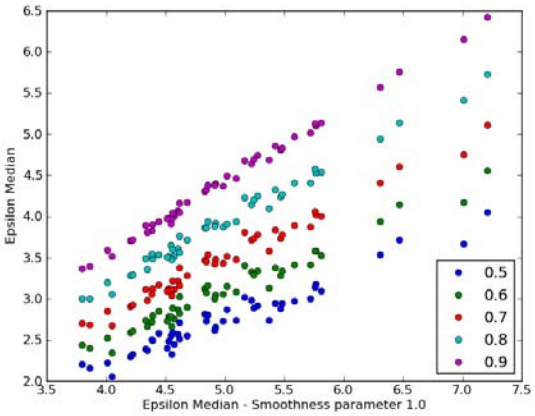

C

Figure 4-18. Temporal profile of epsilon A: peak of histogram, B: median and C: scatter plot of epsilon median from smoothness parameter 1.0 and 0.5 to 0.9; Tile h25v06, epsilon statistics without correlation information

Smoothness parameter	Mean of modes	Mean of medians
0.5	1.923	2.749
0.6	2.168	3.098
0.7	2.484	3.489
0.8	2.782	3.932
0.9	3.178	4.422
1.0	3.523	4.990

Table 4-11. Statistics of epsilon for tile h25v06 not using correlation information.

The overall trends in the behaviour of ε are consistent between the different tiles. The relationship between mode and mean is consistently median = 1.21 mode + 1.59 when the correlations information is used and median = 1.36 mode + 0.14 when not used (data from the tables). The variations in median and mode are very consistent as a function of the smoothness parameter, so either the mode or median is an adequate metric of the distribution of ε. There is a linear relationship between median ε at any particular smoothness parameter and that for the climatology (sub-plots C).

We can therefore take the 'mean of medians' (in the tables) as a characteristic of the typical behaviour of ε (i.e. 50% of samples will tend to have a better goodness of fit than this). This value ranges between around 5.0 and 7.5 if the full correlation information is used, and from around 2.6 to 5.0 if it is not used: the range of values is approximately the same in both, with the inclusion of the full information giving a bias of around 2.5 in ε relative to ignoring it.

The value of ε does not include uncertainty in the reference dataset, as this is unknown. If we assume this to be equal to the parameter uncertainty of the test dataset, we can consider ε as a measure of the number of standard deviations between the reference and test datasets. Clearly taking the full correlation information (especially when correlation coefficients are high) will increase ε. In making choices about an appropriate value of the smoothness parameter and whether or not to include the correlation information, we need to decide which is the most plausible. Our expectation in this experiment is that the test dataset should approximate the reference dataset to a given degree of accuracy. We might reasonably set a threshold for this at around ε=0.477[15]. None of the mean of median values for these experiments fall within that limit. If we include the full correlation information, none of the test datasets appear to match the reference to within this threshold by a factor of at least 10, i.e. the 'best' match obtained (smoothness parameter 0.5) when using the full correlation information is around 10 times worse than we would expect. When not using the full correlation information, the 'best' match is around 5 times poorer than we would expect. This suggests that, even in this 'best' case, we are under-estimating the standard error by a factor of around 5.0. For the climatology, this factor is around 10.

4.4.5 Discussion and Conclusions

The results in section 5.4.1 suggest that the estimate of the mean parameter values is not greatly impacted by the smoothness parameter (over a range 0.5 to 1.0, 1.0 being a 'flat' average, i.e. a climatology). In analysing the standard error (SE) terms in section 5.4.2, we note a very strong relationship between the SE estimated using different values of the smoothness parameter. The main effect of varying the parameter is to simply vary the slope of the relationship, i.e. we can simply scale the SE estimates derived for any value of smoothness parameter to obtain those for any other.

[15] The median is the point at which 0.5 of the epsilon values fall below and 0.5 above. Approximating this in a Normal distribution, the integral of the distribution (erf) is 0.5 at 0.477 standard deviations from the mean, so we would, in a Normal distribution, expect 0.5 of the values to lie within +/-0.477 standard deviations.

Values of the correlation coefficients estimated between the various model parameters are analysed in section 5.4.3. These are seen to be predominantly high (positive or negative). Whilst the value of the smoothness parameter used to estimate them does not greatly change the values, the correlation terms are seen to be rather noisy spatially and temporally. This is sufficient evidence that they are not reliable estimates, and that definition of the prior would better proceed ignoring these terms. This will have the impact of increasing the uncertainty associated with the prior estimate, so fits in with our philosophy of providing a conservative estimate.

In section 5.4.4, the cross-validation experiment, we see consistent behaviour as a function of the smoothness parameters, i.e. we can accurately predict the value of the match between the test and reference datasets from one smoothness parameter from the values obtained from a climatology, simply by a scaling factor. The main conclusions from this experiment are that to achieve a match between the test dataset and the reference data, the standard error estimates need to be multiplied by a factor of 10 (assuming that a climatology is used, and the correlation terms are ignored). Although in practice the climatology will make use of data from all years (and therefore is likely be a better prediction of the 2005 parameters than that using independent data here) applying a gross scaling factor of 10 to all standard error estimates would seem to be reasonable step to provide conservative prior estimates of the parameters. Indeed, to make this a truly conservative estimate, we should inflate the uncertainties by a factor larger than this.

In conclusion, we choose to develop a climatology product in this work to use as a prior estimate of the model parameters. This is a straight mean of the model parameters for a particular (8-day) time step. As we do not have great confidence in the correlation information produced in the estimate, we choose to ignore that and only characterise terms for the leading diagonal of the prior uncertainty matrix. Further, we believe the estimates of standard error produced in the processing to be under-estimates of the true uncertainties by a factor of around 10.0, as so scale all standard error estimates by 10.0 to give the prior uncertainty.

When used to produce the globAlbedo product, these uncertainty estimates should be further inflated (this will be implemented as a constant scaling A_{pr} and a constant offset term B_{pr} in the computer implementation) to guarantee that only a conservative prior estimate is used.

4.5 Snow

As described above, the prior parameter estimate is produced for two scenarios: (i) snow free; and (ii) only snow. This means that two sets of priors will be stored and need to be accessible to the algorithm. A decision will be made on which to use in processing (and which set of samples to use) depending on the snow state of any particular observation. In practice this means that the algorithm is run twice: once for snow pixels and once for non-snow pixels, using appropriate priors and data for each. An additional advantage of this scheme is that, should a new snow albedo algorithm be defined at some later stage, the snow product can simply be replaced by this. Both datasets will record the time (in days) from the current observation to the closest snow or non-snow sample, appropriately. This

will facilitate the production of a merged dataset, which will use the snow observation if the closest sample is flagged snow and the non-snow dataset otherwise.

It should be noted that the snow flags in the MODIS BRDF/albedo product are not entirely reliable. When a 'snow free' dataset is produced, it still can have a significant number of pixels that are clearly snow-contaminated. An example of this is presented for tile h18v04 in figure 37[16], with associated uncertainty information (scaled by the factor of 10 suggested above) shown in figure 38.

[16] N.B. This is the product after stage 2 processing, described below, but the same principles apply.

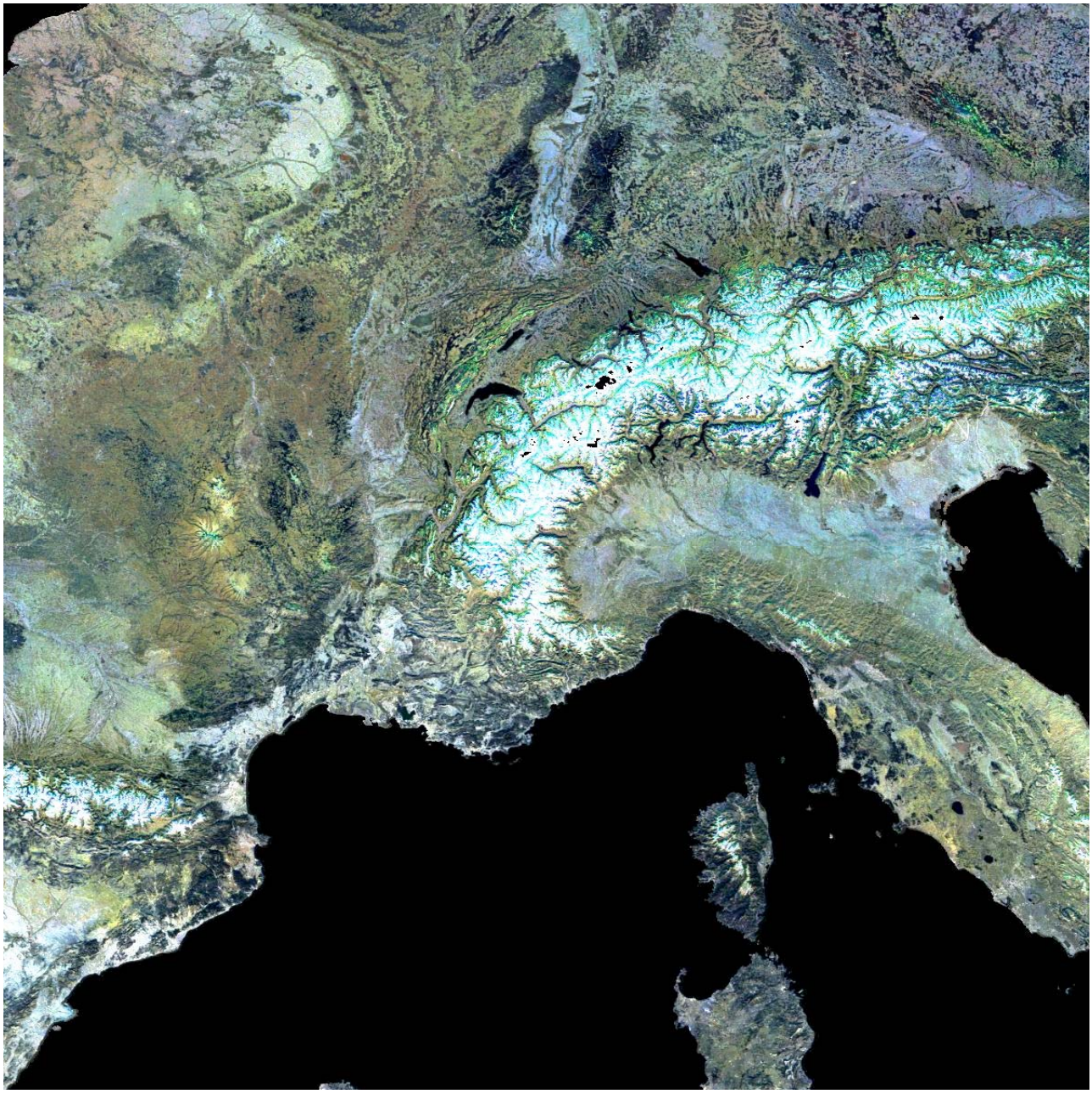

Figure 4-19. MODIS climatology VIS 'snow free' bihemispherical reflectance (white sky albedo) for (DOY 009, 041, 105 on RGB) scaled [0.016:0.128]

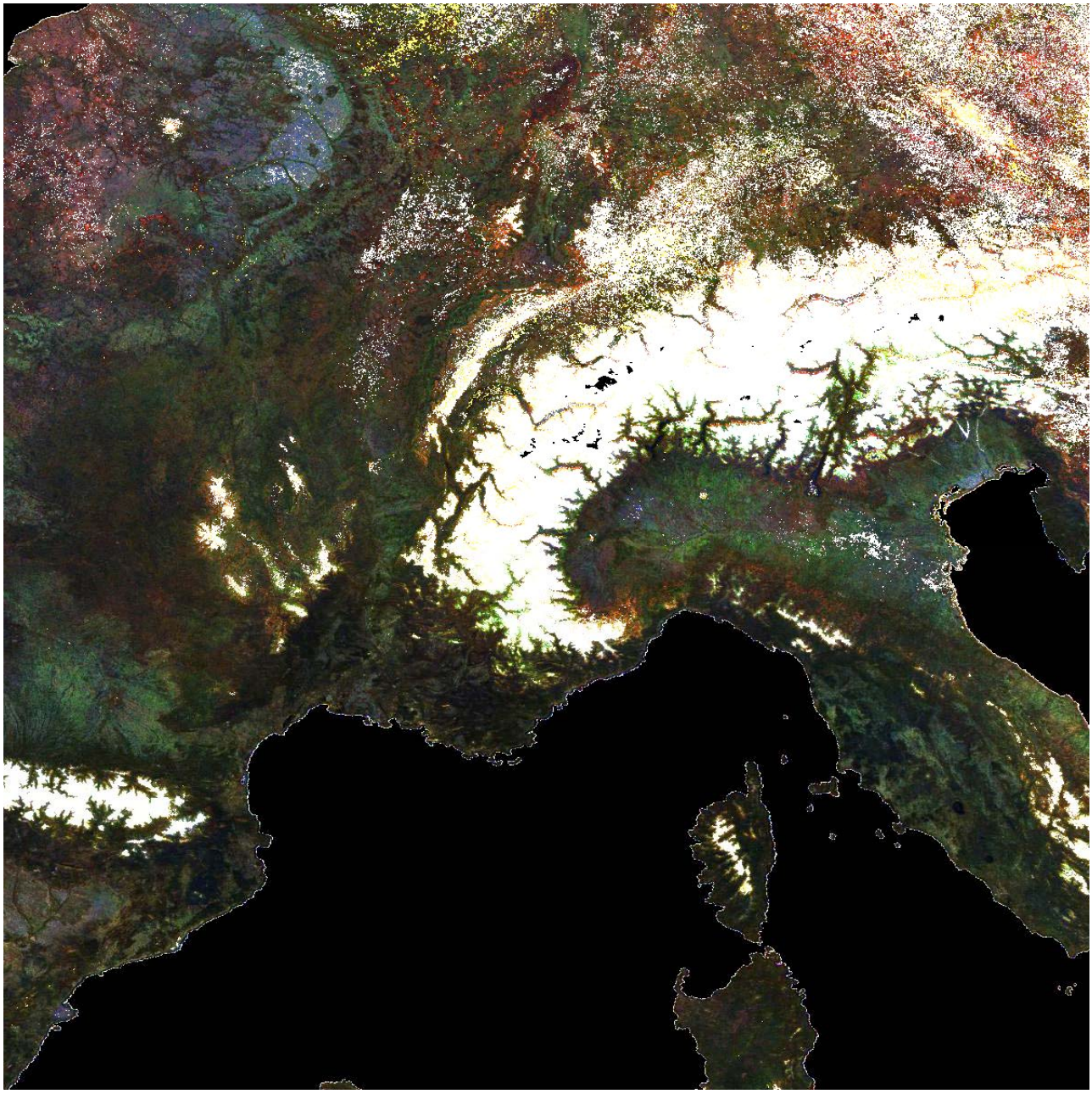

Figure 4-20. MODIS climatology VIS 'snow free' uncertainty in bihemispherical reflectance (white sky albedo) for (DOY 009, 041, 105 on RGB) scaled [0.000:0.065]

Even though the product is supposed to be a summary of only snow-free observations, it is clear that in mountainous regions (such as the Alps and Pyrenees) the prior is dominated by snow observations. The highest values of these have a (white sky) albedo of greater than 0.128, although many values in valleys have lower albedo. Thus, the supposedly snow free prior is inevitably contaminated to a certain extent by snow observations. This is generally in areas of permanent snow however: if no 'true' snow free observation has ever been obtained (because it has been snow covered for the whole of the MODIS archive) there can be no straightforward estimate of the snow free albedo.

Where the 'snow free' product has been contaminated by snow pixels, as in this example, we can note that the uncertainty (figure 38) is always high (>0.061 here) so if a 'true' snow-free pixel happened to be observed, the influence of the prior would be particularly weak in these areas.

4.6 Scaling and gap filling of the prior

The first stage of generating the prior estimates is described above. MODIS estimates of albedo model parameters are assigned a relative weight according to their QA value, then the weighted mean over all years, for a particular sample day, is assigned to the climatology. The standard error of each parameter estimate is calculated, and then scaled by a factor of 10 to put it in line with a conservative estimate of expectations of true uncertainty.

In stage 2, we attempt to gap-fill the prior estimate and reduce its resolution to match that of the globAlbedo product (1 km). The gap filling is achieved by setting each parameter value to a weighted mean of all stage 1 processed data. The time-weighting used is a Laplace distribution function (see above) with a value of γ of 11.54 days (i.e. the same as assumed for regularisation above). A further weighting is applied conditioned by the weighted number of samples used in each parameter estimate. The n-sample-weighted mean is then calculated over groups of 2x2 pixels so that the resulting data product is at the required 1 km resolution (in the projection of the MODIS grid – see figure 22).

This produces a slightly smoother (in time) version of the model parameters. The weighting of a sample 8 days distant is 0.5, but since the MODIS product uses overlapping 16 days windows, there will in any case be some correlation between samples this far apart. It has the advantage of gap filling the prior estimate. Note that where this does occur, it implies that there has never been a MODIS estimate of the model parameters (other than a filler value) at any time in the MODIS archive, for that particular DOY at that location.

The stage 2 uncertainty estimate at the original 500 m resolution is the square root of the n-sample-weighted parameter variances (simply, a weighted mean standard error). When applying the spatial scaling, we sum the total variance over all 4 samples (i.e. do not divide the variance by the number of samples). This is liable to produce a factor of 2 increase in the standard error estimate, but was implemented to provide a conservative estimate of parameter uncertainty. This suggests that a scale factor of 5 should be applied to the stage 2 uncertainty estimates, rather than the factor of 10 for stage 1 results, but this would ideally benefit from further analysis. A factor of 5 has been applied to all stage 2 standard error results presented here.

Figure 39 shows some typical results of stage 1 processing for DOY 185. For most areas, there will be some parameter estimate, because, as noted, there is only a gap if there has never been a MODIS estimate (of QA0-3) for that pixel on the DOY. A large part of tile h25v06 is missing, as this is most likely covered by snow and/or permanent cloud at this time of year. Figure 40 shows the uncertainty associated with that estimate (incorporating the factor of 10 scaling discussed above).

A. DOY 185, tile h18v04

DOY 185, tile h19v08

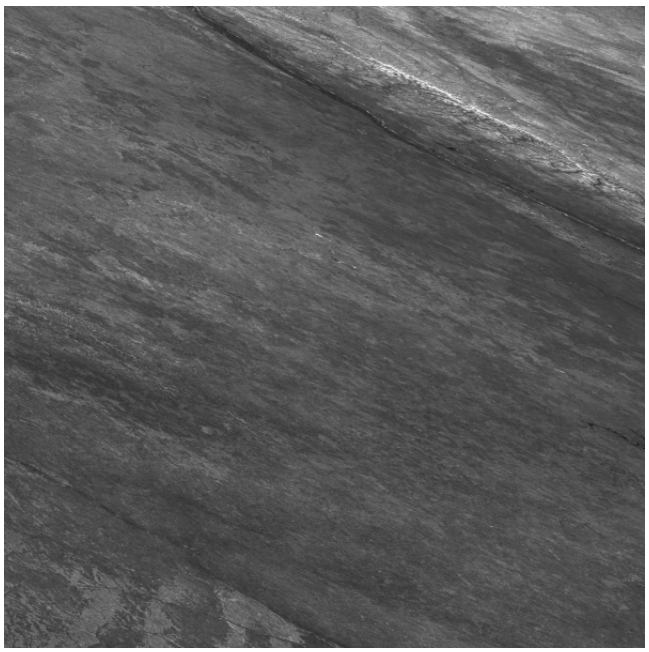

C. DOY 185, tile h22v02

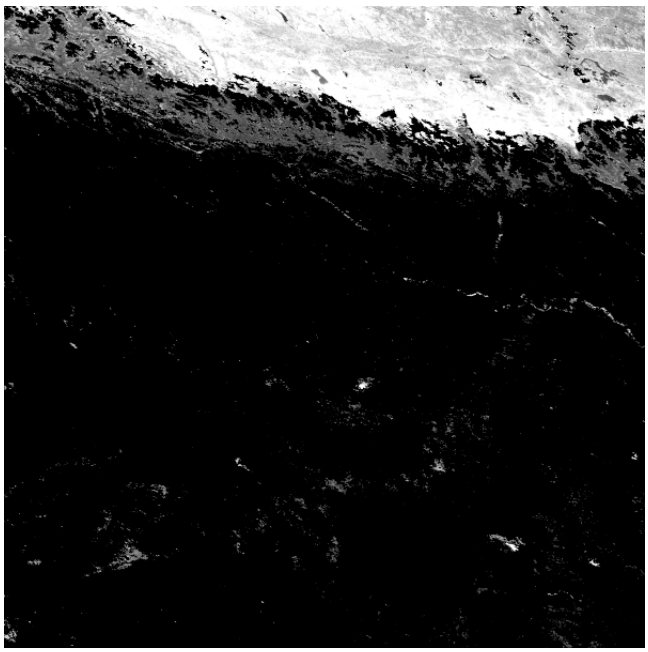

DOY 185, tile h25v06

Figure 4-21. MODIS-derived priors for DOY 185 for the 4 test areas after stage 1 processing. The images shown are for model parameter f_0, i.e. VIS Isotropic parameter. All images scaled 0:0.15. Black pixels are have no data.

A. DOY 185, tile h18v04

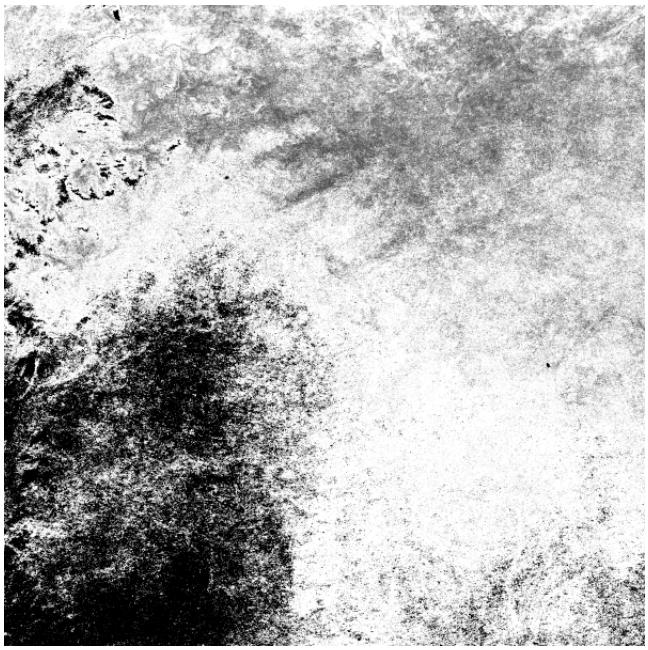

DOY 185, tile h19v08

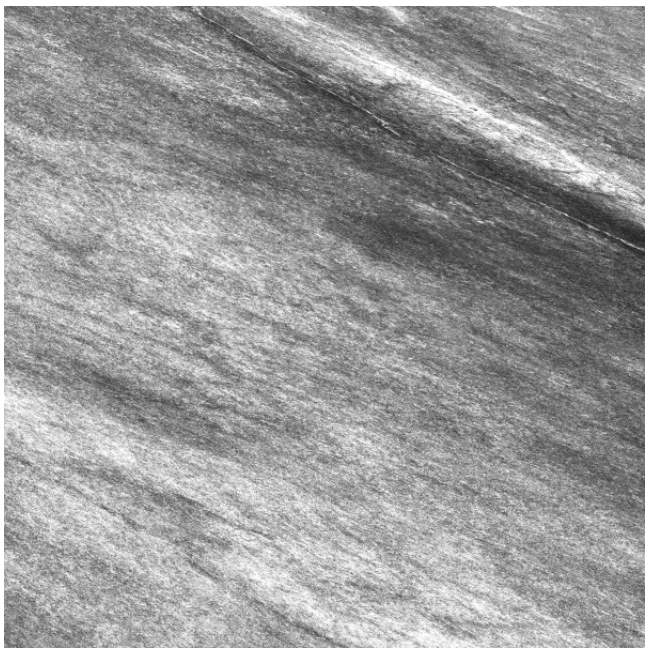

C. DOY 185, tile h22v02

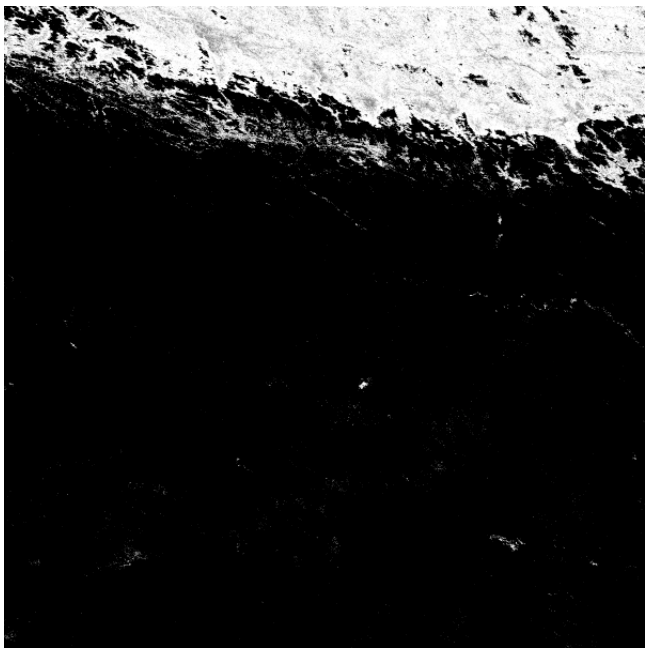

DOY 185, tile h25v06

Figure 4-22. MODIS-derived standard error in priors for DOY 185 for the 4 test areas after stage 1 processing. The images shown are for standard error model parameter f_0, i.e. VIS Isotropic parameter. All images scaled 0:0.075. Black pixels are have no data.

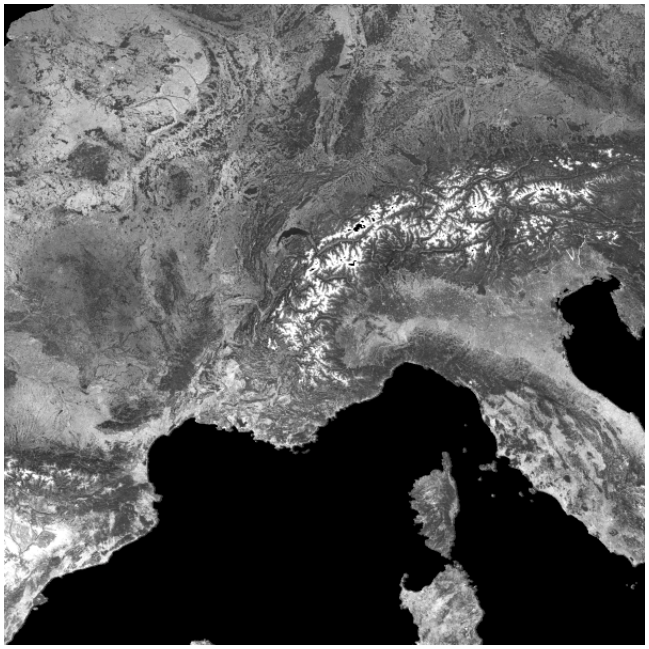

A. DOY 185, tile h18v04

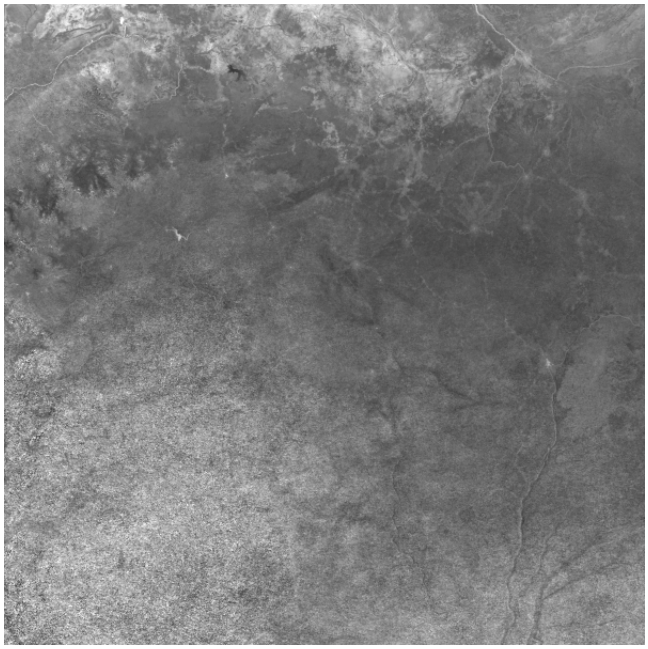

DOY 185, tile h19v08

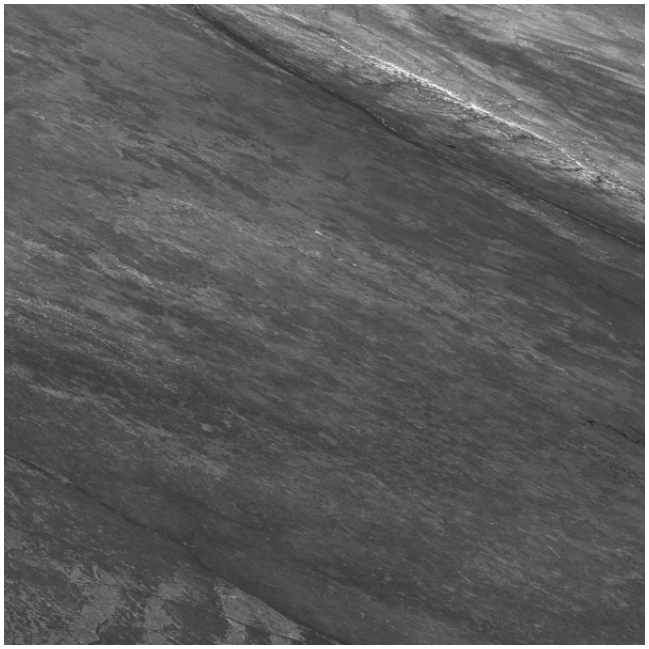

C. DOY 185, tile h22v02

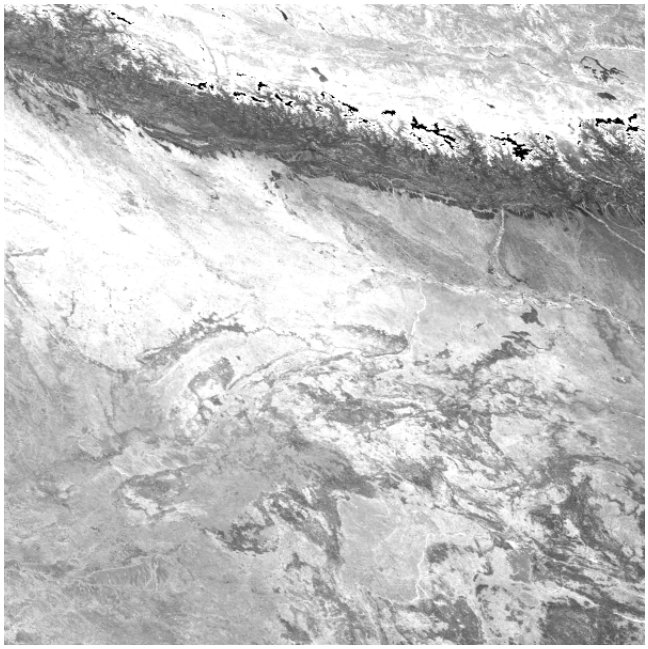

DOY 185, tile h25v06

Figure 4-23. MODIS-derived priors for DOY 185 for the 4 test areas after stage 2 processing. The images shown are for model parameter f_0, i.e. VIS Isotropic parameter. All images scaled 0:0.15. Black pixels are have no data.

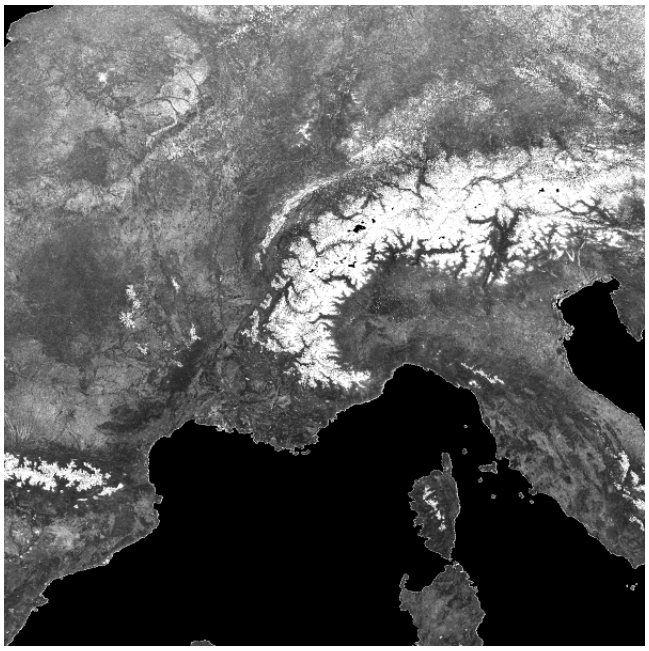

A. DOY 185, tile h18v04

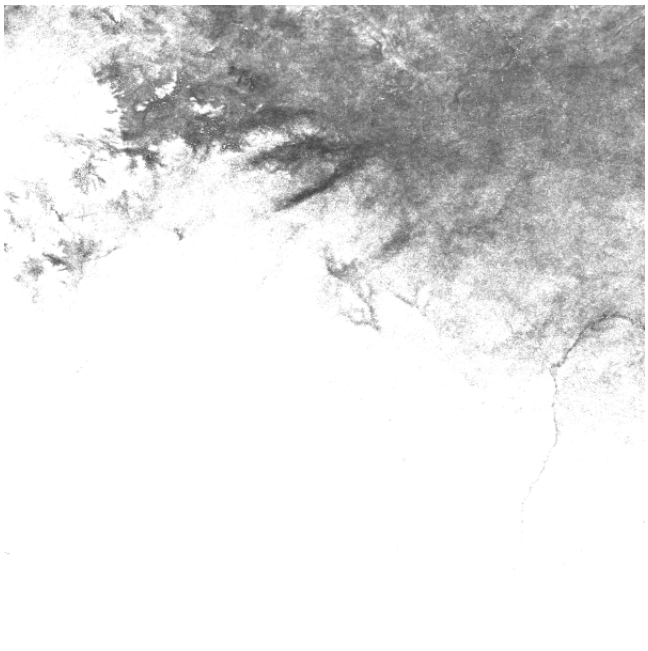

DOY 185, tile h19v08

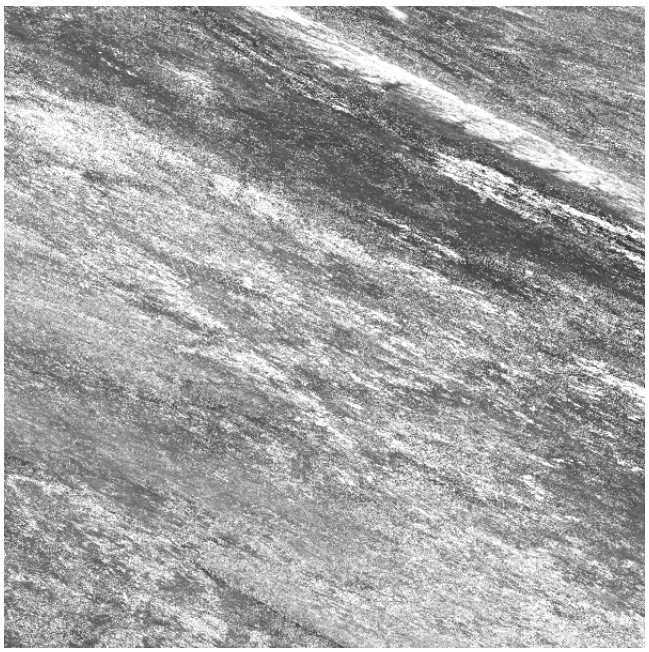

C. DOY 185, tile h22v02

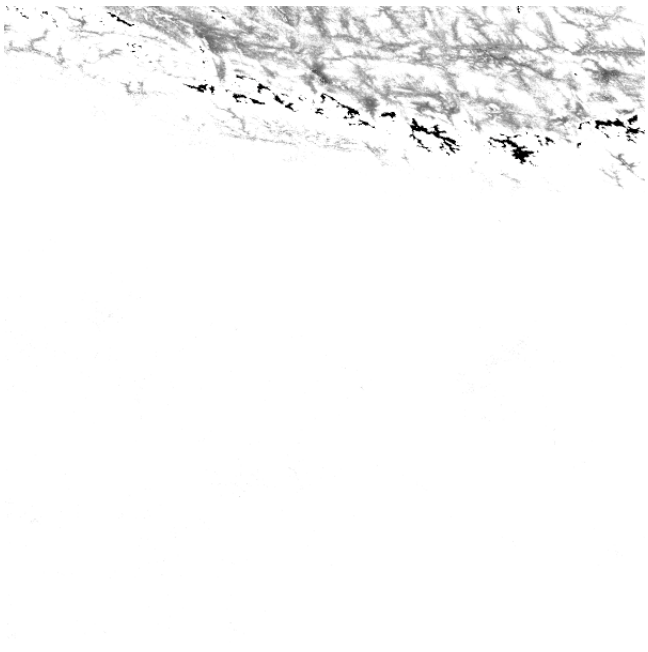

DOY 185, tile h25v06

Figure 4-24. MODIS-derived standard error in priors for DOY 185 for the 4 test areas after stage 2 processing. The images shown are for standard error in model parameter f_0, i.e. VIS Isotropic parameter. All images scaled 0:0.075. Black pixels are have no data.

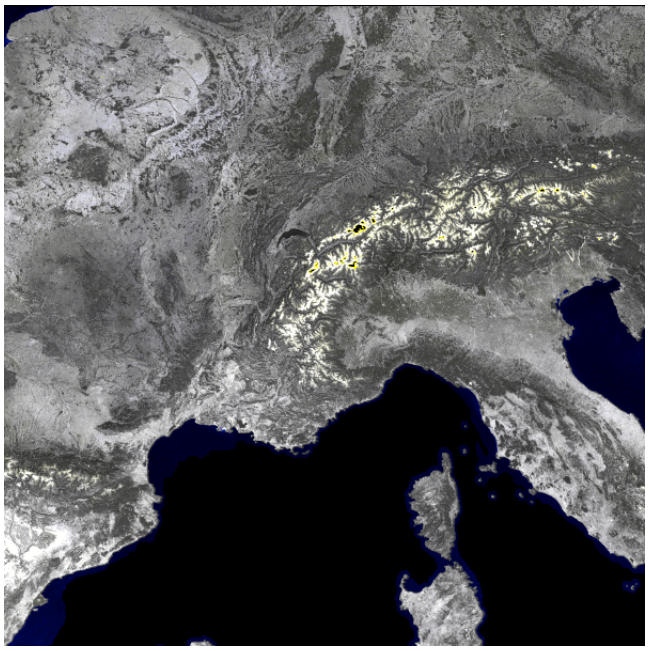

A. DOY 185, tile h18v04

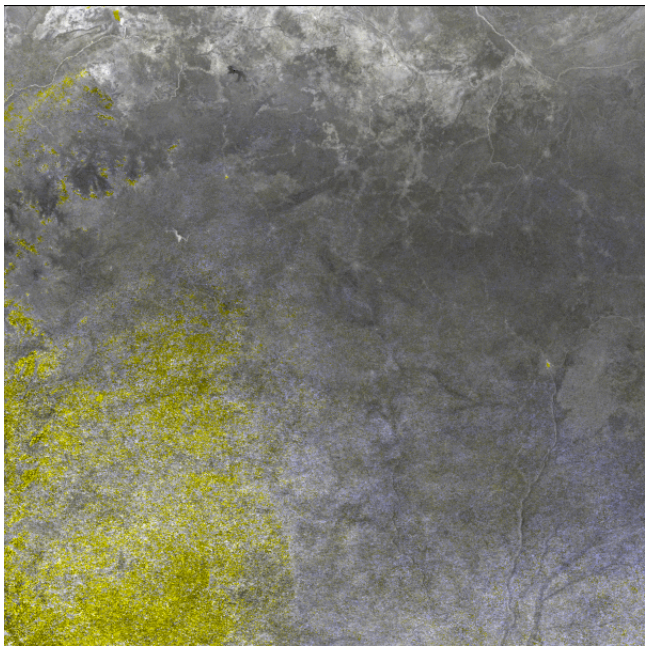

DOY 185, tile h19v08

C. DOY 185, tile h22v02

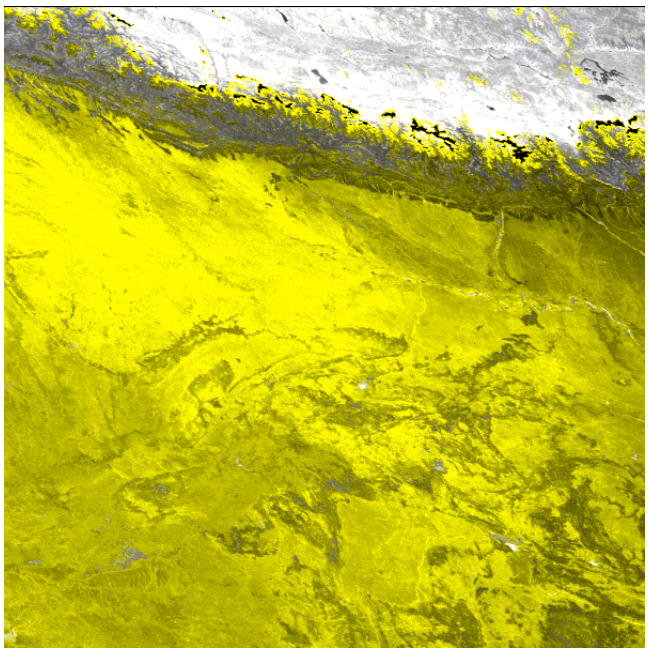

DOY 185, tile h25v06

Figure 4-25. MODIS-derived priors for DOY 185 for the 4 test areas after stage 1 (on blue) and 2 (or red and green) processing. The images shown are for model parameter f_0, i.e. VIS Isotropic parameter. All images scaled 0:0.15. Black pixels are have no data.

The uncertainty images[17] are scaled so that their maximum value is half of that used to scale the parameters (0.075 and 0.15 respectively). Thus, where the pixel values are approximately the same brightness, the uncertainty estimate is around 50% of the parameter value. High uncertainty values are most noticeable in much of tiles h19v08 and h25v06 as these have significant snow and high cloud cover issues.

Figure 40 shows the mean parameter estimates after stage 2 processing. Of particular note is the fact that an estimate of albedo parameters is now provided for tile h25v06 whereas this was missing in the stage 1 processing. These 'snow free' data clearly come from time periods other than that being examined here. The lower left section of tile h19v08 is also effectively gap-filled as well (there is clearly almost permanent cloud cover in that section of the image for DOY 185, shown by the lack of data in the stage 1 processed data). Figure 41 shows the uncertainty associated with the stage 2 estimates (scaled by 5). Where gap filling has been undertaken, or the data were highly uncertain in the stage 1 processing (most of tile h25v06; the lower half of tile h19v08; and snow-affected areas of the other tiles) the uncertainty is set high (in fact, > 0.075 for thresholded values here), so such data will only impact the globAlbedo result if there are no other sources of data.

Figure 41 shows example mean parameter estimates for stage 1 and stage 2 processing, as a false colour composite. The stage 1 result is on blue, with the stage 2 result on red and green. Parts of the images that show saturated yellow are therefore 'gap filled' data (i.e. there were no data in the stage 1 processing results). Areas without 'colour' have undergone no change as a result of the stage 2 processing, which suggests that the mild temporal smoothing has not greatly affected the quality of the climatology. Non-saturated colours (e.g. blue in the bottom right of tile h19v08) indicate that the parameter value has been slightly affected by the smoothing. Blue indicates a decrease from stage 1 to 2, and yellow an increase. These non-saturated colour only seem to appear in areas of the data that are in nay case rather noisy and uncertain.

4.7 Final gap filling

Even after stage 2 processing there will be some land pixels that have no parameter value associated with them. Overall (i.e. combining snow and no-snow datasets) these should be rather small in number, as their presence means that there has never been a MODIS BRDF/albedo parameter estimate for that pixel at *any* time over the MODIS era (i.e. on any day). If a pixel for a specific date has no parameter value, then that same pixel will have no parameter for any date.

This problem is most likely to occur in areas of essentially permanent snow, where no 'snow free' parameter value can be assigned. Alternatively, it could result from variations in the specifications of land masks between the MODIS data and subsequent processing of globAlbedo products. In any case, the processing chain must be able to provide a 'filler' value (with a very high uncertainty attribute) for the prior if a request is made to process it. Such a filler would, of necessity be rather arbitrary and data output QA should be flagged to indicate that such a value has been used.

[17] N.B. with the factor of 10 applied to stage 1 results and 5 to those from stage 2.

One obvious solution would be to use some land cover average value (for instance, a local land cover average per tile). The danger of this is a reliance on land cover products that the product otherwise has no dependence on.

In the 'snow' prior, there will clearly be a large number of pixels that have never experienced snow. In such cases, the use of a snow prior is rather meaningless, although the processing system should allow for such a possibility.

5 Algorithm Overview

5.1 General Overview of Scheme

The task is to provide estimates of land surface albedo as a gridded dataset, globally (for the land surface) at an 8-day sampling step, at a 1 km spatial resolution. The data to drive the estimation are: (i) satellite observations from European sensors; (ii) a decade of estimates of parameters relating to albedo derived from MODIS observations (Wanner et al. 1997; Justice et al., 1998; Schaaf et al., 2002).

The scheme is split into three parts that are covered in the following three sub-sections:

- Pre-processing
- Optimal parameter estimation
- Albedo estimation

5.2 Pre-processing

The BRDF inversion and albedo retrieval procedures described in this document are the last step of the GlobAlbedo processing chain. The processor receives broadband Lambertian equivalent reflectance as input. A series of pre-processing steps are performed to derive such broadband Lambertian equivalent reflectance and associated angular kernel values. These steps are:

5.2.1 Pixel identification

The GlobAlbedo Pixel Identification processor classifies each pixel to be processed according to a series of pixel categories, which include cloud, clear-land, clear-water and clear-snow. Cloudy pixels are not processed in GlobAlbedo, while land, water and snow pixels must be distinguished because of the particular processing steps associated to each surface type. In particular, water pixels must be separated from land surfaces even in the case of continental water bodies, as these are flagged in the final albedo product. Snow and snow-free surfaces will also be considered separately in the albedo product.

5.2.2 Aerosol retrieval

Estimates of aerosol extinction are need for the conversion from top-of-atmosphere measurements to surface reflectance, and for the partitioning of at-surface direct and diffuse irradiance fluxes required to calculate the D variable weighting e.g. the different kernel terms in equation 14. Aerosol optical depth (AOD) and aerosol model plus an

estimate of the uncertainty in AOD are derived by the Aerosol Retrieval processor from every data set to be processed.

It must be noted that AOD and aerosol model are assumed to sufficiently account for the variability in the atmospheric conditions to calculate D, while water vapour and ozone column contents are needed in addition to aerosol parameters in order to retrieve the most accurate Lambertian equivalent reflectance. All other atmospheric constituents are just set to climatology values in the GlobAlbedo processing chain. This selection is justified by the relatively higher impact of aerosol extinction at the spectral channels of the GlobAlbedo instruments.

5.2.3 Spectral directional reflectance retrieval

Pixel classification flags and aerosol maps provided by the Pixel Identification and Aerosol Retrieval processors, respectively, are inputs to the SDR/BBDR processor to derive Lambertian equivalent reflectance from top-of-atmosphere measurements over clear-land and clear-snow surfaces.

SDR retrieval in GlobAlbedo is designed to calculate pixel-wise Lambertian equivalent spectral reflectance plus spectrally uncorrelated uncertainties for each spectral reflectance value. Reflectance retrieval is performed by means of the inversion of equation 4, the different atmospheric parameters being provided by pre-stored look-up tables (LUTs) compiled with the MOMO radiative transfer code. These LUTs are searched for the particular viewing, illumination and atmospheric conditions of each pixel. Uncertainties in the instrument radiometric response and in AOD, columnar water vapour and columnar ozone are propagated to uncertainties in Lambertian equivalent reflectance by means of pre-stored gradients. Spectral *D* terms for albedo retrieval are also calculated from interpolation of the LUT.

5.2.4 Broadband conversion

Narrow-to-broadband conversion of Lambertian equivalent reflectance is also performed by the SDR/BBDR processor. As described in Section 4.4, broadband reflectance is calculated by means of the linear combination of directional reflectance in different narrowband channels. The uncertainty in broadband reflectance including the covariance between the three broadband spectral regions is also calculated in this process by assuming that the linear conversion applied to narrow band reflectance can also be applied for the conversion of narrowband errors to broadband errors.

Narrow-to-broadband conversion coefficients are also used to convert from spectral to broadband D terms.

5.2.5 Kernel-integral estimation

The linear model parameter estimation requires that, if Lambertian equivalent reflectance data are used, the kernels are themselves weighted by the sky radiance and other atmospheric interaction terms (equations 13 and 14). This is estimated as part of the BBDR retrieval, with the new kernels are weighted according to the prevailing atmospheric conditions at the time of acquisition, according to the atmospheric characterisation in MOMO.

5.2.6 Data binning

Data (a QA layer, BBDR for 3 bands, associated uncertainty (6 values), and 9 kernel values (three for each waveband, see 4.6.1) are projected to the MODIS sinusoidal grid[18] and 'binned'; resampling is a nearest neighbour approach. If multiple samples exist for any one grid cell, multiple spatial datasets are created.

5.3 Optimal parameter estimation

The optimal estimation framework is fed observations (BBDR, including weighted kernel values, and associated uncertainty of the BBDR[19]) that have been resampled an equal area projection grid (the same grid as used by MODIS, to have consistency with a widely-used albedo dataset).

The data are masked by QA value, and the BBDR, uncertainty information and weighted kernels read for all pixels in the processing region covered. The uncertainty information (6 values) is assigned to a full (3x3) uncertainty matrix and its inverse calculated[20]. In an initialisation step, two accumulator matrices are zeroed. These are the forward accumulators of section 4.6.3 for $K'^T C_O^{-1} K'$, $K'^T C_O^{-1} R$ and $R^T C_O^{-1} R$. These are a matrix of dimension 9x9 and a vector of 1x9 and a scalar respectively. The matrix is symmetric about the leading diagonal, so 46 elements must be stored.

The accumulator storage cost then is 46+9+1=56 double precision (8 byte) elements to be stored every 8-days (45/year), so for processing e.g. a MODIS tile of 1200 x 1200 pixels, this amounts to 27.1 GB per MODIS tile-area per year, of temporary file storage (or storing in memory of appropriate). The first stage of processing then consists of loading data into these accumulators, and writing out files the time-weighted summations each 8 days. Each of these (45 per year) datasets, indexed t for time, then contains:

$$\sum_{i=t_0}^{i=t} w(|i-t|) K_i'^T C_{O,i}^{-1} K_i'$$

and

$$\sum_{i=t_0}^{i=t} w(|i-t|) K_i'^T C_{O,i}^{-1} R_i$$

[18] http://remotesensing.unh.edu/modis/modis.shtml

[19] Uncertainty in the kernel weightings is not conducted at present, but could be treated as model noise.

[20] An obvious alternative is to store the inverse matrix, but the impact of rounding errors on that needs to be assessed.

To calculate χ^2 we also need to keep track of

$\sum_{i=t_0}^{i=t} w(|i-t|) R_i^T C_{O,i}^{-1} R_i$. From equation 19b then:

$$\chi^2 = \frac{1}{\sum_{i=t_0}^{i=t} w(|i-t|)} \left[F^T \sum_{i=t_0}^{i=t} w(|i-t|) K_i'^T C_{O,i}^{-1} R_i + F^T \left[\sum_{i=t_0}^{i=t} w(|i-t|) K_i'^T C_{O,i}^{-1} K_i' \right] F - 2 \sum_{i=t_0}^{i=t} w(|i-t|) R_i^T C_{O,i}^{-1} R_i \right]$$

where t_0 is the starting time period. The 56th accumulator is for the normalisation term $\sum_{i=t_0}^{i=t} w(|i-t|)$.

After the accumulators have been calculated for time step t, they are readily estimated for time step $t+8$ by multiplying all terms by $e^{-\frac{8}{\gamma}} = 0.5$ and adding all new reflectance data that occur between after day t and before or on $t+8$, as explained in section 4.6.3.

After these accumulators have been calculated for some defined time period, the model parameter estimation can take place. This involves starting at the *end* of the time series just processed and keeping a running accumulator of the same terms as in the stored accumulator. When the (backward, running) accumulator has been calculated for some day $t+1$, it is combined with the forward accumulator for day t and the *a priori* constraint on model parameters for day t.

Thus, as the running accumulator progresses back in time from the end date of the processing period, the relevant file (matching location and date[21]) of *a priori* information is opened and read, the relevant file (matching location and date) of forward accumulator is opened and read, and these are combined to provide (and write out) the optimal estimate of the model parameters at time t.

5.4 Impact of the prior in the model parameters

The optimal estimation framework for the parameter estimation is consistent, no matter what the information content of any observations. The role of the prior then is in better conditioning the parameter estimation. Because we have used a very conservative estimate of the prior, this will not unduly influence parameter estimation when the

[21] Noting that the MODIS product date structure sets a file date field as the *start* day of the 16 days of sampling, i.e. it is 8 days behind the central day of sampling, which is the convention we use in this product. This change in convention is inevitable, as the start sampling day does not have the same meaning in this product as in the MODIS product.

information content of the observations is high, but it will be dominant when it is low. For example, if no observations, or only very few observations are available, the estimate reduces to the climatology. Since the uncertainty on the climatology is set high, any pixels for which this occurs will tend to have high uncertainty.

The formalism for this is:

$$\hat{P} = \left(K^T C_{obs}^{-1} K + C_a^{-1}\right)^{-1} \left(K^T C_{obs}^{-1} R + C_a^{-1} P_a\right)$$

with uncertainty:

$$C_P = \left(K^T C_{obs}^{-1} K + C_a^{-1}\right)^{-1}$$

Interestingly, this can be shown to be equivalent to (Rogers, 2000, p.67):

$$\hat{P} = P_a + G\left(R - KP_a\right)$$

and

$$C_P = C_a - GKC_a$$

where we see the role of the observations as providing a departure from the prior estimate by the product of $G = C_a K^T \left(KC_a K^T + C_{obs}\right)^{-1}$ and the residual between the measurement and that predicted from the *prior*, $\left(R - KP_a\right)$. We clearly see the role of G here as a *gain* term, a measure of how much we depart from the prior prediction, given the measurements. We also note from these expressions that the term GKC_a provides a *reduction* in uncertainty resulting from the measurements. We note that the gain matrix G is a function only of the prior uncertainty, the observation uncertainty and the linear model terms K. Since K are mainly functions of the angular configuration of the sampling (but also partly the atmospheric conditions at the time of imaging) we see the route through which the measurement conditions impact the parameter estimate.

Information content

Whilst the consistent statistical framework used aims to provide not only an optimal estimate of the BRDF model parameters but also the uncertainty on these values, it is still of value to any user of the data to have an appreciation of the impact of the priors on the

parameter estimate. This we achieve in globAlbedo through a calculation of the relative entropy of the posterior uncertainty C_P and the prior uncertainty C_a. The entropy of a Gaussian probability distribution function (pdf) is the logarithm of the volume occupied by the pdf (plus an offset). Thus, for high uncertainty, the volume is high, and the entropy is high. The relative entropy H then is a measure of the (logarithm of the) reduction in this volume achieved by the measurements. This can be written:

$$H = -\frac{1}{2}\ln\left|C_p C_a^{-1}\right|$$

where $|\bullet|$ indicates the matrix determinant. This can also be written:

$$H = \frac{1}{2}\ln\left|C_a^{-1}\right| - \frac{1}{2}\ln\left|C_p\right|$$

If there is no information in the measurements (there are no measurements), then $C_p = C_a$, so $H = 0$. The higher the value of H, the higher the information content of the measurements (in this case, relative to the conservative estimates of uncertainty in the prior). This measure will be our primary metric for passing information through to users on the impact of the assumed *prior* information on the final globAlbedo product. The entropy of the *posterior* estimate of uncertainty:

$$H_p = m\ln(2\pi e)^{\frac{1}{2}} + \frac{1}{2}\ln\left|C_p\right|$$

where *m*=9 here, will appear in the parameter product, along with the relative entropy H above. In the final user albedo product, a 'simplified' version of H will vbe provided:

$$H' = e^{H/m}$$

5.5 Albedo estimation

As noted above, albedo is not an intrinsic surface property. The information contained in the model parameter set, being a representation of an intrinsic surface property, is sufficient to allow the albedo to be estimated under any illumination conditions, and many users will want to make use of this ability in calculating the dynamics of albedo or validating the product. However, many other users will simply want some consistent representation of albedo (under some defined illumination conditions), so a filtered dataset will be output as the 'albedo product' for globAlbedo. This will include black sky albedo (at

an average solar zenith angle) and white sky albedo at all three bands, along with uncertainty (standard deviation for each value), along with associated information on fAPAR, land cover type etc. The general format and contents are defined in the Technical Specification document, but relavant information will be re-iterated here.

6 Algorithm Description

6.1 Introduction

This section describes in detail the algorithm to estimate BRF model parameters and albedo from 'observations' of BBDR.

6.1.1 Input data

The assumed inputs are:

1. **A set of prior estimates of the model parameters**

   $F_{\mathrm{Pr}}(L,DOY)$ $\sigma_{\mathrm{Pr}}(L,DOY)$, the *a priori* estimate of BRF model parameters, over some set of locations L, for day of year (DOY), and contain:

   a. 9 channels of $F_{\mathrm{Pr}}(L,DOY)$, ordered as band 0 (VIS) f_0, band 0 f_1, band 0 f_2, followed by the parameters for band 1 (NIR) and band 2 (SW).

   b. 9 channels of $\sigma_{\mathrm{Pr}}(L,DOY)$, ordered the same as $F_{\mathrm{Pr}}(L,DOY)$.

   Notes: There are 45 sets of these data per L, with DOY in 8-day steps per calendar year, starting at 001 and ending at 361. The DOY represents the central day of the time period that the data represent (i.e. for 16 day MODIS windows, DOY 009 represents data from DOY 001 to 016 inclusive. This corresponds to the MCD43 product of $DOY-8$, i.e. the prior for DOY 009 corresponds to MCD43 data for DOY 001. These data are stored in MODIS tiles for convenience of processing.

2. **A land surface and land cover mask**

   $M(L,DOY)$ is read to determine which pixels should be processed. There is scope for this mask to be dynamic (i.e. a function of DOY), although a static mask will be used in the globAlbedo processing. The mask contains (or can be used to derive) a bit field that is 1 for data to be processed and 0 for data not to be processed.

   The land surface mask also provides a land cover categorisation of the pixel which is used for a LUT to model parameter values should there be no information in the observations or prior estimates. The land cover associated with the closest observation in time is output from the dataset.

3. **A set of observations**

   These come from the products BROADBAND_SDR_*i* where *I* is an index to the data channel number of the product.

   $R(L,DOY,i)$, $C_O(L,DOY,i)$, $K(L,DOY,i)$, $ATM(L,DOY,i)$ $QA(L,DOY,i)$ representing:

   - $R(L,DOY,i)$: BBDR data in 3 wavebands (VIS, NIR, SW) for sample i at grid cell location L, representing data for day DOY.

- $C_O(L,DOY,i)$: the elements of the observation uncertainty matrix are stored and read as: $C_{Op,q}(L,DOY,i)$, in the order $p,q=\{0,0\},\{0,1\},\{0,2\},\{1,1\},\{1,2\},\{2,2\}$. The full matrix $C_{Op,q}(L,DOY,i)$ is populated upon reading, using symmetry relations and the inverse (also symmetric), $C_O^{-1}(L,DOY,i)$ calculated.

- $K(L,DOY,i)$: the values of the 3 kernels weighted for the observation illumination conditions, in the same order as $F_{\mathrm{Pr}}(L,DOY)$ or $\sigma_{\mathrm{Pr}}(L,DOY)$ above. The weighting scheme is defined by equation 14 and 15, for broadband equivalences, noting that the definition of $D_{0\Lambda\uparrow}$ and $D_{0\Lambda\downarrow}$ is relative to an absorbing lower boundary.

- $ATM(L,DOY,i)$: atmospheric parameters required for the treatment of atmospheric effects. Provided full weighted forms of $K(L,DOY,i)$ are provided, only the (broadband equivalent) atmospheric spherical albedo $\overline{\overline{\rho}}_\Lambda$ (one per waveband) may be required[22]. This is read as $\overline{\overline{\rho}}_\Lambda(L,DOY,i)$ and contains the three values for VIS, NIR and SW respectively. This term is not required by the default behaviour of the scheme (see notes below).

- $QA(L,DOY,i)$: QA data associated with the observations at L. The default behaviour is to examine: (i) a snow/no snow bit field, to give $SNOW(L,DOY,i)$ as 1 if snow is detected, and 0 otherwise; (ii) a process/no process bit field (being a summary of cloud/shadow etc. detections), giving $VALID(L,DOY,i)$ as 1 if the pixel is a valid candidate for processing and 0 otherwise. More subtle information, using different thresholds can be processed from the QA data if required (e.g. threshold on AOT or SZA).

Notes: Information about which sensor the data were measured by are contained in Metadata in the file. Although this information is not directly used, it will be passed through to the output file metadata, indicating which sensors were used in processing. It may be appropriate to store (and therefore read) the elements of the inverse observation uncertainty matrix, although further testing of the impacts of quantisation rounding errors on this need to be performed before a final decision.

For a full treatment of atmospheric effects, a multiple interaction term is required, being the product of the (broadband equivalent) atmospheric spherical albedo $\overline{\overline{\rho}}_\Lambda$ and the difference between (unweighted) bihemispherical and weighted bidirectional reflectance (equation 9a). To achieve this, a second iteration of the

[22] If the atmospheric weighting were to be performed in the optimisation code, we would need access to $D_{0\Lambda\uparrow}$, $D_{0\Lambda\downarrow}$ and the two N_{sky} weighted kernel integrals.

optimisation scheme is required, where the input Lambertian equivalent reflectance data are multiplied by the term $1-\overline{\overline{\rho}}_{\Lambda}\left(\overline{\overline{K}}_{\Lambda}-K'_{\Lambda}\left(\Omega_{v},\Omega_{s}\right)\right)$ prior to further processing. The terms $K'_{\Lambda}\left(\Omega_{v},\Omega_{s}\right)$ are simply those available as $K\left(L,DOY,i\right)$. The terms $\overline{\overline{K}}_{\Lambda}$ are the bihemispherical integral of the kernels, given in Table 4-1 (final row). This is implemented in the scheme, and its impact will be investigated, but is not part of the core design of the algorithm as the first pass treatment of atmospheric effects is very likely to be sufficient.

6.1.2 Output data

6.1.2.1 Model parameter estimates

The initial 'full' model output is in the product BROADBAND_Kernels_*i* where *i* is and index to the appropriate data channel. Two versions of the product are generated, where the index is prefixed by either *CLEAR* or *SNOW*. These versions are estimates of the model parameters for non-snow- and snow-flagged data inputs respectively. The detail of each product is identical, so we can refer to a single 'product' below.

This product can be used to estimate broadband albedo in three spectral channels under any viewing and illumination conditions for which the models are valid (by appropriate weighting of kernels). These products are necessary to calculate the GlobAlbedo final product set (below). It is envisaged that these products will be useful to the scientific community in their own right for more detailed investigations into albedo, or for validation exercises under known conditions. Formally, this is an intermediate (temporary) product however (GlobAlbedo, 2010). The GlobAlbedo products are stored in NetCDF format files.

The primary data product is linear kernel model parameter estimates at 1 km spatial resolution at global land locations defined on a sinusoidal grid (SIN) (the same as MODIS products use).

The spectral coverage is:

- Visible/photosynthetically active band: Vis/PAR (0.3–0.7 µm)
- Near infrared band: NIR (0.7–3.0 µm)
- Shortwave band: SW (0.3–3.0 µm)

The temporal coverage is:

- Fully covering the time period: 1995-2010

The time resolution of the products is 8-day, with 45 samples per calendar year using samples centred around DOY 001, 009, etc..

In addition to the 9 model spectral parameters, a full (45 element, this T_9, the triangle number of 9) uncertainty matrix is available per pixel.

A QA field is output. This contains the following information:

- Number of days since most recent sample (0 = sample on central DOY)
- Land/Sea/Inland Water/Coastal Mask (model values available for all Land pixels)
- A measure of the information content of the *a posteriori* data distribution relative to the *a priori*, the relative entropy, is calculated to monitor the impact of the

observations in determining the model parameters (specifically, the SW white sky albedo here).

- Quality metric quantised and summarised from the uncertainty information (square root of determinant of variance/covariance matrix)
- The (time weighted) number of samples used in processing.
- Coding of which sensors contributed observations.

The target accuracy of the product is:

- BHRiso better than 0.005 absolute or 10% relative
- DHR better than 0.01 absolute or 20% relative

6.1.2.2 Albedo

The primary product of GlobAlbedo is the BB Albedo (under given illumination conditions) and associated information for the prevailing snow/no snow conditions. Full details of the output formats and contents are given in the GlobAlbedo Technical Specifgications document (GlobAlbedo, 2010).

This product takes as input BROADBAND_Kernels_*i* (above) for snow and no snow conditions. A decision on whether a snow or no snow dataset is used in the final output product is made based on the QA data (the (time weighted) number of samples used in processing *N*). Originally, it was intended that the QA information on the number of days since last snow or no-snow sample would be used for the merging criterion, but this proved to be overly sensitive to snow detections from the sensors. With this criterion then, the final 'merge' product does not have a binary snow flag, but rather the proportion $N_{snow}/(N_{snow}+N_{no\ snow})$. This can be interpreted as a form of snow probability, providing the weight of evidence of there being snow for a particular time/space sample.

The primary data outputs are three waveband estimates of:

- White-sky albedo - Bi-hemispherical reflectance under isotropic illumination (BHRiso)
- Black-sky albedo - Directional-hemispherical reflectance (DHR) - at solar noon.

The white sky albedo for a particular band is calculated from the model parameters using the coefficients of table 4-1. The black sky albedo weighting is stored as a LUT of values as a function the solar zenith at solar noon. The final product computer code then needs access to an estimate of this angle for each pixel for the given DOY.
Most details of the product are the same as above, with the following exceptions:

- The time resolution of the products is 8-day, calendar-monthly, seasonal and annual.
- The spatial resolution is1 km, 5 km, 60 km
- The products are available in the following map projections: Plate-Carrée grid and MODIS SIN grid.

As above, quantitative uncertainty estimates (standard error estimates) are provided per pixel for both Black-sky and White-sky albedo for each waveband. Note that uncertainty

correlation terms are not output in this product, so only 9 uncertainty terms are required. In addition, the fAPAR for isotropic illumination are calculated via a LUT based on the albedo values, with associated uncertainty values.

Further, the NDVI is calculated from WSA and output (no uncertainty value, since this is a non-linear transform) based on the white sky albedo VIS and NIR channels.

6.2 A Data Class and methods for optimal estimation

The description of the whole algorithm can be simplified by considering the requirements of a set of data holding and processing classes/methods. The core of this is the data class. The purpose of this class is to store and process the observational and model data. As we shall see some operations are most efficiently carried out using data from some set of locations at the same time, whereas others may be 'per location' ('per pixel') operations. We therefore require out data class to hold and process sample values for multiple locations (assumed on a raster grid). The class description in this ATBD is not a full description, rather it is intended as a guide for implementation.

The `Data Class` needs two dimensional, three dimensional and four dimensional datasets, although these latter (matrices) are symmetric and require efficient storage. The class should store and provide access to:

- 'Meta' data
    - The geographic extent and pixel spacing of the samples, projection information etc. This is not altered by the processing, but is required to be carried through.
    - `nk`: The number of kernels (3 by default)
    - `nb`: The number of wavebands (3 by default)
    - `nc, nr`: The number of rows and columns of the spatial datasets (likely to be 1200 x 1200 if a full MODIS tile to be processed)
    - `nmd`: the number of matrix datasets stored (assumed square and all of the same dimensions)
    - `mvd`: : the number of vector datasets stored (this can provide storage for any scale spatial datasets as well)
    - `nindex`: the number of elements in the indexing for the matrices. The full matrix representations are nk x nb, structured as band 1 kernel 1, band 1 kernel 2, band 1 kernel 3, band 2 kernel 1 … Here, `nindex` = $\frac{1}{2}(nk \times nb)(nk \times nb + 1)$ which will by default be 45.
- A spatial dataset of dimensions (`nd,nr,nc,nindex`):

- `MData`: $nmd \times nr \times nc \times nindex$ spatial elements of the matrix (e.g. $K^T C_O^{-1} K$), organised as `MData`(1:nmd,1:nr,1:nc,1:index)
- `VData`: $nvd \times nr \times nc$ spatial elements organised as VData(1:nvd,1:nr,1:nc)
- `NData`: $nvd \times nr \times nc$ spatial elements organised as NData(1:nvd,1:nr,1:nc): the weighted number of samples (floating point) associated with `VData`.
- `Mask`: a binary (or byte) mask of dimensions (nr, nc) that is set to 1 if there are valid data at that location.

- Public Methods:
  - `Allocate / deallocate` the `MData, VData` and `Mask` arrays
  - `Copy`: copy all elements from one `Data Class` instance to another (this might be an initialisation of a new instance as well).
  - `Mzero, Vzero` (zero the `MData/VData` arrays). `Vzero` should zero `NData` as well.
  - `Matrix`: return the full matrix representation for a given row, column and dataset
  - `Scale(s)`: multiply all elements of `MData, VData` and `NData` for which mask is 1 by the factor `s`.
  - `Accumulate(Data Class: new)`: for pixel locations where mask is 1 in both this and the new dataset, add the elements of new.MData to this.MData, new.VData to this.VData new.NData to this.NData and modify `this.Mask` accordingly.
  - Data input/output routines, storing/returning the metadata, `MData, NData, VData` and `Mask`. For metadata, `Mask` and `NData, VData` this is straightforward. For `MData`, we want to be able to determine index as a function of the element index *p,q*; If we assume the indexing system 1-based, setting $N = nk \times nb$, the total number of samples in `MData` is the N^{th} triangular number, $T_N = N(N+1)/2$ (i.e. 1, 3, 6, 10, 15 … or 45 here in the default case). From this, we can show that the index for element $M[p,q]$ is:

$$index = \frac{(3+2N-p)p}{2} - q$$

for the upper triangular elements of the matrix. To go from index to $p.q$ it is probably most convenient to build a LUT.

6.2.1 Data input

We can consider a set of low level data input functions then that read the required datasets into memory and perform any masking or other operations. These are:

6.2.1.1 `Get_Observations(filename,`
`writeDataFile=writeDataFile,`
`landcoverMask=landcoverMask,`
`window=window)`

Inputs:

The main input for this function is the filename associated with a particular set of observations. An instance of a `Data Class, landcoverMask` can also be input that should cover the same area as that to be processed here.

An output filename may be specified, in which case a suitable filename should be passed through the `writeDataFile` option.

A window may be specified through a keyword or similar mechanism to specify some area of the image to read. The default behaviour should be to read the whole of an image in the filename specified.

Other options may be appropriate.

Outputs:

The function should store information from the observational dataset in an instance of a `Data Class` and return this.

It has the possibility to write this out as arrays of `Mask, MData` ($K^T C_O^{-1} K$ for this sample set) and `VData` ($K^T C_O^{-1} R$) for this dataset. This only happens if `writeDataFile` is set, but may be useful, as a 'pre-processing stage' may then be performed that stores all of the observational data as matrices. The storage requirement for that is 45+9+1=55 8-byte elements per pixel (1200 x 1200) = 0.59 GB per image (in fact, slightly less as the `mask` array could be stored as a single bit array or at most a byte array).

Operation:

There is one relevant observation matrix, $K^T C_O^{-1} K$ and one vector term $K^T C_O^{-1} R$ to be stored and operated on so nmd should be set to 1 and nvd to $nk \times nb$. Should $\overline{\overline{\rho}}_\Lambda$ be required, this can be stored in an extended `VData` array, or perhaps better still, a new array member of the `Data Class` defined to hold this.

The `mask, MData, NData` and `VData` need to be allocated and zeroed.

The `Mask` is set to 1 where the `SNOW` flag is zero (for Snow-free processing, and *vice versa*), the land cover mask indicates that a pixel should be processed, and the flag `VALID` is 1 in the dataset. It is set to 2 if the pixel is a valid land sample, but there is no observation.

The term $K^T C_o^{-1} K$ is a symmetric matrix of dimensions $nk \times nb$ by $nk \times nb$ (9x9 typically). The upper triangle of $K^T C_o^{-1} K$ is calculated for all pixels where `MASK`=1 and the elements stored sequentially in `MData` (according to the indexing system defined above).

The vector $K^T C_o^{-1} R$ is of dimension $nk \times nb$. All elements of $K^T C_o^{-1} R$ are calculated for all pixels where `MASK`=1 and the elements stored sequentially in `VData`. `NData` is set to 1 where `MASK`=1.

Comments:

Probably the most computationally-costly part of this function is the calculation of $K^T C_o^{-1} K$. The information required for further processing and for optimal estimation is contained within the terms $K^T C_o^{-1} K$ and $K^T C_o^{-1} R$. If the data are read from the image files into a Data Class instance, the arrays of $K^T C_o^{-1} K$ and $K^T C_o^{-1} R$ could be output for each sample, and this calculation separated from the optimal estimation procedure.

6.2.1.2 Get_Prior(filename,landcoverMask=landcoverMask,window=window)

Inputs:

The main input for this function is the filename associated with a particular *a prior* parameter estimate (associated with DOY and location (MODIS tile) L).

An instance of a `Data Class`, `landcoverMask` can also be input that should cover the same area as that to be processed here.

A window may be specified through a keyword or similar mechanism to specify some area of the image to read. The default behaviour should be to read the whole of an image in the filename specified.

Other options may be appropriate.

Outputs:

The function should store information from the prior dataset in an instance of a `Data Class` and return this.

It has the possibility to write this out as arrays of `Mask`, `MData` and `VData` (the diagonal elements of C_{Pr}^{-1} all of $C_{\mathrm{Pr}}^{-1}F_{\mathrm{Pr}}$ for this sample set) although this is probably not generally worthwhile.

Operation:

There is one relevant (prior uncertainty) matrix, C_{Pr}^{-1} and one vector term $C_{\mathrm{Pr}}^{-1}F_{\mathrm{Pr}}$ to be stored and operated on. **In this case, only the diagonal elements of C_{Pr} are read in**. C_{Pr}^{-1} should still stored in the `MData` representation (off-diagonal terms being set to zero), and $C_{\mathrm{Pr}}^{-1}F_{\mathrm{Pr}}$ in `VData`. nmd should be set to 1 and nvd to $nk \times nb$.

The mask, `MData` and `VData` need to be allocated and zeroed. `NData` is not used and **should be set to zero**.

The Mask is set to 1 where the land cover mask indicates that a pixel should be processed, and the flag `VALID` is 1 in the dataset. It is set to 2 if the land cover mask indicates that a pixel should be processed, and the flag `VALID` is 0.

The prior information F_{Pr} and the leading diagonal elements of $\left(C_{\mathrm{Pr}}\right)^{1/2}$ are read in from file and use to calculate the leading diagonal elements of C_{Pr}^{-1} and $C_{\mathrm{Pr}}^{-1}F_{\mathrm{Pr}}$ which are stored in `VData`.

Comments:

None.

6.2.1.3 Get_LandCoverMask(filename, window=window)

Inputs:

The main input for this function is the filename associated with a particular land cover mask (associated with location (MODIS tile) L). The primary aim of the mask is to identify pixels that should be processed for the globAlbedo product. This is essentially all land surface pixels[23]. When the *a priori* estimate of model parameters fails to provide a valid set of data, the class identified in this land cover map is then used to provide a table look up to a default set of parameters.

A window may be specified through a keyword or similar mechanism to specify some area of the image to read. The default behaviour should be to read the whole of an image in the filename specified.

Other options may be appropriate.

Outputs:

The function should store information from the land cover dataset in an instance of a Data Class and return this.

The mask information should be stored in the Mask structure.

Operation:

The data mask is read from `filename` (possibly over a window) and returned as a byte array that can be stored in a Data Class Mask structure.

Comments:

The mask needs to have agreed coding:

0 not land and/or no data;

1 land and data

2 land but no data

etc. LC categories.

[23] This definition may need to be tightened, e.g. pixels with > 50% of the pixel covered by land or other definitions.

6.2.2 Accumulation

6.2.2.1 `Accumulate_OneStep(dt,gamma, fileNames, DOYS, Accumulator=Accumulator writeDataFile=writeDataFile, landcoverMask=landcoverMask, window=window)`

Inputs:

The inputs to this function are:

(i) the time step δt

(ii) a scaling term, γ, used to calculate $\exp(-\delta t/\gamma)$ (0.5 here);

(iii) a list of *`Nstr`* strings, giving the filenames of observational data to be added to the accumulator;

(iv) the DOYs associated with the *`Nstr`* strings

(v) if defined, an initial Accumulator.

A window may be specified through a keyword or similar mechanism to specify some area of the image to read. The default behaviour should be to read the whole of an image in the filename specified.

An output data filename `writeDataFile` may be specified. A land cover mask file may be specified. Other options may be appropriate.

Outputs:

The function should return a `Data Class` of the updated accumulator.

If no data are to be accumulated, an error code should be returned (non-fatal).

Operation:

The purpose of this function is take an accumulator defined for time period t and update its contents so that it becomes the accumulator for time period $t+\delta t$ (where δt may be positive (for forward steps) or negative (for the reverse sweep). This involves:

- Initialiase an index for which dataset to process, *`thisImage`* to 1 (for a 1-based counting system)
    - If the total number of datasets, *`Nstr`* is zero or negative, return an error code (non-fatal).
- If the accumulator is defined, scale all matrix/vector elements by $\exp(-\delta t/\gamma)$.

  `Accumulator.scale(`$\exp(-\delta t/\gamma)$`)`

- If the accumulator is not defined, initialise and zero it. To do this, we need to know the data dimensions, so the first of the filenames, filenames[1] might be read:
    - `Accumulator= Get_Observations(filenames[thisImage], landcoverMask=landcoverMask, window=window)`
    - Scale these data by $\exp\left(-|t+\delta t-DOY|/\gamma\right)$

      Where *DOY* is the DOY associated with dataset index *thisImage*
    - increment *thisImage* by one.
- The pixel dimensions (number of rows, columns) of `landcoverMask` (if it exists) and `Accumulator` should be the same.
- Loop over *thisImage* until and including when it equals *Nstr* :
    - Read the next dataset:

      `Accumulant = Get_Observations(filenames[thisImage], landcoverMask=landcoverMask, window=window)`
    - Scale these data by $\exp\left(-|t+\delta t-DOY|/\gamma\right)$

      `Accumulant.scale(`$\exp\left(-|t+\delta t-DOY|/\gamma\right)$
      Where *DOY* is the DOY associated with dataset index *thisImage*
    - Set Accumulant.NData to $\exp\left(-|t+\delta t-DOY|/\gamma\right)$ where mask is 1.
        - Accumulate (i.e. sum the matrices & vectors & update mask):

      `Accumulator.accumulate(Accumulant)`
- Write the Accumulator to a file if `writeDataFile` is specified:

  `Accumulator.write(writeDataFile)`
- Return the Accumulator

Comments:

As indicated above, to be efficient, the optimal estimation code needs to run in two modes: (i) an accumulation and storage mode; (ii) a parameter estimation mode. Once the data are read in and the relevant matrices formed in the **Get_Observations()** function**,** all accumulation actions can be efficiently performed for multiple sample locations at the same time as (with one exception) the

accumulations simply requires multiplication and addition which can be performed by vector operations in most languages.

6.2.2.2 `Accumulate_TwoWay(startDOY, endDOY, dt, Gamma,`

6.2.2.3 `filenames, DOYS,`
`writeDataFileExt=writeDataFileExt,`
`writeDataFileDir=writeDataFileDir,`
`landcoverMaskFile=landcoverMaskFile,`
`window=window)`

Inputs:

The inputs to this function are:

(i) the start day for the accumulators `startDOY`.

(i) the end day for the accumulators `endDOY`.

(ii) the time step δt

(iii) a scaling term, γ, used to calculate $\exp(-\delta t/\gamma)$ (0.5 here);

(iv) a list of *`Nstr`* strings, giving the filenames of observational data to be added to the accumulator. **Note that this list should be in time order**.

(v) the DOYs associated with the *`Nstr`* strings

As the method requires writing (temporary) files of the accumulated matrices, some mechanism must be used to specify the output file names. This could, for instance be via using a particular directory (`writeDataFileDir`) and an additional extrension to the input file names (`writeDataFileExt`).

A land (cover) mask (`landcoverMaskFile`) may be specified, so that only land pixels are processed. This could be static, or different land masks could be used for each scene.

A window may be specified through a keyword or similar mechanism to specify some area of the image to read. The default behaviour should be to read the whole of an image in the filename specified.

Outputs:

The set of names of the (reverse plus forward pass) files written out by this function should be returned.

Operation:

The purpose of this function is to calculate and store a set of `Data Class` data: metadata plus `Mask`, `MData` and `VData` data, for the weighted matrices $K^T C_O^{-1} K$ and $K^T C_O^{-1} R$, the mask showing where valid pixels are. `NData` is used to store the weight assigned.

These data are stored to disk by the `Data Class Write` function, and read by the `Read` function. These datasets will be output for DOYs starting from `startDOY` up to and including `endDOY`, in steps of `dt`. The data mask needs to be read in

before further processing. The overall approach is a two-pass system: first DOYS are scanned forward in time over the required range, and (temporary files) of the matrices written for each output sample DOY, using the function **`Accumulate_OneStep()`** to proceed between time steps. Then the process starts at the final day of data, takes samples from that date until *the day after* the final output sample DOY and calculates the associated matrices for those data. The reverse sweep sample is added to the sample for the final output sample DOY, and the new matrices written. Time is then stepped through backwards until the *day after* the first output sample DOY is reached in steps of `dt`, using the function **`Accumulate_OneStep()`** as previously.

There are several options at this point, depending on memory availability.

First, the reverse pass matrices may be stored in memory, rather than written to file. These are required for subsequent processing, although they only need to be accessed one at a time (which is why the default behaviour should probably be to write the data to files).

Second, the forward pass matrices might also be stored in memory. Again, these are only needed one at a time, so there is sense in writing temporary files.

- Read the land cover mask if defined (or pass this through as a Data Class if that is more practical). At present we assume that this is static, i.e. there is a single mask for all pixels to be accumulated.
    - `landcoverMask= Get_LandCoverMask(landcoverMaskFile, window=window)`
- Initialise a variable `prevDOY` to the **first** DOY in the list of `filenames`.
- Initialise `FwdAccumulator` to NULL (or equivalent mechanism to get **`Accumulate_OneStep()`** to realise that it does not exist and must be created).
- Loop over `DOY` from `startDOY` to `endDOY` in steps of `dt`.
    - Generate a list of filenames of files (`theseFiles`) required for forward processing of matrix data for `DOY` (i.e. those in the list that go from `prevDOY` to `DOY`, inclusive), and an associated list of DOYS (`theseDOYS`). The ordering of these files is not important.
    - Generate a filename `writeDataFile`, from the DOY for which this sample is, and information in `writeDataFileExt` and `writeDataFileDir` and the fact that this is a fwd sample.
        - Call `FwdAccumulator=Accumulate_OneStep(dt,gamma, theseFiles,theseDOYS,Accumulator=FwdAccumulator,`

writeDataFile=writeDataFile, landcoverMask=landcoverMask,window=window).

This will write a data file with the forward (weighted) cumulative matrices, reference to DOY.

- Update prevDOY to DOY+1.
- End loop

Note that the current FwdAccumulator is passed on to the next iteration of the loop.

- Initialise a variable prevDOY to the **last** DOY in the list of filenames.
- Initialise RevAccumulator to NULL (or equivalent mechanism to get **Accumulate_OneStep()** to realise that it does not exist and must be created). Alternatively, this could be a zeroed copy of FwdAccumulator.
- Loop over DOY from endDOY to startDOY in steps of -dt.
  - Generate a list of filenames of files (theseFiles) required for reverse processing of matrix data for DOY (i.e. those in the list that go from DOY+1 to prevDOY inclusive), and an associated list of DOYS (theseDOYS). The ordering of these files is not important.
  - Generate a filename writeDataFile, from the DOY for which this sample is, and information in writeDataFileExt and writeDataFileDir and the fact that this will be from both fwd and reverse samples.
  - Call RevAccumulator=**Accumulate_OneStep**(dt,gamma, theseFiles,theseDOYS,Accumulator=RevAccumulator, landcoverMask=landcoverMask,window=window).

    This will generate RevAccumulator with the reverse (weighted) cumulative matrices, reference to DOY+1. Note that there is little point calling the writeDataFile option.
  - Open the Fwd accumulator file for DOY. And store information in FwdAccumulator.
  - Add the results from RevAccumulator to this (using e.g. FwdAccumulator.Accumulate(RevAccumulator).
  - Normalise FwdAccumulator by FwdAccumulator.NData.
  - Write the new FwdAccumulator to the file writeDataFile. storing this filename in a list writeDataFileList.

- Update `prevDOY` to `DOY`.

- Return `writeDataFileList`.

6.2.2.4 `Parameter_estimate(startDOY,, endDOY, dt, PriorWeight, PriorFilenames, ObsDataFileList, writeParamFileExt=writeParamFileExt, writeParamFileDir=writeParamFileDir, window=window)`

Inputs:

The inputs to this function are:

(i) the start day for the accumulators `startDOY`.

(ii) the end day for the accumulators `endDOY`.

(iii) the time step δt

(iv) a weighting term for the priors (`PriorWeight`). A suggested value might be 5.

(v) the DOYs associated with the *`Nstr`* strings (`DOYS`) .

(vi) a list of *`Ndoys`* strings, giving the filenames of prior estimates of model parameters. **Note that this list should be in time order and that *`Ndoys`* should be consistent with `startDOY, endDOY` and `dt`. (**`PriorFilenames`)

(vii) a list of *`Ndoys`* strings, giving the filenames of matrix data for the observations for each DOY. **Note that this list should be in time order and that *`Ndoys`* should be consistent with `startDOY, endDOY` and `dt`.** (`ObsDataFileList`**)**

As the method requires writing (temporary) files of the accumulated matrices, some mechanism must be used to specify the output file names. This could, for instance be via using a particular directory (`writeParamFileDir`) and an additional extension to the input file names (`writeParamFileExt`).

A window may be specified through a keyword or similar mechanism to specify some area of the image to read. The default behaviour should be to read the whole of an image in the filename specified. The window must be consistent with that used in other data access calls (e.g. **`Accumulate_TwoWay()`**.

Outputs:

The set of names of the model parameter files.

Operation:

The purpose of this function is to estimate kernel (actually, general linear) model parameters for a spatial dataset, for a set of sample DOYs, from `startDOY` to `endDOY` inclusive, in steps of `dt`. The optimal parameter estimate is calculated from (pre-calculated and stored) weighted matrices $K^T C_O^{-1} K$ (`MData`) and $K^T C_O^{-1} R$, (`VData`) (with associated weighting terms for normalisation in `NData`) and the mask

showing where valid pixels are (code 1 for valid data, code 2 for valid land pixel but no data).

- Loop over `DOY` from `startDOY` to `endDOY` in steps of `dt`.
  - Read the appropriate entry from `ObsDataFileList` using the `Data Class` **`Read`**() function. (`thisData`)
  - Read the appropriate entry from `PriorFilenames` using **`Get_Prior`**`(PriorFilename,window=window)`. (`thisPrior`).
  - Scale the prior uncertainty by `PriorWeight`: **`thisPrior.Scale`**`(PriorWeight)`.

    This performs a scaling of the terms on the leading diagonal elements of C_{Pr}^{-1} and $C_{\mathrm{Pr}}^{-1}F_{\mathrm{Pr}}$ which are stored in `MData` and `VData`.
  - Zero/create a Data Class instance to hold the results: `Result`
  - Identify 'strange' pixels:

    Category 1: These are pixels that have a 2 or 0 in `thisPrior.Mask` and 1 in `thisData`, i.e. they have no prior, but there are observations that we might use to estimate parameters. The parameters are liable to high uncertainty. Set `Result.Mask` to 1

    Category 2: These are pixels that have a 2 in `thisPrior.Mask` and 2 in `thisData`, i.e. they have no prior and no observations, although the pixel is flagged as a land pixel to be processed. Set `Result.Mask` to 2 and do not process at this point.
  - Process Category 1 strange pixels:

    Loop over each pixel `P` that has `Mask` 1 in `Result`:
    - If `thisData.NData` is above some threshold:
      - Extract the matrix `M` from `MData` for pixel `P`.
      - Extract the vector `V` from `VData` for pixel `P`.
      - Find `F` from the linear equation: `M F = V`
      - Store `F` in `Result.VData` for pixel `P`.
      - Find the inverse of `M`, $\mathtt{M}^{-1}$.
      - Store $\mathtt{M}^{-1}$ in `Result.MData` for pixel `P`.
      - Set `Result.Mask` to 1 for pixel `P`.
    - Otherwise set `Result.Mask` to 2.

- Add the scaled prior to the data in the observation matrices and vectors:

  thisData.Accumulate(thisPrior)
- Process Normal pixels:

  Loop over each pixel `P` that has `Mask` 1 or 2 in `thisData` and for which `Result.Mask` is currently zero:
  - Extract the matrix `M` from `MData` for pixel `P`.
  - Extract the vector `V` from `VData` for pixel `P`.
  - Find `F` from the linear equation: `M F = V`
  - Store `F` in `Result.VData` for pixel `P`.
  - Find the inverse of `M`, M^{-1}.
  - Store M^{-1} in `Result.MData` for pixel `P`.
  - Set `Result.Mask` to 1 for pixel `P`.
- Write out `Result` for `DOY` to appropriate filename using e.g. `writeParamFileExt` and `writeParamFileDir`, storing the names in a list, `writeParamFile`.

- Return the set of names of the model parameter files, `writeParamFile`.

Comments:

This function needs the code to step over each pixel and calculate matrix inverses, so it can be potentially slow.

This function assumes that the data referred to in `ObsDataFileList` have already been processed, e.g. by **`Accumulate_TwoWay()`**.

There are many linear solvers that can be called to solve for `F` from `M F = V`. Many of these do not need to explicitly compute M^{-1}, but we require M^{-1} for uncertainty characterisation.

6.3 Optimal estimation framework

Given the Data Class and methods described above we can simplify the optimal estimation framework to two stages. The first stage, that we might term observation accumulation, is shown in Figure 6-1, the second in Figure 6-2.

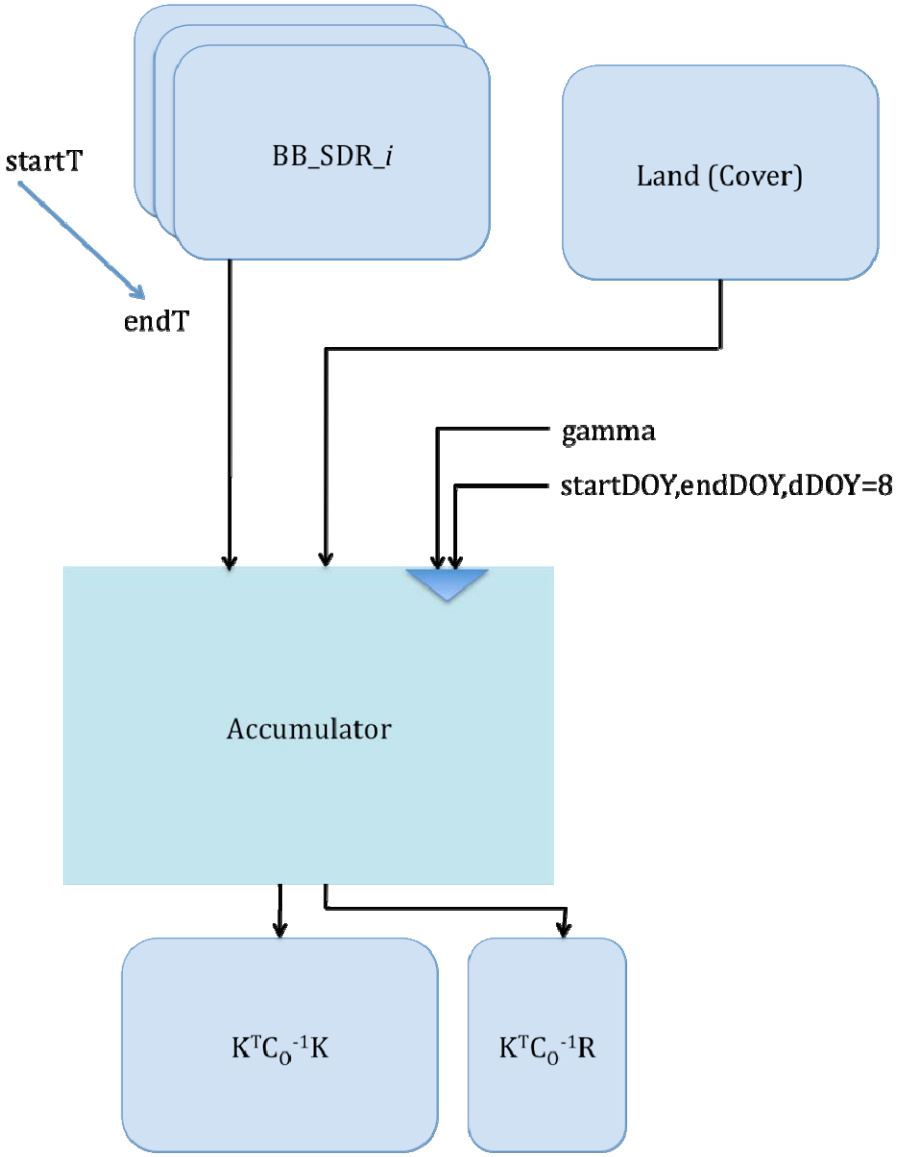

Figure 6-1. Accumulator Flow diagram

A set of BROADBAND_SDR data are available that cover samples over some spatial set of pixels *L* , defined on a grid. These data come from a set of sensors (here, (A)ATSR-2, VEGETATION, and MERIS) can cover a time period start to EndT. There may be more than one dataset for each day, e.g. in cases of orbital convergence and where data from multiple sensors are available. These data have associated pixel classification data

declaring them to be snow and no cloud/shadow or clear and no cloud/shadow (the flags of interest here). These data contain information on the land surface reflectance (assuming the surface to be Lambertian) in 3 broad wavebands, an associated uncertainty matrix, and angular integrals of the BRDF model kernels conditioned for the state of the atmosphere at the time of imaging. The accumulator, explained in detail in section 7.2.2.2, reads a list of the BROADBAND_SDR data files and creates from these (for pixels flagged as Land in the input Land (Cover) product, a matrix and vector of the terms $K^T C_O^{-1} K$ and $K^T C_O^{-1} R$ respectively, every dDOY (8) days from startDOY to endDOY.

The process has two stages: forward accumulation and reverse accumulation that could be preformed in parallel (if the subsequent summation is delayed).

In the second stage (below), the vector/matrix derived for each time step from the observations is combined with the product of (a scalar) weight term and the prior estimate vector/matrix. By summing the two matrices and summing the two vectors, we can solve for the *a posteriori* parameter vector *F* and its associated uncertainty estimate.

This results in a set of model parameter estimates and uncertainty/QA data for all pixels processed.

6.4 Estimation of albedo

6.4.1 Ov

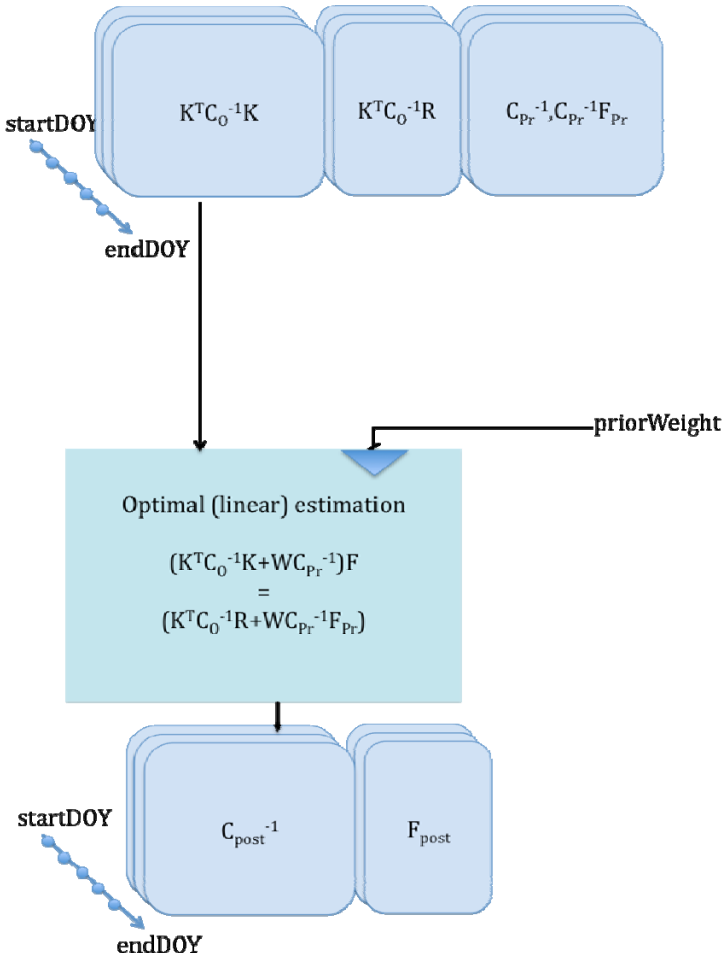

Figure 6-2. Optimal Estimator Flow diagram

erview

Figure 6-3 gives an overview of the processing to infer the final albedo product terms from

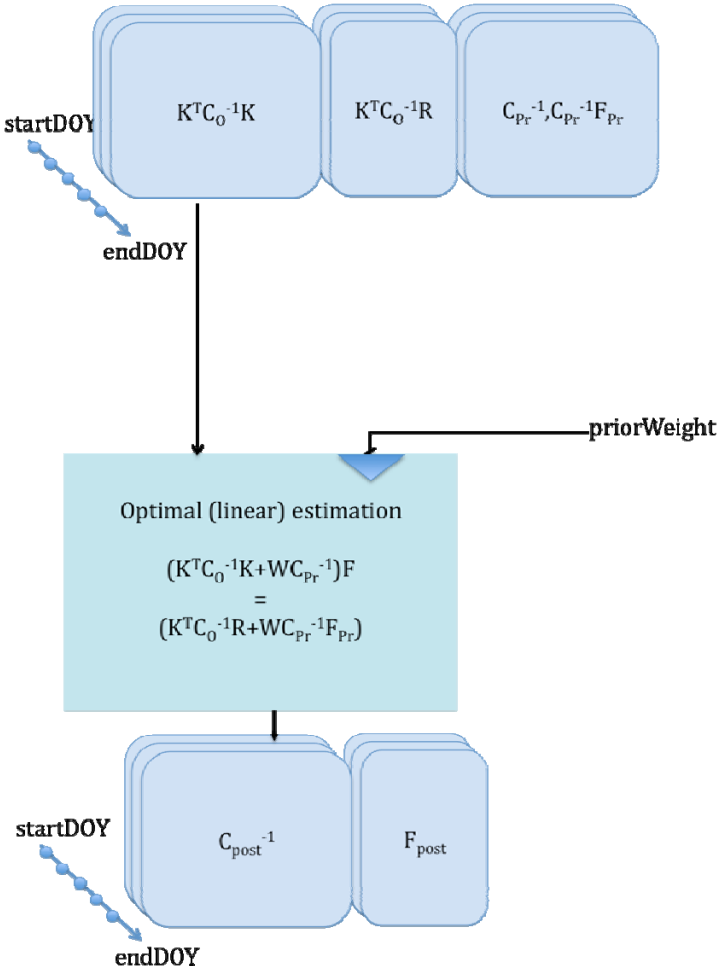

Figure 6-3. Albedo Estimator Flow diagram

the model parameters. In essence, this involves calculation of the local noon solar zenith angle, which then provides access to appropriate kernels weights for BSA noon albedo. These and WSA coefficients are retrieved from internal LUTs, along with a LUT appropriate for the WSA configuration for fAPAR retrival. From the weights, BSA and WSA are calculated for each of the three wavebands.

6.4.2 Uncertainty

Propagation of (assumed Gaussian) uncertainty terms in a linear model is trivial. The uncertainties in WSA, BSA are calculated according to equation 19b, with the vector *U* set to the particular weights used to calculate each term from the model parameters. The uncertainty in the fAPAR terms is estimated from the uncertainties in WSA. Note that formally in this case, the spectral covariance terms in the albedo error estimates are required.

6.4.3 fAPAR

fAPAR products will be produced consistently with the albedo product as by-products of the GlobAlbedo processing chain. The Joint Research Centre Two-stream Inversion Package (JRC-TIP) (Pinty et al., 2007) will be used for this purpose. This package is designed to retrieve a variety of surface land variables through the assimilation of surface albedo products into a state-of-the-art radiation transfer scheme. In the implementation of the JRC-TIP code intended for GlobAlbedo, white-sky visible and near-infrared broadband albedo are used as inputs to JRC-TIP to retrieve a set of effective biophysical parameters, namely the leaf area index and spectrally dependent variables which include the background albedo, and the single scattering albedo and asymmetry of the vegetation. The total absorption by the canopy in the visible is, in that case, equivalent to the total fAPAR. This is estimated from the probability distribution functions of the effective biophysical parameters (Pinty et al., 2006).

In GlobAlbedo a LUT implementation of the package is developed that maps VIS and NIR BHR (white sky albedo) to (diffuse) fAPAR. Since we require only fAPAR here, the intermediate products (effective LAI etc.) are not required. The LUT provides sampled (diffuse) fAPAR and uncertainty in fAPAR (σ_{fAPAR}) as a function of: (1) VIS BHR; (2) NIR BHR; (3) the 3 elements of the uncertainty matrix for VIS and NIR BHR. There are two sets of LUTs generated, one with assumed snow background and one with a bare soil background. In effect then, we have four 5 dimensional LUTs: one for fAPAR, one for σ_{fAPAR}, for the snow and no snow background priors.

The fAPAR LUTs are applied as a post-processing step to the BHR data in the final (merged snow/no snow) albedo product.

It is worth noting that other outputs of JRC-TIP (the transmitted, absorbed and scattered fractions of VIS and NIR radiation in the vegetation and background layers separately) could be produced by additional LUTs or running the JRC-TIP code.

Currently, the fAPAR product currently generated does not fully take into account the uncertainties in the albedo.

In fact, in GlobAlbedo a simple LUT is applied that maps bi-hemispherical reflectance in the visible and near infrared bands to fAPAR. This is seen as a ‘test’ product in GlobAlbedo as it has not been a major focus of development. It is of value in that it is simple and traceable to publications, but should be interpreted with caution.

Pinty et al. (2006) present a two-stream model that models diffuse fluxes in a layered medium over a Lambertian lower boundary. The parameters of this model are: LAI, leaf single scattering albedo, leaf scattering asymmetry, soil reflectance. So, per waveband, there are three spectral terms and one structural. A further parameter, zeta, can be used to account for clumping, but is ignored in this present discussion, meaning that LAI is interpreted as effective LAI. In various papers following this (e.g. Pinty et al., 2010a,b; Pinty et al. 2011), Pinty and colleagues apply a parameter estimation package (JRC-TIP)

that provides an estimate of the model state variables (7 terms if two wavebands are used) for input bihemispherical reflectance in visible and near infrared broad wavebands.

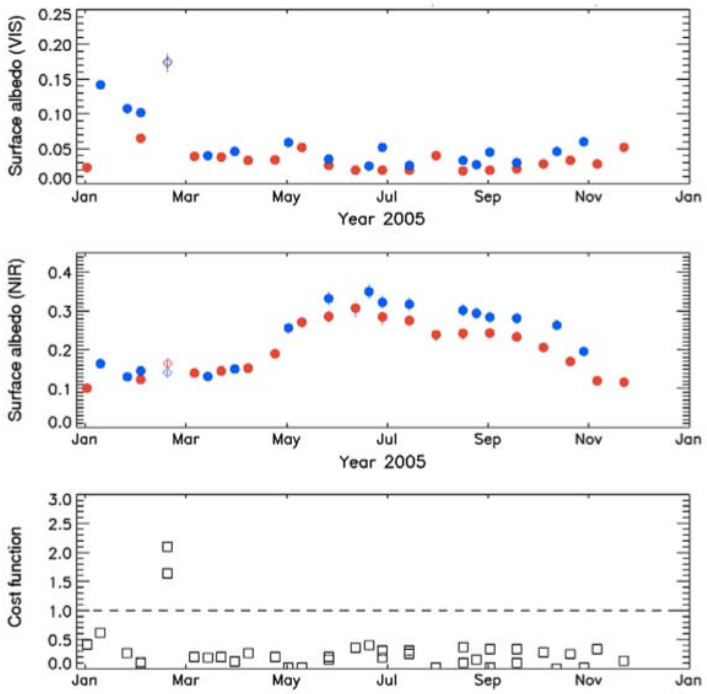

Fig. 2. Time series of the broadband BHR–white sky–surface albedo at 0.01° spatial resolution in the visible (top panel) and near-infrared (middle panel) domain over the site of Hainich (51° 05′ 05″ N; 10° 26′ 41″ E). MODIS (MISR) derived albedo values are featured in red (blue). High cost function values (bottom panel) are identified with an open diamond symbol. The vertical bars display the one-sigma posterior uncertainty values. (For interpretation of the references to color in this figure legend, the reader is referred to the web version of this article.)

Figure 6-4. Figure 2 from Pinty et al. 2011 illustrating input albedo data for a forest site.

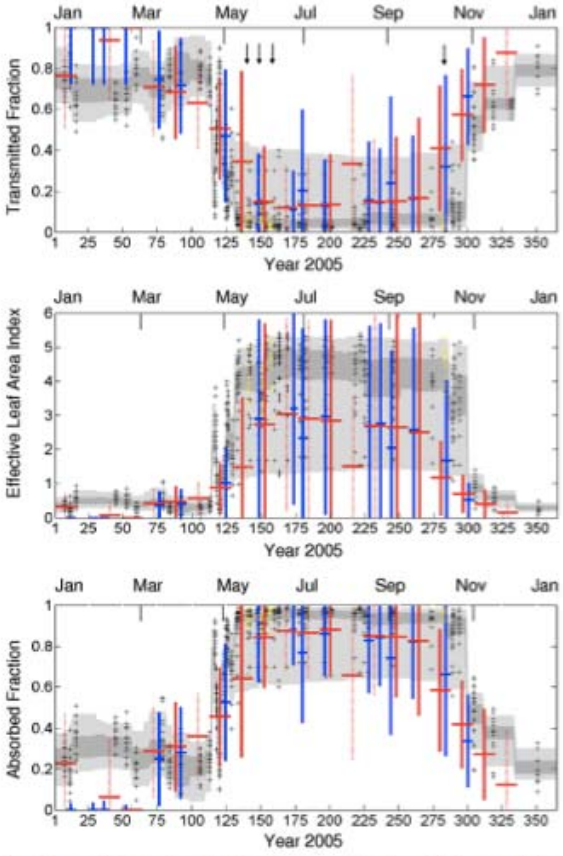

Fig. 3. Top panel: Time series of the domain-averaged fractions of diffuse transmission in the visible spectral domain measured over the Hainich site. The grey shaded zones indicate the range (light grey) and interquartile (dark grey) range estimated both from the individual sampled points over all seven years (black crosses). The points available in 2005 at dates indicated by the downward arrows are shown with yellow crosses. The JRC-TIP derived estimates from MODIS (MISR) are shown in red (blue). The full (dashed) vertical bars indicate the one-sigma posterior uncertainty associated with the best (good) quality MODIS input albedos. Middle and bottom panels: same as above except for the effective LAI and the fraction of absorbed flux in the vegetation layer, respectively. (For interpretation of the references to color in this figure legend, the reader is referred to the web version of this article.)

Figure 6-5. Figure 3 from Pinty et al. 2011 illustrating derived quantities for a forest site.

Variable	$\mathbf{X}_{prior}$	$\sigma_{\mathbf{X}_{\text{prior}}}$
LAI	1.5000	5.0
$\omega_l(\lambda_1)$	0.1700	0.1200
$d_l(\lambda_1)$	1.0000	0.7000
$r_g(\lambda_1)$	0.1000 [1] and 0.50 [2]	0.0959 [1] and 0.346 [2]
$\omega_l(\lambda_2)$	0.7000	0.1500
$d_l(\lambda_2)$	2.0000	1.5000
$r_g(\lambda_2)$	0.1800 [1] and 0.350 [2]	0.2000 [1] and 0.25 [2]

[1(2)] Values adopted for the bare soil (snow) case with a correlation factor of 0.8862 (0.8670) set in $\mathbf{C}_{X_{prior}}$.

Table 6-1. Prior constraints used by Pinty et al.

By using a set of prior constraints on the state variables (items (1) in table 1), a solution to these 7 terms can be derived for given VIS and NIR white sky albedo then, for a given

uncertainty. The cost function involved is a weighting between the prior cost and the observation cost, this weighting being essentially defined by the relative uncertainty of the observations and the priors. Once these state variables are defined, derived radiative quantities can also be output, such as the transmitted or absorbed proportion of radiation for each waveband. In this way, fAPAR, interpreted as the radiation absorbed in the canopy in the VIS band, can be estimated.

In fact, for a given pattern of input data uncertainties, there is a direct mapping between the white sky albedo and any of these state variables or derived quantities. For example, we can illustrate the LUT associated with a 10% (and 5%) relative uncertainty in each input.

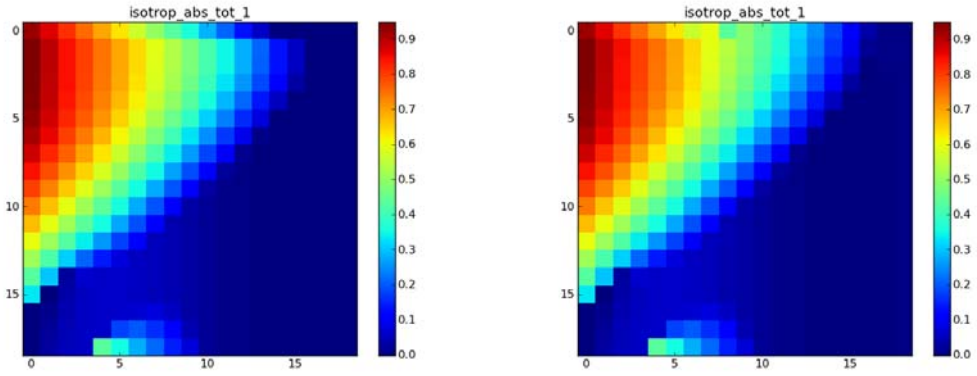

Figure 6-6. LUT for fAPAR for 10% (left) and 5% (right) relative uncertainty in the input data.

The LUTs shown display VIS white sky albedo on the x-axis and NIR on the y-axis, so, for instance for low VIS and high NIR, we have a high fAPAR as expected.

This LUT has been calculated using python code developed at UCL by P. Lewis, that interfaces to the original FORTRAN code of Pinty et al. The FORTRAN code of Thomas Lavergne and Bernard Pinty for the two stream model is available from the JRC website[24]. The LUT illustrated above for sample steps of 0.05 in albedo is quite smooth and higher resolution results can be readily interpolated from a quite coarse LUT of this nature. Processing (without adjoint code as in JRC-TIP) takes around 0.1 seconds per LUT point on a laptop computer.

[24]http://fapar.jrc.ec.europa.eu/WWW/Data/Pages/FAPAR_Software/FAPAR_Software_RTModels_two-stream.php

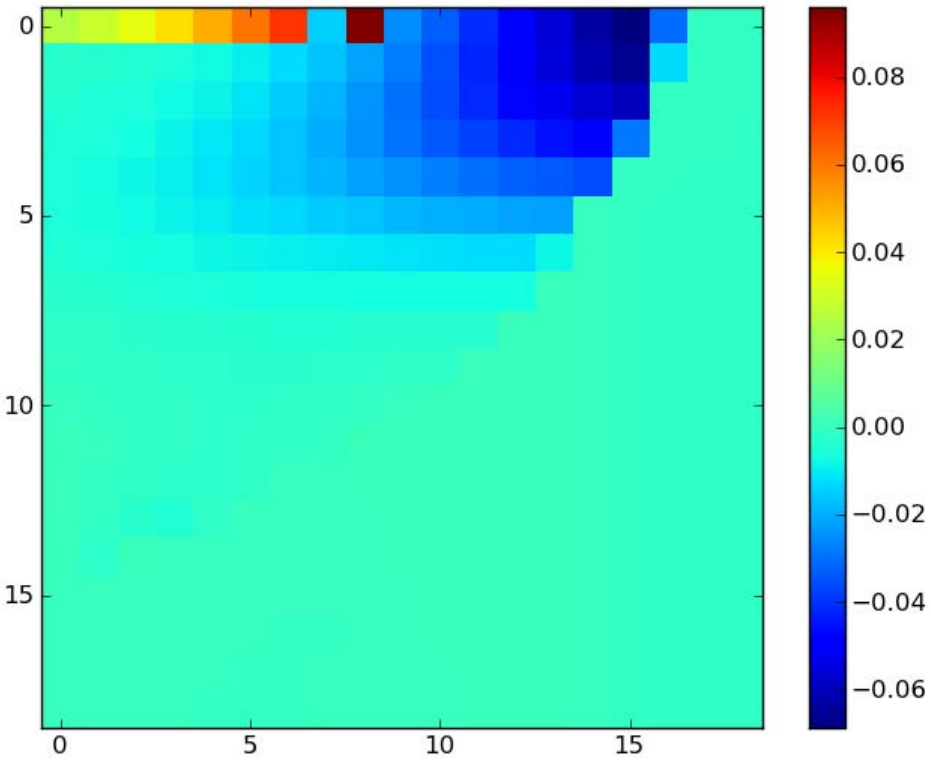

Figure 6-7. Difference between fAPAR for 10% observation relative uncertainty and 5% observation relative uncertainty.

The difference between the inferred fAPAR with 10% and 5% relative error is shown above. Quite surprisingly, other than at very high NIR albedo (which may be an artefact of the LUT generation) the difference between 10% relative error and 5% relative error is mostly quite small in an absolute sense, being generally between +0.02 and -0.02, with a patch around -0.04 for high VIS and NIR.

If we change the prior constraints to the ‘snow’ case in table 1, the inferred fAPAR LUT changes rather drastically. This is essentially because we have changed the ‘soil line’ to a ‘snow line’. The snow fAPAR LUT is used in GlobAlbedo for the snow case.

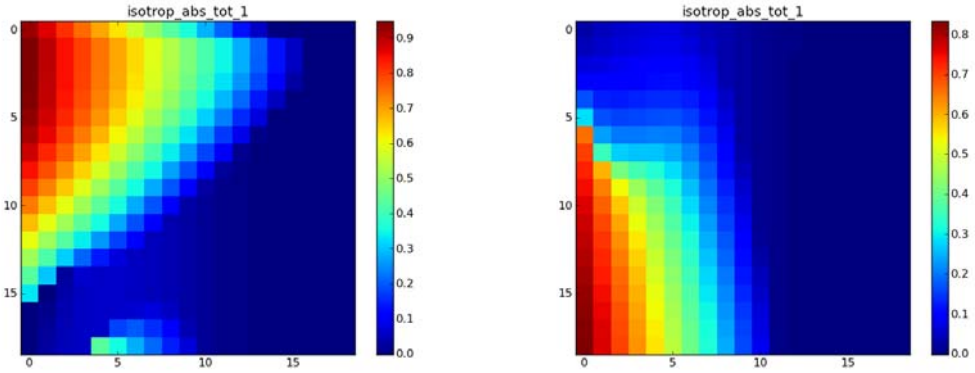

Figure 6-8. LUT for fAPAR for 10% relative uncertainty in the input data for bare soil priors (left) and snow (right).

The 10% relative uncertainty LUT is that used in GlobAlbedo. As noted, it is not very refined, and has not been investigated in any great detail. Further, it assumes a 10% relative uncertainty in albedo, rather than exploiting the actual GlobAlbedo uncertainty values. Further, it is derived only for white sky albedo, so does not directly provide the variation of fAPAR (or other terms) with solar zenith angle.

To illustrate some other issues, it is worthwhile looking at for of the other terms derived.

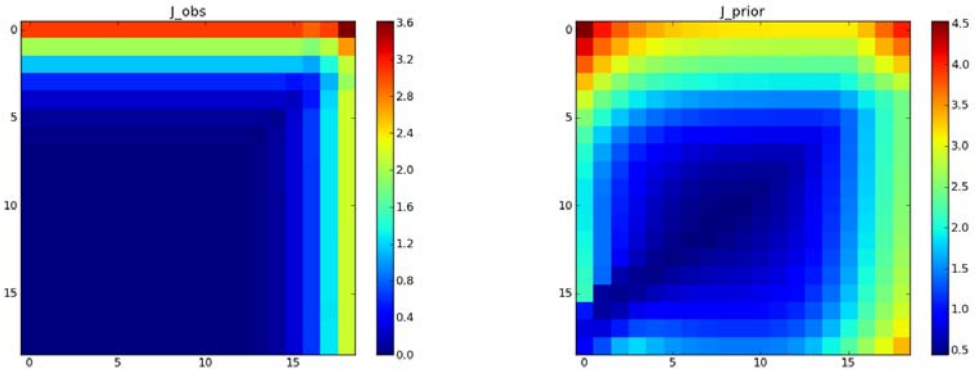

Figure 6-9. Cost functions associated with the LUT: soil prior

Figure 12 shows the cost terms associated with the 10% relative error soil prior case. As expected, as the observation moves away from the expected soil line (and expected other terms), the departure from the prior increases. The minimum of the LUT cost function is essentially a valley along the soil line. For the snow prior similar phenomenon is seen.

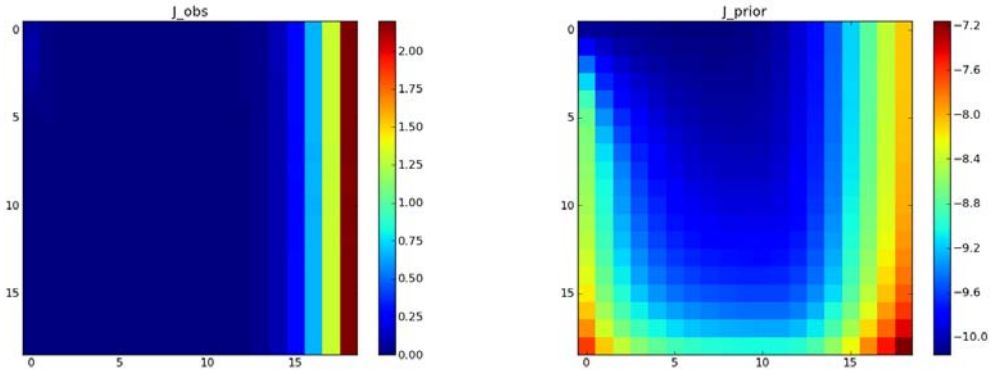

Figure 6-10. Cost functions associated with the LUT: snow prior

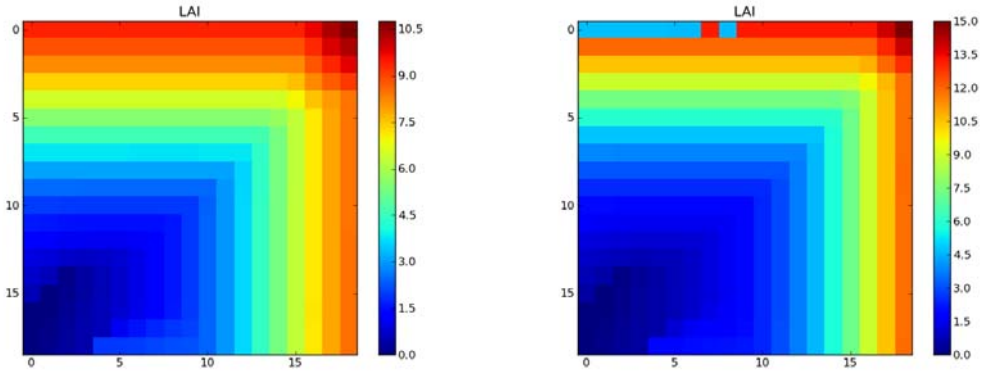

Figure 6-11. LAI for the soil prior: left: 10% relative error; right 5% relative error

The LAI LUTs show an artefact in the top line of the 5% relative observation error. Other than that, the main impact of relative error in the observations is seen to be a higher maximum LAI for the lower relative uncertainty. We see that inferred LAI depends then on the uncertainty attributed to the observations.

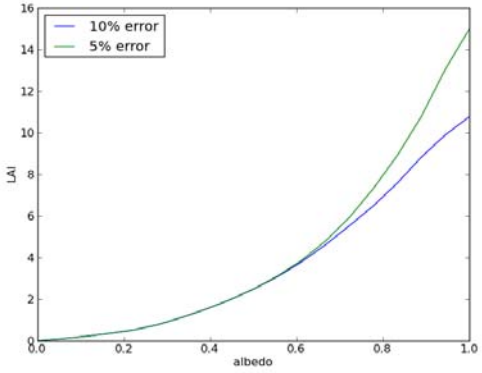

Figure 6-12. LAI along the leading diagonal the soil prior as a function of albedo

If we examine the LAI trends along the leading diagonal of figure 14 (plotted in figure 15) we can see that the reduction in uncertainty in the observations has an impact on LAI values above about 4, so the impact of uncertainty in the observations would seem only to have an impact for high LAI: the lower the uncertainty in albedo, the higher the apparent maximum LAI possible.

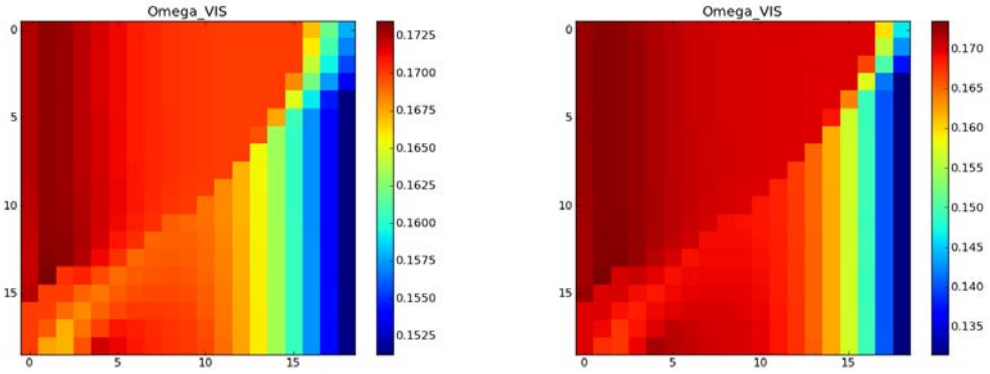

Figure 6-13. Leaf single scattering albedo (VIS) LUT for 10% relative error (left) and 5% relative error (right)

The LUTs for leaf single scattering albedo show (above the soil line) are relatively small variation in this term, with a slight increase for lower VIS albedo. For 5% relative error in the observations, the inferred leaf single scattering albedo is slightly reduced, which probably is the cause of the slightly different albedo-LAI relationships observed above.

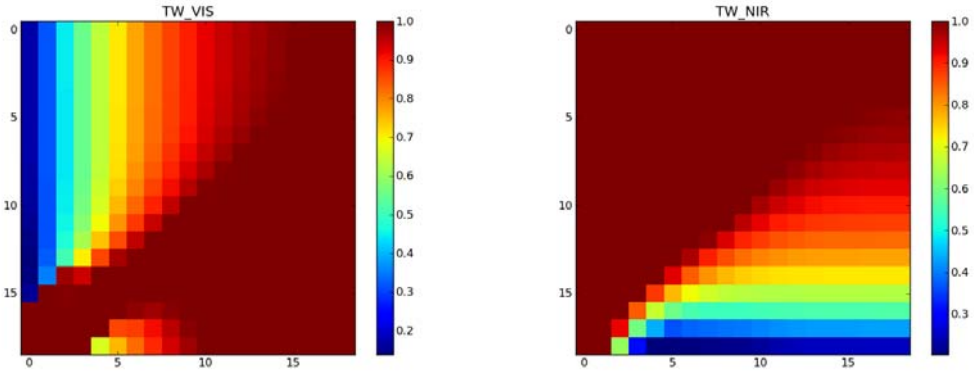

Figure 6-14. Leaf asymmetry for the soil prior case.

The leaf asymmetry shows an interesting pattern, for the soil prior case, for the region above the soil line of fAPAR >> 0, the transmitted radiation is seen to be a monotonic function of albedo. So, as VIS albedo increases, the a higher proportion of the radiation is transmitted rather than reflected.. Similar effects are seen for the snow prior.

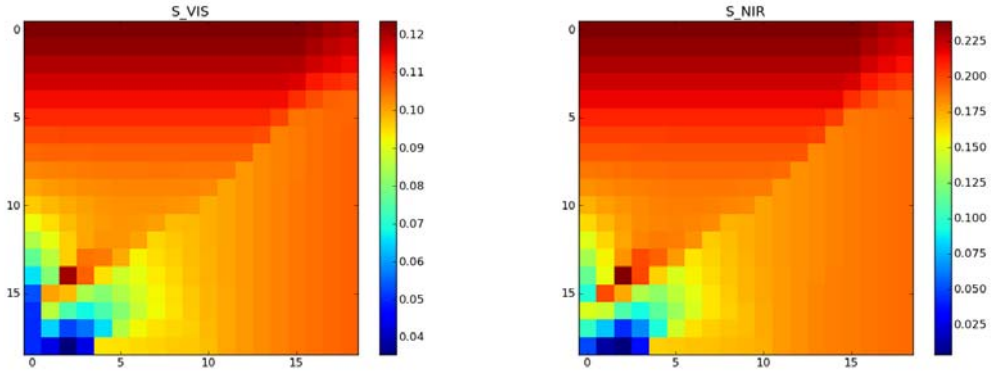

Figure 6-15. soil albedo (VIS) LUT for 10% relative error for VIS (left) and NIR (right)

The inferred soil reflectance LUTs are quite interesting as they have essentially in the same form at both wavelengths, though a different scale. This is clearly because of the correlation in the proscribed priors.

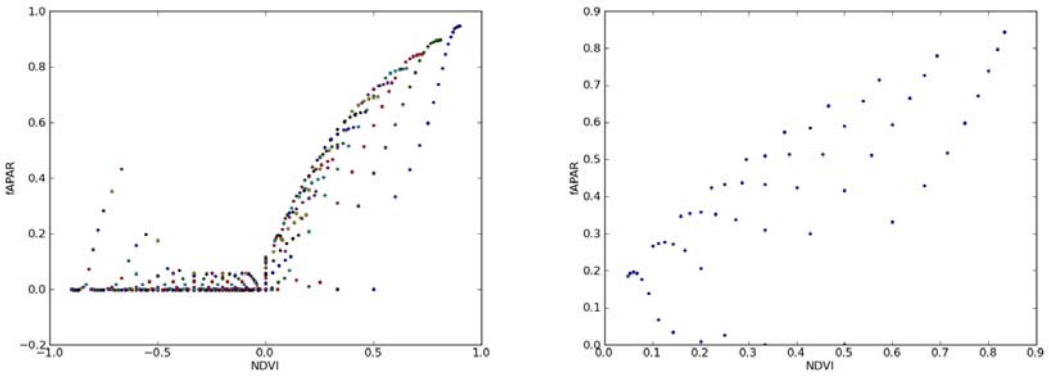

Figure 6-16. fAPAR/NDVI relationship for 10% relative error. Left shows all points (colours are varying NIR albedo). Right shows the relationship for NDVI>0 and NIR < 0.6

It is interesting to examine the fAPAR/NDVI relationship implied by this LUT (figure 18). If we limit the analysis to positive NDVI and NIR albedo to a reasonable range (less than 0.6), then what we see is a series of (near) linear relationships between NDVI and fAPAR where the intercept depends on the NIR reflectance (so, the intercept on the x axis is essentially the implied NDVI of soil). This soil impact is the main effect here. A secondary effect is a slight change in the slope of the relationship.

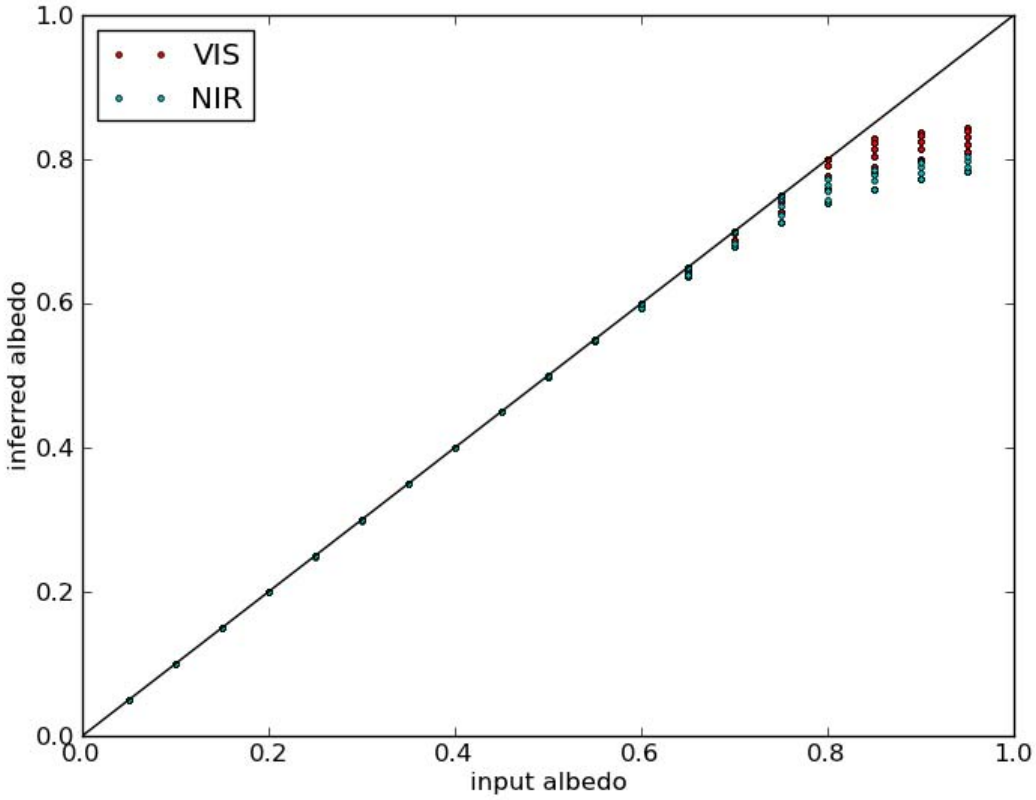

Figure 6-17. Inferred albedo as a function of input albedo for soil prior.

Since we are applying a prior constraint here to the interpretation of uncertain input data (albedo), we might expect that the inferred albedo differs somewhat from that input. We can get a clue to this from the cost function plots above: for the soil prior, the observation cost function is only high for high (VIS or NIR) albedo. Figure 20confirms this, showing the inferred albedo as a function of the input albedo. In effect, it is setting a maximum albedo of around 0.8, so that input values above this are mapped to this maximum value.

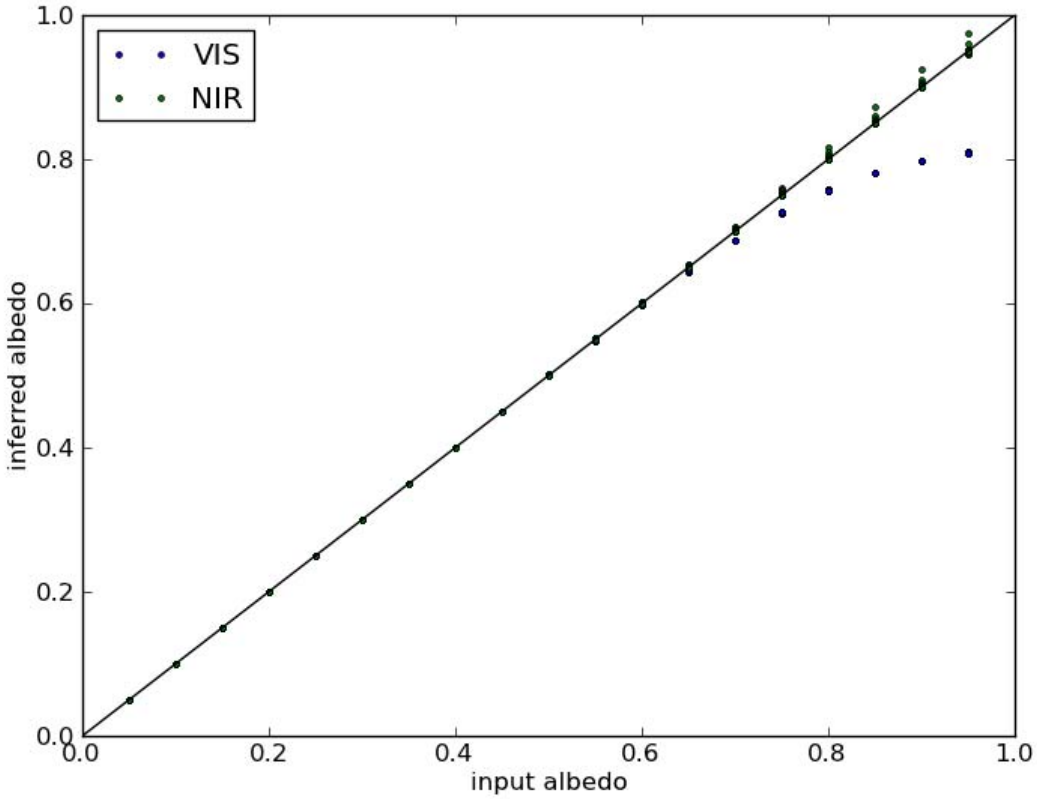

Figure 6-18. Inferred albedo as a function of input albedo for snow prior.

For the snow prior, the visible albedo is still capped at around 0.8, but the NIR albedo can go all the way to 1.0. This is consistent with the patterns we see in the observation cost function for the snow prior above.

The implication of this is that, at least with relative observation uncertainties of 10% or less, input albedo maps to very close to the same value on output for albedo of less than 0.8, so the use of any product of this modelling exercise (e.g. LAI or fAPAR) is directly consistent with the original data for albedo of less than 0.8. For higher albedo values, the posterior estimate of albedo should be used for consistency, rather than the prior value.

As we have noted, the fAPAR product in the current version of GlobAlbedo is applied simply as a LUT on the bihemispherical reflectance without explicit treatment of the uncertainties in the product. This may be improved on in any later releases, but full testing of this product as it stands needs to be first completed. One of the issues that needs further investigation is the treatment of Gaussian uncertainties in the fAPAR estimation. Whilst these might be viable for albedo values not too close to the lower or upper ends of the [0,1] range of albedo values possible, they are clearly not so close to the limits, and it

is close to these limits that we see cost function increases. Further, given the method used, the uncertainties are likely at times to be quite large on the resultant fAPAR, and the impact of Gaussian assumptions within this non-linear model need to be more fully investigated.

For example, taking as input an observation for the Hainich site from Pinty et al. (bihemispherical reflectance of (0.0308, 0.30257) in VIS and NIR respectively) and 7% relative uncertainty, we obtain the following posterior distributions using an MCMC approach:

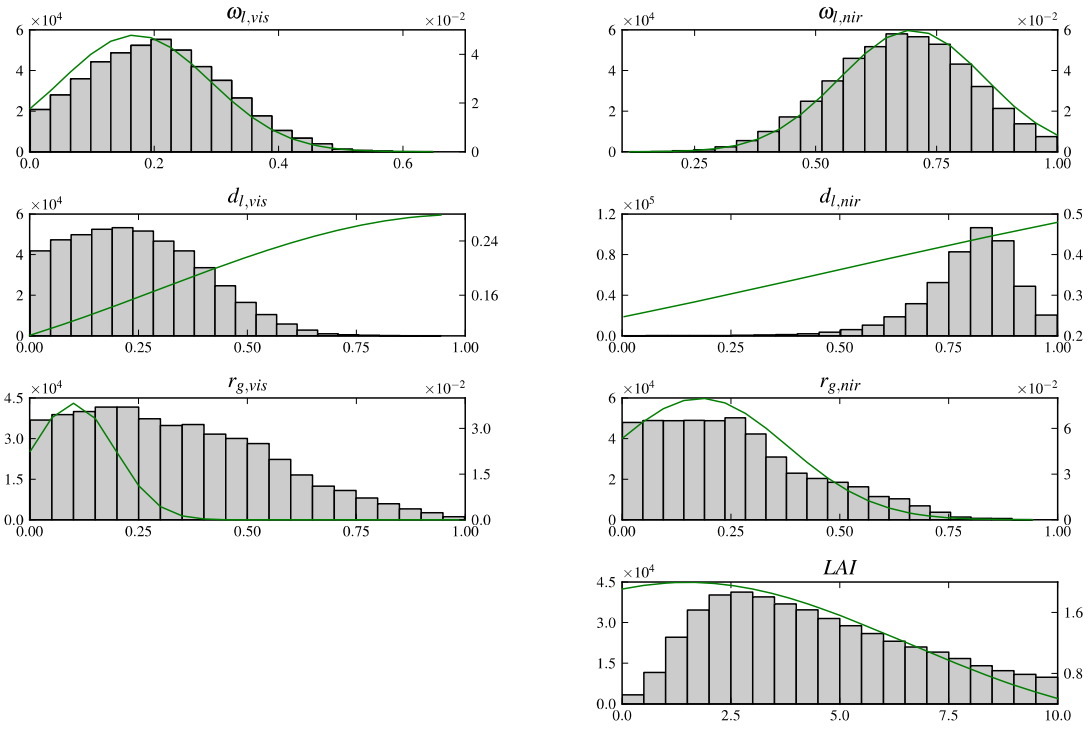

Figure 6-19. Prior (green) and Posterior (bars) distributions for Hainich.

The MCMC approach provides an estimate of the posterior distributions that is not limited to being Gaussian. The prior distributions are shown as green lines. In this case, we see that the single scattering albedo is hardly affected by the observation, but the asymmetry terms are. The VIS soil reflectance is much widened and the LAI becomes non-Gaussian (although the wide uncertainty on the prior 'Gaussian' has no meaning for LAI<1). The results seem to indicate that all we can really say here is that the LAI is greater than 2.

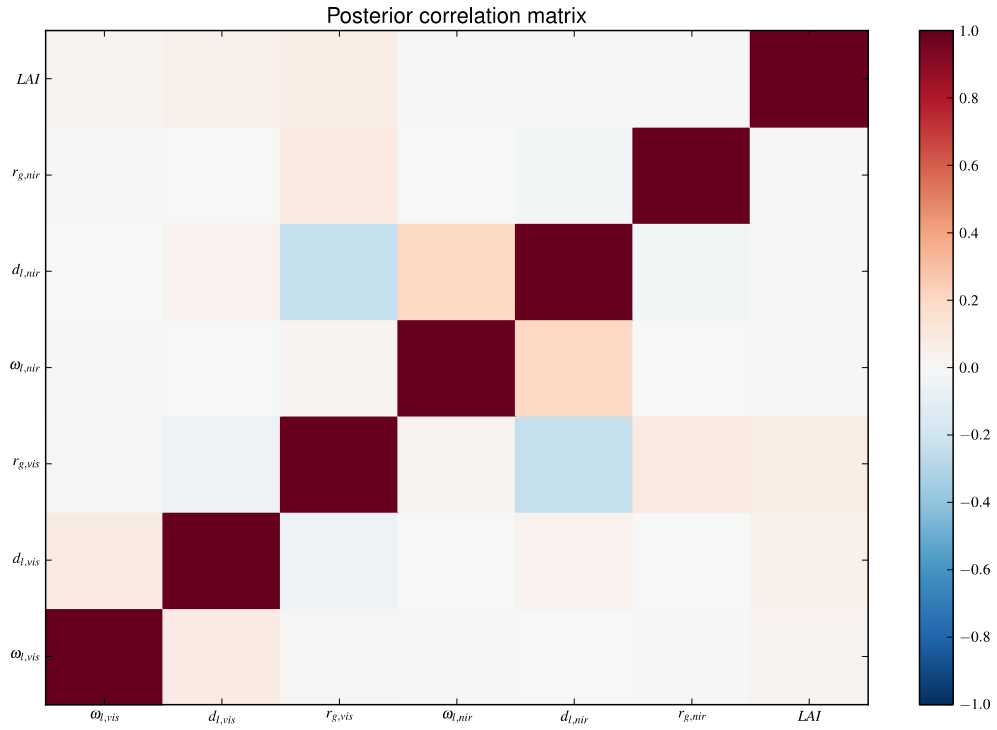

Figure 6-20. Posterior correlation matrix

The posterior correlation matrix (above) shows quite a large negative correlation between the NIR asymmetry term and the VIS soil reflectance and between the same term and NIR single scattering albedo. A physical interpretation of those correlations is not obvious.

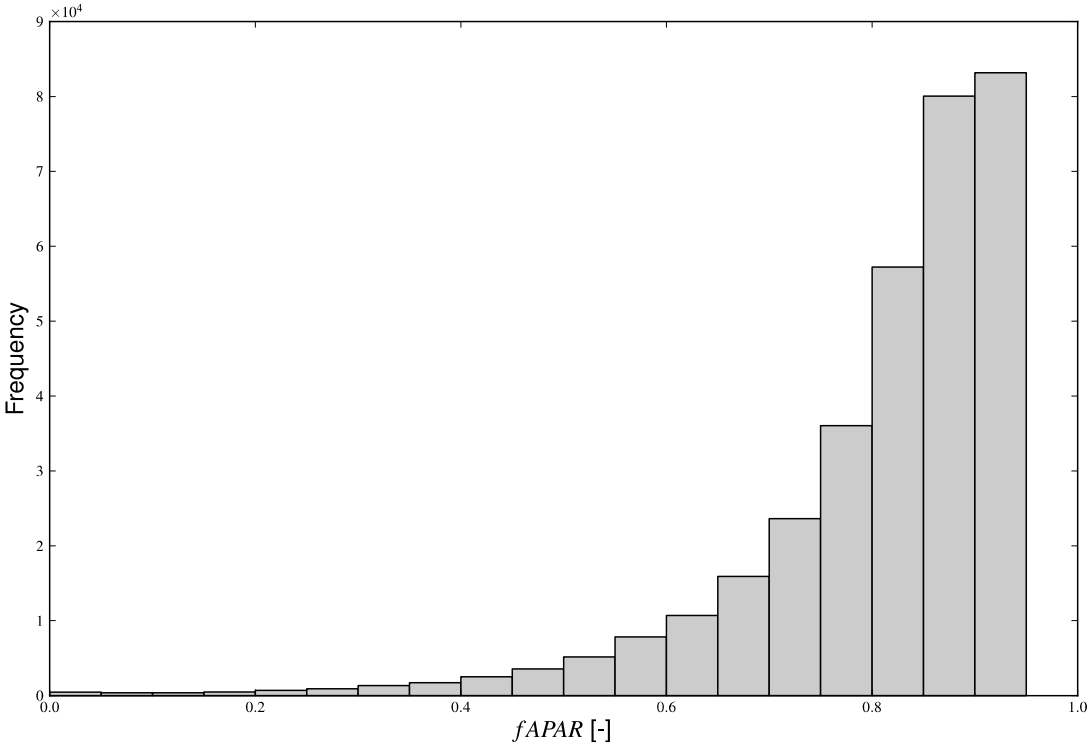

Figure 6-21. Posterior distribution of fAPAR

However, if we examine the resultant posterior distribution of fAPAR, we find the range of viable values to be quite small, and very much what might be expected for a VIS albedo of 0.0308. This distribution is rather skewed and certainly *not* Gaussian. The implications of this need further consideration.

6.5 Practical considerations

6.5.1 Data considerations

6.5.1.1 Atmospheric effects of BBDR

The product is designed to run with Lambertian equivalent BBDR data (and associated weighted kernels), in that it is able to treat the impacts of this assumption on the Broadband BRDF data. This is a novel aspect of the algorithm, and should have the effect of slightly increasing the non-isotropic model parameters over the values that would be obtained if the atmospheric influences were ignored. In this sense, it is a form of BRDF sharpening. The mechanism for doing this effectively in a single pass is solely a result of using linear models for the BRDF.

Under some circumstances, it may be advantageous to run a second iteration of the algorithm to better account for surface-atmosphere multiple scattering, although this is not currently planned for the main processing. Even with this single loop, the algorithm should account for most of the atmospheric effects, and this is of itself an improvement on any existing approach.

Should data that are corrected for non-Lambertian effects and surface-atmosphere interactions be used as inputs at some stage in the future, the code can proceed in its current form: the only change is that the non-smoothed kernels should be used as input with the BBDR data, rather than the atmospherically-treated versions. This implies a degree of ‘future-proofing’ for the code.

6.5.1.2 (A)ATSR(-2), MERIS and VEGETATION

The algorithm is designed to run with data from the European (A)ATSR(-2), MERIS and VEGETATION sensors. These sensors have disparate spectral, spectral and angular sampling. The conversion of all data to broadband estimates prior to processing is an important step in bringing together data that are spectrally different. As with the treatment of non-Lambertain atmospheric interactions on the inputs, the ability to achieve this formally only applies to linear models (though it is likely to hold as a reasonable approximation for non-linear models).

Issues regarding the different spatial sampling regimes are really only partially dealt with in this product: all data are gridded, and a ‘resampling’ uncertainty should be added to the input BBDR data. This is rather a crude mechanism, and it is not straightforward to estimate these uncertainties, but it is pragmatic, given the very large volume of data to be processed.

For a large portion of the time period for which the product will be generated, data from all three sensors will be available. As discussed above however, the angular sampling regimes of (A)TSR(-2) and MERIS in particular are far from ideal for estimating full angular effects and angular integrals. We therefore expect these data sets to contribute only rather weakly to the information content of the final product. This will be manifested through the relative entropy measure that characterises the information content of the data additional to that of the prior estimate. The angular sampling regime of VEGETATION is similar to

that of MODIS, although MODIS benefits from having two sensors in orbit and subsequently a higher probability of cloud-free sampling. For these reasons, and to avoid the arbitrary switching in of a 'backup algorithm' when the data information content is too low, a prior estimate of the model parameters is used to constrain the inversions. Although this has been investigated in some detail, it is in fact only used to weakly constrain the solution. This constraint will be of particular importance prior to the launch of the first SPOT VEGETATION. Since the prior is only applied weakly, it is expected that the parameter uncertainties will be relatively high for that period.

6.5.1.3 Forthcoming European sensors

An additional advantage of the fact that the algorithm treats BBDR data as inputs is that it is very straightforward to apply exactly the same code/algorithm to data of similar spatial resolution from forthcoming (European or other) sensors. Of particular interest in this regard are PROBA-V, the planned replacement for SPOT VEGETATION, and the SENTINEL-3 platforms. Both of these will provide suitable data for this algorithm, and could be treated in an almost identical manner to the existing data streams. This is another example of 'future proofing' built into the approach.

It is also worth mentioning that although in this product we map all data input channels to three broad wavebands, a similar (linear) mapping can be performed from any one band set to any other (with varying degrees of uncertainty, based mainly on spectral sampling). This means that although our system is designed primarily for three wavebands, it should be coded so that it could receive more (or different) channels of input data if so required. The same code could then be used to estimate narrow band (or different broadband) BRDF and spectral albedo.

6.5.2 Numerical computation considerations

The most computationally expensive part of the algorithm is likely to lie in: (i) the accumulation of information into the observation vector and matrix; (ii) estimating the model parameters and uncertainty. The first is because it makes use of large amounts of spatial data. It clearly does not make good sense to process those data a pixel at a time, so an approach has been developed that uses temporary files and a two-pass system to perform the accumulation efficiently.

The estimate of model parameters and uncertainty, once the accumulated matrix and vector have been formed and the prior estimate read, can only really be applied on a pixel-by-pixel basis.

Although the use of the prior should regularise the matrices and avoid numerical issues when the data information content is low, some care needs to be taken when implementing this. This is particularly true if the prior is downweighted too much or the prior uncertainty happens to be very high.

A function such as linsolve from umfpack[25] found in MATLAB/SciPy etc. would be appropriate as a solver in most cases as it uses robust methods for the parameter

[25] http://directory.fsf.org/project/umfpack/

estimation (that do rely on the calculation of the inverse matrix which can be prone to rounding errors). That said, the inverse matrix is required for the uncertainty estimates, so must be calculated in addition.

It is worthwhile calculating the condition number[26] *C* of the matrix, the ratio of the largest to smallest singular value in a singular value decomposition of the matrix to test if numerical issues are likely to occur in solving the linear system. If *C* is too large[27] the matrix needs to be rank reduced, using a threshold on the singular values maintained in the filtering. These are standard methods.

6.5.3 Prototyping and Verification.

A first verification of the products generated using the prototype code was carried out doing a product inter-comparison with MODIS MCD43A3 complete diffuse bihemispherical Albedo.

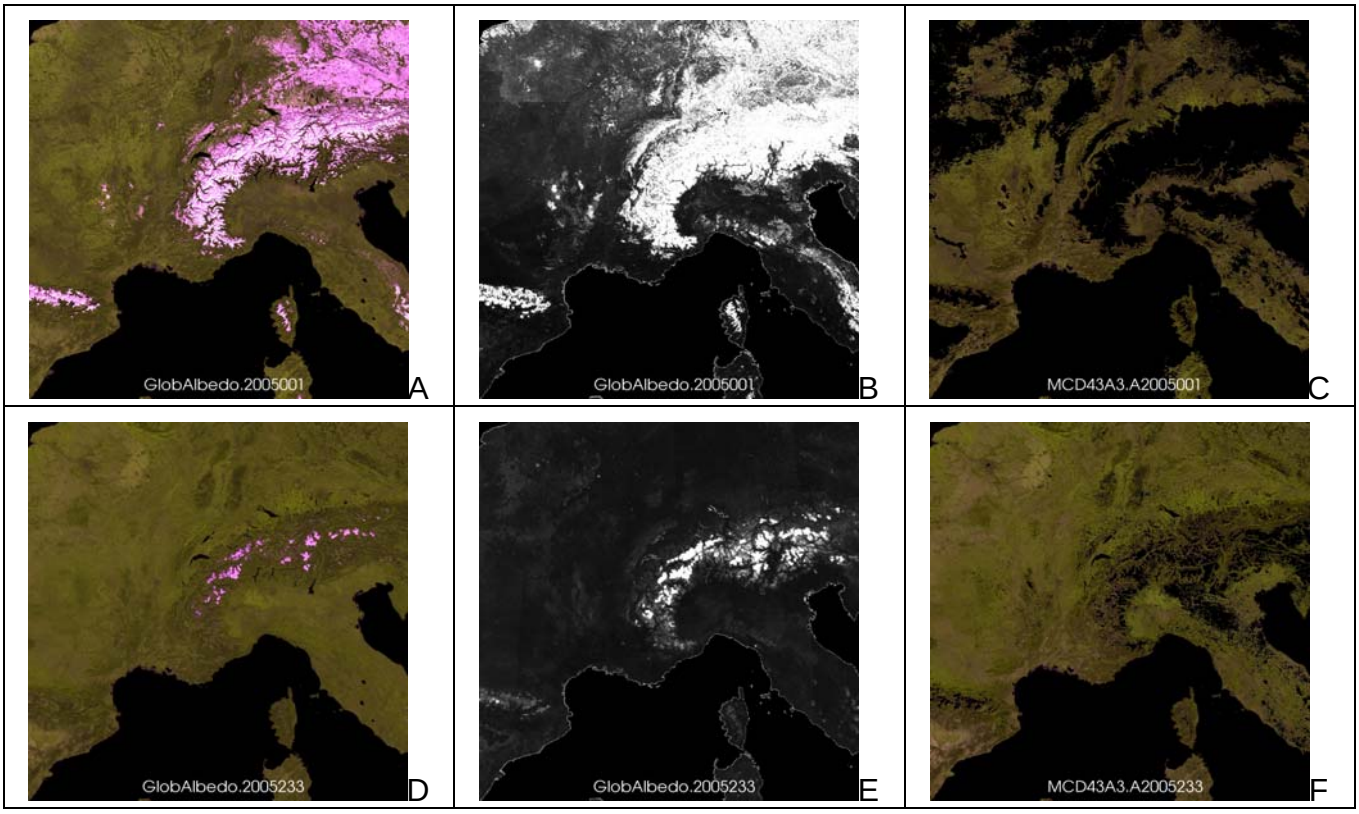

Figure 6-22. Upper row shows products for DoY 1, bottom row for DoY 233 for tile h18v04. Panels A and D show a false colour composite of GlobAlbedo BHR

[26] http://mathworld.wolfram.com/ConditionNumber.html

[27] where "too large" means roughly log(C)>=the precision of matrix entries (mathworld.wolfram.com).

SW,NIR,VIS (RGB), panels B and E the BHR uncertainty in the SW scaled 0:0.1, panels C and F a false colour composite from MODIS MCD43A2 BHR SW,NIR,VIS (RGB) only full inversion and No Snow data.

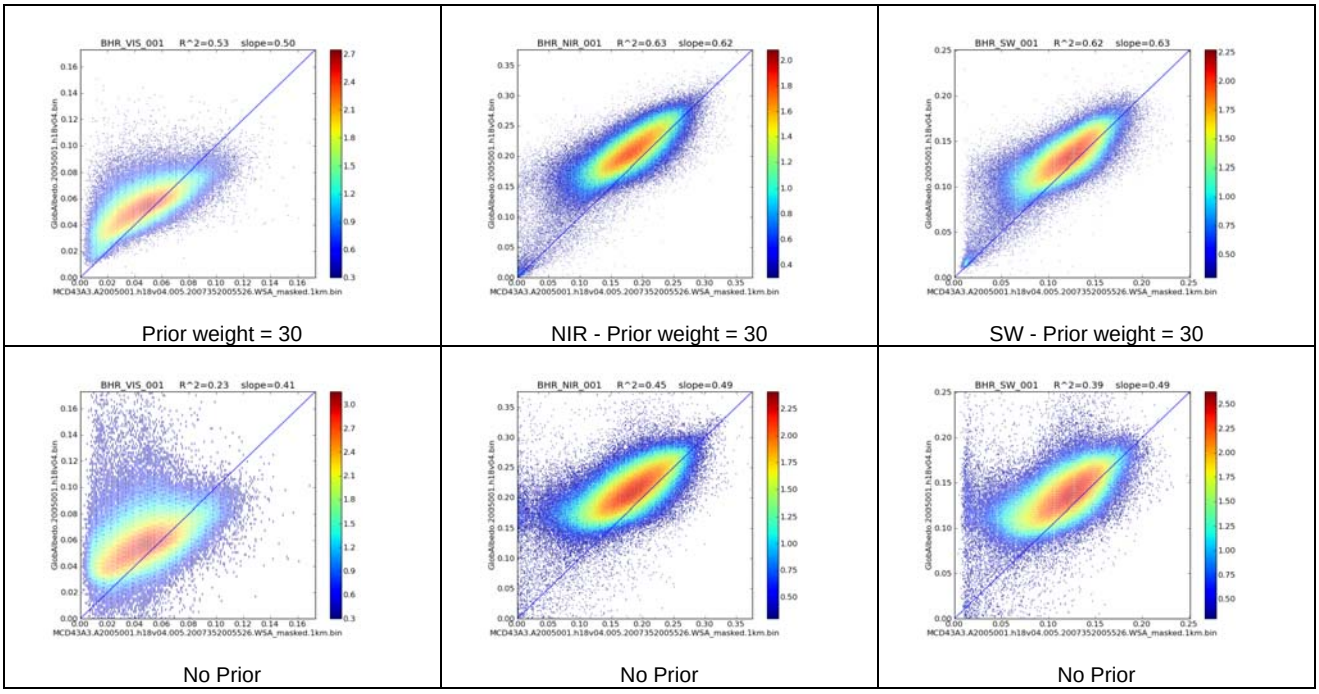

Figure 6-23. BHR inter-comparison of GlobAlbedo, with and without the use of the Prior and MCD43A3, for tile h18v04 DoY = 1

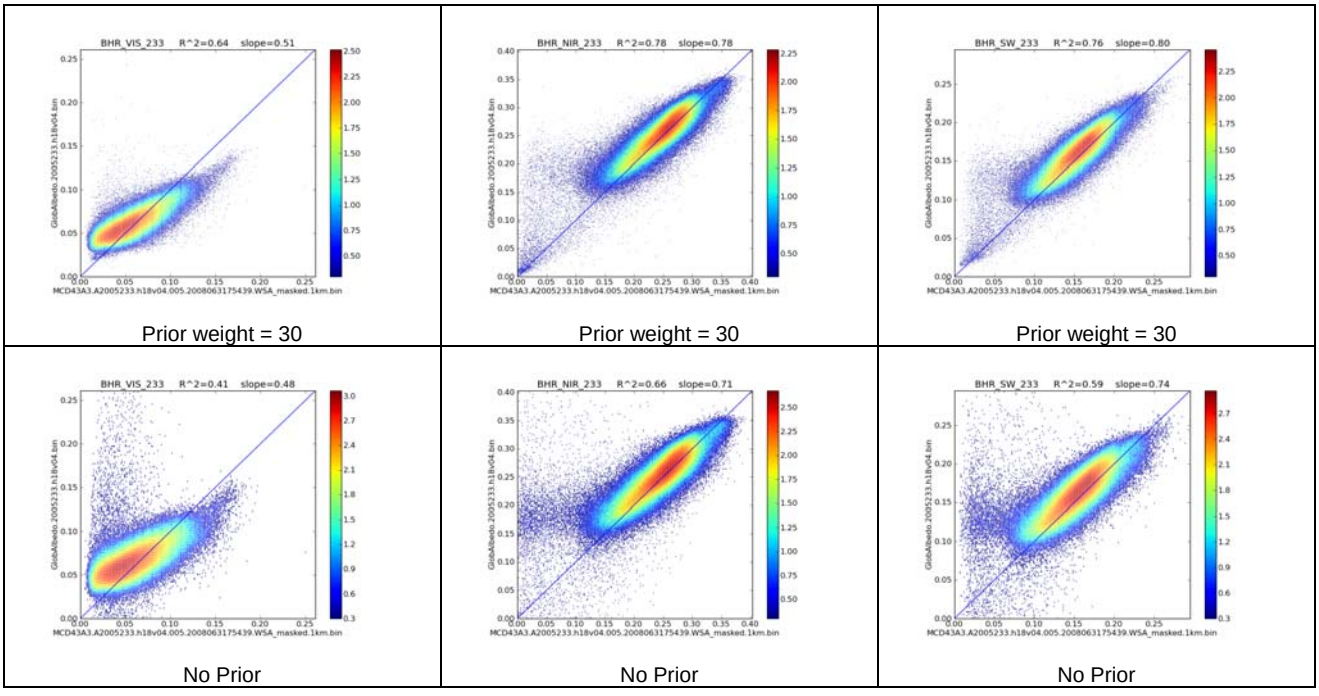

Figure 6-24. BHR inter-comparison of GlobAlbedo, with and without the use of the Prior and MCD43A3, for tile h18v04 DoY = 233

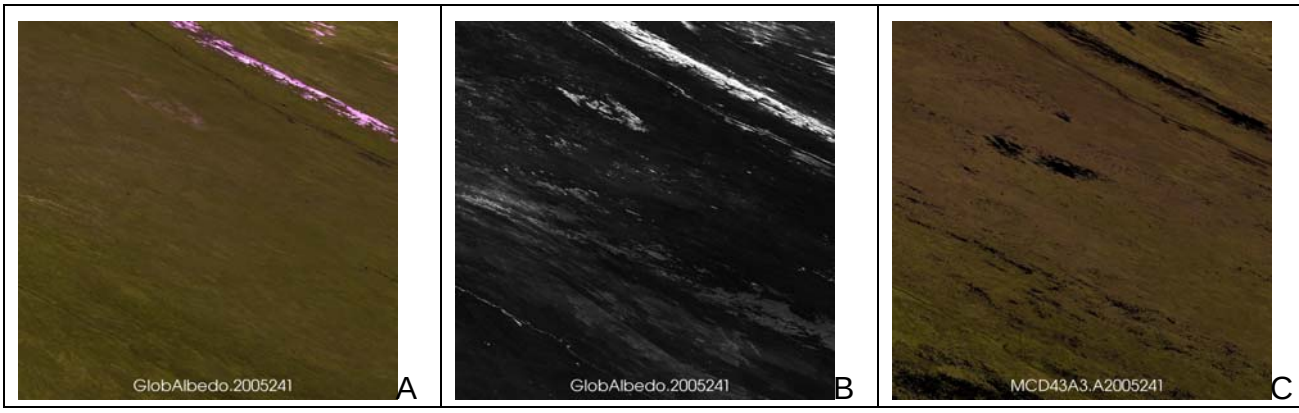

Figure 6-25. Panels A shows a false colour composite of GlobAlbedo BHR SW,NIR,VIS (RGB), panels B the BHR uncertainty in the SW scaled 0:0.1, panels C a false colour composite from MODIS MCD43A2 BHR SW,NIR,VIS (RGB) only full inversion and No Snow data. All products are for DoY 241 tile h22v02.

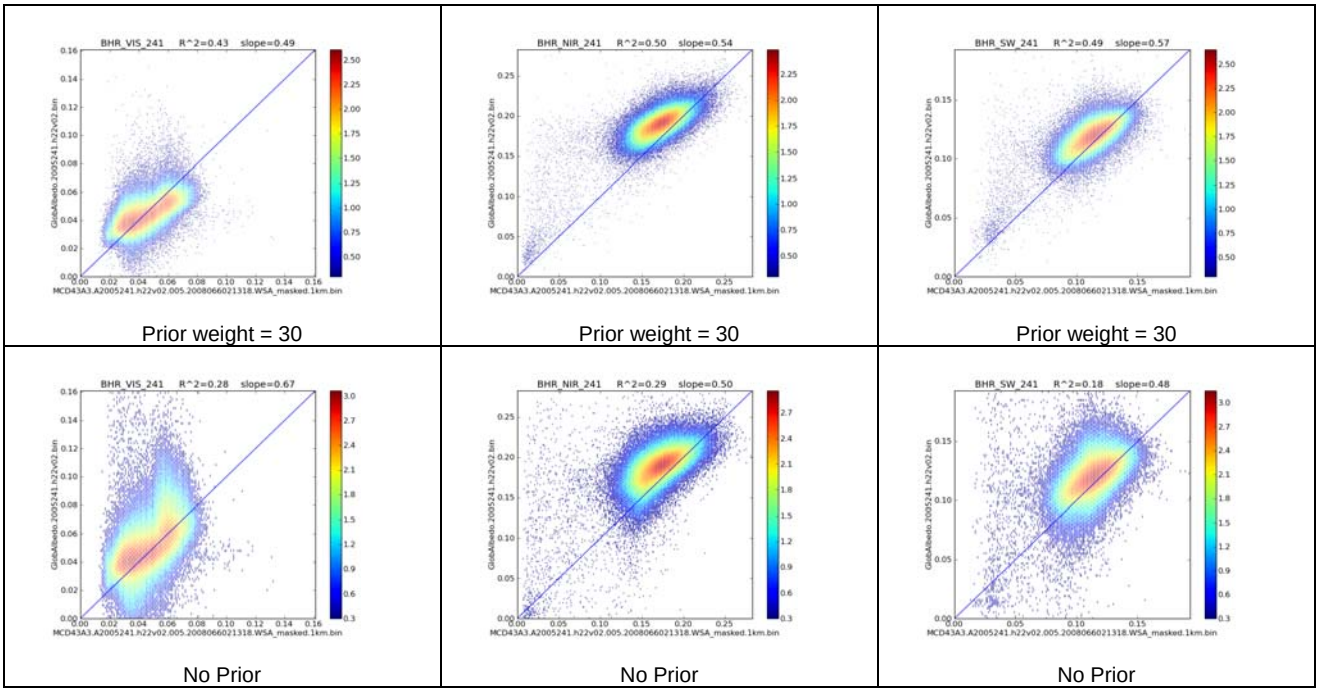

Figure 6-26. BHR inter-comparison of GlobAlbedo, with and without the use of the Prior and MCD43A3, for tile h22v02 DoY = 241

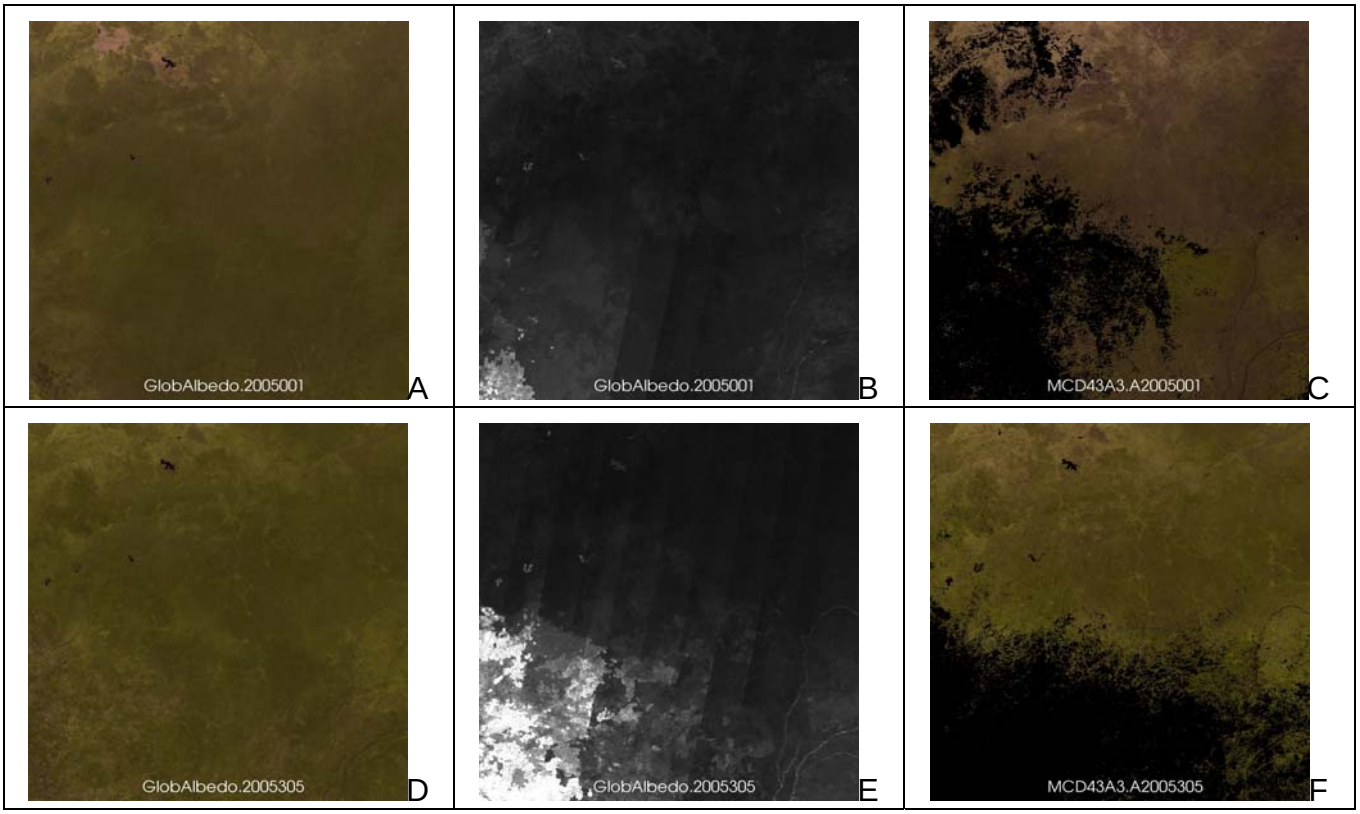

Figure 6-27. Upper row shows products for DoY 1, bottom row for DoY 305 for tile h19v08. Panels A and D show a false colour composite of GlobAlbedo BHR SW,NIR,VIS (RGB), panels B and E the BHR uncertainty in the SW scaled 0:0.1, panels C and F a false colour composite from MODIS MCD43A2 BHR SW,NIR,VIS (RGB) only full inversion and snow free data.

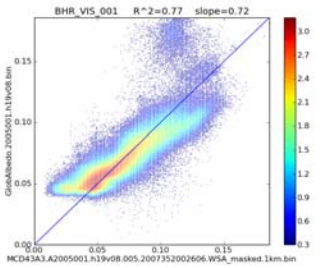

Prior weight = 30

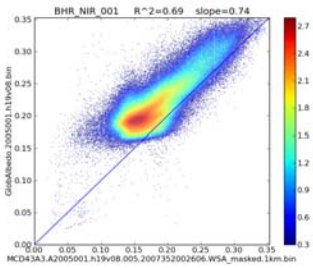

Prior weight = 30

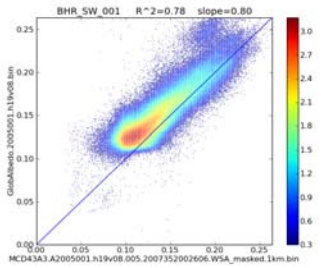

Prior weight = 30

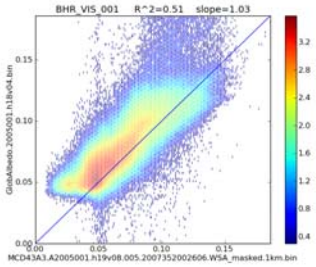	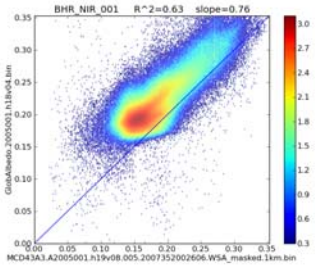	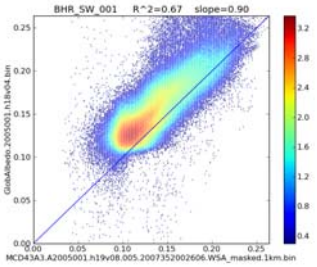
No Prior	No Prior	No Prior

Figure 6-28. BHR inter-comparison of GlobAlbedo, with and without the use of the Prior and MCD43A3, for tile h19v08 DoY = 1

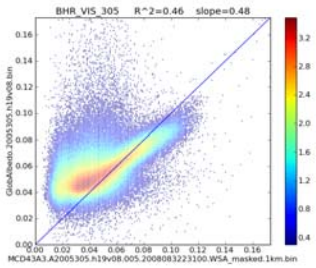	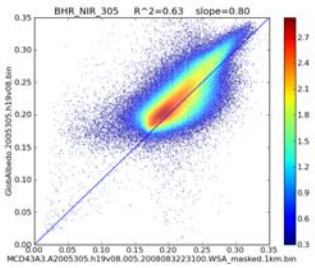	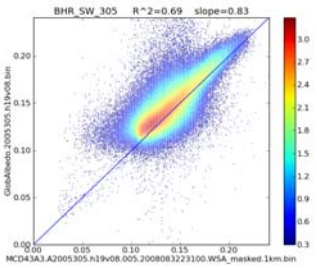
Prior weight = 30	Prior weight = 30	Prior weight = 30
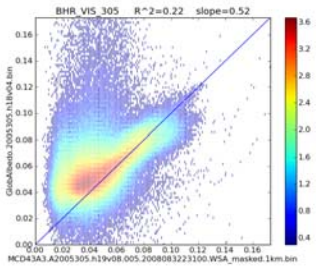	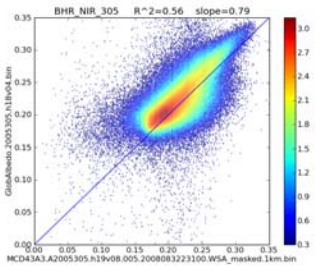	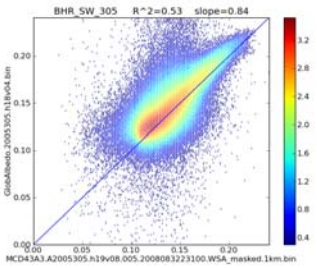
No Prior	No Prior	No Prior
h19v08 DoY=305		

Figure 6-29. BHR inter-comparison of GlobAlbedo, with and without the use of the Prior and MCD43A3, for tile h19v08 DoY = 305

6.5.4 Quality Control and Diagnostics

There is a wide range of quality control metrics that will be produced with the GlobAlbedo products. The main ones of these are:

- Information on the number of days since an observation at the pixel;
- QA information on whether a pixel is Land or not, allowing filtering for 'data' in the scene;
- QA information on whether the model parameters and therefore albedo are arrived at from observations, the prior, or a filler value;
- Data on the information content of the observations additional to that of the prior (i.e. the value of the observations in the parameter estimation);
- Uncertainty matrices associated with the model parameters (also expressed as a quantised QA value)
- Information on which sensors have contributed data to the parameter estimation.

When users make use of the product they should pay keen attention to the uncertainty information provided. The primary information for a first filtering of the data for most users should probably be the quantised uncertainty information as a rough guide to overall uncertainty. Further, if the relative entropy is very low, the observations will have made little different to the result over the information contained in the prior, which is no more than a climatology. Finally though, the most in-depth analyses should make use of the full uncertainty matrix.

6.5.5 Exception Handling

The main exceptions likely to occur are as a result of data that are expected not being present, or the files being correpted, so the code needs to be made robust to this. This mainly implies that all file opening, read, and write operations should fully test that the expected result has actually happened. If a failure occurs on file i/o this should be treated as a fatal error. Since it is frustrating for fatal errors to occur after many hours of processing, these errors should be pre-checked as far as possible, as early as possible in the processing chain.

Potential issues have been identified above in the case of there being land data indicated for a pixel, observations available, but no prior. In this case, an 'unconstrained' inversion may be attempted, but in any case such a pixel (most likely very rare) must be caught and identified in the QA. The same applies to pixels identified as Land, and with no prior and

no observations (this might help identify issues with the Land mask). This is an example of a non-fatal error.

Another non-fatal error should be flagged if the matrix condition number is too large, as discussed above.

Non-fatal errors need to be passed through as flags to the QA data.

Fatal errors should result in wrapping up whatever parts of the process might be profitably continued, then exiting the program.

7 Error budget

The target accuracy requirements identified by and agreed with the GlobAlbedo users in GlobAlbedo_RB_D01_v2_0 (2010) are: Albedo >0.15, 20% and for Albedo <0.15, 0.015, i.e. 10% relative accuracy (or 0.015, whichever is larger).

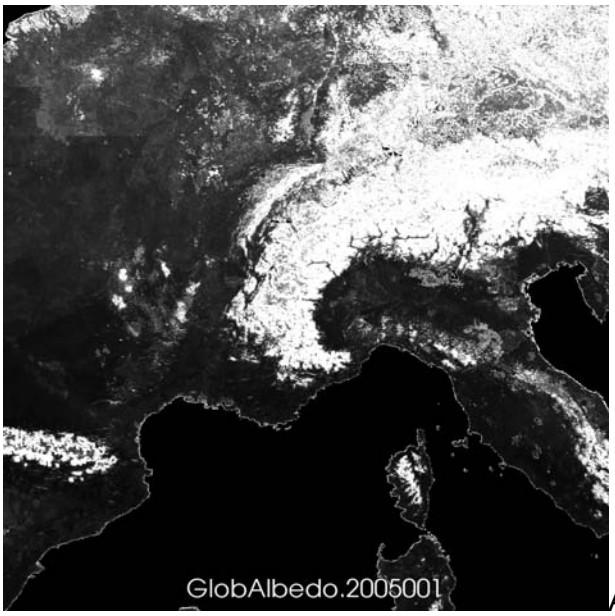

A

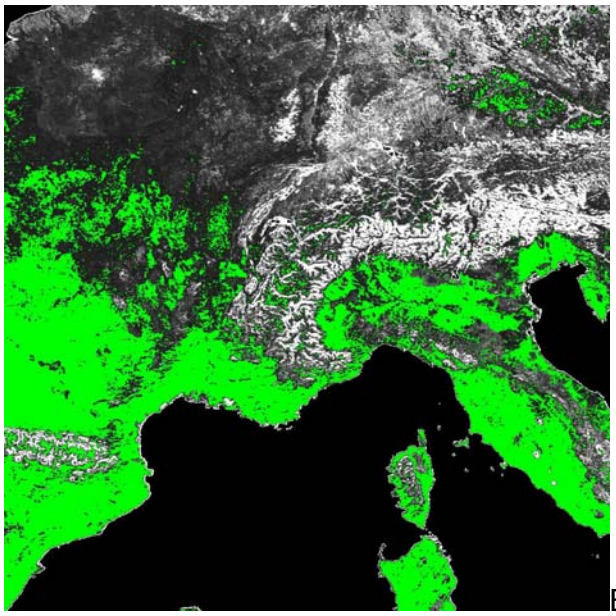

B

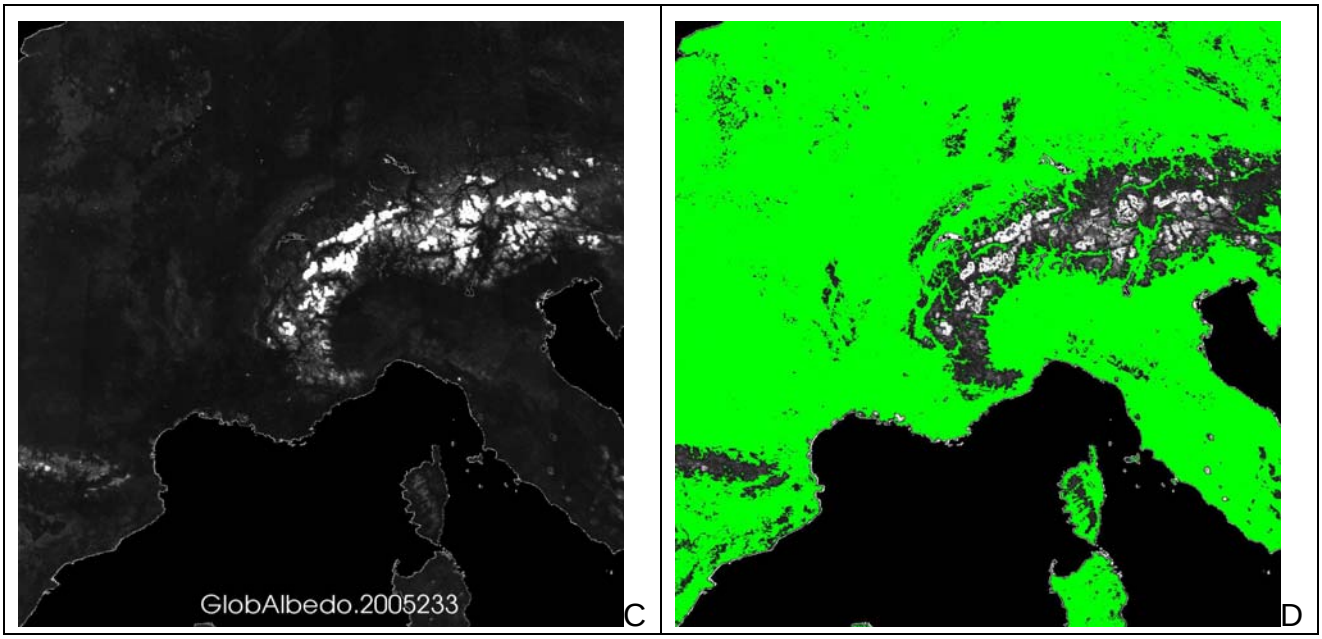

Figure 7-1. Top row shows products for DoY 1, bottom row for DoY 233 for tile h18v04. Panels A and C depict BHR uncertainty in the SW scaled 0:0.1, panels B and D the SW relative error, areas in green have 0-10% error.

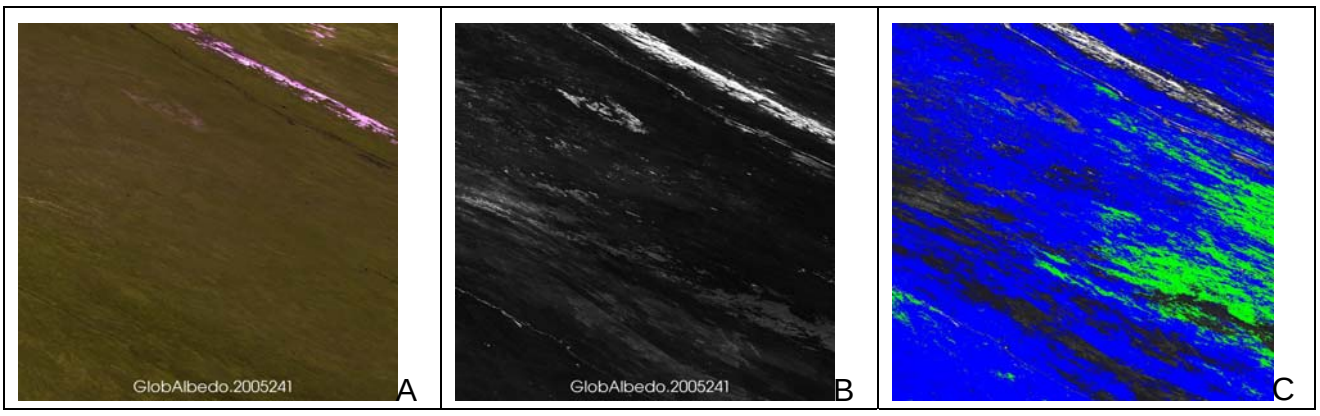

Figure 7-2. Panels A shows a false colour composite of GlobAlbedo BHR SW,NIR,VIS (RGB), panel B uncertainty in the SW scaled 0:0.1, panel C the SW relative error, areas in green have 0-5% error, in blue 5-10% error. Products are for DoY=241 tile h22v02

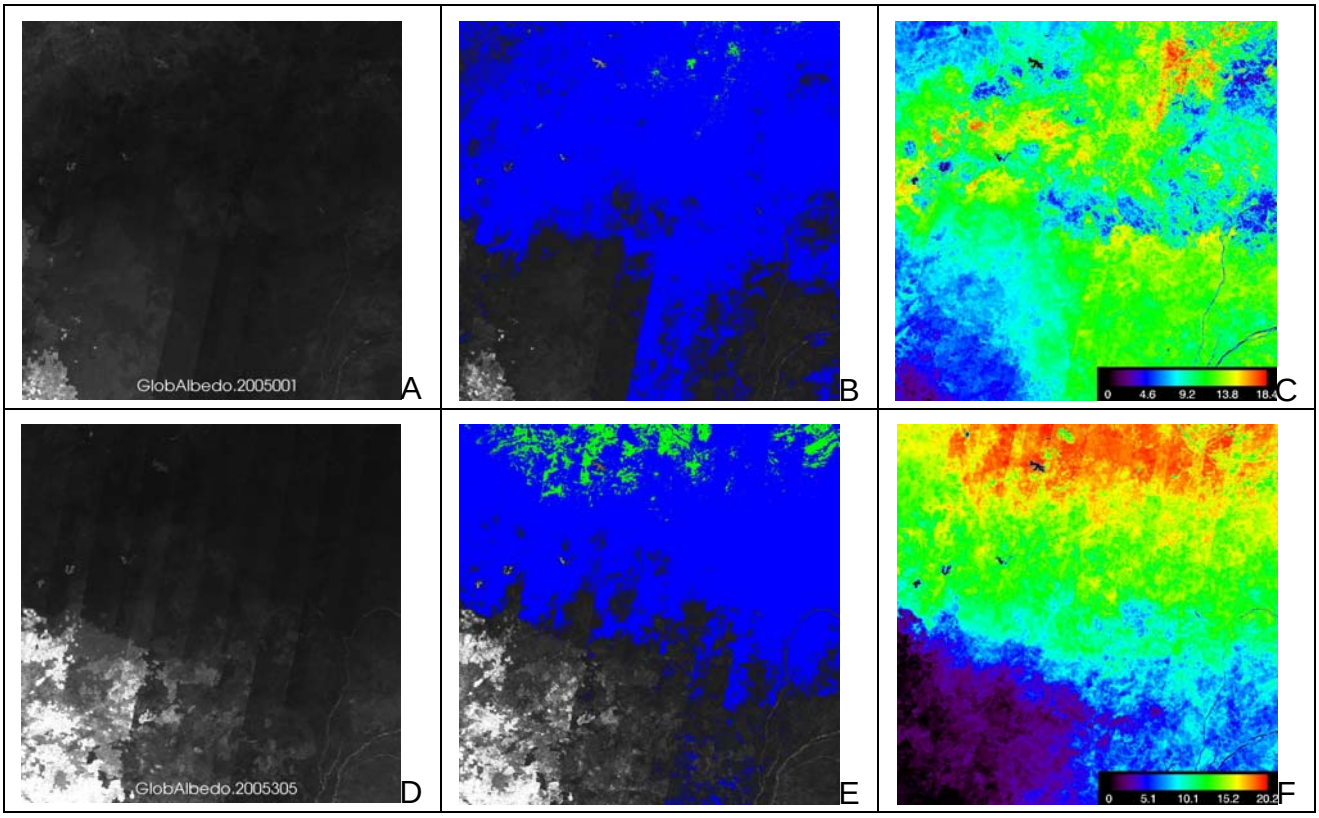

Figure 7-3. Top row shows products for DoY 1, bottom row for DoY 305 for tile h19v08. Panels A and D depict BHR uncertainty in the SW scaled 0:0.1, panels B and E the SW relative error, areas in green have 0-5% error, in blue 5-10% error, panels C and F show the weighted number of samples.

8 Assumptions and Limitations

8.1 Assumptions

The main assumptions underlying the product are presented below and discussed.

- **Assumption 1:** *The input BBDR data from the various European sensors provides an unbiased estimate of the reflectance averaged over the gridcell location and well-characterised uncertainties.*

  This is a necessary assumption for this part of the overall approach. In practice, it means that these claims need to be fully investigated in the validation of the products, and so is not part of this section of the ATBD. One feature to highlight is that the current atmospheric processing takes no account of environment effects in considering multiple scattering between the surface and atmosphere. For many areas this will not be a problem at 1 km resolution, but for some surfaces with high contrast, such as snow/melt ponds, this will produce an over-estimate of the reflectance over dark areas and an under-estimate of the bright ones.
- **Assumption 2:** *The BRDF models used are sufficiently accurate to represent the BBDR of all land surfaces sampled (at the 1 km spatial resolution).*

The wide range of experience with these linear kernel models means that there is a good confidence that the models are generally suitable for global monitoring of this kind *for most cover types*. The main exception to this (for the land surface) is snow, that has been identified as a potential problem area above. As a strategy to deal with this, we have two streams of albedo product: one for snow samples and one for 'no snow'. Thus, although we have not identify at this stage a better model (than the linear kernels) to use in this framework for modelling snow BRDF in the way required, should such a model become available, the data might be reprocessed quite simply. An argument for using the current models is that, for many surfaces, roughness/shadowing effects and a general 'bowl shaped' volumetric scattering may in fact somewhat smooth the forward scattering peak of snow-areas. An argument against using these models is that the current kernels simply are not capable of producing a forward scattering peak.

One particular feature that has received only little attention is the validity of these models over topography. Sites with large topographic influences tend not to be used for validation work, so there is little knowledge to guide us.

- **Assumption 3**: *The use of linear models throughout means that there will be no difference in model parameters*.

  This assumption is quite fundamental to the approach taken here. It is only strictly true for narrow waveband estimates of model parameters. For broader wavebands, it is equivalent to assuming that interacting spectral terms (such as N_{sky}, the proportion of diffuse illumination and spectral variations in model parameters) can be treated as equivalent values constant over the waveband. In that sense, it puts the problem off into the atmospheric correction processing: the requirement for that is to calculate the correct broadband equivalent terms that will result in the correct equivalent broadband parameter.

  Although this is a reasonable assumption to make, and is of such great benefit to the processing framework with the disparate sensors used here, this is an aspect of the algorithm assumptions that would benefit from further investigation and a fuller quantification of the uncertainties involved.
- **Assumption 4**: *All uncertainties can be treated as Gaussian distributions*.

  This is a fundamental assumption underlying the optimal estimation framework and the treatment of uncertainty throughout. It is usual practice in modelling of this sort, although it has not received any particular attention here.
- **Assumption 5**: *An optimal estimate of albedo is not achieved by censoring the model parameters.*

  In the MODIS BRDF/Albedo product, model parameters are constrained so as not to take on negative values. This is to allow them to maintain some physical meaning. Viewed simply as semi-empirical 'shapes' though, there is less justification to such censoring. The downside of not censoring is that it is possible that negative albedo values may be predicted. In such a case however, it is likely that the uncertainties will be high, so the parameter distribution will in any case cover a large portion of positive values. More importantly, censoring of the data

greatly complicates the interpretation of Gaussian uncertainty values, as these (formally) assume uncensored data. Pixels that have negative model parameters are easily identified by the user and can be removed if desired. Also, the conditioning of the matrix by the use of a prior estimate should reduce the occurrence of negative parameter values, as the prior has only positive values (being derived from MODIS).

8.2 Limitations

The major limitations of the product are likely to occur for:

- *Estimating model parameters far away from the angular sampling available*

  For example, at high latitudes, in Spring but even in Summer, the solar zenith angle at the time of the observations will tend to be quite high. This introduces several problems. First, the quality of the atmospheric correction is likely relatively poor, due to the long path length through the atmosphere and the need to treat aspects such as Earth curvature in scattering considerations. Second, the kernel BRDF models are unlikely to operate as well as high solar zenith angles as at lower angles. Third, at high solar zenith angles, N_{sky} can be quite peaked. The kernel BRDF models have only a weak treatment of the retro-reflection peak, so these impacts may become over-smoothed. In such a scenario, terms such as the white sky albedo become rather hard to estimate as well as the angular sampling is not well-distributed enough for a robust calculation of this integral. This problem should be mitigated by the large uncertainty in atmospheric products and BRDF model parameters that will be produced by these angular configurations.
- *Snow albedo, particularly relatively smooth, fresh snow*

  It is acknowledged in the ATBD that there is a perceived need for an improved snow model and that the existing models may be insufficient. There is however debate around this issue, and no suitable replacement model has been successfully used globally in similar products. Issues regarding snow will be worse when the forward scattering peak is larger, which will tend to occur when the snow if flat and fresh (minimal surface roughness effects).
- *Estimating model parameters where no observations or prior are available*

  This is clearly a difficult thing to attempt, but in trying to produce a ‘snow free’ albedo product we are in many cases doing just that: trying to predict the snow free albedo of somewhere that is always covered in snow at a particular sampling time. In such a case, the product will revert to the prior (and the relative entropy will be zero) so such cases will be flagged as potentially unreliable. The most difficult to treat cases occur when there are no estimates available in the prior. This should only happen in a small number of cases however, and those are likely to be areas of *permanent* cloud (no MODIS or other observations ever) or e.g. in trying to predict the snow-free albedo of an area that is permanently snow covered.

9 Error budget

Some examples of error budget ... giving some idea that we will be able to hit the required target uncertainties.

E.g. of uncertainties with different levels of satellite data uncertainties (or different quantities/types). Refer back to some results in 3.2.2 re with/without prior.

10 Appendix A: Broadband reflectance and kernel values (internal product)

In order to derive test broadband albedo data for developing the prototype system, daily surface reflectance data of the MODIS instrument onboard Aqua and Terra platforms with 500 m spatial resolution (MOD09GA) have been employed. The operational surface reflectance computation for bands 1 to 7, ranging from the visible blue to the short-wave infrared, employs several atmospheric products and corrects for atmospheric gases, aerosols, cirrus, and the adjacency effect (Justice et al., 1998; Vermote et al., 2002). With the aim of utilize only pixels with a high data quality, the quality assurance science data set (QA-SDS) provided with the MODIS granules has been analyzed. Only pixels which fulfilled the specifications of Table 11-1 and with a SZA lower than 80° have been preserved.

Quality flag	**Quality setting**
Cloud state	Clear
Cloud shadow	No
Land/water	Shallow ocean, land, ocean coastlines and lake shorelines, shallow inland water, deep inland water.
Aerosol quantity	Climatology, low, average, high
Cirrus detected	None
Internal cloud algorithm	No cloud
Internal fire algorithm	No fire
MOD35 snow/ice	No
Pixel is adjacent to cloud	No
BRDF correction performed	No
Internal snow algorithm	No

Table 11-10-1 MOD09 QA flags

Narrowband to broandband conversion was performed using the formulae provided by Liang (2000), as atmospheric correction produces surface spectral reflectance, under the assumption that the surface is a Lambertian, spectral reflectance is equal to spectral albedo, a similar processing is performed by the MODIS science team in the generation of the BRDF/Albedo generation as the conversion of spectral reflectance to spectral albedo is based on observations accumulated during the period of 16 days surface reflectance (Lucht et al., 2000). An example of the aforementioned product is shown below.

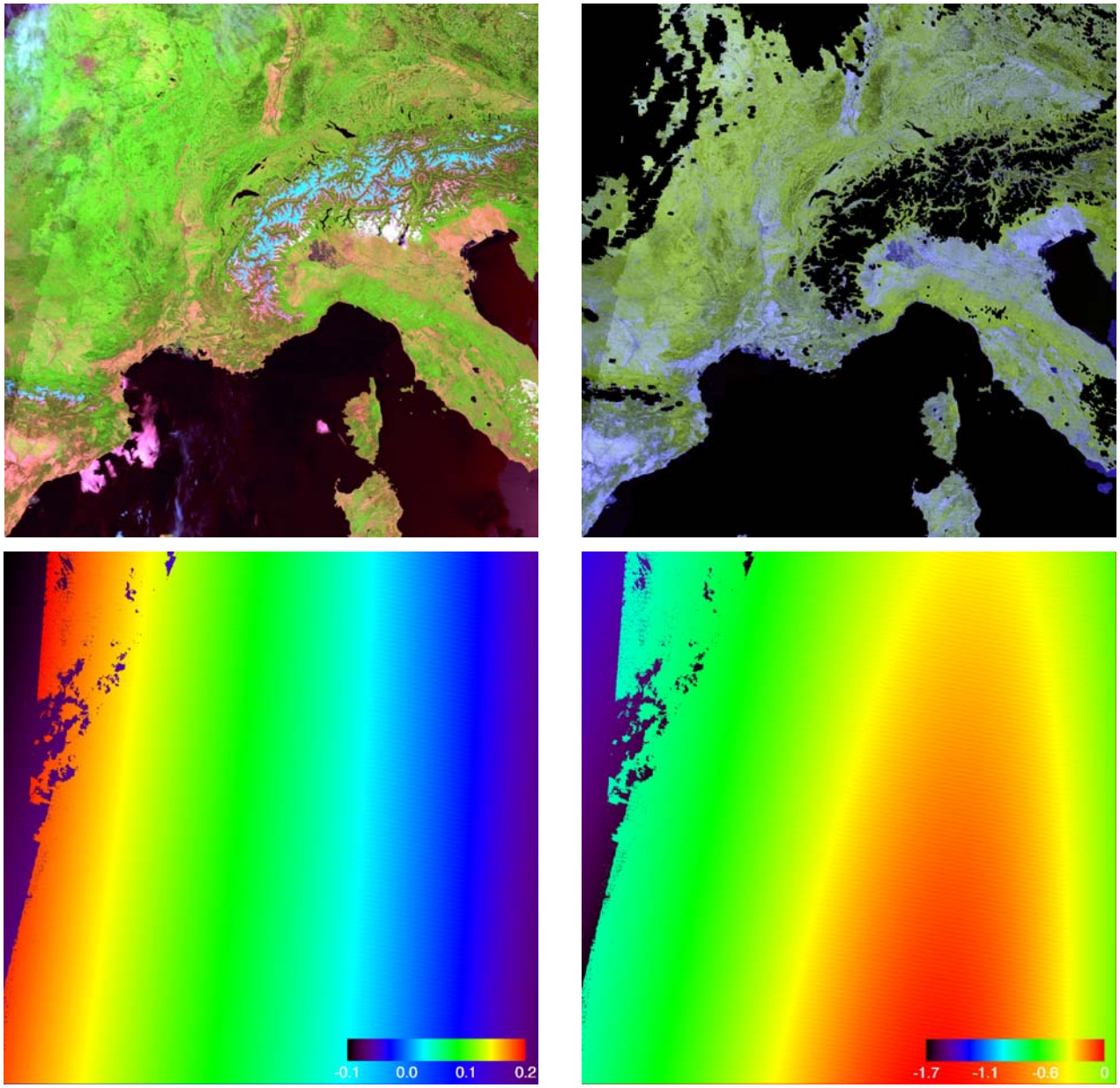

Figure 10-1. On the upper left corner, daily surface reflectance product derived from MODIS in a false color composite bands 7,2,1 RGB, on the upper right corner the conversion to broadband masked from clouds and snow, the Ross-Thick kernel is shown on the lower right corner and, the Li-Sparse reciprocal kernel on the bottom right.

Section A: Algorithm Theoretical Basis Document – Pixel Classification

Version 3.1

Document Number: GlobAlbedo_PixID_ATBD_V3.1 Date 06/06/2012

Distribution:

ESA	O. Leonard	X
	S. Pinnock	X
University College London	J-P. Muller	X
	T. Kennedy	X
	P. Lewis	X
Swansea	P. North	X
Free University of Berlin	J. Fisher	X
	R. Preusker	X
Brockmann Consult	C. Brockmann	X
	N. Fomferra	X
	U. Krämer	X

CHANGE RECORD

ISSUE	DATE	PAGES CHANGED	COMMENTS
A	21/06/10	All new	Draft
0.1	23/07/10	All sections	First Issue
1.0	10/09/10	All sections	Final version
2.0	12/11/10	References	RID response
3.0	05/04/11	Section 3.4	Adjustments regarding Idepix improvements
3.1	06/06/2012	All	New global ToC

11 Introduction

The GlobAlbedo project will develop a broadband albedo map of the entire Earth's land surface (snow and snow-free), which is required for use in climate modelling and research. An initial group of six users are working with the GlobAlbedo project team to define requirements and drive the project towards practical applications of the products.

The final albedo products will include both black and white sky albedo over the entire globe with at least monthly frequency over the 1995-2010 time period, include uncertainty estimates, and be integrated in three spectral broadband ranges, namely the solar spectrum (400-3000nm), the visible (400-700nm) and the near- and shortwave-infrared (700-3000nm).

With the aim of deriving independent estimates making the best use of operational European satellites, GlobAlbedo sets out to create a 15 year time series by employing ATSR2, SPOT4- VEGETATION and SPOT5-VEGETATION2 as well as AATSR and MERIS. Albedo retrieval will use an optimal estimation approach, as well as a novel system for gap-filling.

This document describes the algorithm basis documenet for the Globalbedo pixel classification. The document includes all assumptions, discusses technical tradeoffs and describes the algorithm in terms of physical background as well as mathematical breakdown.

The document shall provide the baseline for understanding the algorithm as well as for implementation in a software processor and its verification.

12 Applicable and Reference documents

12.1.1 Applicable documents

AD1 Doc. Number Doc.. Title

12.1.2 Reference Documents

RD1 Doc. Number Doc.. Title

12.2 Definitions and Abbreviations

12.3 Definitions

Item	Definition

12.4 Abbreviations

AATSR	Advance Along Track Scanning Radiometer
ATBD	Algorithm Theoretical Basis Document
AVHRR	Advanced Very High Resolution Radiometer
BEAM	Basic Envisat Tool for AATSR & MERIS (http://envisat.esa.int/services/beam/)
BRDF	Bidirectional Reflectance Distribution Function
BRF	Bidirectional Reflectance Factor
CLiC	Climate and Cryosphere project
EGD	Effective Grain Diameter
ENVISAT	Environment Satellite (http://envisat.esa.int)
EO	Earth Observation
ERS	European Remote Sensing satellite
ESA	European Space Agency
EUMETSAT	European Meteorological Satellites Agency
FSC	Fractional snow cover

GCOS	Global Climate Observing System
GMES	Global Monitoring for Environment and Security
H-SAF	Hydrology and Water Management SAF
ICSU	International Council for Science
IGOS	Integrated Global Observing Strategy
IOC	Intergovernmental Oceanographic Commission
JAXA	Japan Space Agency
KO	Kick-Off
L1, L2	Level 1, Level 2
LSA SAF	Land Surface Application SAF
MC	Monte-Carlo
MERIS	Medium Resolution Imaging Spectrometer Instrument
MODIS	Moderate Resolution Imaging Spectroradiometer
MSI	Multi-Spectral Imager
MTR	Mid-Term Review
NDII	Normalized Differentiation Ice Index
NDSI	Normalized Differentiation Snow Index
NIR	Near InfraRed
NOAA	National Oceanic and Atmospheric Administration
OLCI	Ocean and Land Colour Instrument
PAR	Preliminary Analysis Report
PM	Progress meeting
POLDER	POLarization and Directionality of the Earth's Reflectances
RB	Requirement Baseline document

RTC	Radiative Transfer Code
RTE	Radiative Transfer Equation
S-2	GMES Sentinel-2 (http://www.esa.int/esaLP/LPgmes.html)
S-3	GMES Sentinel-3 (http://www.esa.int/esaLP/LPgmes.html)
SAF	Satellite Application Facility
SAJF	Sensitivity Analysis Justification File
SAP	Scientific Analysis Plan
SCA	Snow covered area
SCAR	Scientifc Committee for Antarctic Research
SCIAMACHY	Scannin Imaging Spectrometer for Atmospheric CHartographY
SLSTR	Sea and Land Surface Temperature Radiometer
SoW	Statement of Work
SPOT	Satellite Pour l'Observation de la Terre
SSA	Single Scattering Albedo
SSW	Snow surface wetness
STS	Snow temperature for surface
STSE	Support To Science Element
SWE	Snow Water Equivalent
SWIR	Short Wave Infra Red
TIR	Thermal InfraRed
TOA	Top of Atmosphere
UNEP	United Nations Environment Programme
UNESCO	United Nations Educational, Scientific and Cultural Organization
UNFCCC	United Nations Framework Convention on Climate Change

UR	Utility Report
UV	Ultra Violet
VNIR	Visible Near Infrared
WCRP	World Climate Research Programme
WMO	World Meteorological Organization

13 Algorithms' overview

The term "Pixel identification" refers to a classification of a measurement made by a space borne radiometer, for the purpose of identifying properties of the measurement which are influencing further algorithmic processing steps. Most importantly is the classification of a measurement as being made over cloud, a clear sky land surface or a clear sky ocean surface. The term "pixel" is often used for such a measurement in order to express it being part of a spatially oriented collection of many measurements, which all are geo- located and which form, as a whole, an image of the earth below the satellite.

While the information if a pixel is made over water or land can be taken from a static map, provided the geo-location of the pixel is better than the size of the pixel, as a good first guess, the cloud coverage is spatially and temporally highly variable and needs to be derived from the measurement itself. After knowing whether a pixel is cloudy or clear, in the clear sky case the land-water information can be refined using the measurement. This is particularly necessary in the coastal zone where the actual land-water boundary is changing due to tides, when the pixel size is small enough to resolve this difference. Also maps are not always correct so that a radiometric refinement is advisable.

13.1 Background

A large portion of the earth surface is covered by clouds (Paperin et al, 2007). Consequently most earth observation images in the visible spectral domain include a significant amount of cloudy pixels. Such measurements are treated in two opposite ways: either cloud properties are retrieved , e.g. for weather forecast or climate studies (Wylie, D., 1998, Russow et al, 1999; Liou, 1992), or the focus of the interest is the earth surface – being it land or water – which is then masked by the cloud (Luo,2008). In the latter case the presence of the cloud needs to be identified, and the change of the surface reflectance due to the cloud has to be estimated.

An image pixel can be cloud free, totally cloudy, or partly cloudy. In the cloud free case there are no water droplets or ice crystals in the atmosphere which change the surface reflectance. In the totally cloudy case the optical thickness is so high that the portion of surface reflectance at the signal measured by the satellite is negligible. The partly cloudy case comprises all intermediate situations where the measured reflectance is a mixture of a significant portion of the surface reflectance, but modified due to the presence of a cloud. This can be either due to an optically thin cloud, or the cloud is covering only a fraction of a pixel in the field of view of the sensor (Preusker et al, 2006).

Cloud free and totally cloudy pixels can be identified rather easily, and most of the tests used in earth observation processing systems for cloud identification today, assign either of these two stages, and hence also partly cloudy cases have to be assigned to either of these two classes (Eumetsat, 2006). For spatial high resolution instruments such a binary cloud flag is not appropriate if several different higher level processing algorithms are applied, each of which having a different robustness to partial cloudy pixel (Brockmann, 2008). Some novel algorithms therefore deliver a graduated scale, as an indicator of the extend to which a signal is influenced by the presence of clouds (Schiller et al, 2008, Gomez-Chova et al, 2007, Merchant et at, 2006).

Such an indicator can be related to cloud properties, e.g. apparent cloud optical thickness, the atmospheric transmission (Schiller et al, 2008), or cloud features (Gomez-Chova et al, 2007).

Clouds have certain characteristics which can be used for their identification and characterisation (Luo et al, 2008):

- Brightness
- Whiteness
- Cold temperature
- High altitude

However, none of these characteristics is always given if a pixel is cloudy; this is the main problem of cloud identification.

Thin clouds are difficult to differentiate from bright land surfaces and clouds in the mountains can be lower than the mountain ridges around. Then other methods not based on the features given below must be used. In particular, the clouds can be also detected using the spatial and temporal variability of the reflected radiation. In addition, clouds screen the tropospheric gases. This leads to the increase in the reflection inside corresponding gaseous absorption bands (e.g., H_2O, CO_2, O_2), which is routinely used for the cloud top height monitoring (Fisher et al., 2000a).

One way to detect clouds would be to work directly with optical measurements. Further, derived cloud physical properties can be used to characterise clouds and assess their impact on the retrieved signal. This includes, amongst others, cloud fraction, cloud top temperature, cloud top pressure, cloud type, cloud phase, cloud optical depths and cloud effective particle size. Such properties can be studied using the radiative transfer modelling. Fischer and Preusker (2000a,b) have done extensive work in this respect over the past years (see also Mullet et al, 2007, Rathke et al, 2002, Brenguier et al 2000, Pawlowska et all, 2000). They have developed the MERIS algorithms for cloud top pressure, cloud optical thickness, cloud albedo and cloud type retrieval and have translated this knowledge into a probability based cloud detection algorithm (Preusker et al, 2006).

Cloud detection became important with the systematic processing of the NOAA AVHRR instrument in the 1980s. Statistical histogram analysis methods were developed by Phulpin et al (1983). Most common used were threshold algorithms, e.g., Saunders et al. (1988). Large scale textures were identified using pattern recognition techniques as proposed by (Garant and Weinman, 1986). These methods worked quite well over the ocean but exposed problems in polar regions (separation of clouds from ice and snow) and in the tropics (low level, warm clouds). A good overview of the cloud screening techniques at the late 80s is given by Goodman et al. (1988). Improved methods are proposed for the AVHRR (Simpson et al, 1996) and later for ATSR (Simpson et al 1998).

The cloud screening algorithms for the ATSR 1 and 2 in the 1990s were mainly based on previous work for AVHRR and use spectral threshold tests (Birks et al, 2007). The thermal band at 12µm is used as main tool to identify the cold cloud surface by a threshold, supported by other thresholds on band differences and on the histogram of the radiance distribution in the image. The unique feature of two views under different angles of the same pixel and the spatial coherence of the radiance are also exploited. The cloud screening of the AATSR is basically the same with refined and additional tests due to additional bands. Recently, tests on vegetation and snow indices have been introduced (Birks et al, 2007). However, application oriented projects are not satisfied with the standard cloud screening and are proposing alternative methods, for example for the GlobCarbon processing (Plummer et al, 2008).

The MERIS Level 2 cloud screening is a combination of 8 different tests (Santer et al, 1997). Three of those are classical threshold tests on spectral radiances or differences, and five are connected with the pressure estimates derived from the differential oxygen A-band absorption measurements. However, due to the current insufficient quality of the standard pressure products derived from the measurements, these tests are not used.

The potential of the O2A feature has been addressed recently in ESA funded projects, namely “Exploitation of the oxygen absorption band” and “MERIS AATSR Synergy”. The result of this activities has lead to an upgrade of the operational MERIS pixel classification in the third reprocessing. Major improvement is due to including dedicated pressure algorithms for detection of the height of the scattering surface over land and ocean.

The strong water vapour absorption at 1.38µm can be used to detect the presence of high clouds, including thin cirrus under daytime viewing conditions. With sufficient atmospheric water vapour in the beam path, almost no upwelling reflected radiance from the earth’s surface reaches the satellite which is in particular handy for snow covered surfaces. However, precipitable water is often less than 1 cm over polar and in high elevation regions. The 1.38 µm reflectance threshold is set to 0.03 for MODIS (Ackerman et al 2006).

A big problem is the distinction between clouds and snow/ice, in particular for instruments which do not have spectral bands in the NIR and SWIR. An extensive study including the cloud screening over snow and ice has been undertaken by Stamnes, Hori and Aoki for the purpose of snow property retrieval (Aoki et al, 2007; Hori et al, 2007; Stamnes et al, 2007). Snow and ice are less reflective in the NIR spectral region, and the so called normalized differentiation ice index (NDII) and the corresponding snow index (NDSI) is a good tool to differentiate clouds from snow and ice. These indices are defined as follows:

$$NDII = \frac{R(0.545\mu m) - R(1.05\mu m)}{R(0.545\mu m) + R(1.05\mu m)},\ NDSI = \frac{R(0.545\mu m) - R(1.64\mu m)}{R(0.545\mu m) + R(1.64\mu m)}$$

The reflectance for ice decreases with the wavelength must faster as compared to snow. Therefore, large values of NDII signify the bare ice case.

Also measurements of trace gas vertical columns (e.g., SCIAMACHY onboard ENVISAT) are disturbed by cloud presence because corresponding instruments have large fields of view to

enhance the sensitivity to small gaseous concentrations. Cloud clearing algorithms are described in (Cervino et al, 2000) for GOME, and Kokhanosky has recently reported on using MERIS to support the cloud screening for SCIAMACHY (Kokhanovsky et al, 2008).

13.2 Methods

Cloud detection methods can be categorized in the following classes (Brockmann et al, 2008):

- Spectral threshold methods: Spectral characteristics, such as temperature, brightness, whiteness or height of the scatterer are tested against a threshold value. The threshold can be parameterized by viewing geometry, location or time. Most cloud screening algorithms given in the reference list include such tests.

  A special subsection of these tests concern spectral high resolution methods. Feature selection or PCA pre-processing is sometimes applied to reduce the dimensionality of the dataset. Such work is published by Lavant et al. (2005), McNaly et al. (2003), Rathke et al.(2002), Susskind et al. (1998).

- Feature extraction and classification: The spectral data space, if transformed into a feature space, can be statically or dynamically (i.e. scene dependent) separated into cloud or clear classes. This group of algorithms also includes spatial structure based algorithms. Examples are given by Gomez-Chova et al. (2007).

- Learning algorithms: The Baesian probability approach and general data mining techniques are employed. Cloud probability or cloudiness index values are generated after training the algorithm with simulated or measured data. Examples are given by Merchant et al, . (2005), Gomez-Chova et al. (2007) for AATSR and Schiller et al. (2008) for MERIS. A generic approach of a learning algorithm has been developed by Colapicchioni et al. (2004) and D'Elia et al. (2004).

- Multitemporal analysis: Pixels are not always cloud covered and a time series of data is used to separate cloudy from clear cases. For example, such kind of method is applied by Baret in the Cyclopes processing (Baret et al, 2007).

- Multi sensor approach: In cases, where multiple sensors are on the same platform and perform simultaneous measurements, the synergetic algorithms can be used to better identify clouds. This was considered, for example, in the case of MERIS and SCIAMACHY by Kokhanovsky et al. (2008) and MISR and MODIS by Shi et al. (2007).

As it follows from the discussion given above, the screening procedures are of great importance for successful retrievals of snow properties from space.

13.3 Theoretical Description

The current operational detection of clouds in SPOT VGT data relies on spectral threshold tests using the reflectance in the blue and SWIR bands (Lissens et al, 2000). Different threshold combinations are used to identify cloudy and clear pixels. A pixel which does not pass either test is declared uncertain. A snow mask is calculated using spectral threshold tests on the red and MIR channels combined with 3 spectral slope tests which exploit the lower scattering of snow in MIR and SWIR bands compared with clouds. A cloud shadow is finally added based on an estimation of a potential cloud shadow and a test on the NDVI of concerned pixels.

Current MERIS cloud screening uses spectral thresholds on shortwave bands, complemented by spectral slope tests in order to recover bright land surface and snow (Santer, 1997). In the current reprocessing of MERIS these cloud and snow tests are significantly changed and improved (Brockmann and Santer, in preparation) by adding tests on the height of the scattering surface (based on the oxygen absorption measurements in MERIS band 11), and new tests for snow and ice detection using the MERIS Differential Snow Index (MDSI), based on the ratio of bands 13 (865nm) and 14 (885nm).

The AATSR cloud screening is also based primarily on threshold tests (Birks, 2007). The AATSR gross cloud test flags as cloudy those pixels whose brightness temperature in the 12 micron channel falls below a specified threshold. The small-scale spatial coherence test works by calculating the standard deviation of the 11 micron brightness temperature in a 3 x 3 group of pixels and comparing it with a threshold. If the standard deviation exceeds the threshold, the pixels in the group are flagged as cloudy. The Visible Channel Cloud Test can only be used in the daytime. The NDVI (Normalized Differential Vegetation Index) is defined as NDVI = (R87 – R67)/(R87 + R67), where R87 and R67 are the calibrated reflectances in the 0.87 and 0.67 micron channels respectively. Two indices are defined involving the 0.55 micron channel reflectance R55: NDI2 = (R67 – R55)/(R67 + R55). The method uses two of these indices, NDVI and NDI2, to define a two-dimensional classification space. In this space, pixels of different surface types form clusters, and by identifying into which cluster a pixel falls, the surface type at the pixel can be determined. The Snow Index (NDSI) test based uses the bands centred at 0.555 and 1.640 microns respectively, NDSI = (R55 – R16)/(R55 + R16), where R16 is the calibrated reflectivity of the 1.6 micron channel.

Both MERIS and AATSR cloud screening are not optimal because of missing spectral information in each of the single instrument (SWIR and TIR bands in MERIS, O2 and water vapour bands in AATRS). In the framework of the MERIS – AATSR synergy project an algorithm has been developed that combines the data from both instruments (Gomez-Chova, 2009). A thorough analysis has been undertaken on the information content w.r.t to cloud detection in both instruments, and a set of 19 features has been identified as optimal with respect to the number of features (which should be kept low) and information content. These features include the spectral reflectances of the two instruments, and a number of band combinations. The cloud screening

algorithm is a combination of feature extraction and supervised classification and spectral unmixing. The training vectors for the supervised classification have been obtained from a database of radiative transfer calculations. The results of the algorithm are a binary cloud mask resulting from the feature tests and a cloud abundance values (between 0 and 1) from the unmixing. These two values can be used by subsequent algorithms to decide if a pixel can be processed, or a final logic is applied to conclude on the pixel status.

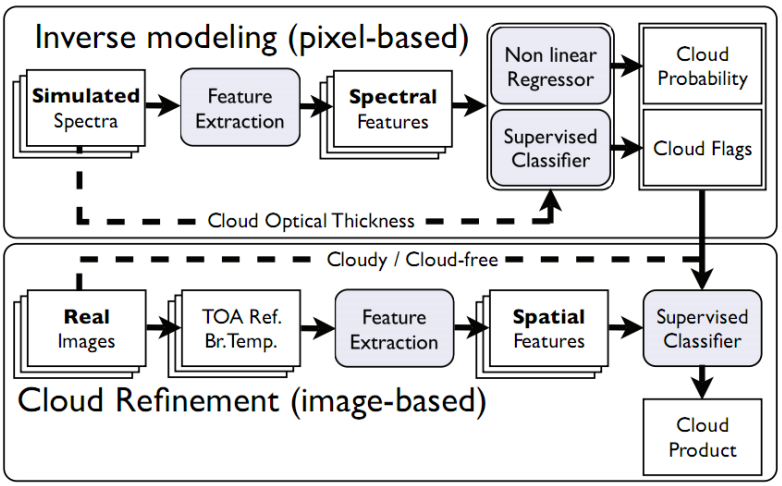

Figure 13-1: Overview of synergistic cloud classification algorithm

A critical step for the synergistic use of MERIS and AATSR is the collocation of the products. Due to the high spatial and temporal dynamic of clouds, misalignment of the two data sets would impact the cloud retrieval. Figure 13-2 shows the steps included in the preprocessing of the data of the two instruments.

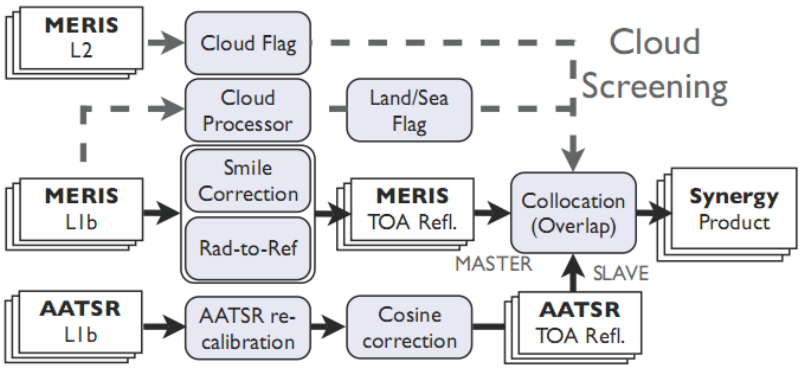

Figure 13-2: Flowchart of the MERIS and AATSR synergy preprocessing module

Neither of the single instrument algorithms discussed in the previous section is considered of sufficient quality for the purpose of the GlobAlbedo project. The MERIS and AATSR cloud screening algorithms have been criticised on the MERIS-AATSR user workshops, and also the SPOT VGT algorithm does not screen out sufficiently the doubtful cloudy pixels. The reason is that

the global Level 2 algorithms cannot be too severe in order to permit analysis of single Level 2 products. On the contrary, for a Level 3 product such as the Albedo, a clear sky conservative (i.e. severe cloud screening) approach is required. Even a small number of undetected clouds can significantly impact the final albedo product. This has been demonstrated in the MERIS Land Albedo and the Globcover projects.

The synergistic method of Gomez-Chova is a significant improvement. It exploits optimally all features available in both instruments and combines these in a non-linear, self trained mathematical way. The comparison shown in the MERIS-AATSR-Synergy Project demonstrates the improvements compared to the standard MERIS and AATSR algorithms.

However, for the Globalbedo a synergistic use of MERIS and AATSR is not possible because of (1) the limitation of AATSR to the center of the MERIS swath, thus not providing data for half of the MERIS swath and (2) the overall design of the processing architecture which does not foresee multi-sensor processing at this stage. The latter point could of course be resolved, however, point (1) still remains valid.

In conclusion the Globalbedo pixel classification will be a unique method, adapting the principles and mathematical implementation of the Gomez-Chova approach, but tailored to the features provided by the three instruments, each treated separately.

In a first step the features will be combined in a logical order of a sequence of threshold tests, but working on and resulting in probability values between [0 … 1]. The combination will be done by arithmetic operations, addition and multiplication. This extends the Boolean logic into a probabilistic space. If tests result in the extreme 0 and 1, the probabilistic calculations are identical with the Boolean expressions.

In a later step, when a large number of products are available from the Globalbedo project and processed with the first version of the pixel identification processor, the data can be used to collect a large number of clear and cloudy pixel, in order to implement the self-learning classifiers on the features, as described by Gomez-Chova.

13.4

13.5 Practical considerations

13.5.1 Overall Principles

The GA pixel identification is a unique classification for all three instruments considered:

- ENVISAT MERIS
- ENVISAT AATSR
- SPOT Vegetation

The uniqueness consists of a certain set of features, which are calculated for each instrument and probabilistic combination of these features in order to calculate a set of pixel classification attributes. The implementation how the features are calculated is instrument specific.

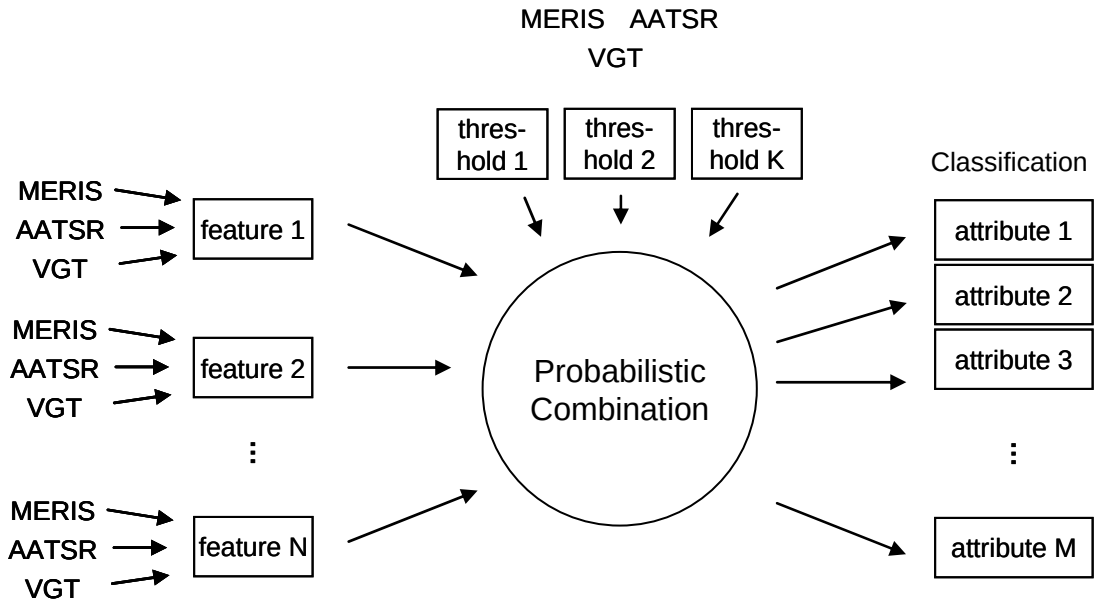

Figure 13-3: Unified Pixel Classification Scheme

13.5.2 Probabilistic Arithmetic

A feature is a probabilistic quantity with a value between 0 and 1, with the following meaning:

Value	Meaning
0	the feature is definitively not true
0.5	status of the feature not known
1	feature is definitively true

Table 13-1: Definition of values for classification features.

Features are combined by simple arithmetic averaging. Let's assume, as an example, two features, f1 and f2, which do have no dependency from each other, and both being an indication that a third feature, f3, is true. Then, f3 is the average of f1 and f2:

f3 = (f1 + f2) / 2

As a first example let's assume the case where we are 100% sure that both f1 and f2 are true, i.e. f1=f2=1.0 then also f3=1.0. Another example is when we are 100% about f1, but less sure about f2, let's say f2= 0.8. Then the resulting probability of f3 is f3=0.9. When don't know anything about f1, i.e. f1=0.5 but are sure that f2 is false, i.e. f2=0, then f3=0.25, i.e. quite likely that it is false. If f1=0 and f2=1, i.e. a contradiction, then f3=0.5, i.e. we can't say if it is true or false.

The introduction of the probability scale [0 … 1] has further the advantage that it enable decoupling of feature values from the instruments. It doesn't matter how a physical quantity is derived because it will be mapped to the interval [0 … 1]. For example, the brightness feature will be calculated from top of atmosphere radiances in the case of MERIS, whereas it will be calculated from reflectances in the case of VGT. These are different physical quantities, but they are both scaled to [0 … 1].

The scaling from a physical quantity, such as radiance or temperature, to a probability value may include a non-linear mapping. This can express the (un-)certainty that we have in value ranges in the physical data space. For example, very low temperatures have a very high probability to be a cloud, whereas above a certain temperature value the probability decreases exponentially.

Not every feature can be calculated for every instrument. In such cases the feature value is constant equal to 0.5. This convention allow to formulate the logical combination of features even if a feature is not available for a certain instrument, and hence the logical combination can be formulated instrument independently.

13.5.3 Features

The following features are used in the probabilistic combination, and how they are calculated from each instrument.

Feature	**Explanation**
Pressure	Indicating a high altitude from where the photons are scattered. Can be derived from measurements in gasous absorption bands, e.g. O2A or water vapour
NDVI	A high vegetation index is an indication of a (semi-) transparent atmosphere
NDSI	The NDSI is a meaningful quantity only above bright surfaces. Then it can be used to separate snow/ice from clouds
White	A bright and spectrally flat signal; can be a cloud or snow/ice
Spectral Flatness	A spectrally flat signal; The colour can be anything from black over grey to white.
Temperature	Temperature of the emitting surface; clouds can be very cold.

Bright	Brightness of the scattering surface
Glint Risk	The glint risk can be calculated from the observation geometry and wind speed, assuming a certain wave distribution (e.g. Cox and Munk). Glint and clouds are hardly separable and hence it is useful to identify glint risk in addition with the cloud/water classification.
Radiometric Land Value	A classification of the surface type as land, provided that the pixel is clear and the measurement can be used to assess the surface type.
Radiometric Water Value	A classification of the surface type as water, provided that the pixel is clear and the measurement can be used to assess the surface type.
A priori Land Value	Classification of the pixel using a static background map and the geolocation of the pixel.
A priori Water Value	Classification of the pixel using a static background map and the geolocation of the pixel.

13.5.3.1 Feature Definition for MERIS

The index used in array notation below is starting with 0.

Feature	**MERIS**	**Comment**

Pressure	`if (isLand()) {`
	`  press_value = (pbaro - p1)/1000.0;`
	`} else if (isWater()) {`
	`  press_value =(pbaro - pscatt)/1000.0;`
	`}`
		p1 and pscatt are apparent pressure products, defined in dedicated ATBDs from R. Santer, developed within the ESA O2 project. pbaro is the barometric pressure.

NDVI	`ndvi_value =` `(brr[b753]-brr[b620])/ (brr[b753]+brr[b620]`	brr is the reflectance corrected for gaseous absorption and Rayleigh scattering
NDSI	`ndsi_value =` `brr[b865]-brr[b885]) / (brr[b865]+brr[b885]`	
White	`if (brightValue()>BRIGHT_FOR_WHITE_THRESH) {`	

	white_value=spectralFlatnessValue();
	} else {
	white_value = 0;
	}	

Spectral Flatness	slope0 = spectralSlope(refl[490], refl[412]) slope1 = spectralSlope(refl[560], refl[620]) slope2 = spectralSlope(refl[665], refl[753]) spectralFlatness = 1.0f - Math.abs(1000.0 * (slope0 + slope1 + slope2) / 3.0);	
Temperature	0.5	
Bright	bright_value = brr[b442] /(6.0 * brr442Thresh)	brr442Thresh is a value read from a LUT; the LUT is a theoretical maximal reflectance for a given geometry and a bright land surface. It has been calculated by R. Santer and is available from the auxiliary data of the MERIS operational processor.
Glint Risk	Shall be calculated from geometry and wind speed from tie points. Not available in current IDEPIX version	currently set to FALSE

Radiometric Land Value	if {
	refl[b753] >= refl[620] && refl[620] > refl620_Land_Thresh
	}
	radiom_land_value = 1.0
	} else {
		in case of cloudy pixel: radiom_land_value = 0.5

	`radiom_land_value = 0.5` `}`	

Radiometric Water Value	`if {`
	`refl[b753] < refl[620] && refl[620] < refl620_Land_Thresh`
	`}`
	`radiom_water_value = 1.0`
	`} else {`
	`value = 0.5`
	`}`
		in case of cloudy pixel: `radiom_water_value = 0.5`

A priori Land Value	`if (l1FlagLand) {`
	`return 1.0f;`
	`} else {`
	`return 0.0f;`
	`}`	

A priori Water Value	`if (!l1FlagLand) {`
	`return 1.0f;`
	`} else {`
	`return 0.0f;`
	`}`	

13.5.3.2 Feature Definition for AATSR

All measurements are taken from the nadir observation.

Feature	AATSR	Comment
Pressure	`0.5`	
NDVI	`ndvi_value =` `(refl[b870]-refl[b670])/(refl[b870]+refl[b670])`	
NDSI	`ndsi_value =` `(refl[b870]-refl[b1600])/(refl[b870]+refl[b1600]`	

White	`if (brightValue()>BRIGHT_FOR_WHITE_THRESH) {`
	`  return spectralFlatnessValue();`
	`} else {`
	`  return 0f;`
	`}`	

Spectral Flatness	`slope0 = spectalSlope(refl[b555], refl[b670])`
	`slope1 = spectalSlope(refl[b670], refl[b870])`
	
	`spectralFlatness = 1.0f - Math.abs(10.0 * (slope0 + slope1));`	

Temperature	`temperature_value = bt[btemp1200]`	
Bright	`bright_value = (refl[b555] + refl[b670] + refl[b870])/3`	
Glint Risk	`0.5`	
Radiometric Land Value	`0.5`	
Radiometric Water Value	`0.5`	

A priori Land Value	`if (l1FlagLand) {`
	`  return 1.0f;`
	`} else {`
	`  return 0.0f;`
	`}`	

A priori Water Value	`if (!l1FlagLand) {`
	`  return 1.0f;`
	`} else {`
	`  return 0.0f;`
	`}`	

13.5.3.3 Feature Definition for VGT

refl[0] … reflectance in band 0 at 450nm

refl[1] … reflectance in band 2 at 645nm

refl[2] … reflectance in band 3 at 835nm

refl[3] … reflectance in band MIR at 1.6nm

Feature	VGT	Comment
Pressure	`0.5`	
NDVI	`ndvi_value = (refl[2] - refl[1])/ (refl[2] + refl[1]`	
NDSI	`ndsi_value = refl[2] - refl[3])/ (refl[2] + refl[3])`	
White	`if (brightValue()>BRIGHT_FOR_WHITE_THRESH) { return spectralFlatnessValue(); } else { return 0f; }`	The spectral flatness gives a high value even if the spectrum is black. In order to be an indicator for white, a minimum brightness is required.
Spectral Flatness	`slope0 = spectralSlope(refl[0], refl[1]) slope1 = spectralSlope(refl[1], refl[2]) spectralFlatness = 1.0f - Math.abs(1000.0 * (slope0 + slope1));`	
Temperature	`0.5`	
Bright	`if (isLand()) { return (refl[0] + refl[1])/2.0f; } else if (isWater()) { return (refl[1] + refl[2]); } else {`	

	`return (refl[0] + refl[1])/2.0f;` `}`	
Glint Risk	`isWater() && isCloud() &&` `spectralSlope(refl[0], refl[1], 450, 645) > GLINT_THRESH)`	

Radiometric Land Value	`if (refl[2] > refl[1] &&`
	`refl[2] > REFL835_LAND_THRESH) {`
	`radiom_land_value = 1.0;`
	`} else if (`
	`refl[2] > REFL835_LAND_THRESH) {`
	`radiom_land_value = 0.75f;`
	`} else {`
	`radiom_land_value = 0.25;`
	`}`
		in case of cloudy pixel: radiom_land_value = 0.5

Radiometric Water Value	`if (refl[0] > refl[1] &&`
	`refl[1] > refl[2] &&`
	`refl[2]<REFL835_WATER_THRESH) {`
	`value=1.0;`
	`} else {`
	`value = 0.25;`
	`}`
		in case of cloudy pixel: radiom_water_value = 0.5

A priori Land Value	`if (smLand) {`
	`return 1.0f;`
	`} else {`
	`return 0.0f;`
	`}`	

A priori Water Value	`if (!smLand) {`
	`return 1.0f;`
	`} else {`
	`return 0.0f;`
	`}`	

13.5.4 Processing Logic

The following classification attributes (binary values, also named flags) are derived from the features with given logic. This logic is no longer instrument dependent.

Classification attribute	Definition	Comment
isCloud	`return (whiteValue() + brightValue() + pressureValue() + temperatureValue() > CLOUD_THRESH && !isClearSnow())`	The final binary cloud flag. A pixel is either Cloud, ClearLand or ClearWater.or ClearSnow

isClearLand	`if (radiometricLandValue() != 0.5) {`
	`  landValue = radiometricLandValue();`
	`} else if (aPrioriLandValue() > 0.5) {`
	`  landValue = aPrioriLandValue();`
	`} else {`
	`  return false;`
	
	`// this means: if we have no information about land, we return isClearLand = false`
	
	`}`
	`return (!isCloud() && landValue > LAND_THRESH)`
		If a radiometric land value is available, i.e. it is not the uncertainty value of 0.5, than this is used in the subsequent test. Otherwsise the a priori land value is used in the test.
		The test simply compares the value with a threshold. The choice of the threshold depends on the user. If he wants to be really sure he should use a value close to 1.

isClearWater	`if (radiometricWaterValue() !=0.5) {`
	`  waterValue = radiometricWaterValue();`
	`} else if (aPrioriWaterValue() > 0.5) {`
	`  waterValue = aPrioriWaterValue();`
	`} else {`
		same logic as for the ClearLand test

	`return false;`
	
	`// this means: if we have no information about water, we return isClearWater = false`
	
	`}`
	`return (!isCloud() && waterValue > WATER_THRESH);`	

isClearSnow	`return (isBrightWhite() && ndsiValue() > NDSI_THRESH)`	isBrightWhite is defined below
isBrightWhite	`return (whiteValue() + brightValue() > BRIGHTWHITE_THRESH)`	A pixel that has one of the two characteristics, bright or white, has a potential to be cloudy. The stronger both features are the higher the probability.
isLand	`return (aPrioriLandValue() > LAND_THRESH)`	This is the surface type of the pixel, regardless if it is snow covered or if a cloud is above during measurement.
isWater	`return (aPrioriWaterValue() > WATER_THRESH)`	
isBright	`return (brightValue() > BRIGHT_THRESH)`	These tests map the real values of the features to binary flags
isWhite	`return (whiteValue() > WHITE_THRESH)`	
isCold	`return (temperatureValue > TEMPERATURE_THRESH)`	
isVegRisk	`return (ndviValue() > NDVI_THRESH)`	
isGlintRisk	`return (glintRiskValue > GLINT_RISK_THRESH)`	
isHigh	`return (pressureValue() > PRESSURE_THRESH)`	

13.5.5 Thresholds

The following table lists the nominal values for the scalar thresholds which are being used in the current version of Idepix, and which may be sensor-dependent. It should be noted that these values are subject to tuning in future Idepix versions, depending on potential improvements of the feature definitions which may result from more advanced validation schemes or new validation resources.

Threshold	**Value**		
	MERIS	**AATSR**	**VGT**
BRIGHTWHITE_THRESH	1.5	0.65	0.65
NDSI_THRESH	0.68	0.5	0.5
PRESSURE_THRESH	0.9	0.9	0.9
CLOUD_THRESH	1.65	1.3	1.65
UNCERTAINTY_VALUE	0.5;	0.5	0.5
LAND_THRESH	0.9	0.9	0.9
WATER_THRESH	0.9	0.9	0.9
BRIGHT_THRESH	0.25	0.2	0.3
WHITE_THRESH	0.9	0.9	0.5
BRIGHT_FOR_WHITE_THRESH	0.4	0.2	0.2
NDVI_THRESH	0.7	0.4	0.4
TEMPERATURE_THRESH	0.9	0.6	0.9
REFL835_LAND_THRESH	n.a	n.a	0.15
REFL835_WATER_THRESH	n.a	n.a	0.1
GLINT_THRESH	n.a	n.a.	0.000365

14 Error budget estimates

The errors of the classification classes are automatically calculated by the probabilistic arithmetic.

15 Assumptions and Limitations

None.

16 References

Ackerman, S., K. Strabala, P. Menzel, R. Frey, C. Moeller, L. Gumley, B. Baum, S. WetzelSeemann, and H. Zhang: Discriminating clear sky from cloud with MODIS algorithm theoretical basis document (MOD35), at http://modis.gsfc.nasa.gov/data/atbd/atbd_mod06.pdf, 2006.

Albert, M.R., Shuman, C., Courville, Z., Bauer, R., Fahnestock, M., and Scambos, T.: Extreme Firn Metamorphism: Impact of Decades of Vapor Transport on Near-Surface Firn at a Low-Accumulation Glazed Site on the East Antarctic Plateau. Annals Glaciol., 39, 73-78, 2004.

Alley, R.B., and Koci B.R.: Ice-core analysis at site A, Greenland : preliminary results. Annals Glaciol. 10, 1-4, 1988.

Alley, R.B., Saltzman, E.S., Cuffey, K.M. and Fitzpatrick, J.J., Summertime formation of depth hoar in central Greenland. Geophys. Res. Lett, 17, 2393-2396,1990.

Aoki, T., Aoki, T., Fukabori, M., Hachikubo, A., Tachibana, Y. and Nishio, F., Effects of snow physical parameters on spectral albedo and bidirectional reflectance of snow surface. J. Geophys. Res., 105D, 10219-10236, 2000.

Aoki, T., M. Hori, H. Motoyoshi, et al., ADEOS-II/GLI snow/ice products — Part II: Validation results using GLI and MODIS data. Remote Sensing Environ., 111, 274-290, 2007.

Baret, F, et al, LAI, fAPAR and fCover CYCLOPES global products derived from VEGETATION Part 1: Principles of the algorithm. Remote Sensing of Environment, Volume 110, Issue 3, 15 October 2007, Pages 275-286, 2007.

Birks et al, Improvements to the AATSR IPF relating to Land Surface Temperature Retrieval and Cloud Clearing over Land, RUTHERFORD APPLETON LABORATORY, 2007.

Bohren, C. F., and Barkstrom, B. R., Theory of the optical properties of snow, J. Geophys. Res., 79, 4527-4535, 1974.

Bohren, C. F., and Beschta, R. L., Snowpack albedo and snow density, Cold Regions Sci. Technol., 1, 47-50, 1979.

Bourdelles, B., and Fily, M., Snow grain-size determination from Landsat imagery over Terre Adelie, Antarctica, Annals Glaciol., 17, 86–92, 1993.

Brenguier, J.-L., H. Pawlowska, L. Schüller, R. Preusker, J. Fischer and Y. Fouquart, Radiative properties of boundary layer clouds: droplet effective radius versus droplet concentration. J. Atmos. Sci., 57, 803-821, 2000.

Brockmann et al, Cloud Screening Algorithms, MERIS - AATSR Workshop, 2008. ESRIN, Frascati, Italy; Workshop Proceedings, 2008.

Brunauer, S., Emmet, P.H. and Teller, E.: Adsorption of gases in multimolecular layers. J. Am. Chem. Soc. 60, 309-319, 1938.

Cervino et al, Cloud fraction within GOME footprint using a refined cloud clearing algorithm, Adv. SpaceRes. Vol. 25, No. 5, pp. 993-996, 2000.

Chandrasekhar, S., Radiative transfer, NY: Dover, 1960.

Colapicchioni et al, Information Mining in Remote Sensing Image - The KIM, KES and KIMV projects, ESA ESRIN Publication, 2004.

Colbeck, S.C., An overview of seasonal snow metamorphism, Rev. Geophys. Space Phys. 20, 45-61, 1982.

Colbeck, S.C., Theory of metamorphism of dry snow, J. Geophys. Res. 88, 5475-5482, 1983.

Colbeck, S.C., The layered character of snow covers, Rev. Geophys. 29, 81-96, 1991.

D'Elia et al, Image Information Mining for Earth Observation at ESA, ESA ESRIN Publication, 2004.

Domine, F., Taillandier, A.-S. and Simpson W.R., A parameterization of the specific surface area of snow in models of snowpack evolution, based on 345 measurements. J. Geophys. Res., 112, F02031, doi:10.1029/2006JF000512, 2007.

Domine, F., Salvatori, R., L. Legagneux, L., Salzano, R., Fily M. and R. Casacchia R., Correlation between the specific surface area and the short wave infrared (SWIR) reflectance of

snow: preliminary investigation. Cold Regions Sci. Technol., *6,* 60-68, doi:10.1016/j.coldregions.2006.06.002, 2006.

Domine F.,M. Albert, T. Huthwelker, H.-W. Jacobi, A. A. Kokhanovsky, M. Lehning, G. Picard, W. R. Simpson, Snow physics as relevant to snow photochemistry, *Atmos. Chem. Physics Discussions*, 7, 1-96, 2008.

Domingue, D., et al.,The scattering properties of natural terrestrial snows versus icy satellite surfaces, Icarus, 128, 28-48, 1997.

Dozier, J., and S. G. Warren, Effect of viewing angle on the thermal infrared brightness temperature of snow, *Water Resour. Res.*, 18, 1424-1434, 1982.

Dozier, J., and Painter, T. H., Multispectral and hyperspectral remote sensing of alpine snow properties. Annual Review of Earth and Planetary Sciences 32, 465-494, 2004.

Eumetsat, Final Report for the Study on Visual Scenes Analysis of AVHRR Data, Issue 2, 16. January 2006.

Eumetsat, Summary Report of the SAF Hydrology Framework Working Group http://www.eumetsat.int/groups/pps/documents/assets/pdf_saf_hsfwg_summaryreport.pdf, 2004

Eumetsat, Land Surface Analysis Satellite Application Facility, Snow Cover product, http://landsaf.meteo.pt/algorithms.jsp;jsessionid=4745E8FF3EBC82A5D6C69D5FE6838E99?seltab=4, 2008

Euroclim Website, Euroclim Website http://www.euroclim.net/, 2008

European Space Agency, Statement of work Globice, EOP-DUEP-EOPS-SW-04-0006 http://dup.esrin.esa.it/files/document/192-171-5-19_200483011918.pdf, 2004

European Space Agency, Statement of work GlobGlacier, EOEP-DUEP-EOPG-SW-06-0005, http://dup.esrin.esa.it/files/document/131-176-149-30_200828162037.pdf, 2006

European Space Agency, STATEMENT OF WORK GLOBSNOW, EOEP-DUEP-EOPS-SW-08-0006, http://dup.esrin.esa.int/STSE/files/document/131-176-149-30_200865103541.pdf, 2008

Fily, M., Bourdelles, B., Dedieu J.P., and Sergent, C., Comparison of in situ and Landsat Thematic Mapper derived snow grain characteristics in the Alps, Remote Sensing Environ., 59, 452–460, 1997.

Fischer, J. et al, MERIS ESL Cloud Cloud Top Pressure ATBD. http://envisat.esa.int/instruments/meris/pdf/atbd_2_03.pdf, 2000a.

Fischer, J. et al, MERIS ESL Cloud Albedo and Cloud Optical Thickness ATBD. http://envisat.esa.int/instruments/meris/pdf/atbd_2_01.pdf, 2000b.

Flanner, M. G.; Zender, C. S.; Randerson, J. T.; Rasch, Philip J., Present-day climate forcing and response from black carbon in snow. J. Geophys. Res., 112, D11202, .doi:10.1029/2006JD008003, 2007.

Flanner, M.G. and Zender, C.S., Linking snowpack microphysics and albedo evolution. J. Geophys. Res. 111, D12208. doi:10.1029/2005JD006834, 2006.

Garant L., and Weinman J. A., A structural stochastic model for the analysis and synthesis of cloud images. J. Clim. Appl. Meteorol. 25, 1052-1068, 1986.

Garret, T. J., P. V. Hobbs, H. Gerber, Shortwave, single scattering properties of arctic ice clouds, J. Geophys. Res., 106, D14, 15,555-15,172, 2001.

GCOS home page, http://www.wmo.int/pages/prog/gcos/index.php?name=about

Globsnow user consultation meeting, presentations, http://dup.esrin.esa.int/news/news152.asp, 2008

Gomez-Chova et al, Cloud-Screening Algorithm for ENVISATMERIS Multispectral Images, IEEE TRANSACTIONS ON GEOSCIENCE AND REMOTE SENSING, VOL. 45, NO. 12, December 2007

Goodman et al, Cloud Detection and Analysis A Review of Recent Progress, Atmospheric Research, 21 (1988) 203-228, 1988.

Grenfell, T. C., Perovich, D. K., and Ogren J. A., Spectral albedos of an alpine snowpack, Cold Regions Sci. Technol., 4, 121-127, 1981.

Grenfell, T. C., Warren, S. G., and Mullen, P. C., Reflection of solar radiation by the Antarctic snow surface at ultraviolet, visible, and near-infrared wavelengths, J. Geophys. Res., 99, 18669-18, 684, 1994.

Hall, D.K., Riggs G.A. and Salomonson, V.V. , Development of methods for mapping global snow cover using Moderate Resolution Imaging Spectroradiometer (MODIS) data Remote Sensing of Environment, vol. 54, pp. 127-140, 1995.

Hall D.K., Riggs, G. A. and Salomonson, V., Algorithm Theoretical Basis Document (ATBD) for the MODIS Snow and Sea Ice-Mapping Algorithms, available at http://modis.gsfc.nasa.gov/data/atbd/atbd_mod10.pdf, 2001.

Hapke, B., Theory of Reflectance and Emittance Spectroscopy (Topics in Remote Sensing), Cambridge: Cambridge University Press, 1993.

Hori, M., et al: In situ measured spectral directional emissivity of snow and ice in the 8-14 μm atmospheric windiow, Remote Sens. Of Env., 100, 486-502., 2006

Hori, M., T. Aoki, K. Stamnes, W. Li, ADEOS-II/GLI snow/ice products — Part III: Retrieved results, Remote Sensing of Environment, 111, 291-336, 2007.

Hudson S. R., S. G. Warren, R. E. Brandt, T. C. Grenfell, D. Six, Spectral bidirectional reflectance of Antarctic snow: Measurements and parameterization, J. Geophys. Res., 111, D18106, doi:10.1029/2006JD007290, 2006.

IGOS, Concept of an IGOS-Cryosphere Theme(IGOS-Cryo), http://www.igospartners.org/docs/theme_reports/IGOS_Cryo_theme_item7.2.pdf , 2005

IGOS home page, http://www.igospartners.org/over.htm, 2008

Kerbrat, M., Pinzer, B., Huthwelker, T., Gäggeler, H. W., Ammann, M., and Schneebeli M.: Measuring the specific surface area of snow with X-ray tomography and gas adsorption: comparison and implications for surface smoothness. Atmos. Chem. Phys. Disc., 7, 10287-10322, 2007.

King J.C., M.J. Varley, T.A. Lachlan-Cope,Using satellite thermal infrared imagery to study boundary layer structure in an Antarctic katabatic wind region. Int. J. Remote Sens. :3335–48, 1998.

King M.D. and Simpson, W.R., Extinction of UV radiation in Arctic snow at Alert, Canada (82° N), J. Geophys. Res., 106 (D12), 12499-12508, 2001.

Klein, A.G. Hall D.K. and Riggs G.A.,. Improving the MODIS global snow-mapping algorithm." Proceedings of the International Geoscience and Remote Sensing Symposium (IGARSS 1997), 4-8 August 1997, Singapore, pp. 619-621, 1997

Koendrink, J. J. and W.A. Richards, 1992: Why snow is so bright, JOSA, A5, 643-648.

Kokhanovsky, A. A., and E. P. Zege, Scattering optics of snow, Appl. Optics, 43, 1589-1602, 2004.

Kokhanovsky, A. A., T. Aoki, A. Hachikubo, M. Hori, E. P. Zege, Reflective properties of natural snow: approximate asymptotic theory versus in situ measurements, IEEE Trans. Geosci. Rem. Sens., 43, 1529-1535, 2004.

Kokhanovsky, A. A., and T. Nauss, Satellite based retrieval of ice cloud properties using semianalytical algorithm, J. Geophys. Res., D110, D19206, doi: 10.1029/2004JD005744, 2005.

Kokhanovsky, A. A., On remote sensing of optically thick ice clouds, Optical Engineering, 45(4), 046201, 2006a.

Kokhanovsky, A. A., Cloud Optics, Dordrecht: Springer, 2006b.

Kokhanovsky, A. A., Scaling constant and its determination from simultaneous measurements of light reflection and methane adsorption by snow samples, Opt. Letters, 31, 3282-3284, 2006c.

Kokhanovsky et al, The determination of the cloud fraction in the fraction in the sciamachy pixels using MERIS, MERIS - AATSR Workshop, 2008. ESRIN, Frascati, Italy; Workshop, 2008.

Kottek, M., J. Grieser, C. Beck, B. Rudolf, and F. Rubel, World Map of the Köppen-Geiger climate classification updated. Meteorol. Z., 15, 259-263. DOI: 10.1127/0941-2948/2006/0130, 2006.

Lavanant et al, A global Cloud detection scheme for high spectral resolution instrument, ITSC14 Conference presentation, 2005.

Legagneux, L., Cabanes, A., and Domine, F., Measurement of the specific surface area of 176 snow samples using methane adsorption at 77 K, J.Geophys.Res. 107 (D17), 4335, doi: 10.1029/2001JD001016, 2002.

Legagneux, L. Lauzier, T., Dominé, F., Kuhs, W.F., Heinrichs, T., and Techmer, K., Rate of decay of the specific surface area of snow during isothermal experiments and morphological changes studied by scanning electron microscopy. Can. J. Phys. 81, 459-468, 2003.

Lenoble, J., Radiative Transfer in Scattering and Absorbing Atmospheres: Standard Computational Procedures, Deepak, Hampton, 1985.

Li, W., Stamnes, K., Chen, B., and Xiong, X., Snow grain size retrieved from near-infrared radiances at multiple wavelengths, Geophys. Res. Let., 28, 1699-1702, doi: 10.1029/2000GL011641, 2001.

Libbrecht, K. G., The physics of snow crystals. Rep. Prog. Phys., 68, 855-895, 2005.

Liou, K.N., Radiation and Cloud Processes in the Atmosphere. Oxford University Press, Oxford, 487pp., 1992.

Luo et al, Developing clear-sky cloud and cloud shadow mask for producing clear-sky composites, Remote Sensing of Environment 2008; in press, 2008.

Macke, A., Mueller, J. and Raschke, E., Single scattering properties of atmospheric ice crystals. J. Atmos. Sci. 53, pp. 2813–2825, 1996.

Matzl, M., and Schneebeli, M.: Measuring specific surface area of snow by near-infrared photography, J. Glaciol., 52, 558-564, 2006.

McNally et al, A cloud detection algorithm for high-spectral-resolution infrared sounders, Q. J. R. Meteorol. Soc. (2003), 129, pp. 3411–3423, 2003.

Merchant et al, Probabilistic physically based cloud screening of satellite infrared imagery for operational sea surface temperature retrievalMerchant 2006 SEA SURFACE TEMPERATURE FOR CLIMATE FROM THE ATSRS,Q. J. R. Meteorol. Soc. (2005), 131, pp. 2735–2755, 2005.

Merchant et al, SEA SURFACE TEMPERATURE FOR CLIMATE FROM THE ATSRS,ESA publication, 2006.

Metsämäki, S.J., Anttila, S.T., Markus, H.J. and Vepsäläinen, J., A feasible method for fractional snow cover mapping in boreal zone based on a reflectance model.Remote Sensing of Envi-ronment, 95, 2005, pp. 77-95, 2005.

Middleton, W. E. K. and A. G. Mungall, The luminous directional reflectance of snow, JOSA, 42, 572-579, 1952.

Mishchenko, M. I., Dlugach, J. M., Yanovitskij, E. G., Zakharova N. T., Bidirectional reflectance of flat, optically thick particulate layers : an efficient radiative transfer solution and applications to snow and soil surfaces, J. Quant. Spectrosc. Radiat. Transfer, 63, 409-432, 1999.

Muller, J.-P. and J. Fischer, The EU-CLOUDMAP project: Cirrus and contrail cloud-top maps from satellites for weather forecasting climate change analysis. Int. J. Remote Sensing, 28, 1915–1919, 2007.

Narita, H.: Specific surface of deposited snow II, Low Temp. Sci. A29, 69-81, 1971.

Neshyba, S., Grenfell, T. C., and Warren, S. G.: Representation of a nonspherical ice particle by a collection of independent spheres for scattering and absorption of radiation: II. Hexagonal columns and plates, J. Geophys. Res., 108, 4448, 2003.

Nolin, A. W., and Dozier, J., A hyperspectral method for remotely sensing the grain size of snow. Remote Sensing Environ., 74, 207– 216, 2000.

Nolin, A. W., and S. Liang: Progress in bidirectional reflectance modeling and applications for surface particulate media: snow and soils, Remote Sens. Rev., 18, 307-342, 2000

Nolin, A.W. and Dozier, J., Estimating snow grain size using AVIRIS data. Remote Sensing Environ., 44, 231–238, 1993.

Painter, T.H., Roberts, D.A., Green, R.O. and Dozier, J. ,The effect of grain size on spectral mix-ture analysis of snow-covered area from AVIRIS data. Remote Sensing of Environ., 65, pp. 320-332, 1998

Painter, T. H., Dozier, J., Roberts, D. A., Davis, R.E., and Greene, R.O.: Retrieval of subpixel snow-covered area and grain size from imaging spectrometer data, Remote Sensing of Environment, 85, 64–77, 2003

Painter, T.H., and J. Dozier, Measurements of the hemispherical – directional reflectance of snow at fine spectral and angular resolutions, J. Geophys. Res., 109, doi: 10.1029/2003JD004458, 2004.

Painter T. H., Barrett, A. P., Landry, C. C., Neff, J. C., Cassidy, M. P., Lawrence, C. R., McBride, K. E., Farmer G. L., Impact of disturbed desert soils on duration of mountain snow cover, Geophys. Res. Lett., 34, L12502, doi:10.1029/2007GL030284, 2007.

Paperin, M., Brockmann, C., 2007: ENVISAT Symposium Montreux (CH), 23-27 April 2007, Conference Proceedings 3P5.8: Atmospheric Properties from Optical/Infrared, Cloud Structures

Pawlowska, H., J.-L. Brenguier, Y. Fouquart, W. Armbruster, S. Bakan, J. Descloitres, J. Fischer, A. Fouilloux, J.-F. Gayet, S. Ghosh, P. Jonas, F. Parol, J. Pelon, L. Schüller, Microphysics/ radiation interaction in a stratocumulus cloud: The EUCREX mission 206 case study. Atmos. Res., 55, 85-102, 2000.

Perla, R., Dozier, J., and Davis, R.E.: Preparation of serial sections in dry snow specimens. J. Microsc. 141, 111-114, 1986.

Phulpin T., Derrien M., and Brard A., A two dimensional histogram procedure to analyse cloud cover from NOAA satellite high resolution imagery. *J. Clim. Appl. Meteorol.* 22, 1332-1345, 1983.

Plummer et al, The GLOBCARBON Cloud Detection System for the Along-Track Scanning Radiometer (ATSR) Sensor Series, IEEE TRANSACTIONS ON GEOSCIENCE AND REMOTE SENSING, VOL. 46, NO. 6, JUNE 2008

Polar View, Service Description: http://www.polarview.org/services/index.htm, 2008

Preusker, R., Hühnerbein, A., Fischer, J., 2006, MERIS Global Land Surfce Albedo Maps, ATBD Cloud Detection. http://www.brockmann-consult.de/albedomap/pdf/MERIS-AlbedoMap-ATBD-CloudDetection1.0.pdf

Prodex, Norway: EuroCryoClim Pilot Project Technical Proposal, http://portal.opengeospatial.org/files/?artifact_id=30103, 2007

Rathke et al, Evaluation of four approximate methods for calculating infrared radiances in cloudy atmospheres, Journal of Quantitative Spectroscopy & Radiative Transfer 75 (2002) 297–321, 2002.

Rathke, C., J. Fischer, S. Neshyba, und M. Shupe, Improving IR cloud phase determination with 20 microns spectral observations, Geophys. Res. Lett., 29 (8), 2002.

Rossow, W.B., and Schiffer, R.A., Advances in Understanding Clouds from ISCCP. Bull. Amer. Meteor. Soc., 80, 2261-2288, 1999.

Sailsbury, J.W., D. M. D'Aria, A. Wald, Measurements of thermal infrared spectral reflectance of frost, snow, and ice, *J. Geophys. Res.*, 99, 24235-24240, 1994.

Salomonson, V.V. and Appel, I. ,Estimating fractional snow cover from MODIS using the normalized difference snow index." Remote Sensing of Environment, Vol. 89, 2004, pp. 351-360, 2004.

Santer, R. et al, MERIS ATBD Pixel identification, http://envisat.esa.int/instruments/meris/pdf/atbd_2_17.pdf, 1997.

Saunders R.W., and Kriebel K.T., An improved method for detecting clear sky and cloudy radiances from AVHRR data.*Int. J. Rem. Sens.* 9: 123-150, (1988)..

Schaaf, C. B., , et al., First operational BRDF, albedo and nadir reflectance products from MODIS, Remote Sens. Env., 83, 135– 148., 2002.

Schiller et al, A METHOD FOR DETECTION AND CLASSIFICATION OF CLOUDS OVER WATER, MERIS - AATSR Workshop, 2008. ESRIN, Frascati, Italy; Workshop Proceedings, 2008.

Shi et al, Detection of daytime arctic clouds using MISR and MODIS, Remote Sensing of Environment 107 (2007) 172–184, 2007.

Simpson et al, Improved cloud detection for daytime AVHRR scenes over land, 1996.

Simpson et al, Improved Cloud Detection in Along Track Scanning Radiometer Data over the Ocean, REMOTE SENS. ENVIRON. 65:1–24, 1998.

Snyder, W.C., Z. Wan, Y. Zhang, Y.Z. Feng, Classification-based emissivity for land surface temperature measurement from space. Int. J. Remote Sens. :2753–74, 1998.

Solberg, Euroclim presentation at GlobSnow User Consultation meeting, http://dup.esrin.esa.int/Files/News/2_Solberg.pdf , Bern, 14.02.2008

Stamnes, K., Tsay, S. C., Wiscombe, W., and Jayaweera K., Numerically stable algorithm for discrete-ordinate method radiative transfer in multiple scattering and emitting layered media, Appl. Optics, 27, 2502-2510, 1988.

Stamnes, K., et al., 2007: ADEOS-II/GLI snow/ice products — Part I: Scientific basis, Remote Sensing of Environment, 111, 258-273.

Steffen, K., Bidirectional reflectance of snow at 500-600nm. In large Scale Effects of Seasonal Snow Cover, ed. by B. Goodison, R. G. Barry, J. Dozier, 436pp. IAHS Publication Series, 166: 415-425, 1987.

Stroeve, J.C., K. K. Steffen, Variability of AVHRR-derived clear-sky surface temperature over the Greenland ice sheet. J. Appl. Meteorol. 37:23–31, 1998

Stroeve et al.,Accuracy assessment of the MODIS 16-day albedo product for snow: comparisons with Greenland in situ measurements, Remote Sens. Env., 94, 46-60, 2005.

Susskind et al, Determination of ATM and surface parameters from simulated Air/AMS/HSB sounding data retrieval and clouds clearing methodology, Adv. Space Rex Vol. 21, No. 3. pp. 36%384,1998

Tanikawa et al., Monte Carlo simulations of spectral albedo of artificial snowpacks composed of spherical and nonspherical prticles, Appl. Optics, 45, 5310-5319.

Tanikawa,T., Aoki, T., and Nishio, F., Remote sensing of snow grain-size and impurities from Airborne Multispectral Scanner data using a snow bidirectional reflectance distribution function model. Annals Glaciol., 34, 74-80, 2002.

Tanikawa et al., Snow bidirectional reflectance model using nonspherical snow particles and its validation with field measurements, EARSeL Proceedings, 5 137-145, 2006b.

Tedesco, M., and Kokhanovsky A. A., The semi-analytical snow retrieval algorithm and its application to MODIS data, Rem. Sens. Env., 110, 317-331, 2007.

Tedesco, M.: Special issue ‘Remote Sensing of the Cryosphere’ Remote Sensing Environ., 111, 135, 2007.

Underwood, E.E.: Quantitative stereology, Addison-Wesley, Reading, MA, 1970.

Vermote, E., and Vermeulen, A., Atmospheric correction algorithm: Spectral reflectances (MOD09), ATBD version 4.0 available at http://eospso.gsfc.nasa.gov/ftp_ATBD/REVIEW/MODIS/ATBD-MOD-08/atbd-mod-08.pdf, 1999.

Wald, AE., Modeling thermal infrared (2–14 m) reflectance spectra of frost and snow. J. Geophys. Res. Solid Earth :24241–50, 1994.

Wan ZM, Y. Zhang, MODIS UCSB Emissivity Library. http://www.icess.ucsb.edu/modis/EMIS/html/em.html, 1999.

Warren, S.G., and Wiscombe, W.J., A model for the spectral albedo of snow. II: Snow containing atmospheric aerosols. J. Atmos. Sci. 37, 2734-2733, 1980.

Warren, S. G., Optical properties of snow, Rev. Geophys., 20, 67-89, 1982.

Warren, S. G., Optical constants of ice from the ultraviolet to the microwave. Appl. Opt., 23, 1206- 1225, 1984.

Warren, S.G., and Wiscombe, W.J.: Dirty snow after nuclear war. Nature, 313, 467-470, 1985.

Warren, S.G., Brandt, R.E., and Grenfell, T.C., Visible and near-ultraviolet absorption spectrum of ice from transmission of solar radiation into snow, Applied Optics, 45, 5320-5334, 2006.

Warren et al., Effects of surface roughness on bidirectional reflectance of Antarctic snow, J. Geophys. Res., 103, 25789-25807., 1998.

Warren S. G., R. E. Brandt , Optical constants of ice from the ultraviolet to the microwave: A revised compilation, J. Geophys. Res., 113, D14220, doi:10.1029/2007JD009744, 2008.

Wiscombe, W. J., The delta-Eddington approximation for a vertically inhomogeneous atmosphere, NCAR Technical Note, NCAR/TN-121+STR, 1-66, 1977.

Wiscombe, W. and Warren, S., A model for the spectral albedo of snow. 1: pure snow, J. Atmos. Sci., 37, 2712-2733, 1980.

WMO, Second Report on the Adequacy of the Global Observing Systems for Climate in Support of the UNFCCC, GCOS-82, (WMO/TD No. 1143) and its Technical Annexes, April 2003

WMO, Systematic Observation Requirements for Satellite-based Products for Climate: Supplemental Details to the satellite-based component of the “Implementation Plan for the Global Observing System for Climate in support of the UNFCCC (GCOS-92)”, GCOS-107, September 2006 (WMO/TD No.1338).

Wylie, D., 1998: Cirrus and Weather: A satellite perspective. OSA Meeting, pp.66-68, Baltimore, U.S.A., 6-8, Oct. 1998

Xie, Y., Yang, P., Gao, B.-C., Kattawar, G. W., Mishchenko M. I., Effect of ice crystal shape and effective size on snow bidirectional reflectance, Journal of Quantitative Spectroscopy and Radiative Transfer, 100, 457-469, 2006.

Zege, E. P., Ivanov A. P., and Katsev I. L., Image transfer through a scattering medium, Berlin: Springer, 1991.

Zhou, X., Li, S. and Stamnes, K., Effects of vertical inhomogeneity on snow spectral albedo and its implications for remote sensing of snow, J. Geophys. Res., 108, 4738, 2003. doi: 10.1029/2003JD003859, 2003.

Section B: Algorithm Theoretical Basis Document – Aerosol

Distribution:

ESA	O. Leonard	X
	S. Pinnock	X
University College London	J-P. Muller	X
	T. Kennedy	X
	P. Lewis	X
	G. Lopez	X
Swansea	P. North	X
	A. Heckel	X
Free University of Berlin	L. Guanter	X
	J. Fisher	X
	R. Preusker	
Brockmann Consult	C. Brockmann	X
	N. Fomferra	X
	U. Krämer	X

CHANGE RECORD

ISSUE	DATE	PAGES CHANGED	COMMENTS
A	23/07/10	All new	Draft
1	10/9/10	All sections	First Issue
2	10/11/2010	26	Clarification of error metric normalisation.
2	10/11/2010	29	Clarification of input and products
3.1	06/06/2012	All	Global ToC added

17 Introduction

17.1 Purpose and Scope of Document

The purpose of this document is to provide the background and theoretical justification for the algorithms employed to estimate aerosol in the ESA GlobAlbedo product. GlobAlbedo sets out to create a 15 year time series by employing ATSR-2, SPOT4 VEGETATION and SPOT5 VEGETATION2 as well as AATSR and MERIS. Aerosol estimates are required for atmospheric correction of all L2 TOA to obtain accurate surface directional reflectance data and their uncertainties.

The primary features of the algorithms developed are:

- Aerosol estimates for all instruments are made using a common set of aerosol models and radiative transfer framework;
- The algorithms avoid the use of a priori assumptions on surface albedo;
- Separate constraints are developed to exploit the characteristics of the instruments used for GlobAlbedo (ATSR-2 and AATSR, SPOT VGT, and MERIS);
- We give a per-retrieval estimate of uncertainty in aerosol to allow propagation of uncertainty through the processing chain to the final albedo product.

17.2 Context

The GlobAlbedo project (RD-1) will develop a broadband albedo map of the entire Earth's land surface (snow and snow-free), which is required for use in climate modelling and research. For estimation of albedo satellite datasets need to be processed from top-of-atmosphere (TOA) observations to obtain surface spectral bidirectional reflectance factors (BRFs), also termed surface directional reflectance (SDR). The initial satellite measurements are strongly affected by molecular and aerosol scattering, and absorption by ozone and water vapour. The high spatial and temporal variability of aerosol scattering typically represents the greatest uncertainty in derivation of surface reflectance over land. While climatology values for aerosol optical thickness (AOT) have been used, for example in processing of SPOT VGT (Berthelot and Dedieu, 2000), derivation of aerosol properties from the satellite data at the time of overpass is needed for accurate correction.

18 Applicable and Reference documents

18.1.1 Applicable documents

	Doc. Number	Title
AD-1	ECSS-E-ST-40C	European Cooperation for Space Standardization: Space Engineering Software, (6 March 2009), available from http://www.ecss.nl

18.1.2 Reference Documents

	Doc. Number	Title
RD-1	EOEP-DUEP-EOPS-SW-09-0001	DUE GlobAlbedo Project Statement of Work, Issue 1, Revision 0 (6 April 2009)

18.2 Definitions and Abbreviations

(A)ATSR	(Advanced) Along Track Scanning Radiometer
AOT	Aerosol Optical Thickness
ATBD	Algorithm Theoretical Basis Document
BEAM	Basic Envisat Tool for AATSR & MERIS
BRDF	Bidirectional Reflectance Distribution Function
BRF	Bidirectional Reflectance Factor
CWV	Columnar Water Vapour
DOM	Dark Object Methods
ELEV	Surface elevation above sea level
ENVISAT	Environment Satellite (http://envisat.esa.int)
ERS	European Remote Sensing satellite
ESA	European Space Agency

L1, L2	Level 1, Level 2
MERIS	Medium Resolution Imaging Spectrometer Instrument
MODIS	Moderate Resolution Imaging Spectroradiometer
MOMO	Matrix Operator Model
NDVI	Normalised Differential Vegetation Index
NIR	Near InfraRed
RAA	Relative Azimuth Angle
RR	Reduced Resolution
RTC	Radiative Transfer Code
SDR	Surface Directional Reflectance
SPOT	Satellite Pour l'Observation de la Terre
SRF	Spectral Response Function
SSA	Single Scattering Albedo
SWIR	Short Wave Infra Red
SZA	Solar Zenith Angle
TIR	Thermal InfraRed
TOA	Top of Atmosphere
TOC	Top of Canopy
VGT	VEGETATION (sensor) onboard the SPOT satellite
VIS	Visible broadband range (400-700 nm)
VNIR	Visible Near Infrared
VZA	View Zenith Angle

19 Instrument characteristics

This section outlines the principal characteristics of the instruments used for GlobAlbedo processing. Five instruments are used to span the period 1995-2010. These are the ATSR-2 instrument on board ERS-2 (1995-), succeeded by the Envisat platform from 2002 including both AATSR and MERIS. In addition, the project uses the SPOT VGT sensor on SPOT 4 (1998-) and SPOT VGT2 on SPOT 5 (2002-). The instrument characteristics and channels are presented in Tables 1 and 2 respectively.

19.1 ATSR-2 and AATSR

The AATSR instrument is a scanning radiometer, sensing at thermal infrared, reflected infra-red and visible wavelengths with two ~500 km wide conical swaths, with 555 pixels across the nadir swath and 371 pixels across the forward swath. The specifications of AATSR and ATSR-2 are the same, except that the ATSR-2 instrument employed a reduced swath of visible channels over and near oceans due to data transmission restrictions. The swath covers approximately half of the MERIS swath. The nominal pixel size is 1 km^2 at the centre of the nadir swath and 1.5 km^2 at the centre of the forward swath. For the AATSR level 1 products the forward pixels are sampled to 1km in order to be the same size as the nadir pixels. This unique feature provides two views of the surface and improves the capacity for atmospheric correction and enables observations of the ocean surface under a solar zenith angle of ~55° in the forward direction. The first 3 bands are common with MERIS bands, however, the bandwidth of the AATSR bands is significantly larger. The channels at 1.6μm and 3.7μm are suited to correct for the impact of aerosols, especially above coastal waters, since at this spectral range there is nearly no backscattering of solar radiation emanating from the water body. For land aerosol retrieval, the bands at shorter wavelengths (550nm and 665nm) where aerosol scattering is greater with respect to surface scattering are important.

19.2 MERIS

MERIS is an imaging radiometer with 15 programmable spectral bands in the range 400 – 1050 nm. The operational band setting positions give 15 bands between 412.5 nm and

Table 19-1: VGT, MERIS and (A)ATSR, MERIS instrument characteristics.

	VGT	MERIS	AATSR
Bands	4	15	7
Swath Width	~2250km	1150 km	~500 km
Spatial Resolution	1.15km	FR: ~300m RR: 1.3km	Forward: 1.3km Nadir 1km
Range of view zenith angles	0-55°	0-45°	Forward: 50-60° Nadir: 0-25°

Table 19-2: Channels on the VGT, MERIS and (A)ATSR, MERIS instruments.

VGT			MERIS			AATSR		
Channel	Wave-length (nm)	Band-width (nm)	Channel	Wave-length (nm)	Band-width (nm)	Channel	Wave-length (nm)	Band-width (nm)
			1	412.5	10			
1	450	40	2	442.5	10			
			3	490	10			
			4	510	10			
			5	560	10	1	550	20
			6	620	10			
2	665	70	7	665	10	2	665	20
			8	681.25	7.5			
			9	708.75	10			
			10	753.75	7.5			
			11	760.625	3.75			
			12	778.75	15			
3	850	110	13	865	20	3	865	20
			14	885	10			
			15	900	10			
4	1660	195				4	1610	60
						5	3740	380
						6	10850	90
						7	12000	1000

900 nm, including one narrow band at 761.4 nm in the Oxygen A absorption band, and 5 bands in the near infrared for the atmospheric correction over the ocean. Three of these bands are dedicated to the retrieval of aerosol properties. The MERIS swath covers 1150 km across-track. The original pixel size is 260 by 290 m in nadir and increases towards the edge of the swath. Onboard these full resolution (FR) data are spatially integrated to the reduced resolution (RR) pixel size, which is equivalent to the size of 4 by 4 full resolution pixels. During processing the FR data are resampled to an equal grid with a pixel a size of 300 by 300 m, and the reduced resolution (RR) data with 1.2 by 1.2 km pixel size. For AOT and surface reflectance retrieval only the MERIS RR products will be used.

19.3 SPOT VEGETATION

The first SPOT VGT sensor was launched on SPOT4 in 1998, and succeeded by VGT2, on SPOT5 in 2002. The instrument has a wide swath width, allowing near-daily collection of global data, at a spatial Resolution of ~1.15 km. While there are a small number of bands (4), they spanning a wide spectral range and the sensor swath width allows more frequent observation the than the other instruments. Characteristics are summarised in Table 19-1 and Table 19-2.

20 Theoretical background for aerosol retrieval

For global satellite data processing, atmospheric correction is normally performed in two stages. In the first step, the atmospheric properties are determined at the time of satellite overpass. Secondly, a radiative transfer model of the atmosphere is inverted to estimate surface reflectance, accounting for the atmospheric scattering and absorption. It is normal to use a pre-calculated look-up table (LUT) for this stage, to allow rapid estimation of surface reflectance on a per-pixel basis (Rahman and Dedieu, 1994; Grey et al 2006a). Of these two stages, the estimation of atmospheric properties is the most challenging and greater source of error (Vermote and Kotchenova, 2008). While vicarious correction techniques, such as the empirical line method, have been applied to individual sites as an extension of calibration, this requires *in situ* measurement of sample surface reflectance.

The high spatial and temporal variability of aerosol scattering typically represents the greatest uncertainty in derivation of surface reflectance over land. While climatology values for AOT have been used, for example in processing of SPOT VGT (Berthelot and Dedieu, 2000), derivation of aerosol properties from the satellite data at the time of overpass is needed for accurate correction. The parameters required to model aerosol radiative effects are AOT for a given reference wavelength, and aerosol model, describing spectral dependence of ATD, single scattering albedo, and phase function.

In general, it is more challenging to retrieve required aerosol properties over the land than the ocean. This is because the scattering from the land surface tends to dominate the satellite signal making it difficult to discern the atmospheric scattering contribution, particularly over bright surfaces. In addition, obtaining an accurate model of the land surface is further complicated because bi-directional reflectance is highly variable, both spatially and temporally.

Currently, atmospheric radiative transfer (RT) codes allow retrieval of surface reflectance with a high degree of precision for a known atmospheric profile, with theoretical error typically <0.01 in surface reflectance (Fischer and Grassl, 1984; Kotchenova et al., 2006). This enables both forward simulation of satellite radiances, and inversion of such models

to estimate surface reflectance given a set of top-of-atmosphere (TOA) radiances. Over land, the key problem in correction of surface reflectance for aerosol effects lies in simultaneous estimation of aerosol at the time of acquisition.

20.1 Aerosol optical depth and scattering models

The parameters required to model aerosol radiative effects are aerosol optical depth (AOT) for a given reference wavelength, its spectral dependence, which may be defined by the Angstrom coefficient, single scattering albedo, and phase function. These properties are closely related to aerosol amount, composition and size distribution. The net effect of aerosol on climate forcing depends on its optical properties (absorption and scattering) (Mishchenko et al., 2007). To date, most retrieval schemes return spatially varying estimates of AOT as the main parameter, and some additionally return information on aerosol size distribution (e.g. Remer et al., 2005) or the related property of Angstrom coefficient (e.g. Veefkind et al 1999). Recent methods have explored search for the most probable candidate aerosol model from a limited database, based on fit to the observations, with further aerosol properties defined by this model (North 2002b; Holzer-Popp et al., 2008; Diner et al., 2009).

20.2 Single-view methods

Most currently available aerosol retrievals are based on data from instruments with a single sampling of the angular domain. These algorithms are based on different assumptions, depending on available spectral sampling. In general the retrievals need to use known wavelength dependence of surface reflectance in order to provide information on the aerosol. The separation of the surface contribution is always based on a priori knowledge about the spectral properties of the surface. A number of assumptions have proven successful:

- Identification of dark targets: where it is possible to identify targets of dark dense vegetation (DDV) with known spectral properties, this may be used to derive aerosol path radiance over these targets (Kaufman and Sendra (1988)). Operational algorithms have been developed for MODIS (Remer et al., 2005), and MERIS (Santer et al., 1999; Santer et al., 2007) on this basis, amongst other instruments. For MERIS, the vegetation index ARVI (Kaufman et al., 1992) is used

to identify vegetation. However, accurate application is limited to regions where such targets are available at the appropriate spatial resolution (i.e. oceans and dark dense vegetation), so we must employ interpolation of the aerosol field to derive values at image points suitable for atmospheric correction. Recent results suggest improvement of this method is possible using calibration of the spectral relationship over a range of representative land covers, corresponding to selected AERONET sites (Levy et al., 2007) allowing correction for view-angle effects on surface spectra and generalisation to brighter surfaces (Hsu et al., 2004).

- Spectral mixing: Independently measured spectra of vegetation and bare soil are taken to construct a basis and the actual surface spectrum is assumed to be a linear combination of both, depending on vegetation cover. The algorithm described by von Hoyningen-Huene et al. (2003), bases the mixture of soil and vegetation spectra on the measured NDVI. The thus defined surface spectrum is then only allowed for scaling. An alternate algorithm developed by Guanter et al. (2007) uses mainly the assumption that aerosol is spatially more homogeneous than surface reflectance. Therefore the algorithm searches locally for pixels with the most and the least vegetation cover (darkest and brightest pixels) and assumes the atmospheric information to be constant. This allows the determination of the aerosol content.

- *A priori* assumptions based on existence of an independent estimate of surface reflectance from other instruments: For example Thomas et al. (2009) used MODIS estimates of surface reflectance to estimate aerosol from (A)ATSR instruments. While potentially allowing spatially continuous mapping of aerosol, important limitations are the reliance on the existence of a recent reflectance map from another instrument which has already been successfully corrected for atmospheric scattering, as well as including errors due to different temporal, angular and spectral sampling.

While potentially offering accurate retrieval where the target reflectance matches well with modelled spectrum, the single spectral measurement can give information on aerosol path radiance only, and not on phase function. Generally these methods, are suitable only for dark targets with relatively low spectral variability, so give a sparse estimate of optical depth, and are normally inappropriate for bright surfaces such as arid or snow covered land.

20.3 Multi-temporal methods

Related to single view retrieval methods are those which allow retrieval from time series, assuming greater stability of land surface reflectance compared to aerosol (Lyapustin, A. and Wang (2009)). The time series allows use of recent reflectance retrievals as a prior in inversion. Such techniques are particularly relevant where high temporal sampling is available, such as from geostationary instruments, for example the method by Govaerts et al., (2010) using optimal estimation theory and including a model of the effects of solar angle change on land surface scattering.

20.4 Multiple view-angle (MVA) methods

While spectral methods may produce very good results in regions where the assumptions are fulfilled, global aerosol retrievals show a number of uncertainties due to the large variability in spectral surface properties. Use of multiple view-angle imagery allows an additional constraint to be placed, since the same area of surface is viewed through different atmospheric path lengths. The concept was pioneered by ATSR on ERS-2, originally for atmospheric correction of SST for the effects of water vapour (Barton et al., 1989). In addition, there is scope to use the increased angular sampling of the land surface to further constrain retrieval of albedo and vegetation biophysical parameters (Diner et al., 1999). Several instruments have been designed to exploit the ability of MVA techniques for aerosol retrieval, including MISR, using 9 cameras tilted at angles in the range ± 70.5° along-track, and POLDER, which employs a CCD array to sample continuousl9 at ± 43° along-track (Martonchik et al., 1998; Leroy et al., 1997).

For the ATSR instrument series, 2 view directions are available, at approximately nadir and 55° along-track requires an approach which exploits the similarity of the surface anisotropy across wavelengths. This is due to the fact the anisotropy is dominated by

geometric shadowing effects, which are wavelength invariant. However other effects contribute to anisotropy; the differential viewing of canopy/understory surfaces with view angle, and the degree of multiple scattering, which tends to reduce anisotropy over bright surfaces. A simple approximation assuming spectral invariance of the BRDF (Mackay et al., 1999; Flowerdew and Haigh, 1996). has been used in inversion schemes (Veefkind et al., 2000) to provide a successful retrieval of aerosol. The method has developed further to include enhanced modelling of the spectral variation of anisotropy (North et al., 1999) to give an operational method from which global retrieval of aerosol properties has been achieved using the ESA Grid Processing on Demand (GPOD) system (North 2002b; Grey et al., 2006a,b). Validation by comparison with AERONET shows robust retrieval over all land surfaces, including deserts (Grey et al., 2006b; Bevan et al., 2009). The method has also recently been applied to estimation of aerosol from the CHRIS PROBA instrument, by exploiting the ability of the instrument to acquire 5 views of the target by satellite pointing (Davies et al., 2010). The use of a cross-spectral constraint on surface anisotropy has also recently been incorporated into the MSR processing algorithm (Diner et al., 2005).

The principal advantage of an MVA approach is that no *a priori* information of the surface spectrum is required and aerosol properties can be retrieved over all surface types, including bright deserts. Limitations of the angular approach are that the algorithms require accurate co-registration of the images acquired from multiple view angles. Normally aerosol is retrieved at a lower resolution than the pixel resolution, to decrease the effect of misregistration errors, for example at 18km for MISR and 8km for ATSR (Diner et al., 2009; North et al., 2002b), and the methods may be sensitive to undetected sub-pixel clouds (North et al., 1999).

21 Algorithm overview

21.1 General Overview of Scheme

The problem is formulated as one of optimisation subject to constraint, which has been widely applied to atmospheric retrievals. Figure 1 illustrates the retrieval framework followed here. The two-stage optimization process is employed: (1) Given a set of satellite TOA radiances, and an initial guess of atmospheric profile, we estimate the corresponding

set of surface reflectances. (2) Testing of this set against a constraint results in an error metric, where a low value of this metric should correspond to a set of surface reflectances (and hence atmospheric profile) which is realistic. Step (1) is repeated with a refined atmospheric profile until convergence at an optimal solution.

The algorithm components are therefore (i) design of an efficient and accurate scheme for deriving surface reflectance for known atmospheric profile, and (ii) formulation of constraints on the land surface reflectance suitable for the angular and spectral sampling of the instruments used ((A)ATSR, SPOT-VGT and MERIS). The method is applied to estimate aerosol at a more coarse spatial resolution (8 x 8 km) than the underlying surface reflectance, and a subsequent interpolation step is used to obtain per-pixel values.

21.2 Pre-processing

The pre-processing requirements for the algorithm are calibration of all instrument data to top of atmosphere reflectance, screening of cloud and water bodies, and, for (A)ATSR, registration of the two views. The cloud screening should be conservative as cloud contamination can lead to high errors in retrieval of AOT. The registration is generally of adequate quality for aerosol retrieval. However, for cloud, the flags provided with the instrument data were considered of insufficient quality for the purpose of the GlobAlbedo project. The pre-processing and pixel classification are discussed in the document GlobAlbedo_PixID_ATBD_V1.0 (2010).

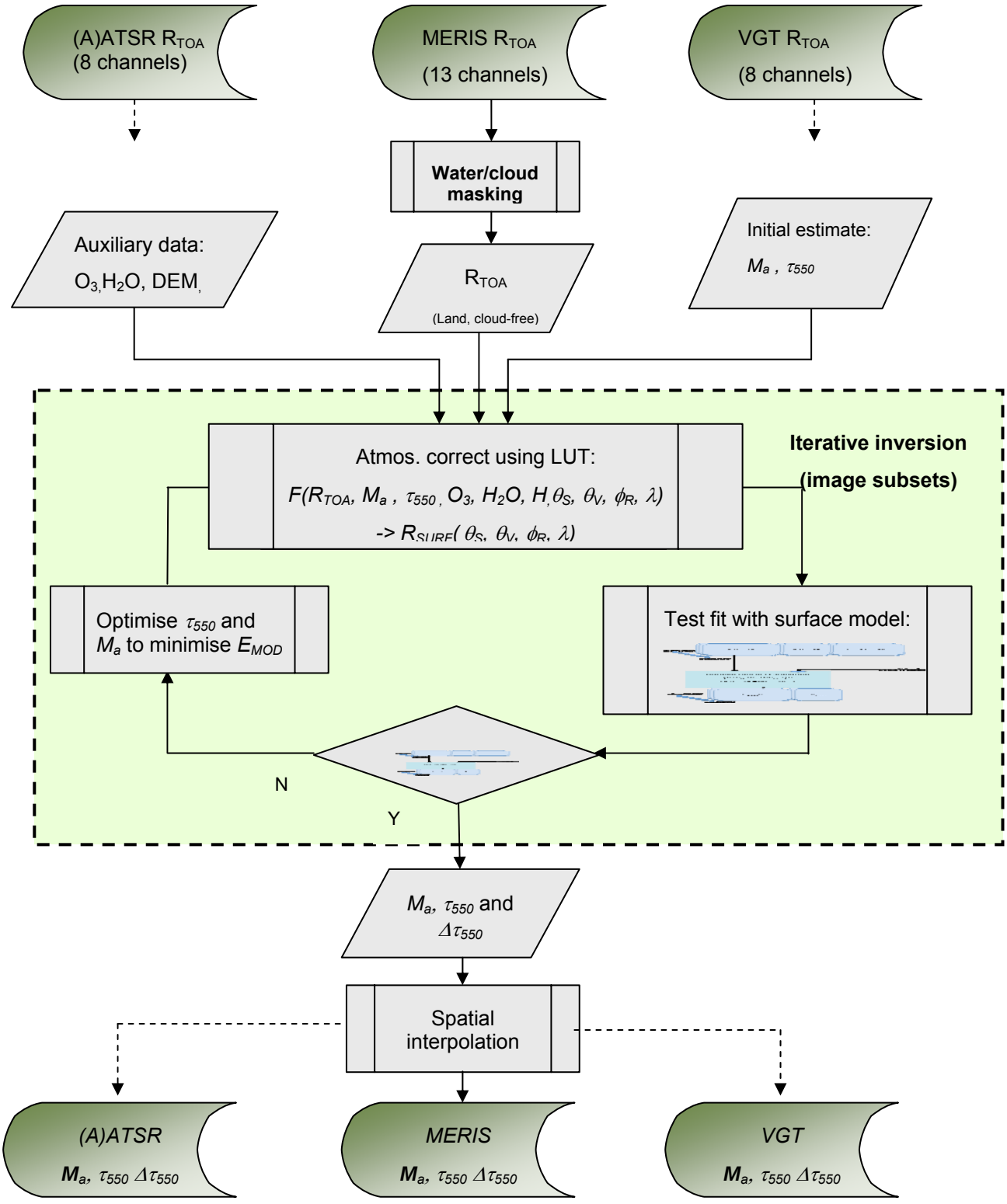

Figure 21-1: Outline processing algorithm for retrieval of aerosol properties for GlobAlbedo

21.3 Approximation of atmospheric radiative transfer

The retrieval of atmospheric aerosol requires a fast approximation of atmospheric radiative transfer, to relate TOA to surface reflectance for varying aerosol loading. Here we use the scheme developed under the GlobAlbedo for SDR and BBDR estimation; this is discussed fully in GlobAlbedo_BBDR_ATBD_V1.0 (2010), and here we give a brief summary of points relevant to aerosol estimation.

For a given sensor waveband and atmospheric profile, the relationship between top of atmosphere reflectance $R^*_\lambda(\Omega_v,\Omega_s)$ and surface directional reflectance R_λ can be approximated by the equation:

$$R^*_\lambda(\Omega_v,\Omega_s) = R_{atm,\lambda}(\Omega_v,\Omega_s) + \gamma_\lambda(-\mu_s)\gamma_\lambda(\mu_v)\frac{R_\lambda}{1-\bar{\bar{\rho}}_\lambda R_\lambda} \qquad (5.1)$$

where $R_{atm,\lambda}$ denotes the atmospheric scattering term (TOA reflectance for zero surface reflectance), γ_λ denotes atmospheric transmission for either sensor to ground or ground to sensor for waveband λ, and $\bar{\bar{\rho}}_\lambda$ denotes atmospheric bi-hemispherical albedo with respect to the surface. The view and solar vectors are denoted by Ω_v and Ω_s respectively, while μ_v and μ_s denote cosines of solar and view zenith.

By rearranging (5.1), the surface reflectance is thus related to the TOA observations by

$$R_\lambda(\Omega_v,\Omega_s) = \frac{R^*_\lambda(\Omega_v,\Omega_s) - R_{atm,\lambda}(\Omega_v,\Omega_s)}{\gamma_\lambda(-\mu_s)\gamma_\lambda(\mu_v) + \bar{\bar{\rho}}_\lambda\left[R^*_\lambda(\Omega_v,\Omega_s) - R_{atm,\lambda}(\Omega_v,\Omega_s)\right]} \qquad (5.2)$$

The calculation is made efficient by pre-compilation of look-up tables for the coefficients $R_{atm,\lambda}$, $\bar{\bar{\rho}}_\lambda$ and γ_λ, defined for each instrument waveband accounting for the spectral response functions. During operation we use multidimensional piecewise linear interpolation to obtain the required atmospheric coefficients. The tables and include the effect of absorption and scattering by fixed gases, aerosols, ozone and water vapour. The 6S code (Vermote et al., 1997) is used for calculation of transmittance terms, while the 6S code (Vermote et al., 1997) is used for calculation of transmittance terms, while the

MOMO code (Fischer and Grassl, 1984; Fell and Fischer, 2001) is used for atmospheric reflectance and albedo accounting for multiple scattering. No correction of adjacency effects was found to be necessary for the GlobAlbedo SDR product, as this is focused on land surfaces and the spatial resolution of the three instruments under consideration is comparable to the atmospheric point spread function. Although observations at differing view angles will recover a differing SDR value, the surface is approximated as Lambertian for the calculation of multiple scattering terms.

21.4 Aerosol model set

The six aerosol models described in Govaerts et al. (2010) and a continental model built up from the Optical Properties of Aerosols and Clouds (OPAC) aerosol model database (Hess et al., 1998) have been used for the generation of the LUTs. The optical properties of the seven models are summarised in Table 3. The six models from Govaerts et al. (2010) result from the clustering of a large data set of AERONET observations (Holben et al., 1998) according to the single scattering albedo and phase function of each observation. The aerosol models derived with this procedure represent combinations of absorbing and non-absorbing aerosol and of spherical and non-spherical particles. The single scattering albedo and phase function of the non-spherical models were calculated with a scattering code based on spheroid models (Dubovik et al., 2006), while the Mie code built-in in MOMO was used for the spherical models. The impact of the particular aerosol model on $R_{atm,\lambda}$ is illustrated in Fig.1. The slope of the derivative of $R_{atm,\lambda}$ with respect to AOD550 changes with the model, which shows that different values of AOD550 would be retrieved by different aerosol models.

		Fine Mode				Coarse Mode			
	Model	r_v	σ	C_v	n(440nm)	r_v	σ	C_v	n(440nm)
Spherical	Contin. I-80	0.021	2.2400	0.950	1.40-0.002i	0.471	2.510	0.050	1.53-0.008i
	ABSORB	0.155	0.404	0.083	1.46-0.018i	3.012	0.649	0.051	1.46-0.018i
	MODABS	0.221	0.497	0.094	1.42-0.009i	2.886	0.598	0.050	1.42-0.009i
	NONABS	0.179	0.426	0.101	1.42-0.006i	3.004	0.623	0.039	1.42-0.006i
Non-spherical	SMARAD	0.145	0.500	0.037	1.50-0.005i	2.423	0.617	0.262	1.50-0.005i
	MEDRAD	0.172	0.636	0.033	1.48-0.005i	1.961	0.549	0.364	1.48-0.005i
	LARRAD	0.202	0.627	0.043	1.43-0.003i	1.978	0.527	0.521	1.43-0.003i

Table 21-1: Properties of the aerosol models used. Each of the two modes compounding each aerosol model is defined by the volume median radius r_v (μm), the radius standard deviation σ (μm), the volume Concentration C_v (μm, %for the Continental I-80 model) and the spectral refractive index n (provided at 440nm in the table for reference purposes).

21.5 Constraints on surface reflectance

To retrieve estimates of aerosol properties from measured satellite radiances, we need to solve the inverse problem to separate the atmospheric and surface scattering contributions to the observed signal. This normally requires some assumptions to be made on the land surface brightness. Within the proposed framework, these assumptions are expressed as constraints defined by error of fit to a parameterized model describing the surface angular or spectral reflectance. For the single view instruments we apply constraints based on the dark object method (DOM), while for (A)ATSR we apply a multiple view-angle (MVA) constraint. In principle further and multiple constraints can be employed within the inversion framework, and the method updated to include best available constraints

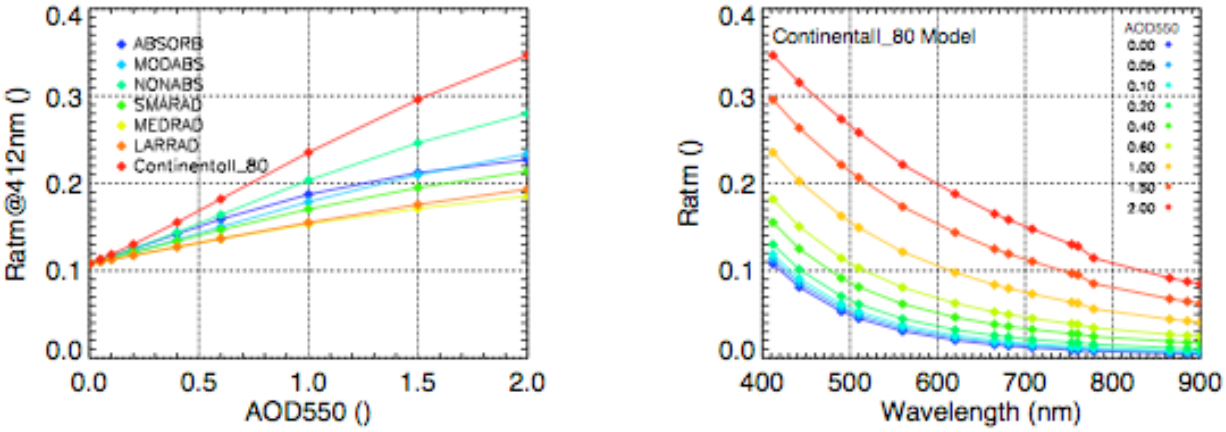

Figure 21-2: $R_{atm,\lambda}$ as a function of the aerosol model. $R_{atm,\lambda}$ in the MERIS band at 412nm is plotted as a function of AOD550 and the seven aerosol models in (a), while spectral $R_{atm,\lambda}$ for the continental model is represented in (b). The reference input configuration is VZA=30◦, SZA=30◦, RAA=120◦, ELEV=200m.

21.5.1 Multiple View-Angle constraint ((A)ATSR)

We have developed a method for simultaneous estimation of AOT and surface reflectance for data where at least two view angles are available, such as the AATSR (North et al., 1999; North 2002; Grey et al., 2006a,b). Methods employing similar principals have also been developed for AATSR and other multi-view sensors, (Veefkind et al., 1999; Diner et al., 2005; Kokhanovsky et al., 2007). The principal advantage of this approach is that no *a priori* information of the surface is required and aerosol properties can be retrieved even over bright surfaces. In the case of multi-view-angle data, a constraint may be made on the angular variation of the land surface reflectance, governed by the BRDF, giving a corresponding error of fit. In particular, the angular variation is assumed to be approximately constant across wavelength, since the angular variation (i.e. shape of the surface bi-directional reflectance distribution) is due principally to geometric effects (e.g. shadowing) which are wavelength independent. This means that for AATSR, the ratio of surface reflectances at the nadir and off-nadir viewing angles (where the view zenith angle is 55°) is well correlated between bands. This avoids the need for assumptions on absolute surface brightness or spectral properties. The method presented here differs from early approaches by using a more sophisticated surface model to account for some

spectral variation of the angular shape owing to the variation of the diffuse fraction of light with wavelength.

Scattering of light by atmospheric aerosols tends is be greater at shorter wavelengths. It is important to model the fraction of diffuse to direct radiation since it influences the anisotropy of the surface. The anisotropy is reduced when the diffuse irradiance is high because the contrast between shadowed and sunlit surfaces decreases. Anisotropy is similarly dependent for bright targets owing to the multiple-scattering of light between the surface elements. The atmospheric scattering elements including aerosols and gas molecules are comparable in size to the wavelength of light at optical wavelengths. As a result, the effect of atmospheric scattering on the anisotropy will be a function of wavelength and the shape of the BRDF will vary. Taking these effects into account results is a physical model of spectral change with view angle ([North et al., 1999)] :

$$\rho_{ang\_\mathrm{mod}}(\lambda,\Omega) = (1 - D(\lambda))v(\Omega)w(\lambda) + \frac{\gamma w(\lambda)}{1-g}\left[D(\lambda) + g(1 - D(\lambda))\right] \qquad (5.3)$$

where $g = 1 - \gamma w(\lambda)$, λ is the wavelength, Ω is the viewing geometry (forward or nadir view in the cases of AATSR), ρ_{mod} is the modelled bidirectional reflectance, γ is the fraction contributing to higher-order scattering and is fixed at 0.3, and D is the fraction of diffuse irradiance at the surface. The model separates the angular effects of the surface into two components, a structural parameter v that is dependent only on the viewing and illumination geometry, and the spectral parameter w, that is dependent only on the wavelength. The free parameters that we need to retrieve through model inversion are the four spectral parameters *w* and two angular parameters *v*.

By inversion of (5.3), this model of surface scattering has been shown theoretically to lead to a tractable method which is potentially more robust than the simple assumption of angular invariance alone (North 1999). The angular reflectance of a wide variety of natural land surfaces fits this simple model. In contrast, reflectance that is a mixture of atmospheric and surface scattering does not fit this model well. As a result, the model can be used to estimate the degree of atmospheric contamination for a particular set of

reflectance measurements and to find the atmospheric parameters which allow retrieval of a realistic surface reflectance.

21.5.2 Dark object method (MERIS and VGT)

When viewing from a single direction, we must rely on the spectral signature to distinguish aerosol from ground scattering. For a given set of surface reflectances derived by assuming a certain atmospheric profile, this may be expressed as an error based on the fit of the retrieved surface reflectance to the assumed target reflectance. This allows estimation retrieval of the atmospheric aerosol by optimal estimation. Where a target of approximately known reflectance can be identified, such as dense vegetation or a body of water, aerosol optical depth at the target location may be estimated on the basis of known correlation of ground reflectance at different wavelengths (Remer et al., 2005). The first stage in such schemes is the identification of dark pixels. One approach to identifying dark pixels is to calculate the Normalized Difference Vegetation Index (NDVI):

$$NDVI_{SC} = \frac{bR_{nir} - aR_{red}}{R_{nir} - R_{red}} \qquad (5.4)$$

where R_{nir} and R_{red} are the TOA reflectances at wavebands for the instruments centred approximately on 865nm and 665nm respectively. The coefficients a and b normalise for spectral differences between the instruments, and values are estimated in the accompanying ATBD GlobAlbedo_BBDR_ATBD_V1.0 (2010) for MERIS (a=1.0, b= 0.999), AATSR (a=1.008, b=0.997) and VGT (a=1.096, b=1.089).

Where a range of wavebands are available it is possible to represent the target reflectance as a linear mixture of an idealized vegetation and soil spectrum, or set of spectra using:

$$\rho_{spec\_\mathrm{mod}}(\lambda) = C_{veg}\rho_{veg}(\lambda) + C_{soil}\rho_{soil}(\lambda) \qquad (5.5)$$

where C_{veg} and C_{soil} are the fractional coverage of vegetation and soil respectively. They may sum to greater than one (equivalent to scaling brightness of these components) and the two fractions are the free parameters that we retrieve. The ρ_{surf}, ρ_{veg} and ρ_{soil} term are the surface reflectance, vegetation and soil reflectance of the input spectra, respectively

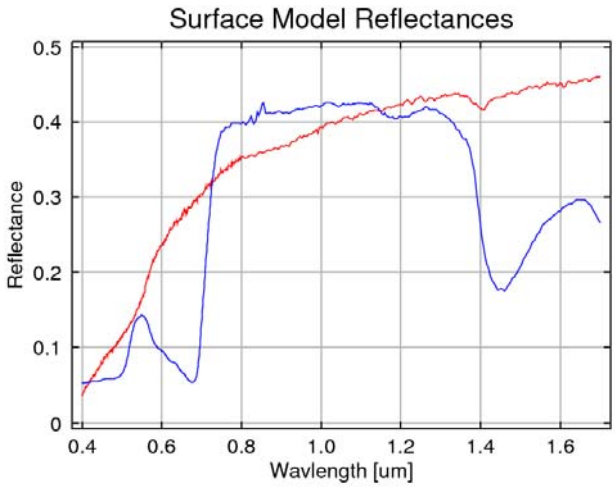

Figure 21-3: Surface reflectance model spectra for soil and vegetation

and are a function of wavelength. Example spectra used for initial tests are shown in figure 3. A number of variations on such methods have been used successfully for aerosol retrieval with MERIS (von Hoyningen-Huene et al., 2006; Guanter et al., 2007; Santer et al., 2007). However, routine application is limited to regions where such targets are available at the appropriate spatial resolution (i.e. oceans and dark dense vegetation), and accuracy is limited to the level of uncertainty in the *a priori* estimate of target reflectance variation. For (A)ATSR, it is also possible to use both spectral and angular constraints simultaneously by minimising a weighted sum of (5.3) and (5.5); this method is based on the ESA MERIS/AATSR Synergy project algorithm, and is currently experimental for use on (A)ATSR alone.

21.6 Numerical inversion

The retrieval algorithm is illustrated in Figure 4. To retrieve the aerosol properties from TOA cloud-free radiances we use a coupled numerical inversion scheme that incorporates the lookup tables derived from the radiative transfer model and a constraint based on a simplified model of land surface scattering. The basis of the inversion is (i) estimation of surface reflectance (R_{SURF}) for all bands and view angles, for an initial estimate of atmospheric profile, and (ii) iterative refinement of the atmospheric profile to minimise an error metric (E_{MOD}) on the retrieved surface reflectance set.

21.6.1 AOT retrieval

The input to the algorithm is the L2 TOA product for each sensor, averaged over a 8km x 8km window for each retrieval. This resolution is appropriate to the spatial scale of aerosol variability, and in the case of AATSR allows minimisation of mis-registration errors. A set of surface reflectances are calculated for a given atmospheric aerosol model and AOT parameterised by value at 550 nm. An error metric is defined on the surface reflectance set based on either the DOM or MVA constraints depending on sensor. For AATSR we use the angular constraint

$$E_{\mathrm{mod}} = \sum_{\Omega=1}^{2} \sum_{\lambda=1}^{4} w_{\lambda,\Omega} [R_{SURF}(\lambda,\Omega) - \rho_{ang\_\mathrm{mod}}(\lambda,\Omega)]^2 \qquad (5.6)$$

while for MERIS we use the spectral model over the 13 available bands

$$E_{\mathrm{mod}} = \sum_{\lambda=1}^{13} w_{\lambda} [R_{SURF}(\lambda,\Omega) - \rho_{spec\_\mathrm{mod}}(\lambda,\Omega)]^2 \qquad (5.7)$$

and for VGT we apply the spectral constraint using 4 bands

$$E_{\mathrm{mod}} = \sum_{\lambda=1}^{4} w_{\lambda} [R_{SURF}(\lambda,\Omega) - \rho_{spec\_\mathrm{mod}}(\lambda,\Omega)]^2 \qquad (5.8)$$

where ρ_{spec_mod} and ρ_{ang_mod} are the surface reflectances estimated using (5.5) and (5.3) respectively, based on the best-fit values of the free parameters, and R_{SURF} is the surface reflectance calculated for an estimate of τ_{550}. Iterative inversion yields the optimal values of the free parameters (AOT and aerosol model).

To optimize the performance of the inversion, normalised values for the set of weights w_i are determined for each constraint (angular and spectral) separately to represent uncertainty in the model fit. For the angular model, the four channels are weighted as follows: {1.5, 1.0, 0.5, 1.0, } for both nadir and forward views. For the spectral model, the channels have weights of 1.0 for all channels in the range 400-700nm, and for SPOT VGT MIR, and 0.05 for remaining channels. Each set of weights are then normalised to men value of 1, so that E_{MOD} is invariant to number of data points used.

For a given atmospheric profile the optimal free parameters of the separate land surface models that minimize (5.6)-(5.8) are found through the *Powell* multi-dimensional minimisation routine (Press et al., 1992), following transformation of TOA to surface reflectance using (5.2). This process is repeated for different AOTs and aerosol models. The optimal aerosol properties are found using the Brent one-dimensional optimisation method, by finding the value of atmospheric AOT which give rise to the lowest value of E_{MOD} in (5.6)-(5.8). Figure 4 illustrates the minimisation procedure, where various estimates of AOT give rise to differing values of the error metric for either angular or spectral model. The minimum point of this curve, typically reached after 3-6 iterations gives the estimate of the AOT. The curvature and error of fit are also used in calculation of the error estimate in AOT.

21.6.2 Selection of optimal aerosol model

The optimal aerosol model is selected by search for the aerosol model which minimises the estimated error from (5.6)-(5.8). Retrievals are run independently with different candidate models, and minimum value of E_{MOD} across the range of models provides an estimate for most likely aerosol type and corresponding properties of Angstrom coefficient, single scattering albedo and phase function.

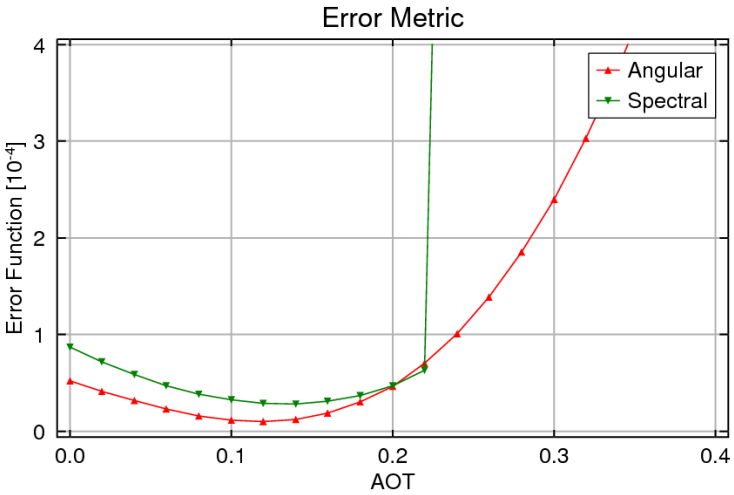

Figure 21-4: Example of variation of angular and spectral error metrics with AOT for a vegetated scene (Tomsk) for AATSR and MERIS respectively.

21.6.3 AOT error estimate

The error in retrieving optical thickness is estimated from the error metric E_{mod} of the fit from (5.6)-(5.8), and the curvature of the error surface near the minimum. The optimization procedure determines the minimum E_{min} of $E_{mod}(\tau)$, where τ represents the aerosol optical thickness defined at a reference wavelength (550nm). The value τ_{min}, where $E_{mod}(\tau_{min}) = E_{min}$, is the resulting aerosol optical thickness. The curvature term (a) of a parabolic fit to the error metric $E_{mod}(\tau)$ is calculated near the minimum. This curvature term allows calculation of the uncertainty of the retrieved aerosol optical thickness τ_{min}. This uncertainty (1 s.d.) can be expressed as:

$$\Delta\tau = k\sqrt{\frac{E_{\min}}{a}} \qquad (5.9)$$

The curvature term (a) of the error surface gives a measure of the sensitivity of the location of the minimum to error in model fit. For a steeply curved error surface, the retrieved value of τ is relatively robust to the estimation of model fit, while for a flat error

surface small perturbation in model fit error gives rise to a large error in τ. As surface reflectance approaches the 'critical point', where the TOA radiance is insensitive to variation in τ, then *a* approaches 0 and we have high uncertainty in τ. Similarly high values of *a* are found where deviation of TOA reflectance is greatest with small change in τ, which is expected for high contrast between aerosol and surface scattering, i.e. for low AOT and dark surfaces. The term E_{min} gives a sample of the combined error due to error in radiative transfer model, instrument noise, and deviation of surface reflectance from the assumed reflectance model. The term *k* is estimated to be 1.58, but this value will be improved by calibration of retrieved AOT against sun-photometer data.

21.6.4 Interpolation of aerosol field

An optimal estimate of surface reflectance for each channel is produced from the aerosol retrieval procedure. However, this is obtained at a coarser grid than the original image (8 x 8 pixels), and may contain missing values where the inversion has not converged. For atmospheric correction we need a further step to interpolate AOT values to all pixels within the image. This is achieved by an iterative coarse-to-fine filtering procedure, which preserves original retrieved AOT values and estimates AOT where there is missing data. Uncertainty in AOT is also interpolated. A final median filter is applied on a 3 x 3 moving window to improve robustness by eliminate outlying retrievals. The same lookup tables of atmospheric parameters as for the aerosol retrieval algorithm are used to produce surface reflectances across the image.

22 Practical considerations

In this section we state the output product for the algorithm, and discuss implementation within BEAM and initial testing.

22.1.1 Summary of inputs

For each satellite, the following inputs are required:

• TOA reflectance image at each solar reflective waveband and view angle

• Tie-point information giving solar/view geometry

• Pixel classification flags to give masks of cloud, snow and water

• Auxiliary data:

- Terrain model to give elevation per pixel (GETASSE 30)
- Column ozone and water vapour

22.1.2 Summary of products

The following products are returned by the procedure:

• aot: retrieved AOT (gap filled)

• aot_uncertainty: retrieved uncertainty of AOT

• aerosol_model: Aerosol model index number

• flags containing information on the retrieval:

- AOT filled by interpolation (not successfully retrieved)

22.1.3 BEAM implementation and processing efficiency

The algorithm has implemented within BEAM to allow ease of use of existing modules, such as recalibration and to link seamlessly with modules for pre-processing, including calibration and cloud detections, and generation of BBDR from the outputs.

Initial results of AOT retrieval within the BEAM implementation are shown in Figures 22-1 to 22-3. Figure 22-1 (a) shows a TOA composite from AATSR centred on the AERONET site at Tomsk, Siberia (15/5/2003). Figure 22-2 shows retrieved AOT throughout the image using inversion based on the angular constraint (5.6). Clouds and other excluded data are shown as original TOA image values. Estimated uncertainty in AOT is shown in Figure 22-3, following closely the retrieved AOT. Figure 22-2a and b shows retrieval with an enhanced version of the algorithm which includes both angular and spectral constraints for (A)ATSR. The reported AERONET value for Tomsk for this time is 0.33, compared with retrieved value for AATSR (angular) of 0.19, and AATSR (angular + spectral) of 0.31. Results for the corresponding segment of a VGT scene, showing retrieved AOT and uncertainty are given in Figure 22-3. Both sensors have equatorial crossing times of 10.30am, and show similar spatial variation of aerosol between the two retrievals. VGT retrieval gave an AOT of 0.35 at the AERONET site.

The code will be optimised with the target to process one orbital stripline in a time of less than 30 processor core minutes. Comparable timings have been reached for the existing AATSR code on ESA GPOD, which is a precursor to the algorithm. Options for optimisation of speed include reducing the set of available aerosol models where automatic selection is used, and retrieval of AOT at a coarse spatial resolution prior to the interpolation stage.

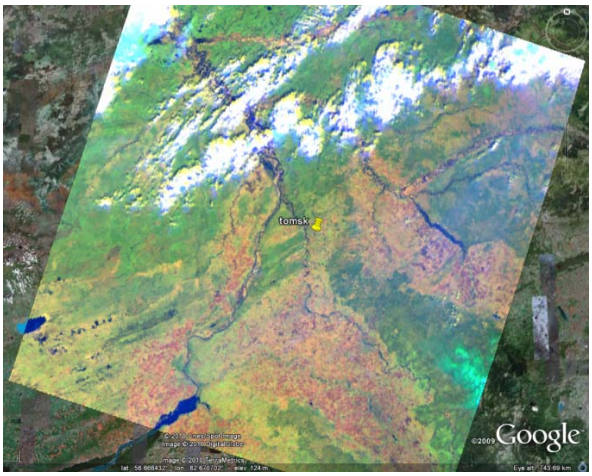

(a)

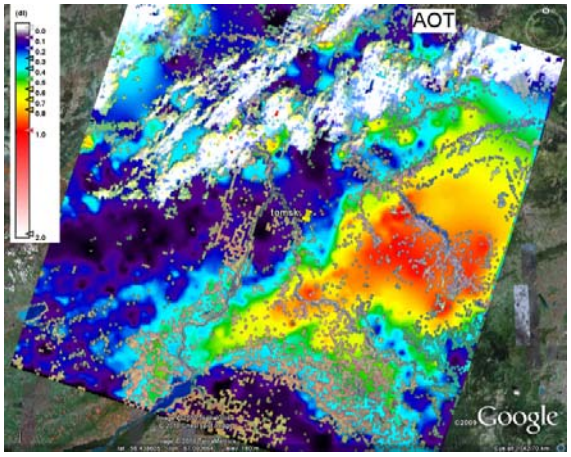

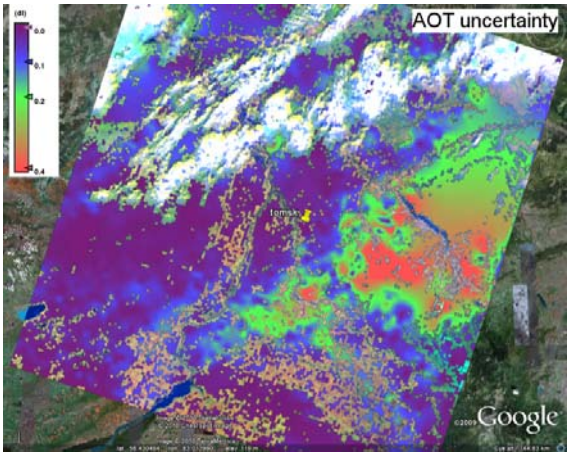

(b) (c)

Figure 22-1: a) RGB composite (1600n, 870n, 550f) around Tomsk Aeronet station on 15. May 2005. b) AOT retrieval for AATSR with angular approach only c) AOT uncertainty.

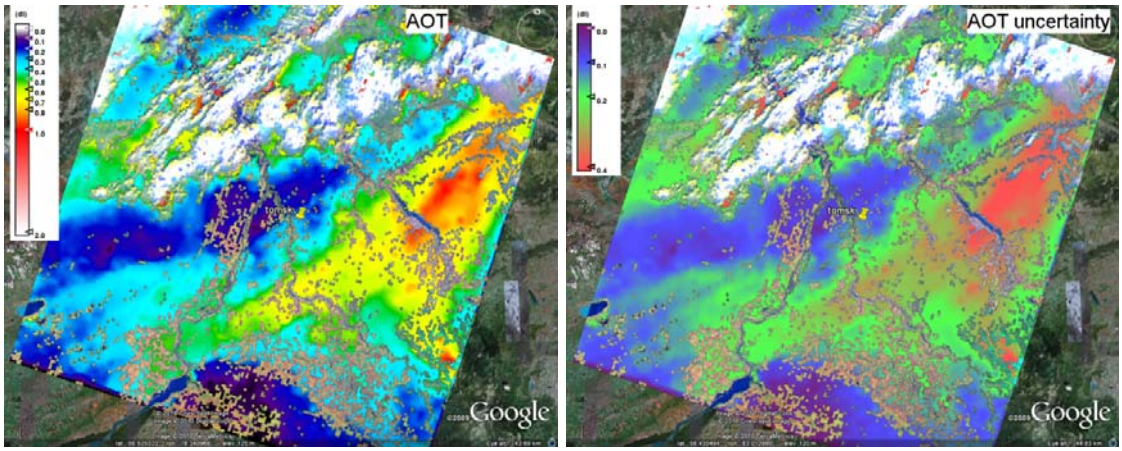

(a) (b)

Figure 22-2: Optional implementation of a mixed surface model based on a combination of the angular and a spectral model. a) AOT b) AOT uncertainty

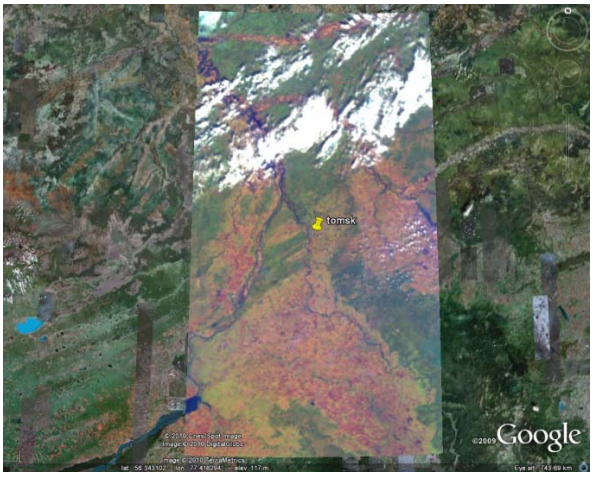

(a)

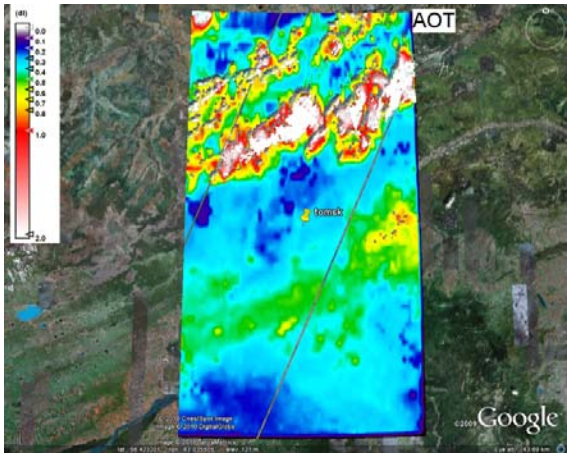

(b)

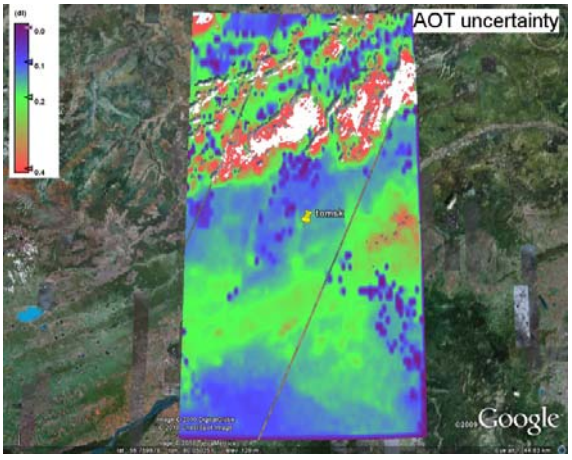

(c)

Figure 22-3: a) VGT RGB for same scene as figure 1 (15. May 2005). b) AOT retrieval for VGT segment based on spectral surface model c) AOT uncertainty.

22.1.4 Comparison with AERONET stations

Testing will take place by automatic output of AOT for a list of all available reliable AERONET sites. Initial testing has taken place of a prototype of the aerosol retrieval implemented within BEAM, and a comparison has been made against AERONET sun photometer measurements for AATSR and MERIS matches. Initial comparison is made using a single aerosol model (continental). A total of 68 images with low cloud amount have been tested giving 51 matches against AERONET, covering a range of sites. Of these matches, 20 are sites containing dark dense vegetation (DDV) in the vicinity of the AERONET station, based on availability of the MERIS L2 aerosol product. Figure 22-4 Figure 22-5 show initial comparison against AERONET for AATSR and MERIS respectively. Over the full dataset MERIS retrievals show correlation coefficient r =0.71, and mean absolute error (MAE) of 0.15, while AATSR retrievals give r =0.78 and MAE of 0.12. Over the DDV subset, the MERIS retrieval shows r = 0.96 and MAE 0.09, while AATSR shows correlation r = 0.86, but MAE of 0.09 also. Testing of SPOT-VGT is currently in progress.

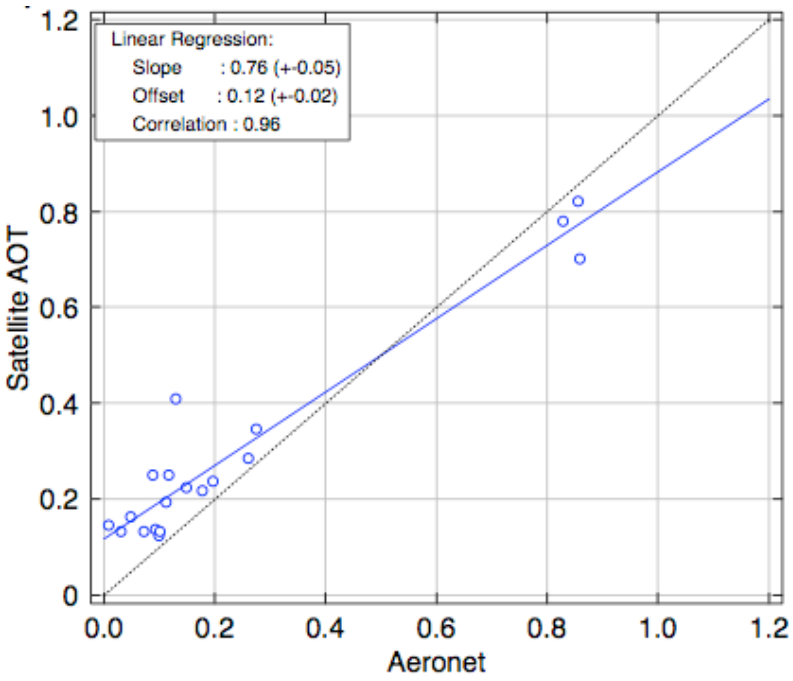

Figure 8

Figure 22-4: Results of MERIS retrieval compared with AERONET sites (DDV targets only).

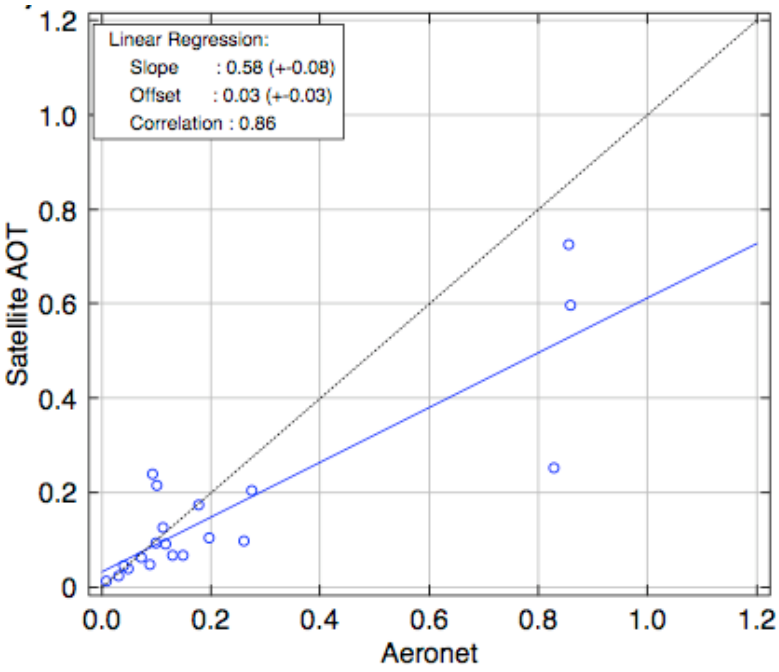

Figure 22-5: Results of AATSR retrieval compared with AERONET sites (DDV targets only).

23 Assumptions and Limitations

The algorithm is intended to provide an efficient global retrieval of aerosol optical thickness and uncertainty for input to SDR processing using a common framework for all sensors. The algorithm assumes as input existence a reliable mask of land/water and cloud (see GlobAlbedo_PixID_ATBD_V1.0 (2010)), registration of the (A)ATSR scenes and availability of a DEM at 1km resolution and fields of column ozone and water vapour. The current algorithm includes several limitations:

.

- **Applicability to bright regions**: While the (A)ATSR retrievals perform well over bright desert targets, for MERIS and VGT, performance over these regions is likely to be degraded where vegetated targets are sparse. In addition, the algorithms for all instruments have not been adapted for snow and ice targets, and would require further development and testing. A background climatology value with suitable error estimate should be used as a default where the retrieval is unreliable.

- **Approximations of RT:** The model uses the RT scheme developed for SDR retrieval and includes the same assumptions and limitations (see GlobAlbedo_BBDR_ATBD_V1.0 (2010)). In particular, although differing values of SDR are retrieved with view angle, the model of atmospheric radiative transfer assumes the surface is Lambertian when modelling the coupling of surface and atmospheric scattering.

- **Aerosol model selection:** The ability to determine an optimal aerosol model from the different algorithms is not yet determined. A default setting of model properties other than AOT according to climatology is likely to be a practical solution for efficiency, and is likely to introduce only low error in SDR.

24 References

Aguirre, M., B. Berruti, J-L. Bezy, M. Drinkwater, F. Heliere, U. Klein, C. Mavrocordatos, P. Silvestrin, B. Greco, J. Benveniste, (2007) Sentinel-3 The Ocean and Medium-Resolution Land Mission for GMES Operational Services, *ESA Bulletin* **131**, 24-29.

Alton, P.B., North, P. R. J. and Los, S. O. (2007). The impact of diffuse sunlight on canopy light-use efficiency, gross photosynthetic product and net ecosystem exchange in three forest biomes, *Global Change Biology*, **13(4)**, doi:10.1111/j.1365-2486.2006.01316.x..

Barton, I. J., Zavody, A. M., O'Brien, D. M., Cutten, D. R., Saunders, R. W., & Llewellyn-Jones, D.T. (1989). Theoretical algorithms for satellite-derived sea-surface temperatures. *Journal of Geophysical Research - Oceans*, **94**, 3365 – 3375.

Bellouin, N., O. Boucher, J. Haywood, and M.S. Reddy, (2005): Global estimation of aerosol direct radiative forcing from satellite measurements, *Science*, **438**, 1138-1141.

Berthelot, B. and Dedieu, G., Operational method to correct VEGETATION satellite measurements from atmospheric effects. Proceedings IGARSS 2000. *IEEE 2000 International*. 01/02/200002/2000; 2:831-833 vol.2. DOI: 10.1109/IGARSS.2000.861718.

Bevan, S.L., North, P.R.J., Grey, W.M.F., Los, S.O. and Plummer, S.E. (2009), Impact of atmospheric aerosol from biomass burning on Amazon dry-season drought. *Journal of Geophysical Research*, **114**, D09204, doi:10.1029/2008JD011112.

Davies, W.H., North, P.R.J., Grey, W.M.F. and Barnsley, M.J. (2010), Improvements in Aerosol Optical Depth Estimation using Multi-angle CHRIS/PROBA Images, *IEEE Transactions on Geoscience and Remote Sensing,* **48**(1), 18-24.

Diner, D. J., Asner, G. P., Davies, R., Knyazikhin, Y., Muller, J. P., Nolin, A. W., Pinty, B., Schaaf, C. B., & Stroeve, J. (1999). New directions in Earth observing: scientific applications of multiangle remote sensing. Bulletin of the American Meteorological Society, **80** (11), 2209 – 2228.

Diner, D., J. Martonchik, R. Kahn, B. Pinty, N. Gobron, D. Nelson, and B. Holben, (2005). Using angular and spectral shape similarity constraints to improve MISR aerosol and surface retrievals over land, *Remote Sensing of Envorinment*, **94**, 155-171.

Dubovik, O., Sinyuk, A., Lapyonok, T., Holben, B. N., Mishchenko, M., Yang, P., Eck, T. F., Volten, H., Munoz, O. M., Veihelmann, B., van der Zande, W. J., Leon, J.-F., Sorokin, M., and Slutsker, I. (2006). Application of spheroid models to account for aerosol particle nonsphericity in remote sensing of desert dust. Journal of Geophysical Research-Atmospheres, **111**:D11208.

Dubovik, O., (2005). Optimization of Numerical Inversion in Photopolarimetric Remote Sensing, in *Photopolarimetry in Remote Sensing, NATO Science Series II: Mathematics, Physics and Chemistry*, Springer Netherlands, ISBN 978-1-4020-2368-2 (Online), 65-106.

Fell F. and J. Fischer, (2001). Numerical simulation of the light field in the atmosphere-ocean system using the matrix-operator method, *JQSRT*, **69**, 351-388.

Fischer, J. and Grassl, H. (1984). Radiative transfer in an atmosphere-ocean system: an azimuthally dependent matrix-operator approach, *Appl. Optics* **23**, 1035-1039.

Fischer and Preusker (2009), Radiative Transfer Model Description Document for ESA AATSR/MERIS Synergy project, available online at http://www.brockmann-consult.de/beam-wiki/display/SYN/Documents.

Flowerdew, R. J., & Haigh, J. D. (1996). Retrieval of aerosol optical thickness over land using the ATSR-2 dual look radiometer. *Geophysical Research Letters*, **23** (4), 351 – 354.

GlobAlbedo_PixID_ATBD_V1.0 (2010) "GlobAlbedo: Algorithm Theoretical Basis Document – Pixel Classification", Version 1.0, Authors: C. Brockmann, O. Krüger, and O. Danne , Date: 10/9/2010.

GlobAlbedo_BBDR_ATBD_V1.0 (2010) "GlobAlbedo: Algorithm Theoretical Basis Document – SDR Retrieval", Version 1.0, Authors: L. Guanter *et al.* , Date: 10/9/2010.

Govaerts, Y. M., S. Wagner, A. Lattanzio, and P. Watts (2010), Joint retrieval of surface reflectance and aerosol optical depth from MSG/SEVIRI observations with an optimal estimation approach: 1. Theory, *J. Geophys. Res.*, **115**, D02203, doi:10.1029/2009JD011779.

Grey., W.M.F., North., P.R.J., Los, S.O., and Mitchell, R.M., (2006). Aerosol optical depth and land surface reflectance from multi-angle AATSR measurements: Global validation and inter-sensor comparisons. *IEEE Transactions on Geoscience and Remote Sensing,* **44(8)**, 2184 – 2197.

Grey., W.M.F, North., P.R.J., and Los, S. (2006b). Computationally efficient method for retrieving aerosol optical depth from ATSR-2 and AATSR data, *App. Optics*, **45(12):** 2786-2795.

Guanter, L.; M. Del Carmen González-Sanpedro, J. Moreno, (2007), A method for the atmospheric correction of ENVISAT/MERIS data over land targets, *International Journal of Remote Sensing*, **28(3-4),** 709-728.

Hess, M., P. Koepke, and I. Schult, 1998: Optical Properties of Aerosols and Clouds: The Software Package OPAC. *Bull. Amer. Meteor. Soc.,* **79**, 831–844.

Holben, B. N., Eck, T. F., Slutsker, I., Tanre, D., Buis, J. P., Setzer, A., Vermote, E., Reagan, J. A., Kaufman, Y., Nakajima, T., Lavenu, F., Jankowiak, I., and Smirnov, A. (1998). AERONET – a federated instrument network and data archive for aerosol characterization. Remote Sensing of Environment, **66**:1– 16.

Holben, B., et al. (2001) An emerging ground-based aerosol climatology: Aerosol optical depth from AERONET, J. Geophys. Res., **106**(D11), 12067-12097.

Holzer-Popp, T., Schroedter, M. and Gesell, G. (1999). High-Resolution Aerosol Maps Exploiting the Synergy of ATSR-2 and GOME , *Earth Observation Quarterly* (**65**): 19-24, ESA Publications Division, ISSN 0256 - 596X.

Holzer-Popp, T., M. Schroedter-Homscheidt, H. Breitkreuz, L. Klüser, D. Martynenko, (2008). Synergetic aerosol retrieval from SCIAMACHY and AATSR onboard ENVISAT, *Atmospheric Chemistry and Physics Discussions*, **8**, 1-49.

Hsu, N. C., S.-C. Tsay, M. D. King, and J. R. Herman, (2004) Aerosol properties over bright-reflecting source regions, *IEEE Transactions on Geoscience and Remote Sensing*, **42**(3), 557– 569.

Jacquemoud, S., & Baret, F. (1990). PROSPECT: a model of leaf optical properties spectra, *Remote Sensing of Environment*, **34**, 75-9.

Jeong, M.-J., and N. C. Hsu (2008), Retrievals of aerosol single-scattering albedo and effective aerosol layer height for biomass-burning smoke: Synergy derived from "A-Train" sensors, *Geophys. Res. Lett.*, **35**, L24801, doi:10.1029/2008GL036279.

Kaufman Y. J. and Sendra, C. (1988). Algorithm for automatic corrections to visible and near IR satellite imagery, *Int. J. Remote Sensing*, **9**, 1357-1381.

Kaufman, Y.J. and Tanré D. (1992), Atmospherically resistant vegetation index (ARVI) for EOS-MODIS, *IEEE Transactions on Geoscience and Remote Sensing*, **30**, 261-270.

Kokhanovsky, A.A., F.-M. Breon, A. Cacciari, E. Carboni, D. Diner, W. Di Nicolantonio, R.G. Grainger, W.M.F.Grey, R. Holler, K.-H. Lee, P.R.J. North, A. Sayer, G. Thomas, W. von Hoyningen-Huene, (2007). Aerosol remote sensing over land: satellite retrievals using different algorithms and instruments. *Atmospheric Research,* **85**, 372-394, doi:10.1016/j.atmosres.2007.02.008.

Kotchenova, S.Y., Vermote, E.F., Matarrese, R. and Klemm, F.J. (2006), Validation of a vector version of the 6S radiative transfer code for atmospheric correction of satellite data. Part I: path radiance. *Applied Optics*. 10/2006; **45**(26):6762-74.

Leroy M., Deuze J.L., Bréon F.M., Hautecoeur O., Herman M., Buriez J.C., Tanre D., Bouffies S., Chazette P., and Roujean J.L., (1997). Retrieval of atmospheric properties and surface bidirectional reflectances over the land from POLDER. *Journal of Geophysical Research* **102** (D14), 17023-17037.

Levy, R.C., Remer, L., Mattoo, S., Vermote, E. and Kaufman, Y.J. (2007), Second-generation algorithm for retrieving aerosol properties over land from MODIS spectral reflectance. *J. Geophys. Res.*, **112**, D13211, doi:10.1029/2006JD007811.

Lyapustin, A. and Wang, Y., (2009). The time series technique for aerosol retrievals over land from MODIS, in Satellite Aerosol Remote Sensing Over Land, A. A. Kokhanovsky and G. DeLeeuw, Eds. Heidelberg: Springer Praxis Books, ISBN: 978-3-540-69396-3, pp. 69–99.

Mackay, G., M.D. Stevens, and J.A. Clark (1998). An atmospheric correction procedure for the ATSR-2 visible and near-infrared land surface data. *Int. J. Remote Sensing* **19**, 2949- 2968.

Martonchik, J.V., D.J. Diner, R. A. Kahn, T.P. Ackerman, M. M. Verstraete, B. Pinty, and H.R. Gordon,(1998). Techniques for retrieval of aerosol properties over land and ocean using multiangle imagery. *IEEE Trans. Geosci. Rem. Sens.* **36**, 1212-1227

McGill, M.J., L. Li, W.D. Hart, G.M. Heymsfield, D.L. Hlavka, P.E. Racette, L. Tian, M.A. Vaughan, and D.M. Winker, (2004). Combined lidar-radar remote sensing: initial results from CRYSTAL-FACE, *Journal of Geophysical Research*, **109**, doi: 10.1029/2003JD004030.

Mishchenko M.I., I.V. Geogdzhayev, B. Cairns, B.M. Carlson, J. Chowdhary, A.A. Lacis, L. Liu, W.B. Rossow, L.D. Travis, (2007). Past, present, and future of global aerosol climatologies derived from satellite observations: A perspective, Journal Of Quantitative Spectroscopy & Radiative Transfer **106 (1-3)**, 325-347.

North, P.R.J. (1996), Three-dimensional forest light interaction model using a Monte Carlo method, *IEEE Transactions on Geoscience and Remote Sensing*, **34(5)**, 946-956.

North, P.R.J., Briggs, S.A., Plummer, S.E. and Settle, J.J., (1999). Retrieval of land surface bidirectional reflectance and aerosol opacity from ATSR-2 multi-angle imagery, *IEEE Transactions on Geoscience and Remote Sensing*, **37(1),** 526-537.

North, P.R.J. (2002a). Estimation of fAPAR, LAI and vegetation fractional cover from ATSR-2 imagery. *Remote Sensing of Environment* **80**:114–121.

North, P. R. J. (2002b). Estimation of aerosol opacity and land surface bidirectional reflectance from ATSR-2 dual-angle imagery: Operational method and validation, *J. Geophys. Res.*, **107**, doi:10.1029/2000JD000,207.

North, P.R.J., Brockmann , C., Fischer, J., Gomez-Chova, L., Grey, W., Hecklel A., Moreno, J., Preusker, R. and Regner, P. (2008). MERIS/AATSR synergy algorithms for cloud screening, aerosol retrieval and atmospheric correction. *In Proc. 2nd MERIS/AATSR User Workshop, ESRIN, Frascati, 22- 26 September 2008.* (CD-ROM), ESA SP-666, ESA Publications Division, European Space Agency, Noordwijk, The Netherlands.

Press, W.H., S.A. Teukolsky, W.T. Vetterling, and B.P. Flannery, (1992). N*umerical Recipes in C, The Art of Scientific Computing (Second Edition)*. Cambridge: Cambridge University Press.

Prieto-Blanco, A., North, P.R.J., Fox, N. and Barnsley, M.J. (2009). Satellite-driven modelling of Net Primary Productivity (NPP): Theoretical analysis. *Remote Sensing of Environment* **113(1),** 137-14.

Rahman, H., and G. Dedieu (1994). SMAC : A simplified method for the atmospheric correction of satellite measurements in the solar spectrum. *International Journal of Remote Sensing*, **15**(1), 123-143.

Rathke, C and Fischer, J, (2002). Efficient parameterization of the infrared effective beam emissivity of semitransparent atmospheric layers, *J. Geophys. Res.,* **107** (D4), doi:10.1029/2001JD000596.

Remer, L. Y. Kaufman, D. Tanre, S. Mattoo, D. Chu, J. Martins, R.-R. Li, C. Ichoku, R. Levy, R. Kleidman, T. Eck, E. Vermote, and B. Holben, (2005). The MODIS Aerosol Algorithm, Products and Validation, *Journal of the Atmospheric Sciences*, **62**, 947-973.

Rosenfeld, D., Y. Rudich, R. Lahav, (2001). Desert dust suppressing precipitation: A possible desertification feedback loop, *Proceedings of the National Academy of Sciences*, **98**, 11, 5975-5980, doi:10.1073/pnas.101122798.

Saint, G., (1994). “VEGETATION” onboard SPOT 4, Products Specifications, Version 2, 18 May 1994.

Santer, R., V. Carrère, P. Dubuisson and J.C. Roger (1999), Atmospheric corrections over land for MERIS, *Int. J. Remote Sensing*, **20** (9), 1819-1840.

Santer, R., D. Ramon, J. Vidot, E. Dilligeard, (2007). A surface reflectance model for aerosol remote sensing over land, *International Journal of Remote Sensing*, **28(3-4)**, 737-760.

Santer, R. (2009): MERIS L2 ATBD 2.15, http://envisat.esa.int/instruments/meris/atbd/atbd_2_15.pdf

Smith, D., Poulsen, C. and Latter, B (2008), Calibration Status of AATSR and MERIS Reflectance Channels, *In Proc. 2nd MERIS/AATSR User Workshop, ESRIN, Frascati*, *22- 26 September 2008*. (CD-ROM), ESA SP-666, ESA Publications Division, European Space Agency, Noordwijk, The Netherlands.

Solomon , S., et al., (2007). "Technical Summary: The Physical Science Basis. Contribution of Working Group I to the Fourth Assessment Report of the Intergovernmental Panel on Climate Change," in Climate Change 2007, S. Solomon, D. Qin, M. Manning, Z. Chen, M. Marquis, K. B. Averyt , M. Tignor, and H. L. Miller, Eds. Cambridge, United Kingdom and New York, NY, USA: Cambridge University Press.

Thomas, G.E., E. Carboni, A.M. Sayer, C.A. Poulsen, R. Siddans, R.G. Grainger (2009), Oxford-RAL Aerosol and Cloud (ORAC): aerosol retrievals from satellite radiometers, in Satellite Aerosol Remote Sensing Over Land, A. A. Kokhanovsky and G. de Leeuw (eds.), Springer, 2009.

Twomey, S.A. (1974). Pollution and the planetary albedo, *Atmospheric Environment*,. **8,** 1251–56.

Veefkind, J. P., de Leeuw, G., Durkee, P. A., Russell, P. B., Hobbs, P. V., & Livingston, J. M. (1999). Aerosol optical depth retrieval using ATSR-2 and AVHRR data during TARFOX. *Journal of Geophysical Research - Atmospheres*, **104** (D2), 2253 – 2260.

Veefkind J.P., G. de Leeuw, P. Stammes , R.B.A. Koelemeijer, (2000). Regional distribution of aerosol over land, derived from ATSR-2 and GOME, *Remote Sensing of Environment*, **74** (3), 377-386.

Vermote E.F., D. Tanré , J.L. Deuze, M. Herman, J.J. Morcrette, (1997): Second Simulation of the Satellite Signal in the Solar Spectrum, 6S: An overview, *IEEE Transactions on Geoscience and Remote Sensing,* **35(3),** 675-686.

Vidot, J., Santer, R., and Aznay, O. (2008) Evaluation of the MERIS aerosol product over land with AERONET, Atmos. Chem. Phys., 8, 7603-7617.

von Hoyningen-Huene W., Freitag M., and Burrows, J.B. (2003), Retrieval of aerosol optical thickness over land surfaces from top-of-atmosphere radiance, *Journal of Geophysical Research*, **108 (D9):** Art. No. 4260.

von Hoyningen-Huene, W. et al. (2006). Simultaneous determination of aerosol and surface characteristics from top-of-atmosphere reflectance using MERIS on board of Envisat, *Advances in Space Research*, **37**, 2172-2177.

Von Hoyningen-Huene, W., et al.: IBAER ATBD, http://www.brockmann-consult.de/beam/software/plugins/baer-1.0.0/BAER_ATBD_NOV-3160-NT-2703_v2.0.pdf

Section C: GlobAlbedo Algorithm Theoretical Basis Document – BBDR

Version 3.1

Document Number: GlobAlbedo_BBDR_ATBD_V3.1 Date 06/06/2012

Distribution:

ESA	O. Leonard	X
	S. Pinnock	X
University College London	J-P. Muller	X
	T. Kennedy	X
	P. Lewis	X
Swansea	P. North	X
Free University of Berlin	J. Fischer	X
	R. Preusker	X
Brockmann Consult	C. Brockmann	X
	N. Fomferra	X
	U. Krämer	X

CHANGE RECORD

ISSUE	DATE	PAGES CHANGED	COMMENTS
A	23/07/10	All new	Draft
1	09/09/2010	All sections	First Issue
2	12/11/2010	All sections	Response to RIDs raised by Simon Pinnock (7/10/12010)
2			Main changes from v1. - Document layout consistent with the rest of the ATBDs (all sections) - Instrument intercalibration (Section 4.1.3 and Appendix II) - Nsky terms (Section 4.1.1 and 4.1.2) - Co-registration errors (Section 4.1.6)
3	15/2/2011	RIDs from UCM adressed	Section 4.1.3
3.1	06/06/2012	All	New global ToC added

25 Introduction

The purpose of this document is to describe the theoretical background of the GlobAlbedo broadband directional reflectance (BBDR) processor. Some requirements to this processor are

- It must be capable of deriving BBDR products from top-of-atmosphere (TOA) radiance or reflectance data measured by the three instruments under consideration in GlobAlbedo. These are ENVISAT/MERIS, ENVISAT/AATSR (and its precursor ATSR-2) and SPOT/VEGETATION.
- The broadband products must be generated for three broadband spectral ranges (visible, near-infrared and shortwave, which correspond to [300-700] nm, [700-3000] nm and [300-3000] nm, respectively).
- The BBDR products must include a reliable tracking of uncertainties within the entire processing including error covariances between the three broadband spectral ranges.

The processor is designed to produce surface spectral directional reflectance (SDR) and the subsequent BBDR products (including uncertainties) from TOA data, but only BBDR are output in the general processing configuration.

Given the high impact of aerosol extinction on the visible and shortwave BBDRs and the complexity of aerosol retrieval over land, it was decided to establish for GlobAlbedo a modular processing approach which would enable the parallel development and refinement of the different pre-processing steps, and in particular of the aerosol and BBDR retrieval processors.

This formal separation (pixel classification-AOD retrieval-reflectance retrieval) is actually performed in most of the atmospheric correction algorithms for optical data over land. In this modular approach, the BBDR processor receives inputs from the GlobAlbedo pixel classification and aerosol retrieval modules, and generates outputs in BEAM-DIMAP format projected to the MODAGG sinusoidal projection system for the latter exploitation by the albedo retrieval module.

26 Applicable and reference documents

Cao, C., Uprety, S., Xiong, J., Wu, A., Jing, P., Smith, D., Chander, G., Nigel Fox, N., Ungar, S. (2010) Establishing the Antarctic Dome C Community Reference Standard Site towards Consistent Measurements from Earth Observation Satellites. Canadian J. of Remote Sensing (in press)).

Dubovik, O., Sinyuk, A., Lapyonok, T., Holben, B. N., Mishchenko, M., Yang, P., Eck, T. F., Volten, H., Muñoz, O. Veihelmann, B., van der Zande, W. J., Leon, J.-F., Sorokin, M., and Slutsker, I. (2006). Application of spheroid models to account for aerosol particle nonsphericity in remote sensing of desert dust. Journal of Geophysical Research- Atmospheres, 111:D11208.

Fell, F. and Fischer, J. (2001). Numerical simulation of the light field in the atmosphereocean system using the matrix-operator method. *Journal of Quantitative Spectroscopy and Radiative Transfer*, 69:351–388.

Fischer, J. and Grassl, H. (1984). Radiative transfer in an atmosphere ocean system: an azimuthally dependent matrix operator approach. *Applied Optics*, 23:1035–1039.

GlobAlbedo-Aer-ATBD-V1.0 (2010). GlobAlbedo: Algorithm Theoretical Basis Document - Aerosol Retrieval. Authors: A. Heckel, P. North, L. Guanter, R. Preusker, J. Fischer, G. López, P. Lewis.

GlobAlbedo-Albedo-ATBD-V1.0 (2010). GlobAlbedo: Algorithm Theoretical Basis Document- Albedo Retrieval. Authors: P. Lewis.

GlobAlbedo-PixID-ATBD-V1.0 (2010). GlobAlbedo: Algorithm Theoretical Basis Document - Pixel Classification. Authors: C. Brockmann, O. Krueger, O. Danne.

Govaerts, Y. M., Wagner, S., Lattanzio, A., and Watts, P. (2010). Joint retrieval of surface reflectance and aerosol optical depth from MSG/SEVIRI observations with an optimal estimation approach: 1. theory. *Journal of Geophysical Research-Atmospheres*, 115:D02203.

Greuell, W. and Oerlemans, J. (2004). Narrowband-to-broadband albedo conversion

for glacier ice and snow: equations based on modeling and ranges of validity of the equations. *Remote Sensing of Environment*, 89:95–105.

Guanter, L., Gómez-Chova, L., and Moreno, J. (2008). Coupled retrieval of aerosol optical thickness, columnar water vapor and surface reflectance maps from ENVISAT/ MERIS data over land. *Remote Sensing of Environment*, 112:2898–2913.

Hess, M., Koepke, P., and Schult, I. (1998). Optical properties of aerosols and clouds: The software package OPAC. *Bulletin of the American Meteorological Society*, 79:831–844.

Holben, B. N., Eck, T. F., Slutsker, I., Tanre, D., Buis, J. P., Setzer, A., Vermote, E., Reagan, J. A., Kaufman, Y., Nakajima, T., Lavenu, F., Jankowiak, I., and Smirnov, A. (1998). AERONET – a federated instrument network and data archive for aerosol characterization. *Remote Sensing of Environment*, 66:1–16.

Hu, B., Lucht, W., and Strahler, A. H. (1999). The interrrelationship of atmospheric correction of reflectances and surface BRDF retrieval: a sensitivity study. *IEEE Transactions on Geoscience and Remote Sensing*, 37:724–738.

Hudson, S.R., G. Warren, S.G., Brandt R.E., Grenfell, T.C., Six, D. (2006). Spectral bidirectional reflectance of Antarctic snow: Measurements and parameterization, *Journal of Geophysical Research,* 111: D18106

Kaufman, Y. J. (1989). The atmospheric effect on remote sensing and its correction. In Asrar, G., editor, *Theory and Applications of optical Remote Sensing*, pages 336–428. Wiley and Sons, New York.

Liang, S. (2000). Narrowband to broadband conversions of land surface albedo. I algorithms. *Remote Sensing of Environment*, 76:213–238.

Mekler, Y. and Kaufman, Y. J. (1982). Contrast reduction by atmosphere and retrieval of nonuniform surface reflectance. *Applied Optics*, 21:310–316.

Peltoniemi, J. I., Manninen, T., Suomalainen, J., Hakala, T., Puttonen, E., and Riihelä, A. (2010). Land surface albedos computed from BRF measurements with a study of conversion formulae. *Remote Sensing*, 2:1918–1940.

Samain, O., Geiger, B., and Roujean, J.-L. (2006). Spectral normalization and fusion of optical sensors for the retrieval of BRDF and albedo: application to VEGETATION, MODIS and MERIS data sets. *IEEE Transactions on Geoscience and Remote Sensing*, 44:3166–3179.

Tanré, D., Herman, M., and Deschamps, P. Y. (1983). Influence of the atmosphere on space measurements of directional properties. *Applied Optics*, 21:733–741.

Tucker, C. J. (1979). Red and photographic infrared linear combinations for monitoring vegetation. *Remote Sensing of Environment*, 8:127–150.

Vermote, E. F., El-Saleous, N., Justice, C. O., Kaufman, Y. J., Privette, J. L., Remer, L., Roger, J. C., and Tanr ´e, D. (1997a). Atmospheric correction of visible to middle infrared EOS-MODIS data over land surface: Background, operational algorithm and validation. *Journal of Geophysical Research*, 102:17131–17141.

Vermote, E. F., Tanré, D., Deuzé, J. L., Herman, M., and Morcrette, J. J. (1997b). Second Simulation of the Satellite Signal in the Solar Spectrum, 6S: An overview. *IEEE Transactions on Geoscience and Remote Sensing*, 35:675–686.

Wang, Y., Lyapustin, A. I., Privette, J. L., Cook, R. B., SanthanaVannan, S. K., Vermote, E. F., and Schaaf, C. L. (2010). Assessment of biases in MODIS surface reflectance due to Lambertian approximation. *Remote Sensing of Environment*, 114:2791–2801.

27 Definitions and abbreviations

27.1 Acronyms and Abbreviations

AATSR	Advanced Along-Track Scanning Radiometer
AOD550	Aerosol Optical Depth in 550 nm
BBDR	Broadband Directional Reflectance
BRDF	Bidirectional Reflectance Distribution Function
CWV	Columnar water vapor
ELEV	Surface elevation above sea level
LUT	Look-up table
MERIS	MEdium Resolution Imaging Spectrometer
MOMO	Matrix Operator MOdel
N2B	Narrow to broadband
NDVI	Normalized Difference Vegetation Index
NIR	Near-infrared broadband range (700-3000 nm)
OZO	Columnar ozone
RAA	Relative Azimuth Angle
SDR	Surface Spectral Directional Reflectance
SRF	Spectral Response Function
SW	Shortwave broadband range (300-3000 nm)
SZA	Sun Zenith Angle
TOA	Top Of Atmosphere
VGT	Vegetation instrument
VIS	Visible broadband range (300-700 nm)
VNIR	Visible and near-infrared
VZA	View Zenith Angle

27.2 Terms and Symbols

- R_λ^* - Top-of-atmosphere spectral directional reflectance
- R_λ - Surface spectral directional reflectance, SDR
- R_Λ - Broadband directional reflectance, BBDR
- σ_λ - SDR error matrix

- σ_Λ - BBDR error matrix
- σ^{rel}_Λ - BBDR relative error matrix
- J_x - Gradient $\partial R_\lambda / \partial x$, with x = AOD, CWV, OZO
- $k_x(\Omega_v, \Omega_s)$ - BRDF model kernel x, with x = VOL (volumetric RossThick) or GEO (geometric LiSparseModisReciprocal)
- $K'_x(\Omega_s)$ - Directional-hemispherical integral of $k_x(\Omega_v, \Omega_s)$ for direction Ω_s, with x = VOL, GEO
- $K'_x(\Omega_v)$ - Hemispherical-Directional integral of $k_x(\Omega_v, \Omega_s)$ for direction Ω_v, with x = VOL, GEO
- K_x - Hemispherical-hemispherical integral of $k_x(\Omega_v, \Omega_s)$, with x = VOL, GEO
- $N_{sky\downarrow}(\Omega_s)$ ($N_{sky\uparrow}(\Omega_v)$) - Downward (upward) normalised sky radiance distribution
- $D_{0\lambda\downarrow}$ ($D_{0\lambda\uparrow}$) - Fraction of diffuse-to-total downward (upward) radiation at ground.

28 Algorithm Theoretical Background

28.1 Theoretical description

28.1.1 Formulation of the atmosphere-surface radiative transfer

The apparent spectral directional reflectance of the coupled surface-atmosphere system (R_λ^*) is related to the radiance L_λ measured by a satellite at the TOA by

$$R_\lambda^*(\Omega_v, \Omega_s) = \frac{\pi L_\lambda(\Omega_v, \Omega_s)}{\mu_s E_{s,\lambda}}. \quad (5.1)$$

where $E_{s,\lambda}$ is the extraterrestrial irradiance at the time of the measurement and (Ω_v, Ω_s) denote the observation and illumination directions, which can also be expressed as (μ_v,μ_s,ϕ), where μ_v is the cosine of the view zenith angle (VZA), μ_s the cosine of the sun zenith angle (SZA) and ϕ is the relative azimuth angle (RAA). The subscript λ refers in this text to the "narrowband" spectral interval specified by the spectral response function (SRF) of a given spaceborne sensor.

In the most general case of solar radiation interacting with a non-Lambertian surface, the TOA reflectance can be formulated by four additive contributions (Tanré et al., 1983; Vermote et al., 1997b): (1) the photons directly transmitted from the sun to the target and directly reflected back to the sensor, (2) the photons scattered by the atmosphere then reflected by the target and directly transmitted to the sensor, (3) the photons directly transmitted to the target but scattered by the atmosphere on their way to the sensor, and finally (4) the photons having at least two interactions with the atmosphere and one with the target. Following the notation in GlobAlbedo-Albedo-ATBD-V1.0 (2010), this leads to the expression

$$R_\lambda^*(\Omega_v, \Omega_s) = R_{atm,\lambda}(\Omega_v, \Omega_s) + \gamma_\lambda(-\mu_s)\gamma_\lambda(\mu_v)\left[\frac{\bar{\rho}_\lambda R_\lambda''^2}{1 - \bar{\rho}_\lambda R_\lambda''} + R_\lambda'(\Omega_v, \Omega_s)\right] \quad (5.2)$$

where $R_{atm,\lambda}$ is the atmospheric intrinsic reflectance; $\gamma_\lambda(-\mu_s)$, $\gamma_\lambda(\mu_v)$ are the total atmospheric transmittance in the downward and upward direction, respectively; ρ_λ is the atmospheric spherical albedo, which gives the reflectance of the atmosphere for isotropic light entering it from the surface; R'_λ and R''_λ are functions of the surface bidirectional reflectance distribution function (BRDF):

- R'_λ includes the BRDF $R_\lambda(\Omega_v, \Omega_s)$ and the so-called atmosphere-surface coupling terms, which are $R'_\lambda(\mu_v)$, $R'_\lambda(\mu_s)$ and R_λ for irradiance-weighted hemispherical-directional, directional-hemispherical and hemispherical-hemispherical reflectance, respectively,

$$R''_\lambda(\Omega_v,\Omega_s) = (1-D_{0\lambda\downarrow})(1-D_{0\lambda\uparrow})R_\lambda(\Omega_v,\Omega_s) + (1-D_{0\lambda\downarrow})D_{0\lambda\uparrow}\bar{R}'_\lambda(\mu_v) + D_{0\lambda\downarrow}(1-D_{0\lambda\uparrow})\bar{R}'_\lambda(\mu_s) + D_{0\lambda\downarrow}D_{0\lambda\uparrow}\bar{R}_\lambda \quad (5.3)$$

$D_{0\lambda\downarrow}$ ($D_{0\lambda\uparrow}$) are the ratio of diffuse-to-total transmittance in the downward (upward) direction weighting the contribution of each term to R'_λ.

- R''_λ is the hemispherical-hemispherical reflectance for radiation involving at least two interactions between the atmosphere and the surface. It can be approximated by the bihemispherical reflectance R_λ if the target is assumed to be homogeneous or if the local spatial averaging of the target and its environment is ignored.

The ultimate purpose of atmospheric correction is the inversion of the surface BRDF $R_\lambda(\Omega_v, \Omega_s)$ from the TOA reflectance R_λ^* derived from the radiance measured by the sensor at the satellite. However, Eq. 5.2 is not invertible in R_λ, which is included in the angular integrals leading to $R'_\lambda(\mu_v)$, $R'_\lambda(\mu_s)$ and R_λ. These integrals cannot be performed if $R_\lambda(\Omega_v, \Omega_s)$ is not known for the entire hemisphere.

Some approaches can be adopted for the estimation of an a priori $R_\lambda(\Omega_v, \Omega_s)$ based on either multi-angular acquisitions or in the use of ancillary surface products (Vermote et al., 1997a). However, these approaches are not usable for operational atmospheric correction algorithms of single-view instruments, which cannot rely on existing external surface products, nor involve temporal or spatial data composites. For this reason, a uniform Lambertian surface is normally assumed as a basis for the modelling of the atmosphere-surface radiative transfer. Under this assumption Eq. 5.2 becomes

$$R^*_\lambda(\Omega_v,\Omega_s) = R_{atm,\lambda}(\Omega_v,\Omega_s) + \gamma_\lambda(-\mu_s)\gamma_\lambda(\mu_v)\frac{R_\lambda(\Omega_v,\Omega_s)}{1-\bar{\rho}_\lambda R_\lambda(\Omega_v,\Omega_s)} \quad (5.4)$$

which can be inverted analytically to retrieve $R_\lambda(\Omega_v, \Omega_s)$ from R_λ^* and the atmospheric parameters $R_{atm,\lambda}$, γ_λ and ρ_λ.

As discussed in GlobAlbedo-Albedo-ATBD-V1.0 (2010), the Lambertian equivalent reflectance $R_\lambda(\Omega_v, \Omega_s)$ derived from Eq. 5.4, which is taken as SDR in the GlobAlbedo processing chain, represents a smoothed version of the surface BRDF. Relative errors in reflectance retrieval were shown to be up to 15% for turbid atmospheres (Hu et al., 1999). In turn, Wang et al. (2010) estimated the slope of regression of Lambertian surface reflectance with respect to the actual bidirectional reflectance factor to be about 0.85 in the red and 0.6 in the green bands.

This error in R_λ associated to the Lambertian assumption will be reduced at the albedo retrieval step by the use of linear kernel models weighted with the distribution of sky radiance by means of a formulation analogue to that in Eq. 5.3. Using the formulation in GlobAlbedo-Albedo-ATBD-V1.0 (2010) (Eq. 13), the sky radiance-weighted volumetric (RossThick) and geometric (LiSparseModisReciprocal) kernels $K'_{vol,geo}$ are expressed as

$$K'_r(\Omega_r,\Omega_s) = (1-D_{0s\downarrow})(1-D_{0s\uparrow})k_r(\Omega_r,\Omega_s) - (1-D_{0s\downarrow})D_{0s\uparrow}\bar{K}'_r(\mu_r) + D_{0s\downarrow}(1-D_{0s\uparrow})\bar{K}'_r(\mu_s) + D_{0s\downarrow}D_{0s\uparrow}\bar{\bar{K}}_r \quad (5.5)$$

where k_x are the RossThick and LiSparseModisReciprocal kernels in their original form, and

$$\bar{K}'_r(\Omega_s) = \int_{\Omega_s} k_r(\Omega_r,\Omega_s)N_{sky\uparrow}(\Omega_s)d\Omega_s \quad (5.6)$$

$$\bar{K}'_r(\Omega_r) = \int_{\Omega_i} k_r(\Omega_r,\Omega_i)N_{sky\downarrow}(\Omega_i)d\Omega_i \quad (5.7)$$

$$\bar{\bar{K}}_r = \int_{\Omega_r} d\Omega_r \int_{\Omega_i} k_r(\Omega_r,\Omega_i)d\Omega_i \quad (5.8)$$

The term $N_{sky\downarrow}$ ($N_{sky\uparrow}$) is the normalised downwelling (upwelling) sky-radiance. This modified version of the kernels is designed so that the errors due to the Lambertian approach are cancelled out at the albedo retrieval step. The K terms in Eq. 5.5 are also an output of the GlobAlbedo BBDR processor.

28.1.2 Atmospheric look-up tables

The atmospheric parameters $R_{atm,\lambda}$, $\gamma_\lambda(\mu_v)$, $\gamma_\lambda(-\mu_s)$ and ρ_λ in Eq. 5.4 and the $D_{0\lambda\downarrow}$ and $D_{0\lambda\uparrow}$ terms in Eq. 5.3 are stored in look-up tables (LUTs) for fast access during the processing. A series of LUTs have been compiled for each one of the three instruments under consideration in GlobAlbedo:

- LUT-1 (x7 aerosol models): Provides $R_{atm,\lambda}$, $\gamma_\lambda(\mu_v)\gamma_\lambda(-\mu_s)$, ρ_λ, $D_{0\lambda\downarrow}$ and $D_{0\lambda\uparrow}$ as a function of VZA, SZA, PHI, height of the surface (HSF) and aerosol optical depth at 550 nm (AOD550). No gaseous absorption is considered, but extinction is only calculated for scattering and aerosol absorption. LUT-1 is intended for aerosol and SDR retrieval.
- LUT-2 (x7 aerosol models): Provides the gradient $J_{AOD} = \partial R_\lambda / \partial AOD550$ as a function of R_λ and the same input parameter grid of LUT-1. It is intended for error propagation along the SDR retrieval process.
- LUT-3: Provides total gaseous transmittance T_g as a function of the geometric air-mass factor (AMF), the water vapor column content (CWV) and the ozone column content (OZO). It is intended for gas correction prior to aerosol and SDR retrieval.
- LUT-4: Provides the gradients $J_{CWV} = \partial R_\lambda / \partial CWV$ and $J_{OZO} = \partial R_\lambda / \partial OZO$ as a function of R_λ and the same input parameter grid of LUT-3. It is intended for error propagation along the SDR retrieval process.
- LUT-5: Provides the Nsky-weighted $K'_x(\Omega_s)$ ($K'_x(\Omega_v)$) kernel integrals as a function of SZA (VZA), HSF, AOD550 and broadband spectral range. The invariant K_x is also provided by these LUTs.

The spectral response functions of the three instruments used for the compilation of the LUTs are displayed in Fig. 9.

LUT-1 and LUT-2 have been compiled with the Matrix Operator MOdel (MOMO) radiative transfer code (Fischer and Grassl, 1984; Fell and Fischer, 2001). MOMO is a widely accepted radiative transfer code which provides all the features required for atmospheric radiative transfer simulations in GlobAlbedo. It is currently part of the models used to generate the operational auxiliary data tables in the MEdium Resolution Imaging Spectrometer (MERIS) ground segment of ESA. MOMO has been successfully validated and applied for the development of new remote sensing techniques, e.g. to perform the radiative transfer calculations for the development of several MERIS remote sensing algorithms for ESAs ground- segment, particularly for the water vapour, clouds and aerosol retrieval algorithms. It is based on the adding-doubling principle.

The six aerosol models described in Govaerts et al. (2010) and a continental model built up from the Optical Properties of Aerosols and Clouds (OPAC) aerosol model database (Hess et al., 1998) have been used for the generation of LUT-1 and LUT-2. The optical properties of the seven models are summarised in Table 1. The six models from Govaerts et al. (2010) result from the clustering of a large data set of AERONET observations (Holben et al., 1998) according to the single scattering albedo and phase function of each observation. The aerosol models derived with this procedure represent combinations of absorbing and non-absorbing aerosol and of spherical and non-spherical particles. The single scattering albedo and phase function of the non-spherical models were calculated with a scattering code based on spheroid models (Dubovik et al., 2006), while the Mie code built-in in MOMO was used for the spherical models.

Table 1: Properties of the aerosol models used to generate LUT-1 and LUT-2. Each of the two modes compounding each aerosol model is defined by the volume median radius r_v (μm), the radius standard deviation σ (μm), the volume concetration C_v (μm, % for the Continental I-80 model) and the spectral refractive index n (provided at 440 nm in the table for reference purposes).

		Fine Mode				Coarse Mode			
	Model	r_v	σ	C_v	n(440nm)	r_v	σ	C_v	n(440nm)
Spherical	Contin. I-80	0.021	2.2400	0.950	1.40-0.002i	0.471	2.510	0.050	1.53-0.008i
	ABSORB	0.155	0.404	0.083	1.46-0.018i	3.012	0.649	0.051	1.46-0.018i
	MODABS	0.221	0.497	0.094	1.42-0.009i	2.886	0.598	0.050	1.42-0.009i
	NONABS	0.179	0.426	0.101	1.42-0.006i	3.004	0.623	0.039	1.42-0.006i
Non-Spherical	SMARAD	0.145	0.500	0.037	1.50-0.005i	2.423	0.617	0.262	1.50-0.005i
	MEDRAD	0.172	0.636	0.033	1.48-0.005i	1.961	0.549	0.364	1.48-0.005i
	LARRAD	0.202	0.627	0.043	1.43-0.003i	1.978	0.527	0.521	1.43-0.003i

The impact of the particular aerosol model on Ratm,λ is illustrated in Fig. 11. The slope of the derivative of Ratm,λ with respect to AOD550 changes with the model, which shows that different values of AOD550 would be retrieved by different aerosol models. This implies that the aerosol model used in surface reflectance retrieval must be the same model used in the prior aerosol retrieval in order to minimise the different Ratm,λ given for the same AOD550 by the different aerosol models.

The impact of the particular aerosol model on Ratm,λ is illustrated in Fig. 11. The slope of the derivative of Ratm,λ with respect to AOD550 changes with the model, which shows that different values of AOD550 would be retrieved by different aerosol models. This implies that the aerosol model used in surface reflectance retrieval must be the same model used in the prior aerosol retrieval in order to minimise the different Ratm,λ given for the same AOD550 by the different aerosol models.

The continental model-I is selected as default to specify the aerosol extinction properties. It is considered that the characterisation of the downward irradiance and the atmospheric path reflectance can be achieved with enough accuracy with this aerosol model as long as the same model is used for the estimation of AOD by the aerosol retrieval processor. The AOD550 value to be ingested by the BBDR retrieval processor will then be consistent with the continental-I model so that the downward irradiance and the atmospheric path reflectance provide a reliable representation of the actual atmospheric conditions. However, the option to process some areas around the globe with a different aerosol model, e.g. with a model made of large non-spherical particles (yet to be determined), is kept as an option by the BBDR processor.

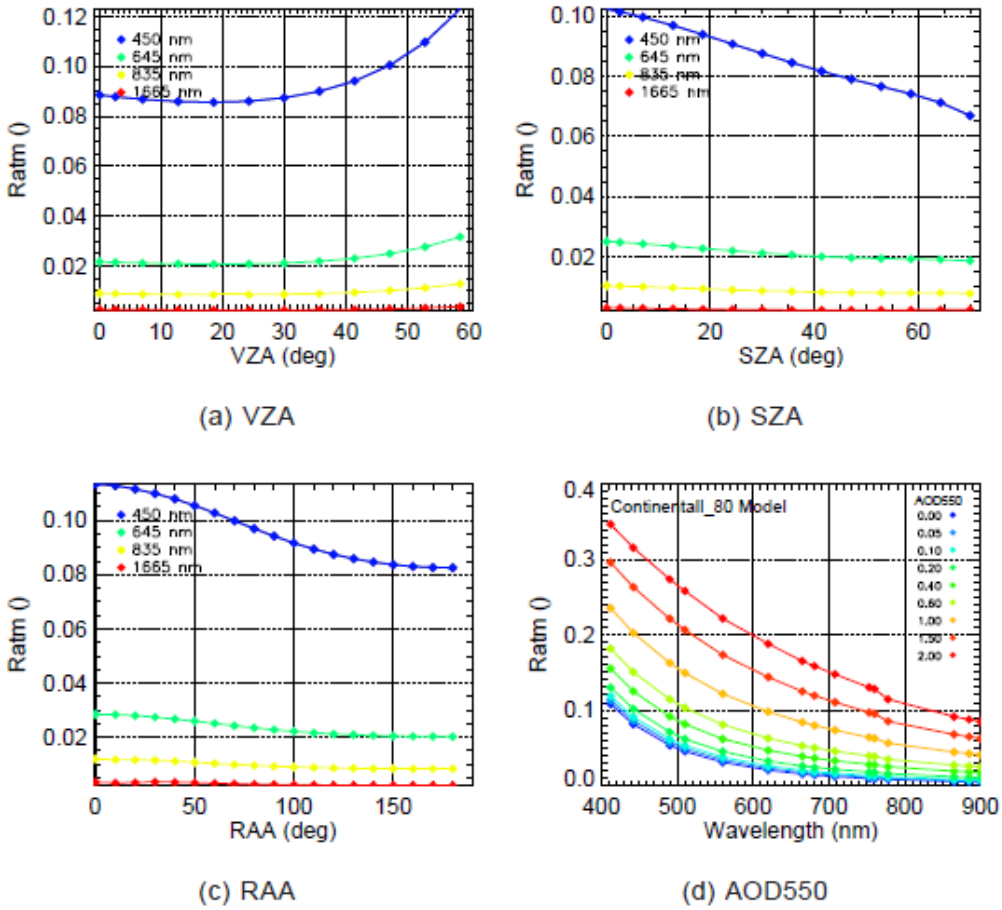

Figure 1: $R_{atm,\lambda}$ as a function of VZA, SZA and RAA for the 4 VGT channels as extracted from LUT-1 (Continental I-80 aerosol model). The reference input configuration is VZA=30°, SZA=30°, RAA=120°, ELEV=200 m and AOD550=0.2.

The distribution of the breakpoints in LUT-1 and LUT-2 has been set so that the maximum variation range in the parameter space is covered. The resulting distribution of input parameters in LUT-1 and LUT-2 is shown in Table 2 and in Fig. 1. Given a certain set of inputs, the values of the atmospheric parameters are calculated through linear interpolation in the 5 directions of the input parameter space. It must be remarked that possible errors due to deviations from linearity at any combination of optical parameters and input values tend to compensate along the whole atmospheric correction process. For example, if a small bias in path radiance is introduced by linear interpolation during the estimation of AOT, it is cancelled off to a large extent when the resulting AOT value is re-inserted in the process to calculate surface reflectance, as the same LUT and interpolation technique are used in both steps.

Table 2: Distribution of input parameters in LUT-1 and LUT-2.

Input parameter	Sampling	Number of breakpoints
VZA	[0 - 60] deg	12
SZA	[0 - 70] deg	14
RAA	[0 - 180] deg	18
ELEV	[0, 700, 2500, 8000] m	3
AOD550	0 - 2	9

LUT-3 and LUT-4 are calculated with the 6S (Second Simulation of the Satellite Signal in the Solar Spectrum) radiative transfer code (Vermote et al., 1997b). This code is intended for fast radiative transfer calculations at a relatively coarse internal spectral sampling of 2.5 nm. The atmospheric transmittance due to gaseous absorption (water vapour, ozone, oxygen, carbon dioxide, methane and nitrous oxide are included in 6S) has been calculated with 6S as a function of the geometric AMF, CWV and OZO for the spectral response functions of MERIS, AATSR and VGT. The geometric AMF is calculated for seven pairs of illumination and observation angles between 0 and 70◦, while four breakpoints are used for CWV ([0, 1.5, 3, 4.5] g cm^{-2}) and OZO ([0.1, 0.3, 0.5, 0.6] atm cm^{-1}). Sample transmittance functions for MERIS are plotted in Fig. 2. The 15 MERIS bands are plotted for illustration purposes, although bands 11 and 15 will not be processed to generate the GlobAlbedo products because of the high contamination by oxygen and water vapour absorptions, respectively.

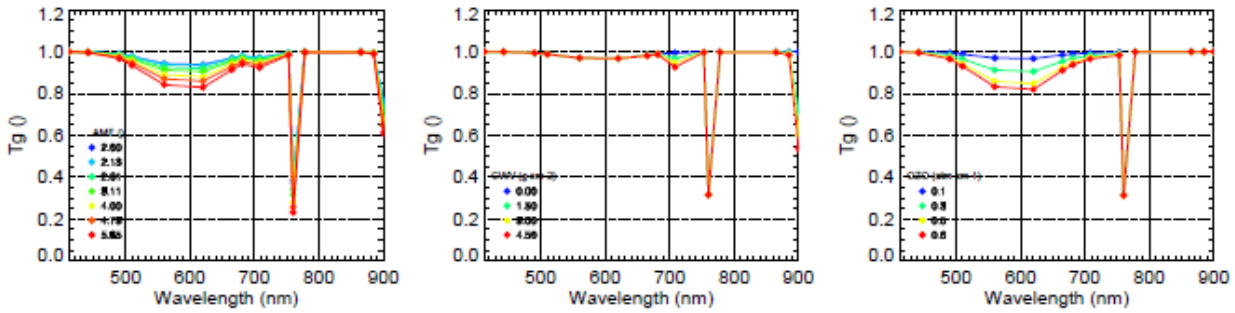

Figure 2: Sample spectral T_g as a function of AMF, CWV and OZO for the 15 MERIS channels as extracted from LUT-3.

The gradients J_{AOD}, J_{CWV} and J_{OZO} used for error propagation are provided by LUT-2 and LUT-4 for the same input parameters as LUT-1 and LUT-3, respectively. The value of these gradients depends strongly on surface reflectance. For this reason, each J is stored in the LUTs as a pair J_0,J_1, which are the offset and the slope of a linear relationship between J and R. Sample J_{AOD}, J_{CWV} and J_{OZO} are displayed in the Fig. 12 of Section 7.

An example of the Nsky-weighted integral of the kernels K'x(Ωs), K'x(Ωv) is displayed in Fig. 3. It can be observed that K'x(Ωs) and K'x(Ωv) are not interchangeable for the most general case of non-isotropic atmospheres, especially for the geometric kernel. Sample Nsky patterns are displayed in Fig. 13 for upward and downward radiation, different illumination and observation angles, aerosol models and spectral channels.

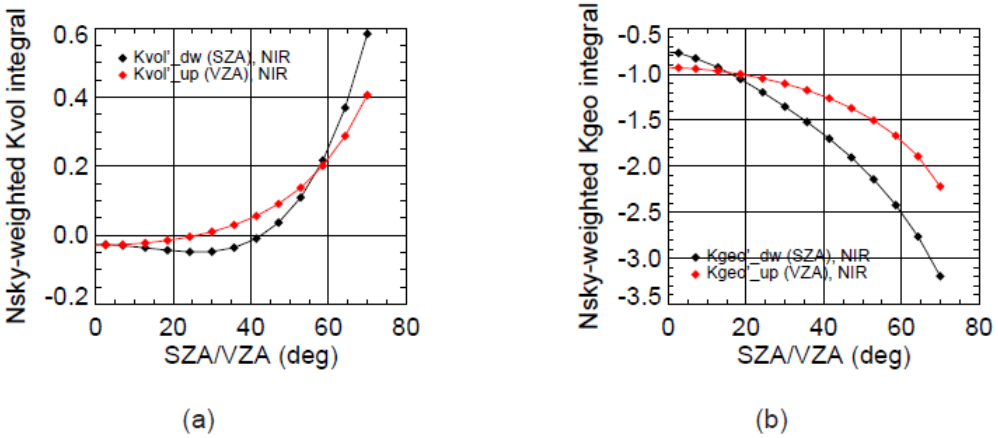

Figure 3: Example of $\bar{K}'_x(\Omega_s)$ and $\bar{K}'_x(\Omega_v)$ as a function of illumination and observation angle, respectively, in the NIR broadband range.

28.1.3 Instrument intercalibration

The first processing step is the refinement of the radiometric calibration in order to guarantee the consistency of the data from the three instruments. The TOA data from the three instruments are re-calibrated with the coefficients obtained from the intercomparison exercise performed over Dome-C. Based on a-priori instrument specifications and onboard calibration means, MERIS is considered the calibration reference. AATSR and VGT are calibrated against MERIS with coefficients 1/[1.0253, 1.0093, 1.0265, 1] and 1/ [1.012, 0.953, 0.971, 1], respectively. The methodology and the main results of the intercomparison exercise leading to these coefficients are described in the Appendix II of this document.

28.1.4 SDR and NDVI retrieval

Spectral directional reflectance R_λ is derived from TOA reflectance by means of the analytical inversion of Eq. 5.4,

$$R_\lambda(\Omega_v,\Omega_s) = \frac{R^*_\lambda(\Omega_v,\Omega_s) - R_{atm,\lambda}(\Omega_v,\Omega_s)}{\gamma_\lambda(-\mu_s)\gamma_\lambda(\mu_v) + \bar{\rho}_\lambda\left[R^*_\lambda(\Omega_v,\Omega_s) - R_{atm,\lambda}(\Omega_v,\Omega_s)\right]} \quad (5.9)$$

$R_\lambda{}^*(\Omega_v, \Omega_s)$ is calculated from TOA radiance with Eq. 5.1. $R_\lambda{}^*(\Omega_v, \Omega_s)$ is first corrected from gaseous absorption with LUT-3 for a set of input AMF, CWV and OZO. The atmospheric parameters $R_{atm,\lambda}$, γ_λ and ρ_λ

are provided by LUT-1 per-pixel, being the input VZA, SZA, RAA, ELEV and AOD550 also provided on a per-pixel basis. For the correction of gas absorptions, one single spatially-averaged value is used for either CWV or OZO, depending on the sensor. For MERIS and AATSR, AMF and CWV are considered pixel-wise, and a mean value representative of the imaged area is used for OZO. For VGT, AMF and OZO are considered per-pixel and CWV spatially-constant. This is done in order to enable fast 2-D interpolations rather than more time-consuming 3-D interpolations. The selection of CWV or OZO as the spatially-constant parameter is performed according to which one has the lowest relative impact on reflectance, which is illustrated in the J gradients displayed in Fig. 12 of Section 7.

No correction of adjacency effects (Mekler and Kaufman, 1982; Kaufman, 1989) has been found to be necessary for the GlobAlbedo SDR product, as this is focused on land surfaces and the spatial resolution of the three instruments under consideration is comparable to the atmospheric point spread function.

The normalized difference vegetation index (NDVI) (Tucker, 1979) is also part of the GlobAlbedo products. It is defined as

$$\mathrm{NDVI} = \frac{R_{nir} - R_{red}}{R_{nir} + R_{red}}. \quad (5.10)$$

where R where R_{nir} and R_{red} represent the SDR in the near-infrared and red spectral regions, respectively. The selected red and near-infrared narrow bands are 7 and 13 for MERIS (centered at 665 and 865 nm, respectively), 2 and 3 for AATSR (centered at 665 and 865 nm, respectively) and 2 and 3 for VGT (centered at 645 and 835 nm, respectively).

However, the spectral difference in both the channel position and width for the three instruments is expected to cause biases in the NDVI (Samain et al., 2006). For this reason, the NDVI expression in Eq. 5.10 is calculated in GlobAlbedo as

$$\mathrm{NDVI}_{sc} = \frac{b\,R_{nir} - a\,R_{red}}{R_{nir} + R_{red}}. \qquad \mathrm{red} \equiv 665\ nm,\ \mathrm{nir} \equiv 865\ nm. \quad (5.11)$$

NDVI_{sc} represents a spectrally-corrected NDVI. The a, b parameters are intended to weight R_{red} and R_{nir} so that the NDVI calculated from the three sensors is comparable. The procedure followed to calculate a, b for each sensor consists in the use of a spectral library of vegetation, bare soil and snow/ice spectral reflectance patterns provided at a high spectral resolution to calculate a reference NDVI for each pattern. The reference spectral wavelengths were 665 and 865 nm for red and near-infrared, respectively, in order to take advantage of the MERIS and AATSR channels centered at those values. The a, b coefficients are calculated by means of linear regression between the NDVI derived from the high spectral resolution spectra and the red and near-infrared reflectance

derived from the same set of reflectance spectra after convolution to the instrument spectral response function. Results from this procedure are shown in Fig. 4. The NDVI calculated from the R_{red} and R_{nir} sampled at the instrument channels, before and after the spectral correction, is compared with the NDVI derived from the high resolution reflectance patterns. The data in the x-axis is the same for the three cases. It can be stated that the correction is negligible for MERIS and AATSR, because 665 and 865 nm (at which MERIS and AATSR channels are centered) were taken as reference wavelengths, and because the bandwidths are relatively narrow in both instruments. However, a noticeable improvement is found in the case of VGT, whose red and near-inrfared channels are at 645 and 835 nm and have a bandwidth of 70 and 110 nm, respectively.

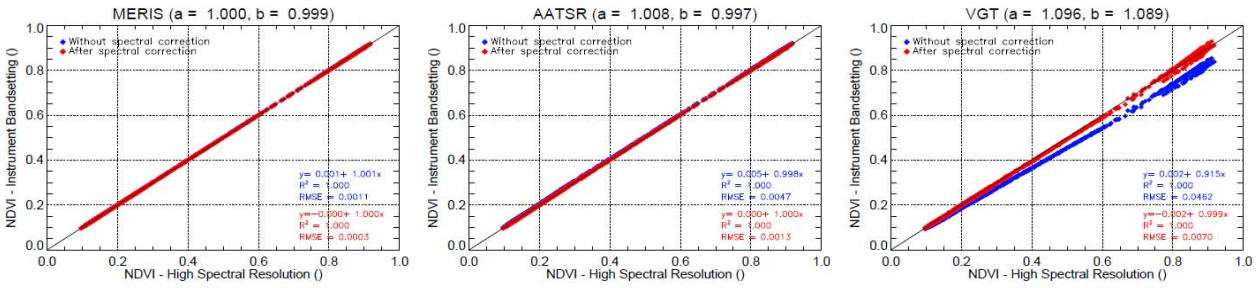

Figure 4: Comparison of the NDVI calculated with and without spectral correction with the reference NDVI generated from the high spectral resolution spectral patterns. The data in the x-axis is the same for the three instruments.

28.1.5 Narrow-to-broadband conversion (BBDR retrieval)

Broadband directional reflectance (BBDR, R_Λ) is directly derived from SDR data by means of a linear narrow-to-broadband (N2B) conversion process. The output from this conversion directional reflectance integrated in three broadband spectral ranges: visible (VIS, 300-700 nm), near-infrared (NIR, 700-3000 nm) and shortwave (SW, 300-3000 nm).

The linear N2B conversion has the form

$$R_\Lambda = \sum_\lambda \alpha_\lambda(\Lambda) R_\lambda + \alpha_0(\Lambda). \quad (5.12)$$

where α is the vector of N2B conversion coefficients and Λ is each of the three broadband regions.

The procedure to calculate the N2B coefficients is based on that proposed by Liang (2000). The assumption is that a reduced number of spectral measurements linearly weighted can be used to perform spectral

integrals in broad spectral regions. Furthermore, the procedure by Liang (2000) assumes that a single set of conversion coefficient is valid for a wide range of illumination and atmospheric conditions.

Under those assumptions, the procedure to calculate the set of α coefficients for each Λ is based on simulating a large data base of theoretical R_Λ by means of

$$R_\Lambda = \frac{\int_\Lambda F^\downarrow(\lambda) R(\lambda) d\lambda}{\int_\Lambda F^\downarrow(\lambda) d\lambda} \quad (5.13)$$

where $F^\downarrow(\lambda)$ and $R(\lambda)$ are the incoming irradiance and surface reflectance in the 300-3000 nm spectral range with a spectral sampling of 2.5 nm. A large number of R_Λ values is produced for different illumination and atmospheric conditions (variations in SZA, ELEV, AOD550 and CWV) and land surface reflectance patterns. Ranges of variation ranges are SZA=[0, 15, 30, 45, 60] deg, ELEV= [0., 700, 2000] m, AOD550=[0., 0.1, 0.2, 0.3, 0.6, 1.0, 1.5, 2.0] and CWV=[0., 0.5, 1, 2, 3, 4, 5] g cm-2, which total 840 cases. The influence of ozone has been considered negligible for this study. The at-surface downward irradiance $F \downarrow (\lambda)$ in Eq. 5.13 is calculated for this combination of input parameters as

$$F^\downarrow(\lambda) = \mu_s E_s(\lambda) \tau(-\mu_s; \lambda) \left[1 + \frac{\bar{\rho}(\lambda) R(\lambda)}{1 - \bar{\rho}(\lambda) R(\lambda)} \right] \quad (5.14)$$

Concerning surface reflectance, a spectral library consisting of 905 spectra extracted from existing spectral libraries and real hyperspectral data acquired by the HyMAP airborne imaging spectrometer has been used. A subset of those reflectance spectra is displayed in Fig. 5. The reflectance patterns in the library are focused on characteristic vegetation and soil spectra. A subset of ice/snow patterns (coarse, fine, frost and medium spectra from the JHU spectral library) is also included in order to account for the brightest surfaces. It is considered that this range of spectral reflectance patterns can cover most of the natural land surfaces for which the BBDR product is to be generated. A smaller number of 256 spectra was used by Liang (2000).

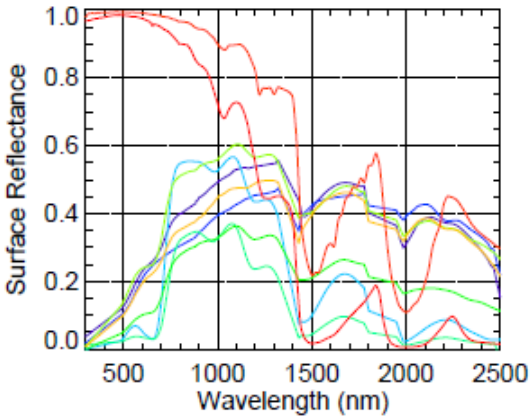

Figure 5: Sample set of surface reflectance spectra from the spectral library used for the calculation of the narrow-to-broadband conversion coefficients.

These input high resolution spectra are convolved to the instrument spectral response function (convolution from R(λ) to R_λ in the expressions above) so that the N2B conversion coefficients α(Λ) can be calculated by linear regression of R_λ (840 atmospheric cases × 905 reflectance patterns) and R_Λ (905 patterns). The result is a single set of N2B conversion coefficients for each Λ so that the N2B conversion process is independent of the atmospheric state. Errors in the conversion process are then mostly given by the deviation of each single atmospheric state from the average atmospheric conditions represented by the coefficients. This is illustrated in Fig. 6, where theoretical and retrieved BBDR for the VGT instrument, the NIR spectral range and the three types of incoming irradiance are compared. The N2B conversion performed with a single set of α for all the atmospheric conditions is compared with the equivalent case presented in Liang (2000) and with the result that would be obtained if the N2B conversion were performed independently for each atmospheric case. The differences observed between the first two cases are in principle due to the differences in the data bases used for the calculation of the coefficients: the retrieved GlobAlbedo BBDRs in the plot are produced for the same data base used for the calculation of the coefficients, so a better performance is expected than with Liang's coefficients. On the other hand, the large improvement in the N2B conversion performance when the atmospheric conditions are taken into account can also be noted in Fig. 6. However, the particular nature of the GlobAlbedo processing chain, which performs the angular integration for albedo retrieval in the broadband space and that requires BBDRs to be independent of the atmospheric conditions (GlobAlbedo-Albedo-ATBD-V1.0, 2010), does not enable to take the knowledge of the atmospheric state into account when performing the N2B conversion. The estimation of the associated error is considered in the total BBDR error budget.

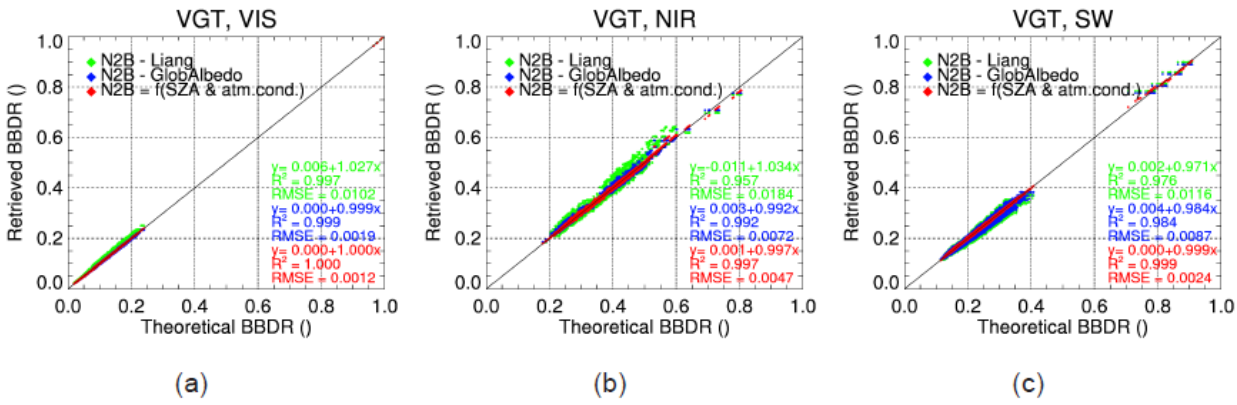

Figure 6: Comparison between the theoretical BBDR given by Eq. 5.13 and the retrieved BBDR generated from the calculated α coefficients for VGT in the three broadband spectral ranges. The comparison is provided for N2B conversion performed for all the simulated atmospheric conditions, for N2B conversion performed independently for each atmospheric state in the training data base and for N2B conversion based on the coefficients calculated by Liang (2000).

The fits for the calculation of the $\alpha_\lambda(\Lambda)$ coefficients for GlobAlbedo are presented in Section 7. The fits are in general comparable to those presented in Liang (2000). The N2B conversion presents small errors for the three instruments in the VIS spectral range, while the errors are larger for the NIR and SW regions.The different SZAs do not have a big influence in the conversion. This was also stated by Peltoniemi et al. (2010). It must be remarked that the slope of the fit is very close to 1 in all cases, which validates the conversion for both low and high reflectance values. For this reason, no additional set of specific conversion coefficients for only snow and ice pixels (Greuell and Oerlemans, 2004) has been considered as necessary. On the other hand, it can also be noted that a similar performance of the N2B conversion is found in the three spectral ranges for the three instruments. No inter-instrument biases in the BBDR products are then expected to be caused by the N2B conversion process.

The N2B conversion equations are listed below. The negative values obtained for the weighted of some of the bands result from the non-constrained linear regression. Even though some sort of non-negative least squares (NNLS) algorithm could have been applied to the data set in order to obtain positive coefficients, it was preferred to be consistent with the Liang (2000) set-up selected as the reference.

MERIS

$$\alpha_{BS} = 0.4578R_2 - 0.3139R_5 + 0.2248R_7 + 0.0009$$

$$\alpha_{BH} = -1.5395R_2 + 1.1420R_5 + 0.5412R_7 + 0.6560R_{13} - 0.0107$$

$$\alpha_{SW} = -0.3318R_2 + 0.4973R_5 + 0.3737R_7 + 0.3555R_{13} - 0.0041$$

AATSR

$$\alpha_{BS} = 0.9283R_1 - 0.0376R_2 - 0.0163$$

$$\alpha_{BH} = 0.0854R_2 - 0.6015R_3 + 0.3333R_1 + 0.0133$$

$$\alpha_{SW} = 0.3086R_1 - 0.1347R_2 + 0.3185R_3 + 0.1332R_4 + 0.0015$$

VGT

$$\alpha_{BS} = 0.6503R_1 - 0.3500R_2 + 0.0017$$

$$\alpha_{BH} = 0.0861R_2 - 0.5819R_3 + 0.3290R_1 + 0.0108$$

$$\alpha_{SW} = 0.2702R_1 - 0.2532R_2 + 0.3170R_3 + 0.1610R_4 + 0.0031$$

A similar approach has been performed for the N2B conversion of the $D_{0\lambda\downarrow}$, $D_{0\lambda\uparrow}$ parameters needed for albedo retrieval, which are provided as narrowband variables by LUT-1. Due to the spectral smoothness of these functions, very small errors are committed in the N2B conversion of $D_{0\lambda\downarrow}$ and $D_{0\lambda\uparrow}$.

28.1.6 Estimation of uncertainties in SDR and BBDR

Tracking of uncertainties is one of the specific requirements for the GlobAlbedo processing chain. The purpose in this part of the processing is to generate a reliable estimation of the errors in the BBDR products propagated along the processing including the error covariance between the different spectral ranges.

It must be noted that R_λ retrieval in GlobAlbedo is performed by means of an analytical expression (Eq. 5.9) based on a Lambertian surface reflectance, which is a common approach for operational atmospheric correction of single-view instruments. For this reason, no optimal estimation framework is needed for this step of the processing, which has an impact on error propagation. No posterior error covariance matrix is then automatically generated throughout the processing from TOA radiance to BBDR as it would be the case of an optimal estimation based retrieval approach, but the final error covariance matrix is derived by explicitly calculating the errors at each step.

The error covariance terms in the BBDR products are given by the SDR error covariance matrices and the spectral covariance between the R_Λ in the three broadband ranges. For the linear conversion in Eq. 5.12, the propagation of variance-covariances between the narrowband and the broadband spaces is given by

$$M^{\Lambda} = a^{T}(\Lambda) M^{\lambda} a(\Lambda). \quad (5.15)$$

where M is the variance-covariance matrix of narrowband reflectance. From that relationship, the BBDR error variance-covariance matrix σ_Λ^2 is given by

$$\sigma_\Lambda^2 = a^T(\lambda)\sigma_\lambda^2 a(\lambda) + \sigma_{\Lambda,N2B}^2 \quad (5.16)$$

where σ_λ is the SDR error matrix, and $\sigma_{\Lambda,N2B}$ is the error intrinsic to the N2B conversion, which is assumed to be given by the RMSE of the fits for the calculation of the N2B conversion coefficients in Fig. 14.

Different error sources are considered to contribute to the total σ_λ:

- Instrumental calibration and noise: Based on each instrument's specifications, relative radiometric accuracy of 2%, 5% and 5% are assumed for MERIS, AATSR and VGT, respectively. These errors are taken as random and are assumed to represent the entire instrumental contribution to the total error budget. It must be remarked that those numbers are based on mission requirements rather than on real instrument performance reports, which are difficult to find and to interprete in some cases. Systematic radiometric calibration errors are assumed to have been reduced by with the results from the intercalibration experiment performed over the Dome-C site described in Appendix II. The potential contributions of inter-band calibration and spectral calibration errors are neglected in this analysis because of the difficulties to obtain relible data.
- Atmosphere: Errors in the knowledge of the atmospheric parameters (AOD, CWV and OZO) are converted to errors in SDR by means of the J_{AOD}, J_{CWV} and J_{OZO} gradients provided by LUT-2 and LUT-4 (e.g. Fig 12). The uncertainty in AOD is expected to be provided by the GlobAlbedo AOD retrieval module. The uncertainties in CWV are an input to the processor. Both must be calculated per-pixel. In the case of OZO, due to its low spatial variability a single value of OZO and its error is assumed to be representative of the entire imaged area. The uncertainty in OZO is calculated as the standard deviation of OZO within the image.

  The propagation of errors due to the atmospheric components is illustrated in Figs. 15-16 of Section 7. Input R_λ and the errors calculated from the gradients J_x are compared with the R_λ retrieved for the AOD, CWV and OZO in the limits of the input $x \pm \sigma_x$ intervals in order to validate the error propagation approach implemented.

- Spatial co-registration: The different spatial response and acquisition geometry of the three instruments leads to severe instrument-dependent spatial co-registration errors. In particular, the worst case is expected for AATSR-forward view due to the conical scan approach and the tilted observation. In the case of VGT data, even though no important co-location errors seem to be present, the plate carrée projection on which the level-1b data are provided causes the final resolution of the

data to be degraded after the BBDRs are resampled to the GlobAlbedo sinusoidal grid, which makes that the BBDRs can no longer be considered to have a 1 km resolution. The effect of co-registration errors between MERIS and AATSR-nadir (bands 3 and 13, respectively) is illustrated in Fig. 7. The data sets are projected to the sinusoidal grid. Most of the scattering found in the comparison between the two data sets disappears when 2- and 4-pixel binning is performed, which demonstrates the importance of co-registration errors. The highest uncertainties are calculated for snow surfaces in the VIS and land/water interfaces in the NIR.

Spatial co-registration errors are calculated from the local spatial heterogeneity. The local standard deviation calculated for each spectral band in 3×3 pixel windows is used as an estimate of the co-registration error, which is weighted with factors 1, 1.1, 1.2 and 1.3 for MERIS, VGT, AATSR-nadir and AATSR-forward, respectively, selected according to our experience with the data. An example of the estimated a-priori co-registration error is displayed in Fig. 21.

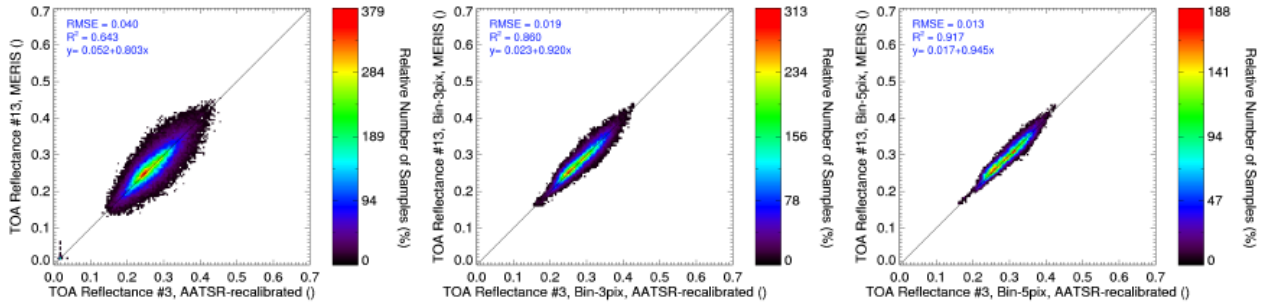

(a) No binning (b) Binning ×3 (c) Binning ×5

Figure 7: Illustration of the co-registration error between MERIS and AATSR-nadir data (channels 13 and 3, respectively). Binning of 3 and 5 pixels is applied to both data sets before the comparison. The improvement in the correlation between the two data sets with the increase of the number of pixels in the binning (co-registration relative impact decreased) is shown.

Modelling errors associated to the neglection of directional reflectance effects could also be added to the error budget, as this error is transferred to the SDR and BBDR products. However, as it is demonstrated in GlobAlbedo-Albedo-ATBD-V1.0 (2010), this is compensated in the albedo retrieval step by including the Nsky-weighting in the integral of the BRDF kernels. For this reason, this error does not propagate from BBDR to albedo and is therefore not included in the error propagation.

The total reflectance error (σ_λ^2) in the narrowband channels i,j is then calculated as

$$\sigma_\lambda^2(i,j) = |r^{ij}_{iso} f_{i,iso} f_{j,iso}|\,\sigma^2_{iso} + |r^{ij}_{cwv} f_{i,cwv} f_{j,cwv}|\,\sigma^2_{cwv} + |r^{ij}_{ozo} f_{i,ozo} f_{j,ozo}|\,\sigma^2_{ozo} + r^{ij}_{sac}\sigma_{i,sac}\sigma_{j,sac} + r^{ij}_{co\text{-}reg}\sigma_{i,co\text{-}reg}\sigma_{j,co\text{-}reg} \quad (5.17)$$

where $\sigma_{\lambda,radiom}^2$ and $\sigma_{\lambda,co\text{-}reg}^2$ are the square of the errors due to instruments radiometric calibration and the co-registration, respectively, and r^{ij} is the correlation between bands. Each of the five contributions is calculated on a per-pixel basis. In principle, the spectral correlation r depends on the particular reflectance pattern. For example, the red and near-infrared bands from a bare soil reflectance spectrum are expected to be positively correlated under variations in AOD550, while the correlation could even be negative (e.g. higher red reflectance and lower near-infrared reflectance for an increase in AOD) for a green vegetation spectrum. However, the calculation of per-pixel r would complicate the design an efficiency of the processor considerably. For the sake of simplicity, r is assumed to be 1 in all cases, which corresponds to the worst case error. The impact of these error sources (other than co-registration) on the total SDR error is illustrated in the Fig. 17 of Section 7.

Examples of the impact of each contribution to the total σ_Λ for the vegetation, soil and now spectral patterns in Fig. 15 are displayed in Fig. 8. It can be observed that the magnitude of the total error presents a relatively high dependence on both the instrument and the surface type. The error is largest for snow surfaces due to the multiplicative nature of the instrumental error. The N2B conversion is the most important error source for MERIS data over vegetation and soil patterns, while the radiometric error is most important contribution for snow and for the three surfaces as observed by AATSR and VGT. The atmosphere has less influence and is highly dependent on the instrument band setting and the channels used for the N2B conversion. Only the impact of AOD is important for the VIS region; CWV is only noticeable for VGT, for which OZO is negligible; the AOD contribution is generally negligible for the brigthest surfaces and the SW spectral region; OZO is relatively important for the NIR and the VIS spectral ranges when they are calculated from MERIS and AATSR, respectively.

A complete view of the σ_Λ matrices is provided in Fig. 18. The matrices are calculated with the same iput uncertainties as the σ_Λ represented in Fig. 8, which represent the diagonal errors in Fig. 18. As already stated from Fig. 8, the largest absolute errors correspond to the snow surface. Very low error covariance is found between the VIS and NIR ranges. The comparison between the three instruments shows that relatively similar results are to be expected from the three instruments over vegetation and bare soil surfaces, and also over snow between AATSR and VGT, while a different performance is expected for MERIS data over snow.

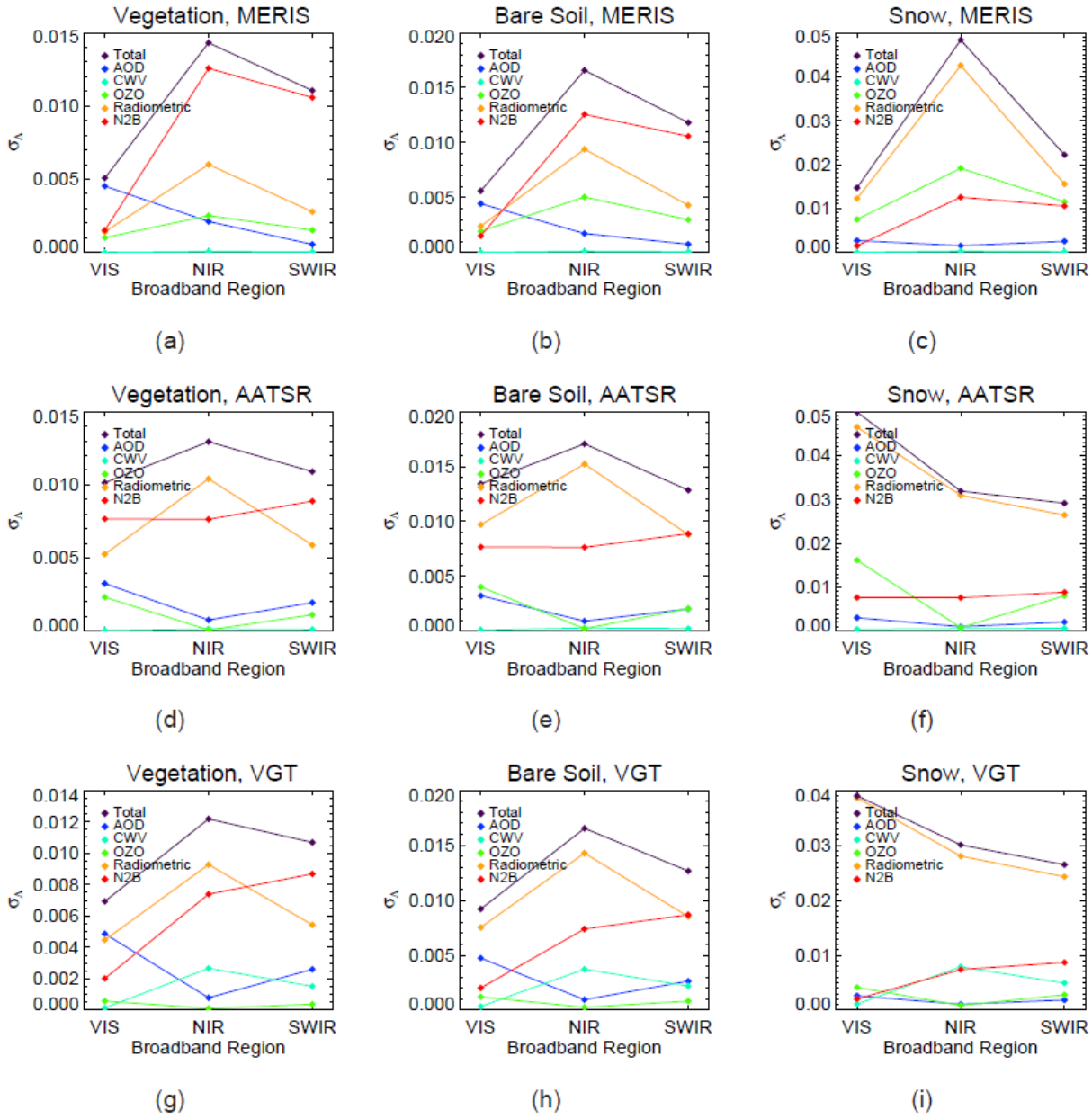

Figure 8: Contribution of the different error sources considered in this study to the diagonal terms of σ_Λ for the vegetation, soil and snow spectral patterns in Fig. 15 and the three instruments. The reference input configuration is VZA=15°, SZA=35°, RAA=123°, ELEV=450 m, AOD=0.25, CWV=2 g cm^{-2}, OZO=0.265 atm cm^{-1}, σ^{rel}_{AOD}=30%, σ^{rel}_{CWV}=20%, σ^{rel}_{OZO}=30%.

The relative error matrix σ_Λ^{rel} in Fig. 19 is calculated as

$$\sigma_{ij}^{rel} = |\rho| \frac{\sigma_{ij}}{\sqrt{R_i R_j}}, \qquad i,j = \text{VIS, NIR, SW,} \quad (5.18)$$

Relative errors are normally below 5% except for the vegetation cover in the VIS range, for which relative errors can grow up > 10%.

The error correlation matrix Σ in Fig. 20 is defined as

$$\Sigma_{ij} = \frac{\tau_{ij}}{\sqrt{\sigma_{ii}\sigma_{jj}}}, \qquad i,j = \text{VIS, NIR, SW,} \quad (5.19)$$

such that $-1 \leq \Sigma_{ij} \leq +1$. When $\Sigma_{ij} \rightarrow 0$, uncertainties on the broadband ranges i,j are uncorrelated, while when $\Sigma_{ij} \rightarrow \pm 1$ uncertainties are either positively (+1) of negatively (-1) correlated. The largest positive correlation in our study cases is found between NIR and SW for the snow cover, while a strong negative correlation is observed in vegetation between VIS and NIR in MERIS data, which is probably due to the lack of a spectral channel arogun 1600 nm as AATSR and VGT have.

According to the definition in Eq. 5.11, the uncertainty of the NDVI product σ_{NDVI} can be calculated as

$$\sigma_{\text{NDVI}} = \left[\left[\frac{(a+b)R_{\text{nir}}}{(R_{\text{nir}}+R_{\text{red}})^2} \sigma_{\text{red}} \right]^2 + \left[\frac{(a+b)R_{\text{red}}}{(R_{\text{nir}}+R_{\text{red}})^2} \sigma_{\text{nir}} \right]^2 \right]^{1/2} \quad (5.20)$$

where σλ is calculated for the SDR in the red and near-infrared channels selected for each instrument.

28.2 Processor Description

The BBDR processor described in this document converts from TOA radiance to BBDR data (and uncertainties) for the three instruments considered in Globalbedo. SDR data and uncertainties are intermediate products generated by the processor which are not stored in the operational processing pipe. The processor is designed to follow the pixel classification processor (GlobAlbedo-PixID-ATBD-V1.0, 2010) and the aerosol retrieval processor (GlobAlbedo-Aer-ATBD-V1.0, 2010) in the GlobAlbedo processing chain. The BBDR product generated by this processor will in turn be input to the albedo retrieval processor (GlobAlbedo-Albedo-ATBD-V1.0, 2010).

Input and output data to the BBDR processor are in BEAM-DIMAP format. The following information bands are ingested by the processor:

- Land-mask: A series of binary flags classifying pixels as clear-sky or cloudy, as well as land, snow cover or water, among other categories.

- VZA, SZA, RAA: Provided as tie-points in BEAM-DIMAP MERIS and AATSR data, and as information bands for VGT.

- Digital Elevation Model (DEM): For correction of elevation (Rayleigh) effects. The GETASSE30 DEM integrated in BEAM is assumed to have sufficient accuracy.

- AOD, CWV, OZO and uncertainties: AOD550 (plus uncertainty) is provided by the GlobAlbedo aerosol retrieval module. OZO data is also provided as tie-points with MERIS, and CWV and OZO are provided as information bands for VGT. Climatology values must be used for CWV in MERIS and for CWV and OZO in AATSR.

- Spectral TOA Radiance or reflectance: Level-1b data for the three sensors. This is radiometrically calibrated radiance for MERIS, TOA normalised radiance for AATSR and TOA reflectance for VGT.

Using information bands, the BBDR processor produces a series of outputs in BEAM-DIMAP format projected to the MODAGG (MODIS Aggregation Product) sinusoidal projection system. The processor output consists of the following bands at the moment:

- BBDR for three broadband spectral ranges (VIS, NIR, SW).

- Uncertainty in BBDR including spectral covariance errors (6 bands: VIS-VIS, NIRNIR, SW-SW, VIS-NIR, VIS-SW, NIR-SW).

- NDVI and uncertainty calculated from SDR for each data set to be processed.

- Volumetric (RossThick) and geometric (LiSparseModisReciprocal) kernels and N_{sky}-weighted integrals muliplied by the fraction of diffuse radiation at-ground D_0 as specified in Eq. 5.5.

- Meta-data: snow mask, digital elevation model and VZA, SZA and RAA.

All the resulting products are reprojected onto the MODIS sinusoidal grid[1] using the Reproject operator implemented in BEAM-4.8.

An example of BBDR and NDVI derived from MERIS Level-1b data with the methodology described in this document is displayed in Fig. 9. The original MERIS image was aquired over the Iberian Peninsula on 14/7/2003. The corresponding σ_{Λ} are in Fig. 22.

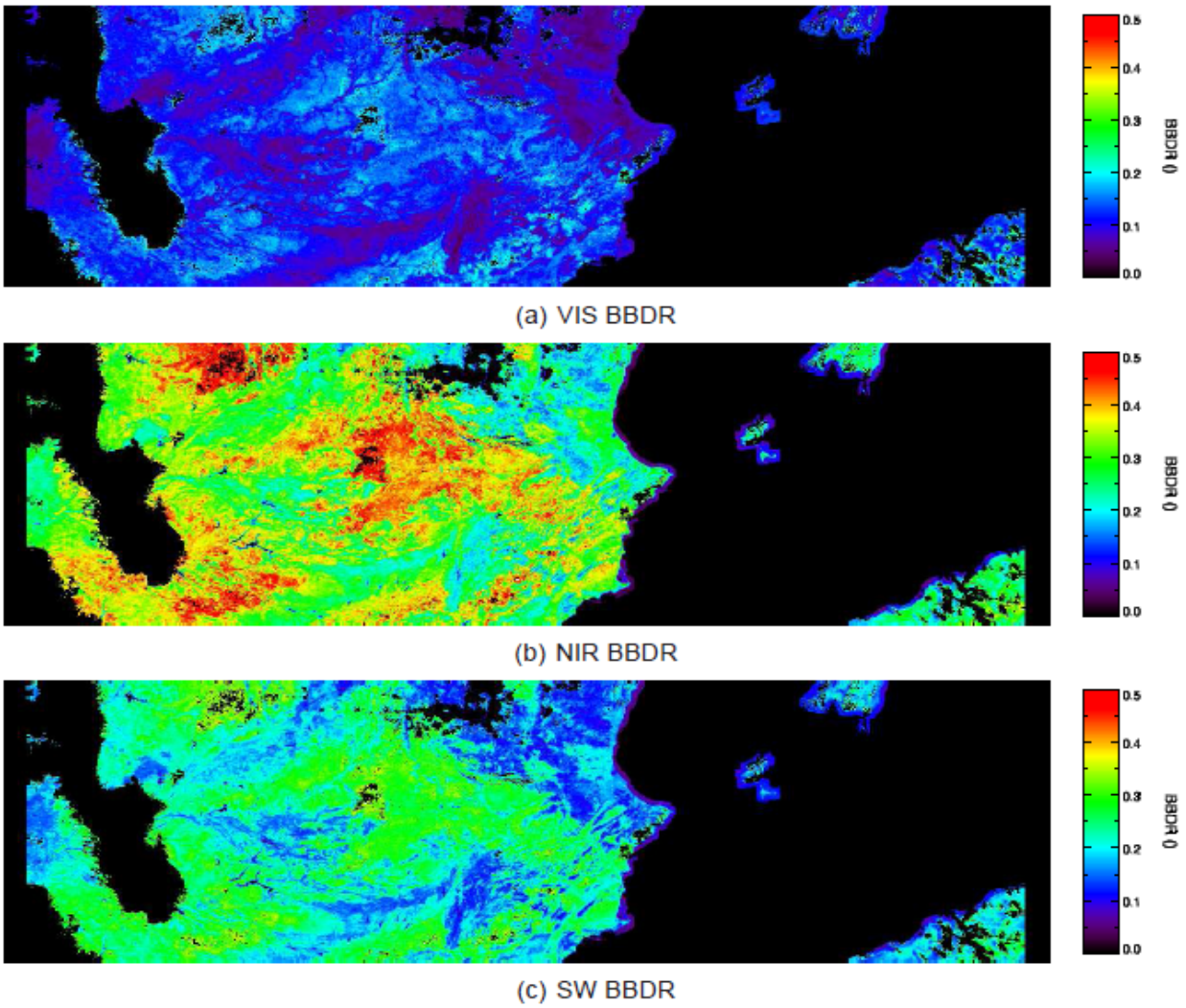

(a) VIS BBDR

(b) NIR BBDR

(c) SW BBDR

Figure 9: BBDRs derived from a MERIS Level-1b image acquired over the Iberian Peninsula on 14/7/2003.

28.3 Assumptions and Limitations

A number of assumptions and limitations are appreciated in the current version of this processor:

- **Lambertian surface reflectance assumption:** A Lambertian surface is assumed when modelling the atmosphere-surface radiative transfer with Eq. 5.4, which was found to be necessary to have a processor capable of processing single acquisition with a minimum need for ancillary measurements. This assumption leads to smoothing the actual BRDF, which is taken into account in the albedo retrieval module (GlobAlbedo-Albedo-ATBD-V1.0, 2010), but the error associated to this assumption still affects the SDR and BBDR products.

- **Error sources considered in the error budget:** It has been shown that BRDF effects in the surface reflectance and the N2B conversion process are in general the most important error sources for the SDR and BBDR products. However, no accurate description of these errors and of their dependence on the scene characteristics and the atmospehric state is yet available, but only average values depending on few parameters are considered so far. The development of a more sophisticated description of these terms is expected for upcoming versions of the processor. The inclusion of other error sources, such as the error covariance between the two AATSR views or topographic effects in the imaged area, will also be considered.

- **No dedicated processing of snow/ice pixels:** SDR retrieval and N2B conversion are common to all land surfaces, including snow and ice, at this stage. The availability of input data (cloud mask, AOD, CWV) over snow pixels and the suitability of the N2B conversion approach proposed must still be confirmed.

- **Neglection of topographic effects:** No correction of topographic effects, defined as the assumption of a wrong illumination angle in tilted surfaces, is performed by the processor. Even though the methodology for such a correction is available (Guanter et al., 2008), it is still under discussion if these topographic effects are intrinsic to the definition of albedo on a global scale so that they should not be removed from the SDR product.

- **Aerosol model:** No pixel-wise variations of the aerosol model are enabled, but one single model is assumed to be characteristic for the land areas in a given orbit. The assumption of a fixed aerosol model is acknowledged to be a significant limitation in aerosol retrieval at a global scale. However, the impact on SDR retrieval is strongly reduced when the same aerosol models are used for AOD and SDR retrieval, as the errors tend to cancel out.

- **Range of application of the SDR processor:** The SDR/BBDR processor is designed to work in the range of scene conditions described in Table 1. This means that pixels with SZAs larger than 70deg and surfaces located higher than 8000 m will not be processed. Those limits are selected as the top SZA and elevation for which the atmospheric radiative transfer modelling can be considered to be relatively accurate.

29 Appendix I - Image Gallery

Spectral Response Functions

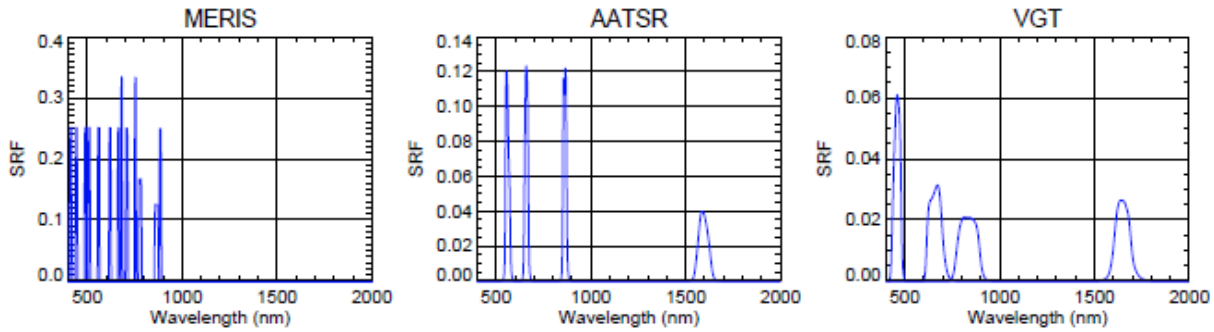

Figure 10: Spectral response functions (SRFs) of the three instruments under consideration in GlobAlbedo.

Aerosol models

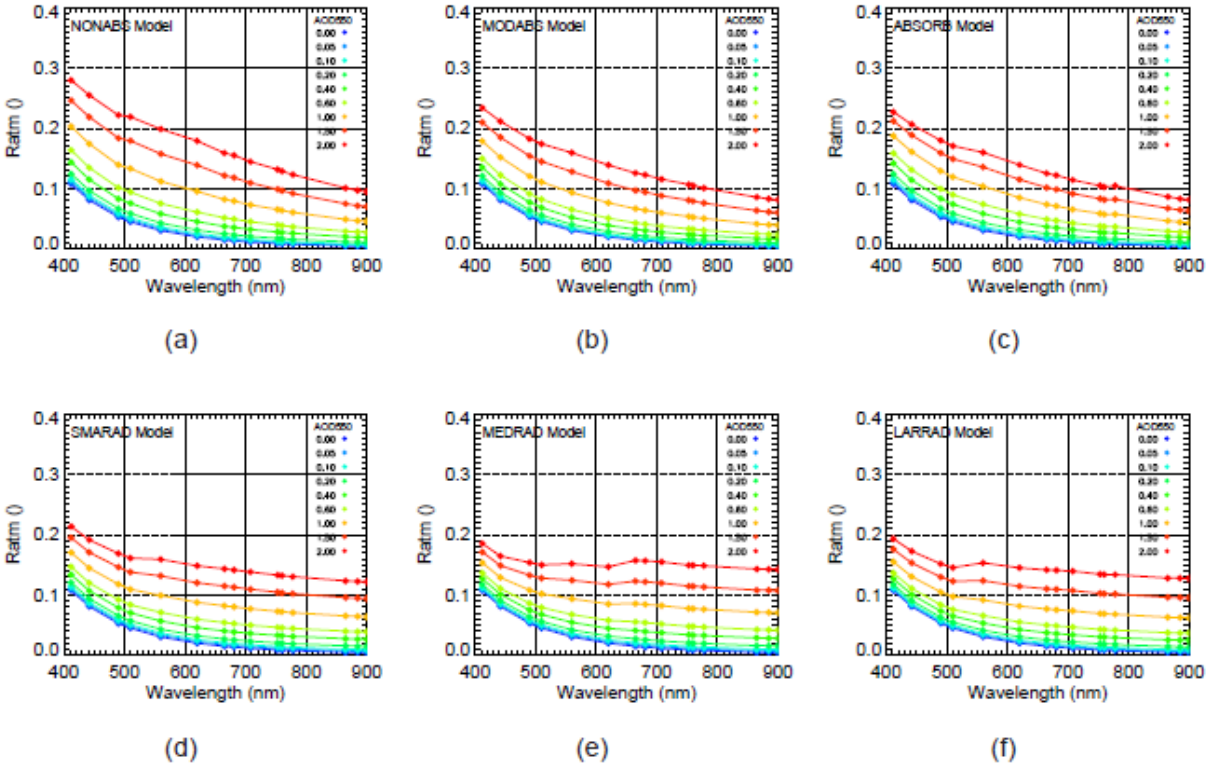

Figure 11: Spectral $R_{atm,\lambda}$ for the six aerosol model proposed by Govaerts et al. (2010). The reference input configuration is VZA=30°, SZA=30°, RAA=120°, ELEV=200 m.

J_x gradients for error propagation

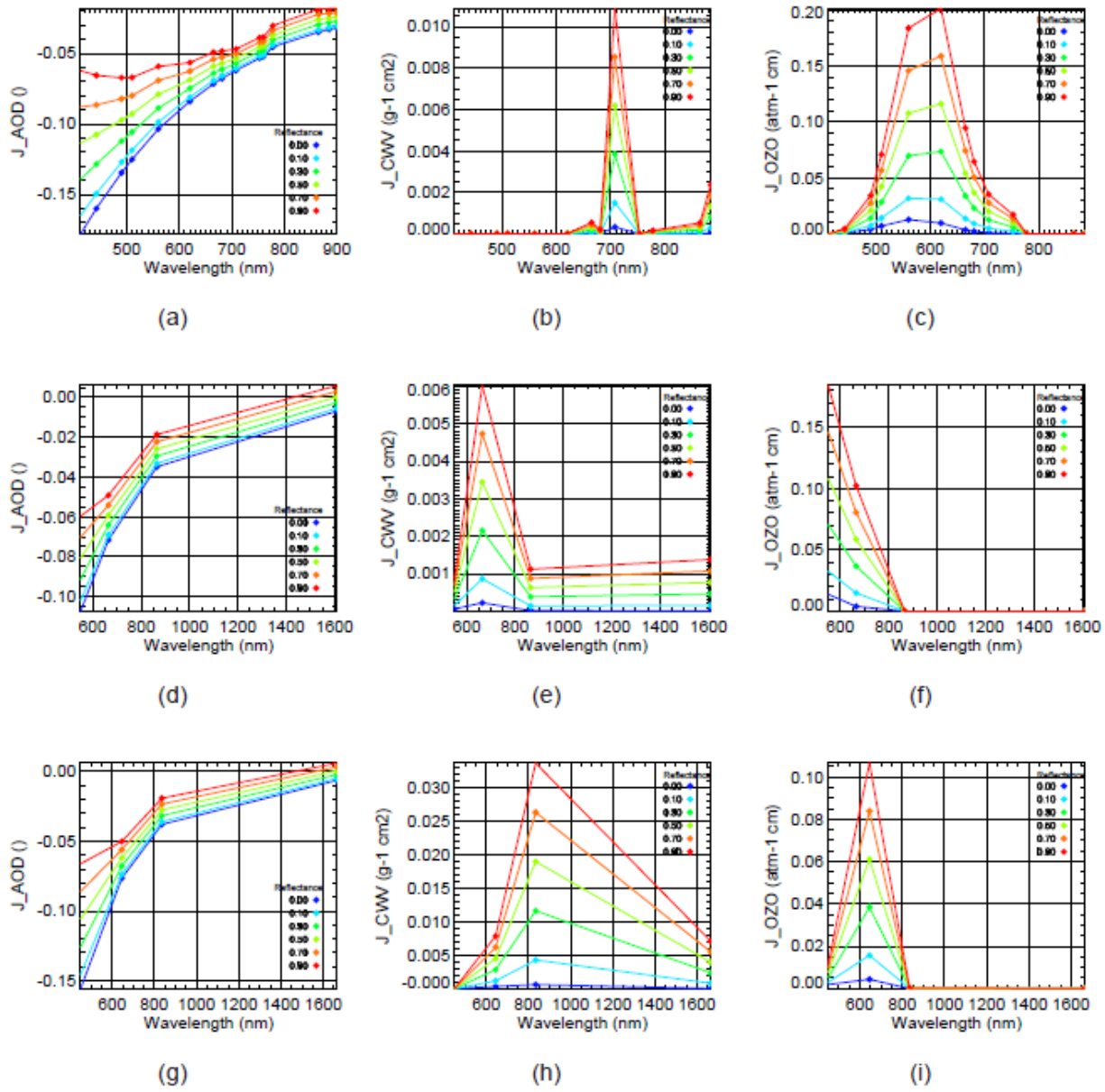

Figure 12: Sample spectral J_{AOD}, J_{CWV} and J_{OZO} for the three instruments as a function of surface reflectance.

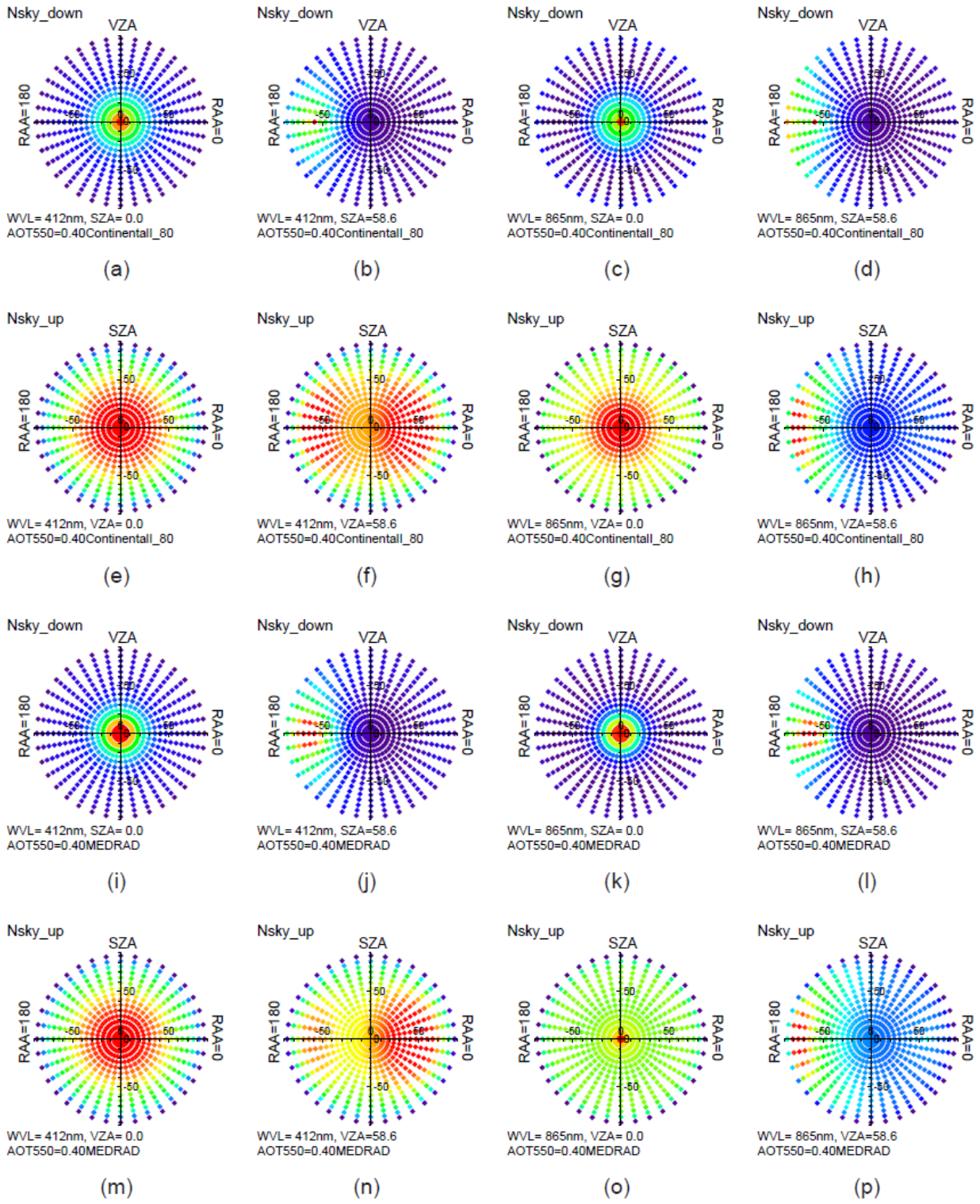

Figure 13: Sample $N_{\text{sky}\downarrow}(\Omega_s)$ and $N_{\text{sky}\uparrow}(\Omega_v)$ functions for AOD550=0.4 and different reference SZA and VZA, aerosol models and spectral wavelengths. Colours indicate the intensity of scattering for each direction in the hemisphere (purple is minumum intensity, red is maximum).

Fits for the calculation of the narrow-to-broadband conversion coefficients

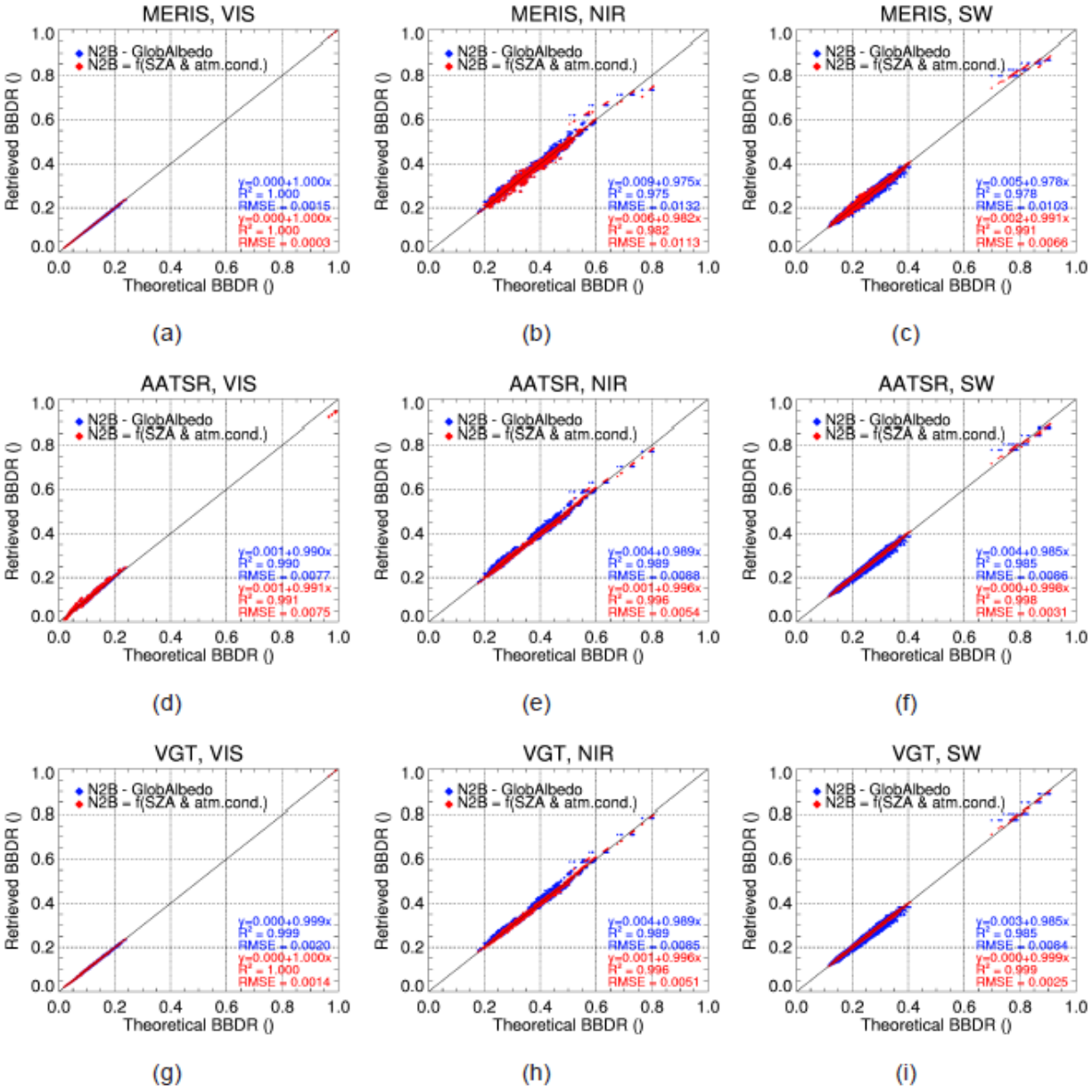

Figure 14: Comparison between the theoretical BBDR (simulated with Eq. 5.13) and the retrieved BBDR (generated from the calculated α coefficients) for the three instruments and the three spectral ranges. The comparison is provided for N2B conversion performed for all the simulated atmospheric conditions and for N2B conversion performed independently for each atmospheric condition.

Error propagation in SDR

Propagation of atmospheric uncertainty (SDR)

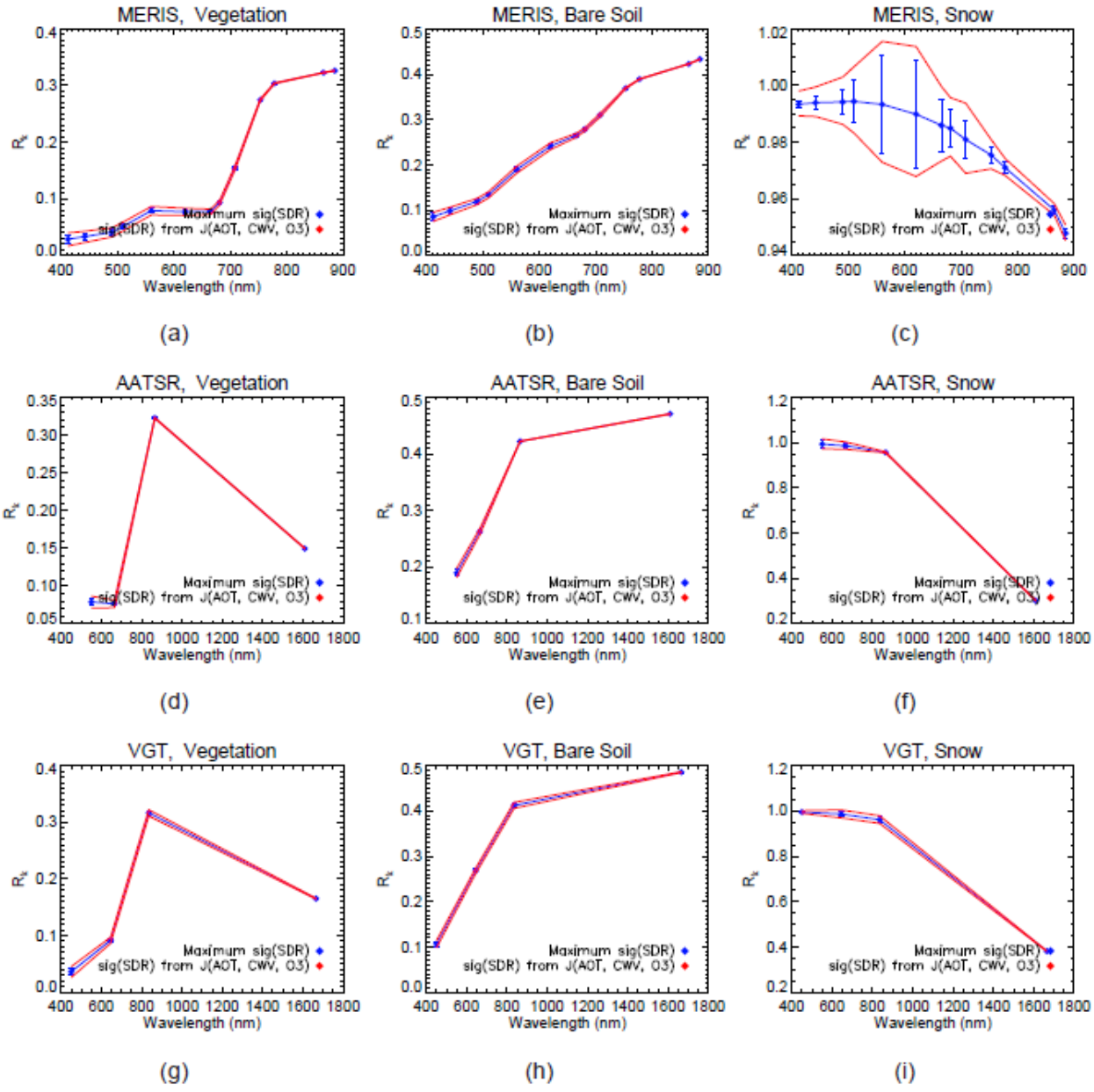

Figure 15: SDR retrieval error (σ_λ) associated to AOD, CWV and OZO for the three instruments and three characteristic land cover types. Error bars have been calculated by means of the J_{AOD}, J_{CWV} and J_{OZO} gradients. The red lines represents R_λ retrieved for the extreme values of AOD $\pm\ \sigma_{AOD}$, CWV $\pm\ \sigma_{CWV}$ and OZO $\pm\ \sigma_{OZO}$. The reference input configuration is VZA=15°, SZA=35°, RAA=123°, ELEV=450 m, AOD=0.25, CWV=2 g cm^{-2}, OZO=0.265 atm cm^{-1}, σ^{rel}_{AOD}=30%, σ^{rel}_{CWV}=20%, σ^{rel}_{OZO}=30%.

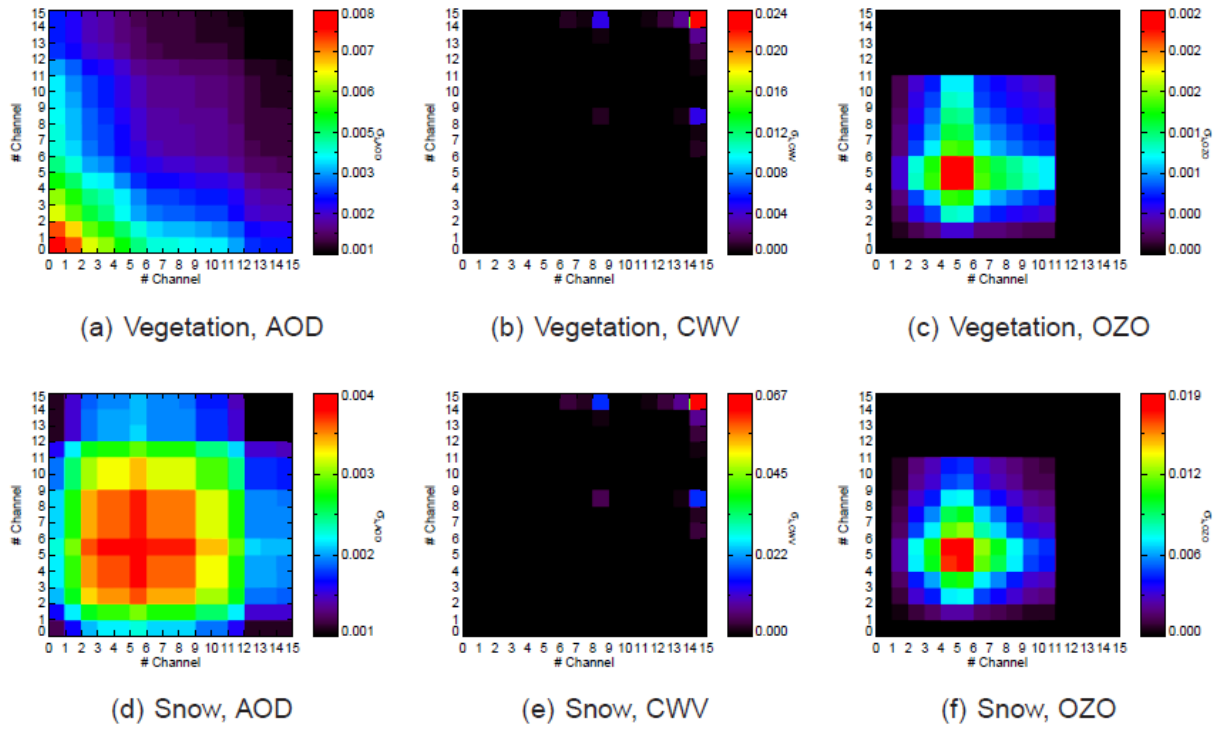

Figure 16: σ_λ matrices associated to AOD, CWV and OZO for MERIS and vegetation and snow land cover types. The reference input configuration is VZA=15°, SZA=35°, RAA=123°, ELEV=450 m, AOD=0.25, CWV=2 g cm^{-2}, OZO=0.265 atm cm^{-1}, $\sigma^{\text{rel}}_{\text{AOD}}$=30%, $\sigma^{\text{rel}}_{\text{CWV}}$=20%, $\sigma^{\text{rel}}_{\text{OZO}}$=30%.

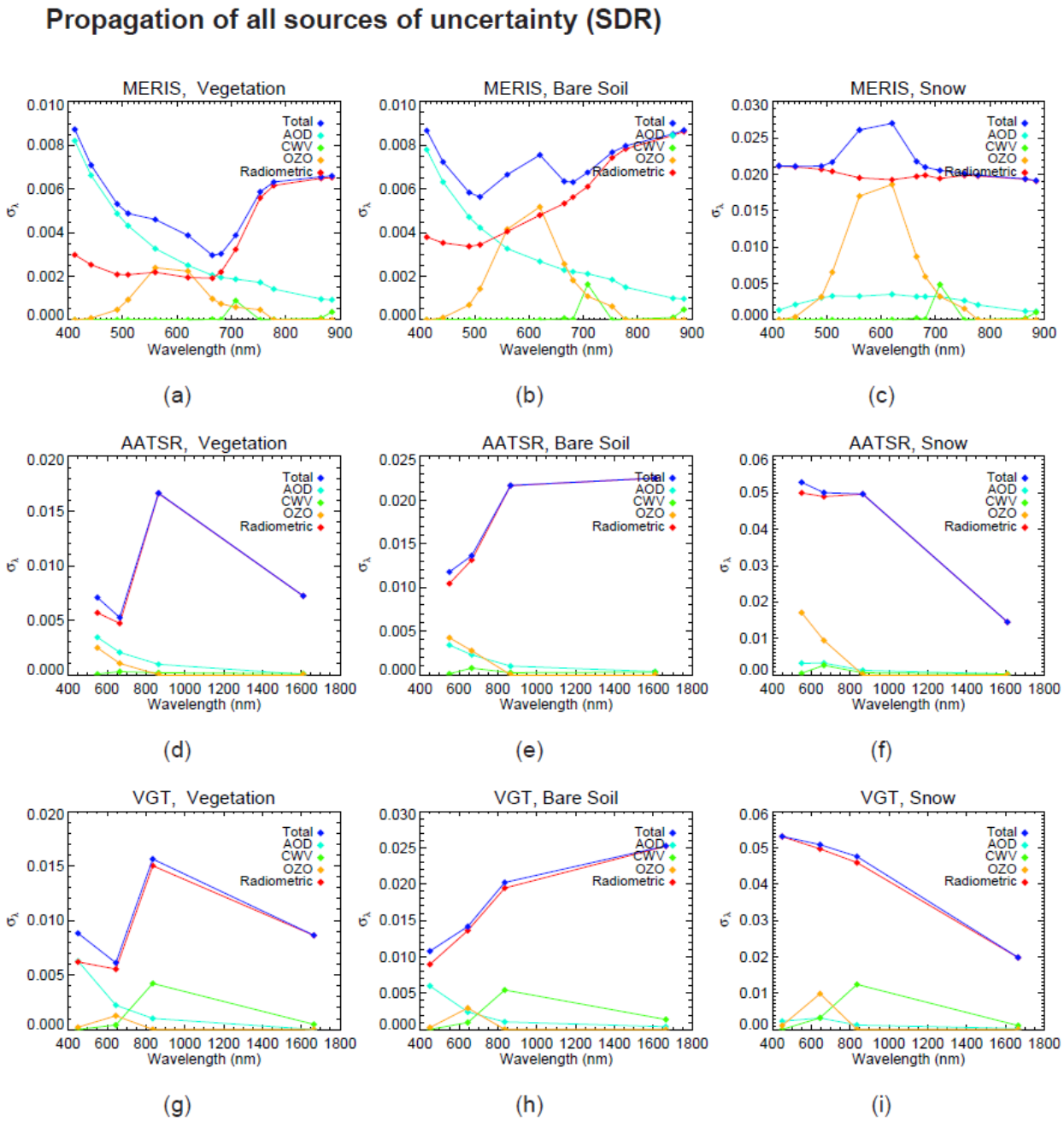

Figure 17: SDR retrieval error (σ_λ) associated to each of the error sources considered for the three instruments and three characteristic land cover types. The reference input configuration is VZA=15°, SZA=35°, RAA=123°, ELEV=450 m, AOD=0.25, CWV=2 g cm^{-2}, OZO=0.265 atm cm^{-1}, $\sigma^{\text{rel}}_{\text{AOD}}$=30%, $\sigma^{\text{rel}}_{\text{CWV}}$=20%, $\sigma^{\text{rel}}_{\text{OZO}}$=30%. Input reflectance patterns are those in Fig. 15.

Error propagation in BBDR

Error covariance matrices (σ_Λ) for MERIS

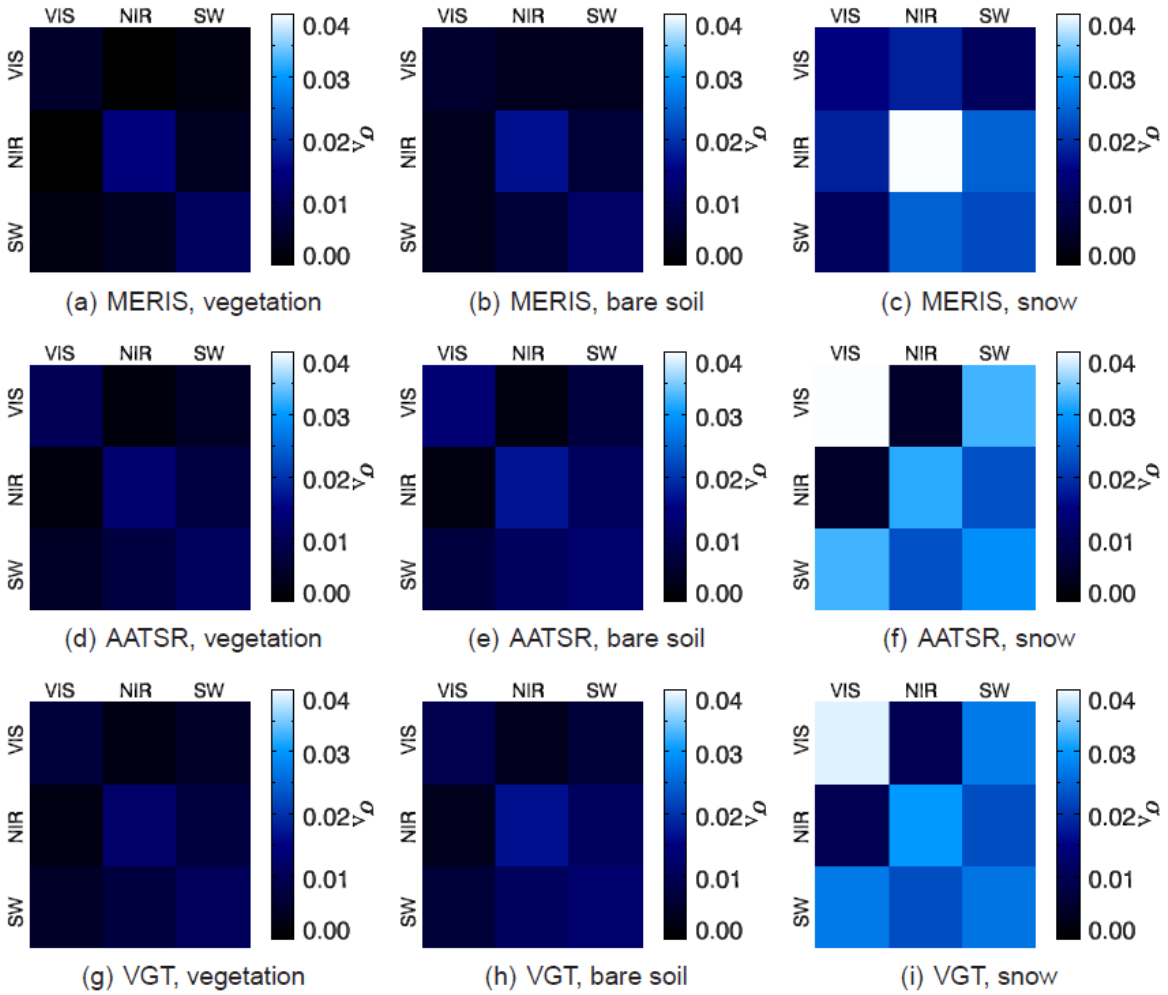

Figure 18: σ_Λ for the vegetation, soil and snow spectral patterns in Fig. 15 and the three instruments. The reference input configuration is VZA=15°, SZA=35°, RAA=123°, ELEV=450 m, AOD=0.25, CWV=2 g cm^{-2}, OZO=0.265 atm cm^{-1}, $\sigma^{\text{rel}}_{\text{AOD}}$=30%, $\sigma^{\text{rel}}_{\text{CWV}}$=20%, $\sigma^{\text{rel}}_{\text{OZO}}$=30%.

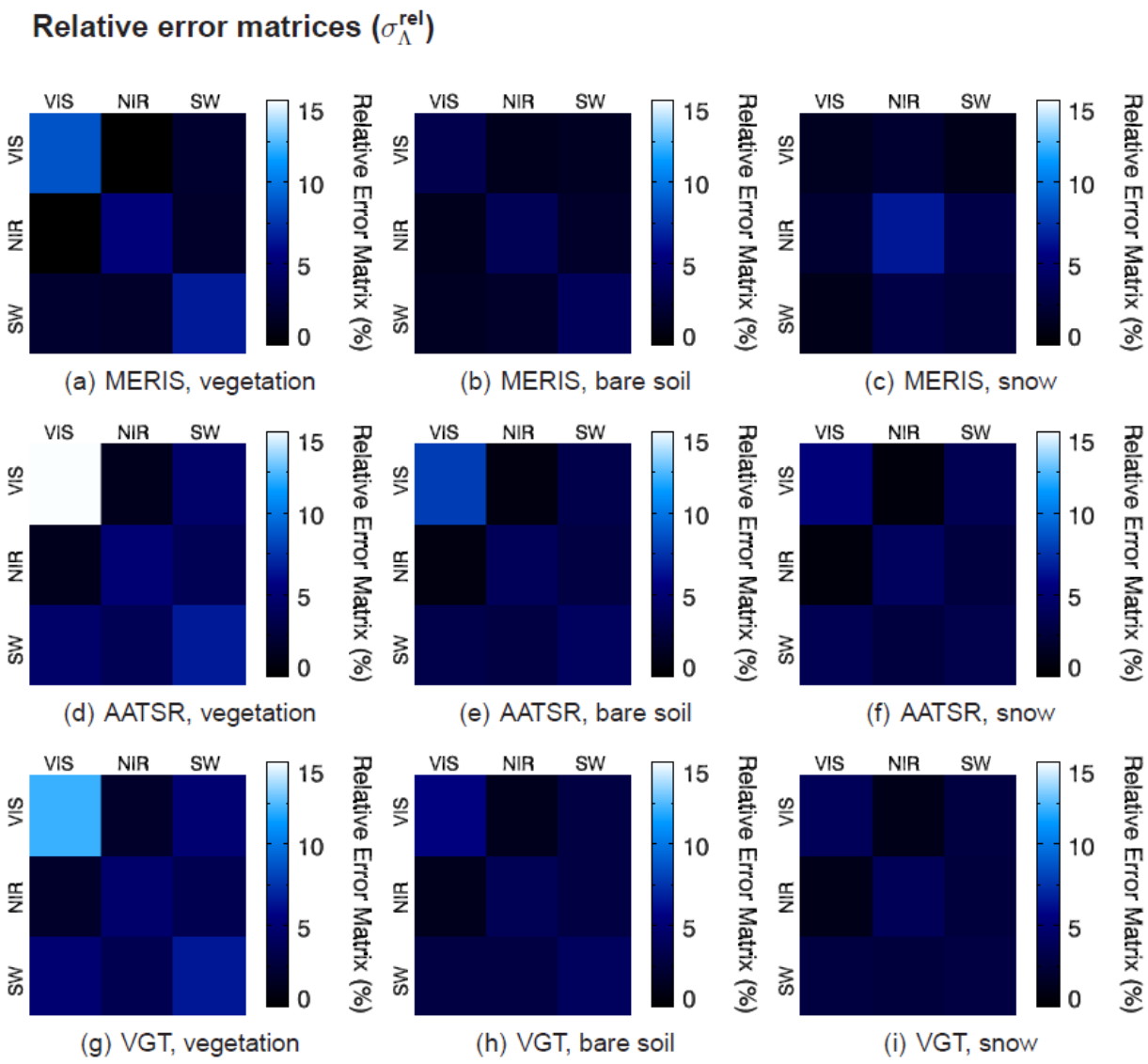

Figure 19: Same as Fig. 18 for the relative error matrix σ_Λ^{rel} defined in Eq. 5.18.

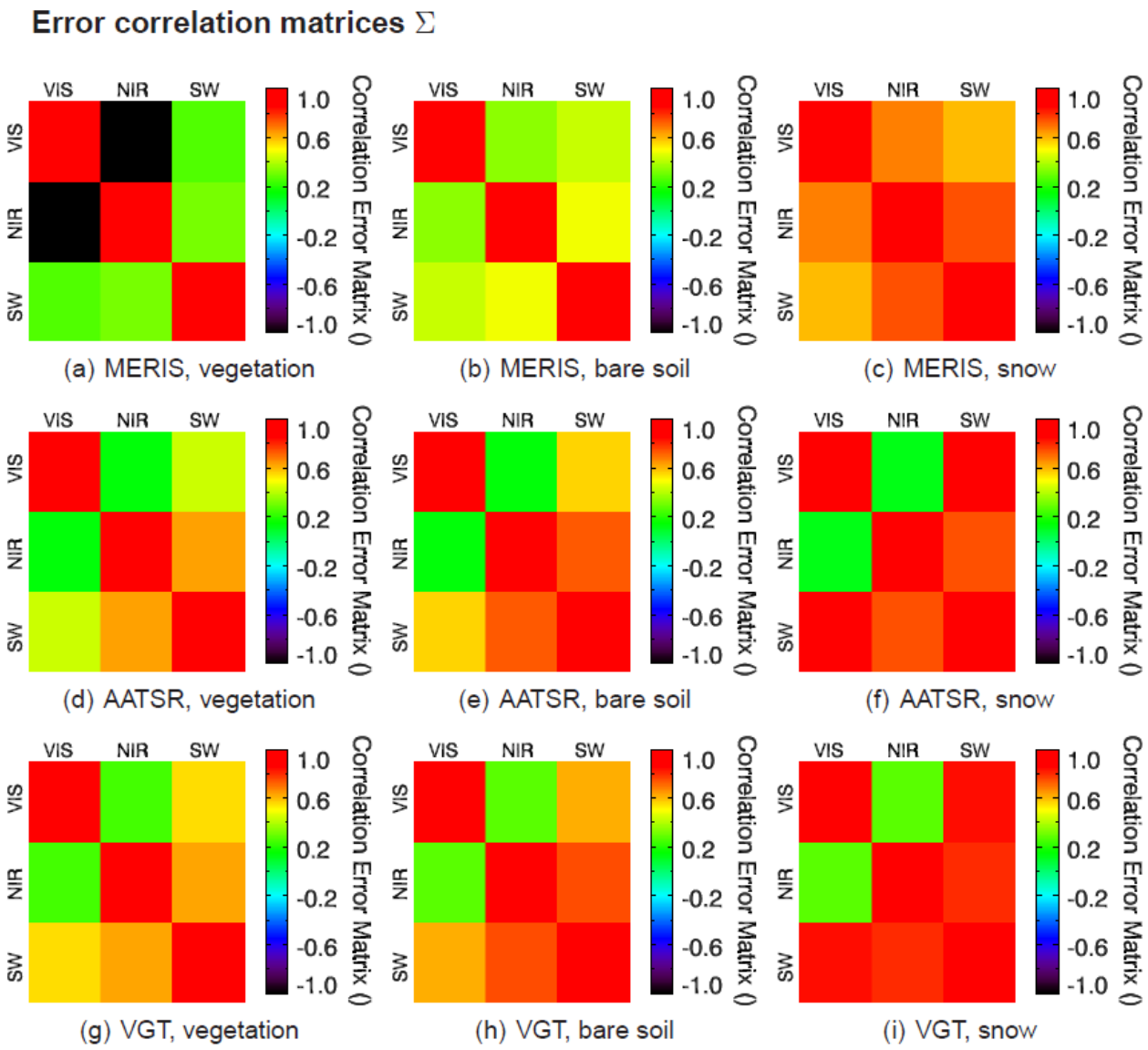

Figure 20: Same as Fig. 18 for the error correlation matrix Σ defined in Eq. 5.19.

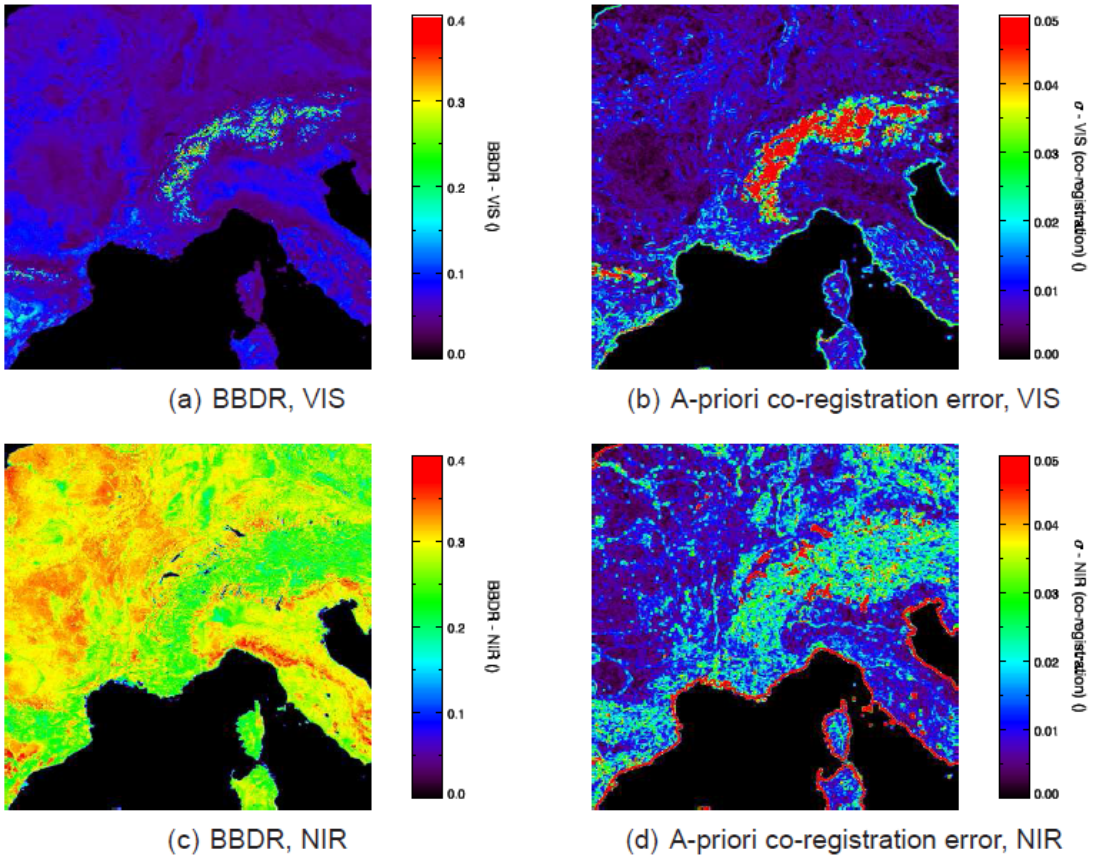

Figure 21: Illustration of the a-priori co-registration error estimated by means of the local standard deviation in each spectral channel.

σ_Λ **from real MERIS data**

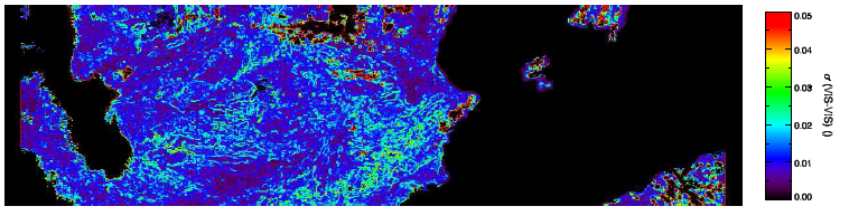

(a) Black-sky, $\sigma_{VIS\text{-}VIS}$

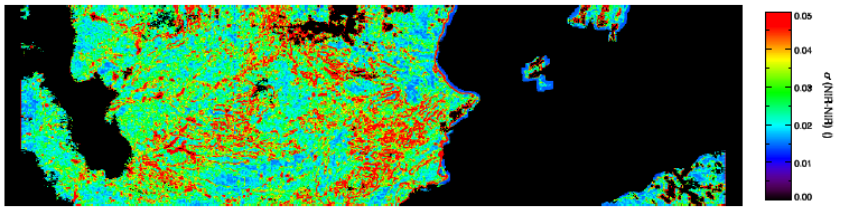

(b) Black-sky, $\sigma_{NIR\text{-}NIR}$

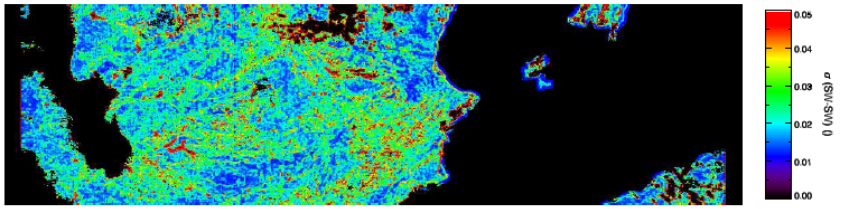

(c) Black-sky, $\sigma_{SW\text{-}SW}$

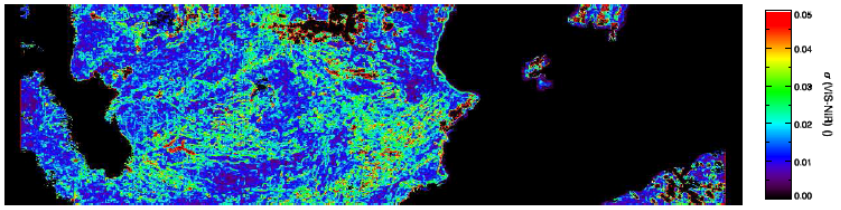

(d) Black-sky, $\sigma_{VIS\text{-}NIR}$

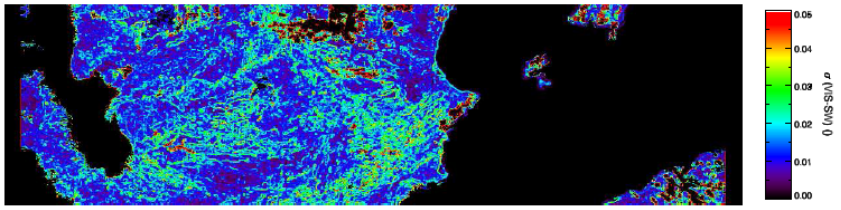

(e) Black-sky, $\sigma_{VIS\text{-}SW}$

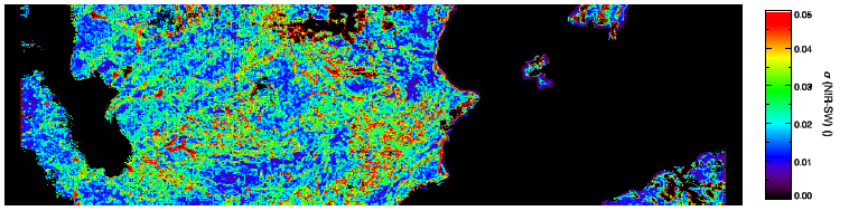

(f) Black-sky, $\sigma_{NIR\text{-}SW}$

Figure 22: σ_Λ derived from a MERIS Level-1b image acquired over the Iberian Peninsula on 14/7/2003.

30 Appendix II – Instrument intercalibration

Over the last decade, the CEOS-WGCV (CEOS Working Group on Calibration & Validation) have been developing guidelines and protocols for best practice under the aegis of Quality Assurance for Earth Observation, QA4EO (http://qa4eo.org). As a result of disparate practices over a wide variety of different test sites, QA4EO provides both a framework and a set of global test sites and standardised procedures for the radiometric calibration and inter-calibration of spaceborne visible and near IR sensors. In order to minimise the need for excessive demands on costly "ground truth" measurements, the first such QA4EO site was agreed to be DOME-C on the Antarctic continent. This strategy is discussed in Cao et al., (2010). The choice of DOME-C fulfils both the requirement for a near aerosol/dust-free pristine environment on a flat plane with minimal surface landscape features but more importantly, a site which is viewed many times every day by polar-orbiting satellites within ±1 hour each other. Such SNO (Simultaneous Nadir Observations) acquisitions allow different sensors covering similar spectral regions on the same or different platforms to be inter-calibrated. In the Antarctic, aerosols are very rare and below instrument detectability limit. However, Ozone absorption can change ToA (Top of Atmosphere) reflectance by a factor of 2-3 so to be able to normalise between one set of ToA-R and another we need to perform an Ozone correction which is sensor responsivity limited.

As part of a CEOS-WGCV-IVOS (IR and Visible Optical Sensors) and QA4EO experiment to follow up the work of Cao et al. (loc.cit.) but focus on non-US sensors, level-1 data was acquired over DOME-C from AATSR, MERIS and VEGETATION2 for the December 2008 to January 2009 time period. Ground-based Ozone measurements in Dobson units were acquired from the French Space Agency, CNES, although space-based measurements from GOME-2 or TOMS could have been employed in their place. Ozone was used in the radiative transfer scheme MODTRAN to calculate a set of spectral absorption coefficients that were then applied to each sensor. A set of spectral BRDF coefficient parameterisations were employed from Hudson & Warren (2006) to correct for surface BRDF effects.

The overall processing schema is shown in Fig. 23 below where ρ is the TOA reflectance, d is the Earth-Sun distance, θ the solar zenith angle and the normalised TOA radiance is = L/E_0 The TOA reflectance is then given by

$$R_{scene} = r_{scene}\cos\theta = \rho\cos\theta = \frac{\pi d^2 L}{E_0}$$

$$\therefore \rho = \frac{R_{scene}}{100\cos\theta}$$

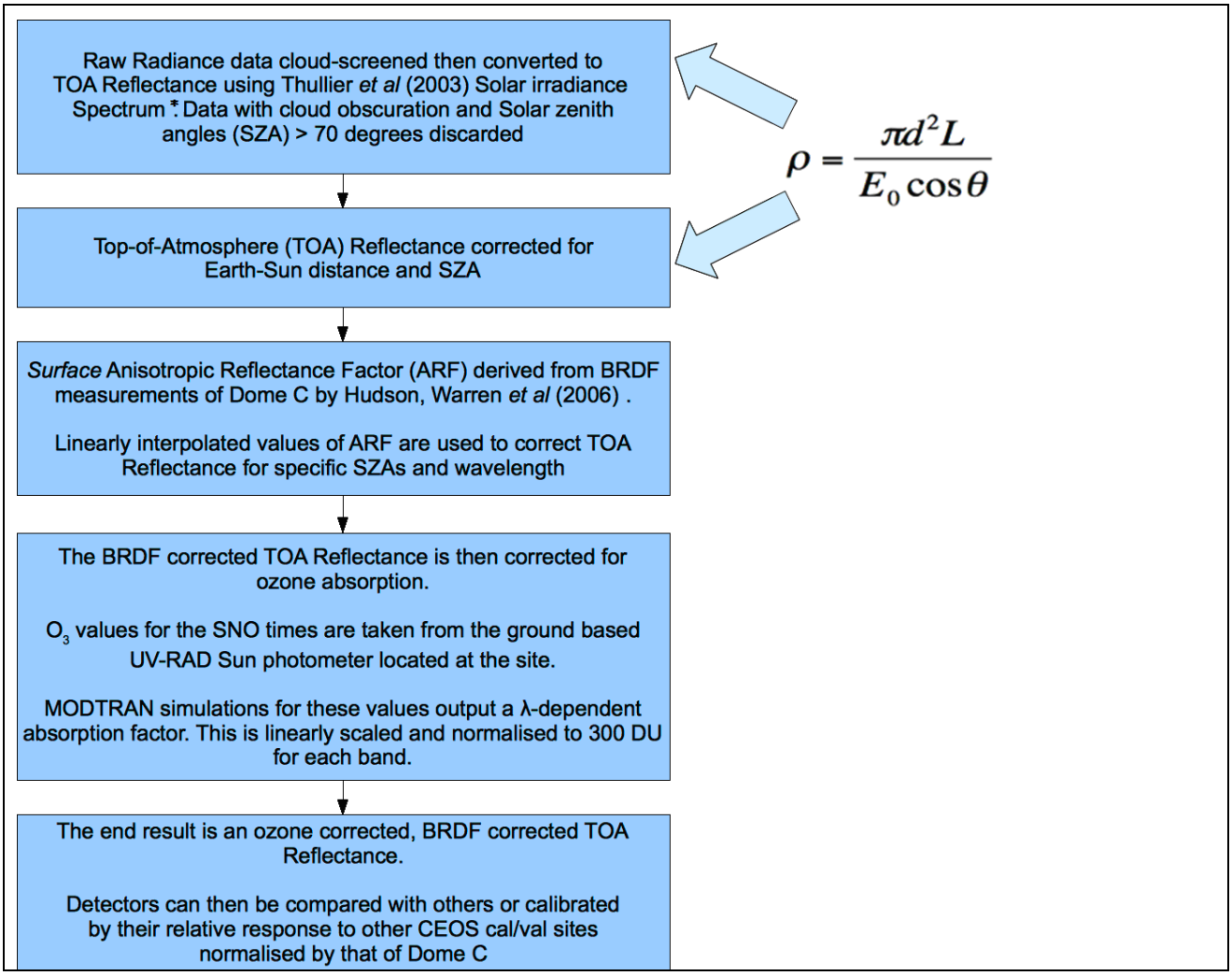

Figure 23. Schematic of Sensor inter-calibration method

A critical stage in this process is cloud masking as it is extremely challenging to detect clouds over snow/ice. The GlobAlbedo PixelID cloud detection was employed. From visual inspection of VEGETATION 2 B3 (NIR) this cloud mask looks reasonable in the 25 x 25km region around the DOME-C site as shown for one example in Fig. 24.

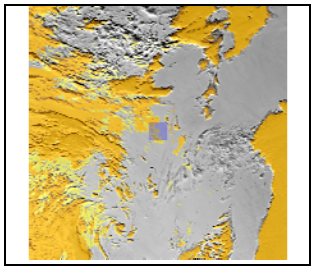

Figure 24. VEGETATION 2 B3 (NIR) showing superimposed cloud masks from original (VITO-supplied) and new Pixel ID mask (orange). Also showing 25 x 25km area around the DOME-C site.

Using the cloud mask and the retrieved ToA reflectance, all pixels which were masked as cloud-free were used for all possible match-ups over the 2 month time period. A summary of the results is shown in Fig.25 below.

AATSR vs MERIS	AATSR Report PO-RP-RAL-AT-0599 intercomparison results (page 32 and 33)				
RAL (2002-2008)	Ratio AATSR/MERIS	StdDev	Offset	Slope	Number of data points
550/560nm band	1.0374	0.0152	0.6956	1.0176	Unspecified
660/665nm band	1.0288	0.0108	0.4993	1.0152	Unspecified
870/865nm band	1.0369	0.0079	0.6179	1.0198	Unspecified

Dec09+Jan10 results	Best fit coefficients of bandwidth and ARF corrected, normalised TOA reflectance AFTER ozone correction					
AATSR vs MERIS	Ratio AATSR/MERIS	StdDev	Offset	Slope	R-squared	Number of data points
550/560nm band	1.025273127	0.0072287	-0.169	1.2189	0.7585	15
660/665nm band	1.009335959	0.0099814	0.0726	0.93	0.4636	15
870/865nm band	1.026507198	0.0072884	-0.023	1.0523	0.8741	15

MERIS vs VGT						
	Mean ratio VGT/MERIS	StdDev	Offset	Slope	R-squared	Number of data points
442 vs 450 nm band	1.012482984	0.0397508	1.395	-0.4961	0.5801	8
665 vs 645 nm band	0.95342094	0.0067775	-0.0835	1.0447	0.471	8
865 vs 835 nm band	0.970944006	0.0083773	0.3891	0.5376	0.4385	8

AATSR vs VGT						
	Mean ratio VGT/AATSR	StdDev	Offset	Slope	R-squared	Number of data points
660 vs 645 nm band	0.947402892	0.0077898	0.3805	0.5341	0.7431	8
870 vs 840 nm band	0.945720049	0.0085332	0.4086	0.5025	0.4745	8
1600 vs 1665 nm band	1.134511487	0.0790827	0.0226	0.977	0.9189	8

Figure 25. Sensor intercalibration coefficients for AATSR, MERIS and VEGETATION for December 2008-January 2009 over DOME-C. Number of points refers to the mean value over a maximum of 225 pixels if all are cloud-free.

CNES have produced sensor degradation summaries for VEGETATION and VEGETATION 2 back to 1998 which will be available through CEOS from the SADE database whilst David Smith and colleagues at RAL have produced statistics from 1995-2007 for AATSR-MERIS inter-comparisons but without Ozone corrections and over larger areas. GlobAlbedo will continue to work with CEOS-IVOS (through Dr Nigel Fox) to compile these sensor values over a longer time period.

Section D: Algorithm Theoretical Basis Document

Version 3.1

Document Number: GlobAlbedo_ATBD_V3.1 Date 06/06/2012

Distribution:

ESA	O. Leonard	X
	S. Pinnock	X
University College London	J-P. Muller	X
	T. Kennedy	X
	P. Lewis	X
Swansea	P. North	X
Free University of Berlin	J. Fisher	X
	R. Preusker	X
Brockmann Consult	C. Brockmann	X
	N. Fomferra	X
	U. Krämer	X

CHANGE RECORD

ISSUE	DATE	PAGES CHANGED	COMMENTS
A	23/07/10	All new	Draft
1	09/09/2010	All sections	First Issue
2	11/11/2010	Throughout, but only minor text changes in this chapter.	Response to RIDs raised by Simon Pinnock (7/10/12010): none directly for this section, but document detail updated.
3	15/04/2011	All	Minor updates & references sorted. Includes new timing estimates.
3.1	06/06/2012	ToC	Global ToC added

31 Introduction

The aim of the GlobAlbedo project, as given in the SoW, is to support users' requirements for a long time series of global land surface albedo. This is to be achieved by meeting the following objectives:

(1) Developing and delivering a multi-annual global albedo data set that has the potential to be sustained into the future using data from operational European satellites, such as the GMES Sentinels.

(2) Validating and providing intercomparisons of the albedo product against ground based and satellite based measurements.

(3) Providing the global user community with free and easy access to the albedo products.

(4) Demonstrating the utility of the albedo product by performing a series of scientific studies exploiting the data set produced.

The ESA GlobAlbedo project will develop a broadband albedo map of the entire Earth's land surface (snow and snow-free), which is required for use in climate modelling and research. An initial group of six users are working with the GlobAlbedo project team to define requirements and drive the project towards practical applications of the products.

The final albedo products will include both black and white sky albedo over the entire globe with a core 8-day frequency and 1 km spatial resolution over the 1995-2010 time period. The product includes uncertainty estimates, and provides albedo integrated in three spectral broadband ranges, namely the solar spectrum (300-3000nm), the visible (300-700nm) and the near- and shortwave-infrared (700-3000nm). Supplementary information of fAPAR is calculated, and a range of other datasets made available with the product.

With the aim of deriving independent estimates making the best use of operational European satellites, GlobAlbedo will create a 15 year time series by employing ATSR-2, SPOT4-VEGETATION and SPOT5-VEGETATION2 as well as AATSR and MERIS. Albedo retrieval will use an optimal estimation approach that produces a gap free product, using information from all available sensors at any given time. First order non-Lambertian atmospheric interaction effects on the input satellite data are treated as part of the optimal estimation approach. The target accuracy requirements identified and agreed with the GlobAlbedo users in GlobAlbedo_RB_D01_v2_0 (2010) are:

- Albedo >0.15, 20% and for Albedo <0.15, 0.015

This document is a master document for a set of individual ATBDs on particular aspects of the overall algorithm to go from level-1b to albedo. The individual documents are:

- Pixel identification: GlobAlbedo_PixID_ATBD_V3.0
- Aerosol retrieval: GlobAlbedo_Aer_ATBD_V3.0
- BBDR estimation: GlobAlbedo_BBDR_ATBD_V3.0

- Albedo estimation: GlobAlbedo_Albedo_ATBD_V3.0

Each document provides an overview of its own particular aspect of the processing chain, includes information on assumptions and technical tradeoffs and describes each component of the algorithm in terms of physical background as well as mathematical breakdown.

Each individual document provides the baseline for understanding the algorithm as well as for implementation in a software processor and its verification.

This master document provides an overview of the whole processing chain and key aspects of each of the components.

32 Applicable and Reference documents

32.1.1 Applicable documents

32.1.2 Reference Documents

Barnsley, M. J., A. H. Strahler, K. P. Morris and J-P. Muller. 1994. Sampling the surface bidirectional reflectance distribution function (BRDF): 1. Evaluation of current and future satellite sensors. Remote Sensing Reviews. 8(4):271-311.

EOEP-DUEP-EOPS-SW-09-0001SoW Statement of Work for DUE-GlobAlbedo Project, Version 1.0, April 2009

GlobAlbedo_RB_D01_v2_0 (2010) "GlobAlbedo Requirements Baseline (including User Requirements)", Version 1.2, Principal Author: J.-P. Muller, Date: 29/05/2010

GlobAlbedo_TS_D02_V_2.1 (2010) "GlobAlbedo : Technical Specifications", Version 1.2, Principal Authors: J.-P. Muller, P. Lewis, P. North, C. Brockmann, U. Kramer, J. Fischer, Date: 17/6/2010

ESA (2009) DUE GlobAlbedo Project, Statement of Work, EOEP-DUEP-EOPS-SW-09-0001, Issue 1, Revision 0, 6 April 2009.

Gao, F., X. Li, A. H. Strahler, and C. B. Schaaf, "Evaluation of the Li-transit kernel for BRDF modeling," *Remote Sens. Rev.*, vol. 19, pp. 205–224, 2000.

GCOS. 2006: satellite- based products for climate. supplemental details to the satellite-based component of the "Implementation plan for the Global observing system for Climate in support of the UnFCCC", GCOS-107 (WMo/Td no. 1338). 90p.

GCOS. 2004: Implementation plan for the Global observing system for Climate in support of the UnFCCC. Report GCOS – 92 (WMO/TD No. 1219). 136p.

Geiger, B.; Carrer, D.; Franchisteguy, L.; Roujean, J.-L.; Meurey, C.; , "Land Surface Albedo Derived on a Daily Basis From Meteosat Second Generation Observations," *Geoscience and Remote Sensing, IEEE Transactions on* , vol.46, no.11, pp.3841-3856, Nov. 2008

GlobAlbedo (2010) Technical Specifications Document: GlobAlbedo_TS_D02_V2_0 Date 17/06/10

Hagolle, O., A. Lobo, P. Maisongrande, F. Cabot, B. Duchemin, and A. de Pereyra, "Quality assessment and improvement of temporally composited products of remotely sensed imagery by combination of VEGETATION 1 & 2 images," *Remote Sens. Environ.*, vol. 94, no. 2, pp. 172–186, Jan. 2001.

Hansen, P.C., Nagy, J,G., O'Leary, D.P.O. (2006) Deblurring Images: matrices, spectra and filtering, SIAM series on Fundamentals of Algorithms, Society for Industrial and Applied Mathematics. ISBN 0-89871-618-7.

Hu, B., W. Lucht, and A.H. Strahler, The Interrelationship of Atmospheric Correction of Reflectances and Surface BRDF Retrieval : A Sensitivity Study, *IEEE Trans. Geosci. Remote Sensing* **37** (2) : 724-738 (1999)

Huber, P. J., 1973, Robust regression: Asymptotics, conjectures, and Monte Carlo: Ann. Statist., **1**, 799-821.

Justice, C., E. Vermote, J. Townshend, R. Defries, D. Roy, D. Hall, V. Salomonson, J. Privette, G. Riggs, A. Strahler , W. Lucht, R. Myneni, Y. knyazi, S. Running, R. Nemani, Z. Wan, A. Huete, W. van Leeuwen, R. Wolfe, L. Giglio, JJ-P. Muller , P. Lewis and M. Barnsley (1998) The Moderate Resolution Imaging Spectroradiometer (MODIS): Land Remote Sensing for Global Change Research. *IEEE Trans. Geosci. and Rem. Sens.* 36(4), 1228-1249.

Klein, A. G., & Stroeve, J. (2002). Development and validation of a snow albedo algorithm for the MODIS instrument. Annals of Glaciology, 34, 45−52.

Lewis, P., & Barnsley, M. (1994). Influence of the sky radiance distribution on various formulations of the Earth surface albedo. Proceedings of the Colloque International Mesures Physiques et Signatures en Teledetection (pp. 707−716). Val d'Isere: France.

Lewis, P. (1995), The Utility of Linear Kernel-Driven BRDF Models in Global BRDF and Albedo Studies. Proc IGARSS'95, Firenze, Italy.Volume 2,10-14 July 1995 Page(s):1186 - 1188 vol.2

Li, X., F. Gao, L. Chen, and A. H. Strahler, “Derivation and validation of a new kernel for kernel-driven BRDF models,” in *Remote Sensing for Earth Science, Ocean and Sea Ice Applications*, 1999, vol. 3868, SPIE Proc. Series, pp. 368–379

Li, X., F. Gao, J. Wang, and A. Strahler, “A priori knowledge accumulation and its application to linear BRDF model inversion,” *J. Geophys. Res.*, vol. 106, no. D11, pp. 11 925–11 935, 2001.

Liang, S., Narrowband to broadband conversions of land surface albedo I Algorithms, Remote Sensing of Environment 76, 213-238, 2000

Liang, S. and P. Lewis (1996), A Parametric Radiative Transfer Model for Sky Radiance Distribution. *J. Quant. Spectrosc. Radiat.eTransfer*, 55(2), 181-189.

Liang, S., Stroeve, J., & Box, J. E. (2005). Mapping daily snow/ice shortwave broadband albedo from Moderate Resolution Imaging Spectroradiometer (MODIS): The improved direct retrieval algorithm and validation with Greenland in situ measurement. Journal of Geophysical Research, 110, D10109.

Lucht, W., C. B. Schaaf, and A. H. Strahler, An algorithm for the retrieval of albedo from space using semiempirical BRDF models, IEEE Trans. Geosci. Remote Sensing, 38, 977-998, 2000.

Lucht, W., and P. Lewis, Theoretical noise sensitivity of BRDF and albedo retrieval from the EOS-MODIS and MISR sensors with respect to angular sampling, Int. J. Remote Sensing, 21, 81-98, 2000.

Lyapustin, A., Y. Wang, J. Martonchik, J.L. Privette, B. Holben, I. Slutsker, A. Sinyuk, and A. Smirnov, (2006), Local analysis of MISR surface BRF and albedo over GSFC and Mongu AERONET sites, IEEE Trans. Geosci. Rem. Sens., 44, 1707-1718.

Maignan, F., F.-M. Bréon and R. Lacaze, Bidirectional reflectance of Earth targets: Evaluation of analytical models using a large set of spaceborne measurements with emphasis on the hot spot, *Remote Sensing of Environment* 90 (2004), pp. 210–220.

Moody, E. G., M. D. King, C. B. Schaaf, and S. Platnick, MODIS-Derived Spatially Complete Surface Albedo Products: Spatial and Temporal Pixel Distribution and Zonal Averages, Journal of Applied Meteorology and Climatology, 47,2879-2894,2008.

Moody, E. G., M. D. King, C. B. Schaaf, D. K. Hall Northern Hemisphere five-year average (2000-2004) spectral albedos of surfaces in the presence of snow: Statistics computed from Terra MODIS land productsRemote Sensing of Environment 111 (2007) 337-345

Nilson, T., and A. Kuusk, A reflectance model for the homogeneous plant canopy and its inversion, Remote Sensing of Environment, 27,157-167, 1989.

Pinker, R. T. and I. Laszlo, Modelling surface solar irradiance for satellite applications on a global scale, Journal of Applied Meteorology, 31,194-211, 1992.

Pinty, B., T. Lavergne, R. E. Dickinson, J.-L. Widlowski, N. Gobron, and M. M. Verstraete (2006), Simplifying the interaction of land surfaces with radiation for relating remote sensing products to climate models, *J. Geophys. Res.*, 111, D02116, doi:10.1029/2005JD005952.

Pinty, B., T. Lavergne, M. Voßbeck, T. Kaminski, O. Aussedat, R. Giering, N. Gobron, M. Taberner, M. M. Verstraete, and J.-L. Widlowski (2007), Retrieving surface parameters for climate models from Moderate Resolution Imaging Spectroradiometer (MODIS)-Multiangle Imaging Spectroradiometer (MISR) albedo products, *J. Geophys. Res.*, 112, D10116, doi:10.1029/2006JD008105.

Pokrovsky, I.O., O.M.Pokrovsky,and J.-L.Roujean, “Development of an operational procedure to estimate surface albedo from the SEVIRI/MSG observing system in using POLDER BRDF measurements,” *Remote Sens. Environ.*, vol. 87, no. 2/3, pp. 198–242, Oct. 2003.

Qin, J., G. Yan , S. Liu , S. Liang , H. Zhang , J. Wang and X. Li "Application of ensemble kalman filter to geophysical parameters retrieval in remote sensing: A case study of kernel-driven BRDF model inversion", *Sci. China Ser. D, Earth Sci.*, vol. 49, pp. 632 2006.

Quaife T. and P. Lewis (2010) Temporal constraints on linear BRF model parameters IEEE Transactions on Geoscience and Remote Sensing, doi:10.1109/TGRS.2009.2038901

Rebelo, L. P. Lewis, and D. Roy, “A temporal-BRDF model-based approach to change detection,” in *Proc. IEEE IGARSS*, 2004, vol. 3, pp. 2103–2106.

Ridgwell, A., J. S. Singarayer, A. M. Hetherington and P.J. Valdes, (2009), Tackling Regional Climate Change By Leaf Albedo Bio-geoengineering, Current Biology 19, 146–150, DOI 10.1016/j.cub.2008.12.025

Román, M. O., C. B. Schaaf, P. Lewis, F. Gao, G. P. Anderson, J. L. Privette, A. H. Strahler, C. E. Woodcock, M. Barnsley, Assessing the coupling between surface albedo derived from MODIS and the fraction of diffuse skylight over spatially-characterized landscapes, Remote Sensing of Environment, 114, 738-760,2010.

Roujean, J.L., M. Leroy and P.Y. Deschamps, A Bidirectional Reflectance Model of the Earth's Surface for the Correction of Remote Sensing Data, *J. Geophys. Res.*, **97** (D18) : 20455-20468 (1992)

Samain, O. B. Geiger, and J. Roujean, "Spectral normalization and fusion of optical sensors for the retrieval of BRDF and albedo: Application to VEGETATION, MODIS, and MERIS data sets," *IEEE Trans. Geosci. Remote Sens.*, vol. 44, no. 11, pp. 3166–3179, Nov. 2006.

Samain, O., Jean-Louis Roujean, Bernhard Geiger, Use of a Kalman filter for the retrieval of surface BRDF coefficients with a time-evolving model based on the ECOCLIMAP land cover classification, Remote Sensing of Environment, Volume 112, Issue 4, Remote Sensing Data Assimilation Special Issue, 15 April 2008, Pages 1337-1346.

Schaaf, C. B., A. H. Strahler, F. Gao, W. Lucht, X. Li, X. Zhang, Y. Jin, E. Tsvetsinskaya, J.-P. Muller, P. Lewis, M. Barnsley, G. Roberts, C. Doll, S. Liang, and J. L. Privette, (2002) First operational BRDF, albedo nadir reflectance products from MODIS, *Remote Sensing of Environment*, 83, 135-148.

Schaaf, C.B., J. Cihlar, A. Belward, E. Dutton, and M. Verstraete, Albedo and Reflectance Anisotropy, ECV-T8: GTOS Assessment of the status of the development of standards for the Terrestrial Essential Climate Variables, ed., R. Sessa, FAO, Rome, May 2009.

Schaepman-Strub, G.; M.E. Schaepman, T.H. Painter, S. Dangel, J.V. Martonchik (2006). "Reflectance quantities in optical remote sensing--definitions and case studies". *Remote Sensing of Environment* **103** (1): 27–42. doi:10.1016/j.rse.2006.03.002

Stroeve, J., Box, J., Gao, F., Liang, S., Nolin, A., & Schaaf, C. (2005). Accuracy assessment of the MODIS 16-day snow albedo product: Comparisons with Greenland in situ measurements. Remote Sensing of the Environment, 94, 46−60.

Twomey, S. (1977) Introduction to the mathematics of inversion in remote sensing and indirect measurement, Elsevier. ISBN 0-486-69451-8.

Vermote, E. F., D. Tanré, J.L. Deuzé, M. Herman, J.J. Morcrette, Second Simulation of the Satellite Signal in the Solar Spectrum, 6S : An Overview, *IEEE Transactions On Geoscience And Remote Sensing* **35** (3) : 675-686 (1997)

Vermote, E. C. Justice, and F. Breon, "Towards a generalized approach for correction of the BRDF effect in MODIS directional reflectances," *IEEE Trans. Geosci. Remote Sens.*, vol. 47, no. 3, pp. 898–908, Mar. 2009.

Wanner, W., X. Li, and A. H. Strahler, 1995, On the derivation of kernels for kernel-driven models of bidirectional reflectance, J. Geophys. Res., 100(D10), 21,077-21,089.

Wanner , W., A. Strahler , B. Hu, P. Lewis , J-P. Muller X. Li , C. Schaaf , M. Barnsley, (1997), Global retrieval of Bidirectional reflectance and albedo over land from EOS

MODIS and MISR Data: Theory and Algorithms.*Journal of Geophysical Research,* Vol. 102 , pp. 17,143 - 17,162

Walthall, C. L., J. M. Norman, J. M. Welles, G. Campbell, and B. L. Blad. Simple equation to approximate the bidirectional reflectance from vegetation canopies and bare soil surfaces. Appl. Opt., 24,383-387, 1985.

Wang, Y., Alexei I. Lyapustin, Jeffrey L. Privette, Robert B. Cook, Suresh K. SanthanaVannan, Eric F. Vermote, Crystal L. Schaaf, Assessment of biases in MODIS surface reflectance due to Lambertian approximation, Remote Sensing of Environment, Volume 114, Issue 11, 15 November 2010, Pages 2791-2801, ISSN 0034-4257, DOI: 10.1016/j.rse.2010.06.013.

WWW1. https://lpdaac.usgs.gov/lpdaac/products/modis_products_table/brdf_albedo_quality/16_day_l3_global_500m/v5/combined, accessed 05 January 2010

Zibordi, G and Voss, K.J. (1989) Geometrical and spectral distribution of sky radiance – comparison between simulations and field measurements, Remote Sensing of Environment, 27(3), 343-358.

32.2 Definitions

Item	Definition

32.3 Abbreviations

AATSR	Advance Along Track Scanning Radiometer
ATBD	Algorithm Theoretical Basis Document
BEAM	Basic Envisat Tool for AATSR & MERIS (http://envisat.esa.int/services/beam/)
BBDR	Broadband Directional Reflectance
BOA	Bottom of Atmosphere
BRDF	Bidirectional Reflectance Distribution Function
BRF	Bidirectional Reflectance Factor
ENVISAT	Environment Satellite (http://envisat.esa.int)

EO	Earth Observation
ERS	European Remote Sensing satellite
ESA	European Space Agency
EUMETSAT	European Meteorological Satellites Agency
GCOS	Global Climate Observing System
GMES	Global Monitoring for Environment and Security
HCFR	Hemispherical-conical reflectance factor
HDRF	Hemispherical-directional reflectance factor
MERIS	Medium Resolution Imaging Spectrometer Instrument
MODIS	Moderate Resolution Imaging Spectroradiometer
NIR	Near InfraRed
S-2	GMES Sentinel-2 (http://www.esa.int/esaLP/LPgmes.html)
S-3	GMES Sentinel-3 (http://www.esa.int/esaLP/LPgmes.html)
SDR	Surface Spectral Directional Reflectance, i.e. BOA spectral HCRF, approximating BOA spectral HDRF and equivalent to BOA spectral BRF if the surface is assumed Lambertian.
SoW	Statement of Work
SPOT	Satellite Pour l'Observation de la Terre
SW	Short Wave
TOA	Top of Atmosphere
VIS	Visible wavelengths

33 Algorithm overview

33.1 Introduction to the problem and design philosophy

The purpose of the algorithm is to produce global estimates of albedo in three broad spectral wavebands every 8 days, at 1 km spatial resolution (GlobAlbedo_TS_D02_V_2.1). This section provides an overview of the algorithm developed. Detailed technical issues are discussed in the specific ATBDs associated with each stage of the processing.

The first issue which needed to be addressed is trying to define an albedo product, as albedo is not an intrinsic surface product, i.e. it is not simply a property of the land surface, but conditioned by the spectral and directional nature of the overlying atmosphere. This means that users must pay careful attention to what we mean by albedo in this product and what they suppose the term to mean when they use it. The use they make of the data will depend on their particular application, so we provide data and functions to predict albedo under any desired atmospheric conditions, but have a simpler 'summary' set of albedo-related terms in the final output product.

The quantities we need to estimate albedo are all spectral and directional integrals of surface spectral BRDF, so in many ways the task is quite straightforward: so long as we can access estimates of the surface spectral BRDF over a range of angles and wavelengths, we only require some model to perform the integrations. In many related problems, we use samples at fixed quadrature points which are weighted to estimate integrals. However, when estimating surface spectral BRDF from satellite data we have no control on the angular and spectral sampling. These are conditioned by the spectral characteristics of the particular sensors to be used and the platform sun-synchronous orbits and sensor optical/scanning mechanisms involved. Furthermore, the angular samples available vary considerably with latitude and time of year, and importantly, are restricted by clouds, cloud shadow and, to a lesser extent, by large-scale topographic shadowing.

At this point, it is worthwhile clarifying the terminology we will use for reflectance-related terms. The term BRDF has a formal definition (see Schaepman-Strub et al. 2006 for details), being the incremental reflected radiance from a surface in an infinitesimal solid angle around a ('viewing') vector relative to the local normal vector due relative to the incremental irradiance in an infinitesimal solid angle around an ('illumination') vector relative to the local normal vector. It has units of sr^{-1}. We use this term when referring to intrinsic properties of the surface, and equally to a mathematical model of this. The spectral BRDF is this same term as a function of wavelength. When considering Earth surface properties, the local normal is the tangent to an assumed geoid. The BRF (unitless) (or spectral BRF, its equivalent as a function of wavelength) is the radiance leaving the surface in an infinitesimal solid angle around a ('viewing') vector due to illumination in an infinitesimal solid angle around an ('illumination') vector, divided by the radiance leaving the surface due to the same illumination conditions from a perfect Lambertian reflector. When the illumination is from the entire hemisphere, we should formally refer to the HDRF, the hemispherical-directional reflectance factor. As the field of view of a sensor has a finite field of view, we should refer to the HCRF the hemispherical-conical reflectance factor, although for a small instantaneous field of view, we may consider this an approximation to the HDRF. We can think of the HDRF then as something we can relate to a measurement (with a small instantaneous field of view as is the case for data here) under ambient illumination conditions. If the surface were

assumed Lambertian in nature, then any measurement of the HDRF could be treated as an estimate of the BRF. As we shall see later, many schemes for dealing with atmospheric influences on estimating the surface reflectance do make this Lambertian assumption, so we can also think of a HDRF 'measurement' as a form of Lambertian-equivalent BRF. Throughout this text, we will use the term BRDF (or spectral BRDF) where appropriate and will generally refer to a 'measurement' of HDRF at the Earth surface (or more formally HCRF) derived from a treatment of atmospheric influences on a TOA measurement of radiance, more simply as SDR (Surface spectral Directional Reflectance), where the spectral variation is over some finite sensor waveband. Remember that where a Lambertian assumption is made (e.g. in the atmospheric correction) the HDRF is equivalent to the BRF and so the text may equate (spectral) BRF with SDR. When this information is more formally treated, we use the term Lambertian-equivalent BRF to describe this quantity. In more general usage, we refer to SDRs.

To produce a useful albedo product from ATSR-2, SPOT4-VEGETATION, SPOT5-VEGETATION2, AATSR and MERIS, the disparate spectral and angular sampling of the different instruments needs to be carefully considered.

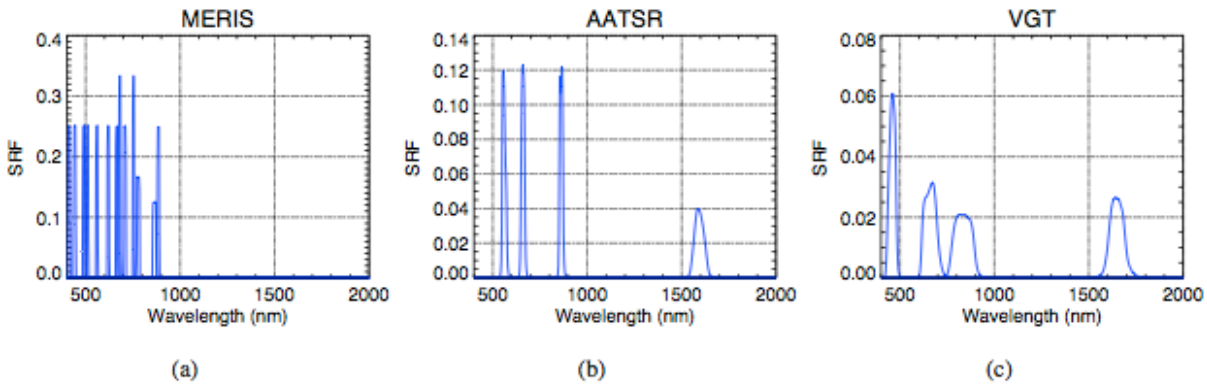

Figure 33-1. Spectral response functions of the different sensors (from GlobAlbedo_BBDR_ATBD_V2.0, 2010)

Figure 33-1 shows the spectral response functions for MERIS, AATSR and SPOT4-VEGETATION. The functions for the other instruments are very similar to these (ATSR-2 to AATSR, and SPOT5-VEGETATION2 to SPOT4-VEGETATION). Each sensor has distinct angular sampling capabilities as well (see section 4.6.2 of GlobAlbedo_Albedo_ATBD_V2.0, 2010).

The model that we require then needs to be able to take sample estimates of surface spectral BRDF and estimate the appropriate spectral and angular integrals. Issues relating to model selection are discussed in detail in section 4.3 of GlobAlbedo_Albedo_ATBD_V2.0 (2010), where it is noted that there are distinct advantages to using linear models of the BRDF, and for reasons of direct compatibility with the corresponding MODIS Collection 5 product, MCD43, these are chosen to be the linear kernel models RossThick, LiSparseReciprocal described in Wanner et al. (1995). However, the current state of these models is that they have a distinct set of (3) model parameters for each waveband considered, so they have no mechanism, other than

defining the parameters for each waveband required, in dealing with spectral integration and associated issues. Whilst other spectral-directional models of surface reflectance do exist, they are not considered appropriate (or general enough) for this task. There are, in addition, distinct advantages in processing time to the use of linear models.

When estimating albedo-related quantities from a single sensor, where the wavebands used are invariant (such as in MCD43 and the MSG/SEVIRI[28] products), processing can proceed from the surface spectral BRDF (or HDRF/BRF) estimates by fitting the linear kernel models to sets of observations at each waveband, to permit angular integration of reflectance. Spectral integration is performed as a second step, being typically implemented as a linear weighting of the particular wavebands available (Liang, 2000).

The process can be visualised as:

$$L_1\left(SDR_\lambda\right) \rightarrow F_\lambda$$

$$L_2\left(F_\lambda\right) \rightarrow F_\Lambda$$

$$L_3\left(F_\Lambda\right) \rightarrow A_\Lambda$$

where SDR_λ are sets of surface spectral directional reflectance data in the sensor wavebands, F_λ are sets of spectral model parameters, F_Λ are sets of broadband model parameters and A_Λ is broadband albedo. We can state that since the functions $L_i(x)$ all involve linear models (they can all be specified by matrices that depend only on the particular sampling characteristics), the order of the operations is not important. This is a fundamental assumption made in the GlobAlbedo product. It would be strictly true if albedo and SDR_λ were intrinsic surface properties, but is slightly complicated by spectral variation in atmospheric interactions. This can, however, be treated by applying appropriate broadband terms for weighting factors such as the proportion of diffuse illumination or the downwelling sky radiance.

Since we can change the order of the operations, we can write:

$$L_2\left(SDR_\lambda\right) \rightarrow SDR_\Lambda$$

$$L_1\left(SDR_\Lambda\right) \rightarrow F_\Lambda$$

$$L_3\left(F_\Lambda\right) \rightarrow A_\Lambda$$

Thus, when only disparate spectral sampling is available we can apply the spectral integration as the first step (to estimate broadband directional reflectance), and then apply the linear directional model to estimate the broadband model parameters. This will result in the same albedo estimate as if the original order had been maintained, but this has the distinct advantages that:

(1) processing costs are reduced, as BRDF model operations need only be performed on the 3 broad wavebands;

[28] http://landsaf.meteo.pt/algorithms.jsp?seltab=3

(2) data from sensors with disparate spectral sampling can be directly combined (with appropriate uncertainty estimates) in the modelling framework.

There is therefore no need to produce separate albedo products from each individual sensor and then combine these: all spectral input data can be converted to its broadband equivalent prior to angular modelling.

An additional advantage of this framework is that data from any sensor can be input to the scheme (provided it is first converted to a broadband equivalent) with no further modification of the code. The algorithm and its implementation are therefore 'future proofed' to be able to take data from forthcoming sensors such as those on Sentinel-3.

Most, if not all, current albedo products operate by performing an 'atmospheric correction' on 'valid' pixel samples, binning these samples into a grid representation, and proceeding from that to model albedo from those samples. The GlobAlbedo product follows this same general line of processing. One issue with this approach is that if atmospheric correction is performed on a per scene basis, with no prior knowledge of the surface reflectance assumed, the directional nature of the surface reflectance cannot be treated in decoupling the surface signal from that measured by the sensor through the atmosphere. This leads to the decoupling being performed under the Lambertian surface assumption, i.e. assuming that there are no variations in BRDF with angle at the surface (even though this is an important element of what we are trying to characterise), i.e. HDRF is treated as if it were BRF. Most, if not all products then make the assumption that this has no impact on the retrieved BRF. In fact, the impact can be quite large at high zenith angles and more turbid atmospheres (Wang et al., 2010). However, we will tend to have large uncertainties associated with such samples in this case, so this could formally be treated simply as an additional error term. That said, we show in GlobAlbedo_Albedo_ATBD_V2.0 (2010) section 4.3 that the first-order impacts of the coupling can easily be treated in an optimal estimation framework with linear models. This provides another unique feature of the GlobAlbedo product.

A further important aspect of the product is that all merging of data and estimation of albedo is conducted in an optimal estimation framework, where we attempt to characterise the uncertainty at each stage of the processing, and propagate these uncertainties through to the final product. Therefore, even if some of the data used happens to be of relatively poor estimated quality (e.g. lack of spectral sampling at longer wavelengths for the MERIS instrument – see Figure 33-1 – means that the ability to predict reflectance over the full SW spectrum is limited), this will be recognised in the processing chain by assigning a relatively high uncertainty to such samples. This attempt to quantify uncertainties should also aid in interpretation of the data, beyond the simple QA measures that are typically output from current products.

The design philosophy of this algorithm then is to first convert all (valid) input satellite data, *no matter what the sensor*, to broadband equivalent directional reflectance (BBDR) data, with associated uncertainty matrices. These are then combined in an optimal estimation framework to retrieve the model parameters allowing description of albedo (through appropriate angular integrals).

33.2 Overview of the ATBDs

Figure 33-2 shows an overview of the processing scheme. Satellite images, comprising DN data in a spatial array in the sensor swath coordinate system, along with ancillary information (on the atmospheric state and related information such as surface pressure/altitude) are ingested into a pre-processing step. All sensor information is treated the same way here, although minor details such as the specific LUTs and thresholds may vary between sensors.

The output of the pre-processing stage is a set of BBDR data in three spectral channels (VIS, NIR, SW) on a SIN grid (see below), along with associated uncertainty and ancillary information (primarily, weighted linear kernel integrals here), as well as pixel classification information (the primary items of interest being snow/no snow and land flags).

Sets of these data over some time window are then fed into an optimal estimation framework, along with a **prior** estimate of the model parameters. This produces a set of kernel model parameter estimates (with associated uncertainty) from which albedo may be estimated under any atmospheric conditions by the determination of appropriately weighted integrals. The model parameters are fed into a post-processing step, which summarises the information into black sky albedo (directional-hemispherical integral reflectance at local solar noon) and white sky albedo (bihemispherical integral of reflectance). During the post-processing phase, fAPAR (bihemispherical) is estimated from the white sky albedo data and other required datasets are passed through to the output product.

More details concerning the pre-processing stage are illustrated in Figure 33-3. Here we see that there are five main processes involved:

1. pixel identification
2. aerosol concentration estimation
3. atmospheric correction
4. spectral integration of reflectance
5. binning/gridding

The first of these, pixel identification, involves taking the raw DN value and attempting to assign a classification to the pixel (e.g. cloud). This is covered in detail in the document GlobAlbedo_PixID_ATBD_V2.0 (2010) and outlined briefly below.

The second stage involves attempting to estimate the aerosol optical thickness from the data and supplementary datasets. This is detailed in GlobAlbedo_Aer_ATBD_V2.0 (2010) and outlined briefly below.

The final stages of processing involve applying the atmospheric correction to the data identified as clear of cloud in the classifier to give spectral directional reflectance factors (Lambertian equivalent). These are then converted into estimates of broadband directional reflectance, and finally each pixel of the input swath data is assigned to processing grid

cell (SIN projection grid). These stages of pre-processing are dealt with in detail in the document GlobAlbedo_BBDR_ATBD_V2.0 (2010).

All information on the optimal estimation framework and post-processing to albedo (and related information) are given in GlobAlbedo_Albedo_ATBD_V2.0 (2010).

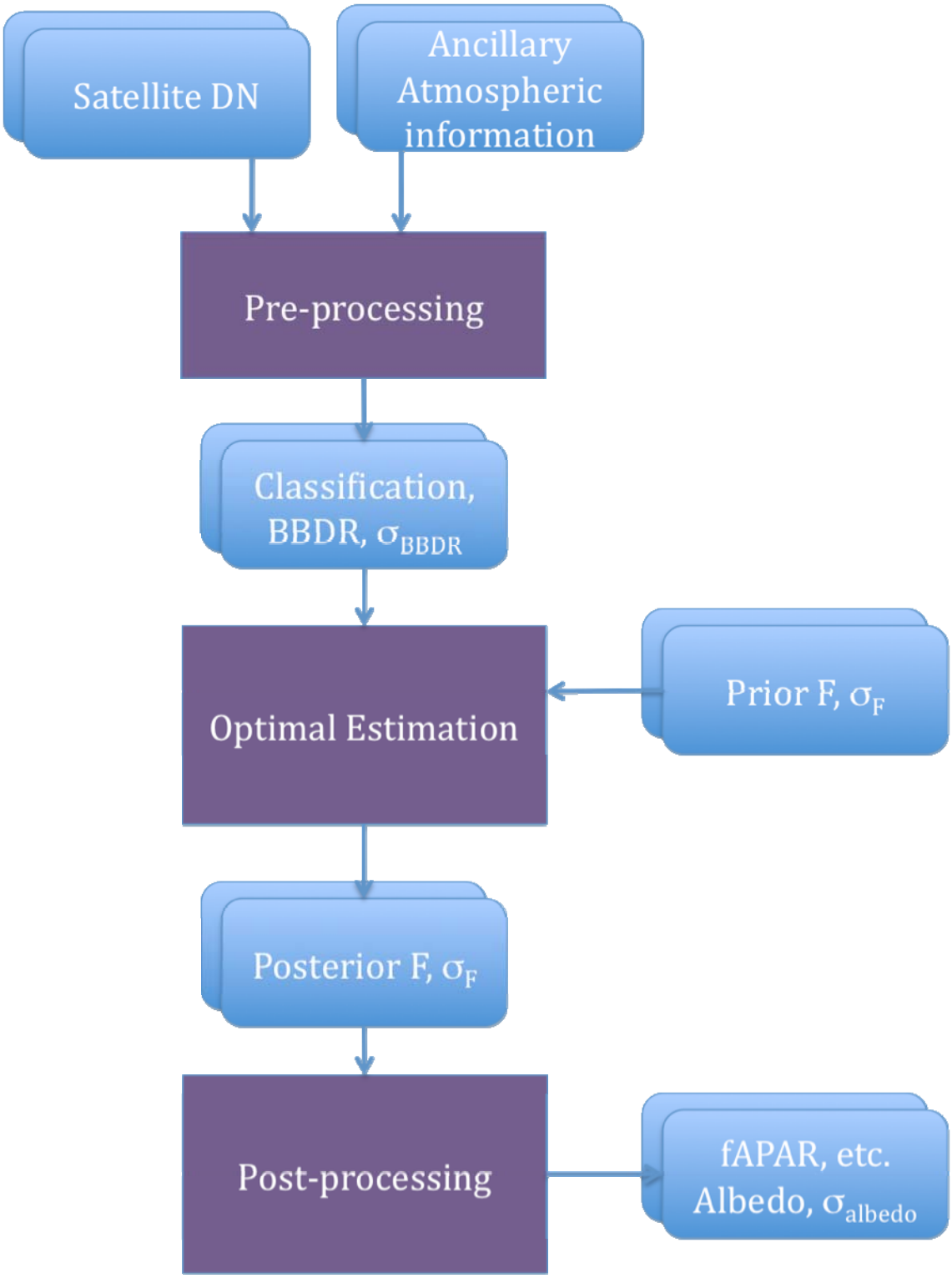

Figure 33-2. GlobAlbedo Overall processing chain

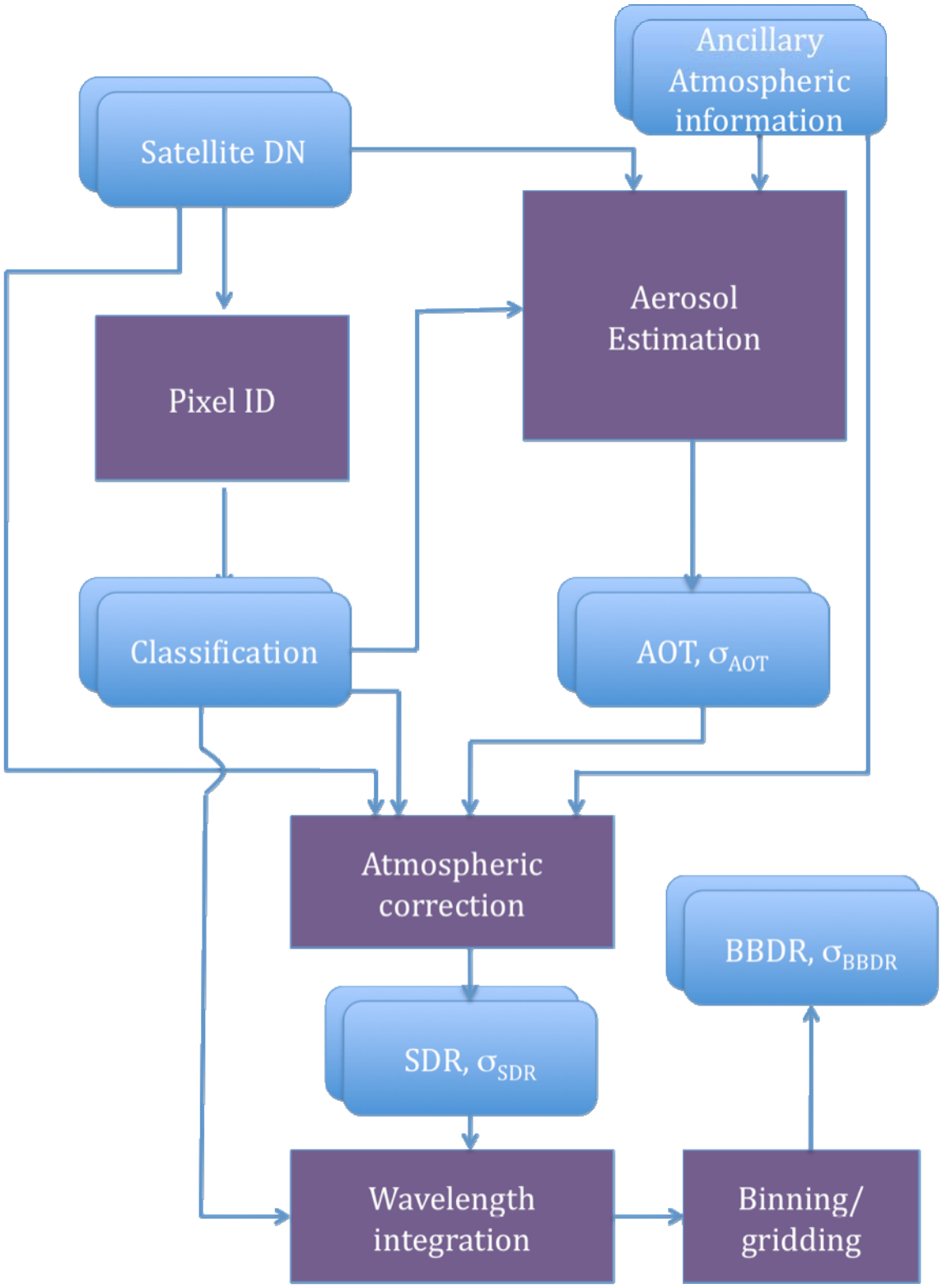

Figure 33-3. GlobAlbedo Pre-processing Steps

33.3 Pre-processing

A series of pre-processing steps are performed to derive broadband Lambertian equivalent reflectance and associated angular kernel values. These steps are:

33.3.1 Pixel identification

The GlobAlbedo Pixel Identification processor (see GlobAlbedo_PixID_ATBD_V3.0 (2011)) classifies each pixel to be processed according to a series of pixel categories, which include cloud, clear-land, clear-water and clear-snow. Cloudy pixels are not processed in GlobAlbedo, while land, water and snow pixels must be distinguished because of the particular processing steps associated to each surface type. In particular, water pixels must be separated from land surfaces even in the case of continental water bodies, as these are flagged in the final albedo product. Snow and snow-free surfaces will also be considered separately in the albedo product.

33.3.2 Aerosol retrieval

Estimates of aerosol extinction are need for the conversion from top-of-atmosphere measurements to surface reflectance, and for the partitioning of at-surface direct and diffuse irradiance fluxes required to calculate atmospheric weighting e.g. the different kernel terms in equation 14 of GlobAlbedo_Albedo_ATBD_V3.0 (2011). The approach is detailed in GlobAlbedo_Albedo_Aer_V3.0 (2011). Aerosol optical depth (AOD) and aerosol model plus an estimate of the uncertainty in AOD are derived by the Aerosol Retrieval processor from every data set to be processed. It must be noted that AOD and aerosol models are assumed to sufficiently account for the variability in the atmospheric conditions to calculate these terms, while water vapour and ozone column contents are needed in addition to aerosol parameters in order to retrieve the most accurate Lambertian equivalent reflectance. All other atmospheric constituents are just set to climatology values in the GlobAlbedo processing chain. This selection is justified by the relatively higher impact of aerosol extinction in the spectral channels of the GlobAlbedo instruments, particularly in the visible.

33.3.3 Spectral directional reflectance retrieval

Pixel classification flags and aerosol maps provided by the Pixel Identification and Aerosol Retrieval processors, respectively, are inputs to the SDR/BBDR processor to derive Lambertian equivalent reflectance from top-of-atmosphere measurements over clear-land and clear-snow surfaces.

SDR retrieval in GlobAlbedo (GlobAlbedo_BBDR_ATBD_V3.0, 2011) is designed to calculate pixel-wise Lambertian equivalent spectral reflectance plus spectrally uncorrelated uncertainties for each spectral reflectance value. Reflectance retrieval is performed by means of the inversion of equation 4, the different atmospheric parameters being provided by pre-stored look-up tables (LUTs) compiled with the MOMO radiative transfer code. These LUTs are searched for the particular viewing, illumination and atmospheric conditions of each pixel. Uncertainties in the instrument radiometric response and in AOD, columnar water vapour and columnar ozone are propagated to uncertainties

in Lambertian equivalent reflectance by means of pre-stored gradients. Spectral weighting terms for albedo retrieval are also calculated from interpolation of the LUT.

33.3.4 Broadband conversion

Narrow-to-broadband conversion (GlobAlbedo_BBDR_ATBD_V3.0, (2011)) of Lambertian equivalent reflectance is also performed by the SDR/BBDR processor. Broadband reflectance is calculated by means of the linear combination of directional reflectance in different narrowband channels. The uncertainty in broadband reflectance including the covariance between the three broadband spectral regions is also calculated in this process by assuming that the linear conversion applied to narrow band reflectance can also be applied for the conversion of narrowband errors to broadband errors.

Narrow-to-broadband conversion coefficients are also used to convert from spectral to broadband weighting terms.

33.3.5 Kernel-integral estimation

The linear model parameter estimation requires that, if Lambertian equivalent reflectance data are used, the kernels are themselves weighted by the sky radiance and other atmospheric interaction terms (equations 13 and 14 in GlobAlbedo_Albedo_ATBD_V3.0, (2011)). This is estimated as part of the BBDR retrieval, with the new kernels are weighted according to the prevailing atmospheric conditions at the time of acquisition, according to the atmospheric characterisation in MOMO.

33.3.6 Data binning

Data (a QA layer, BBDR for 3 bands, associated uncertainty (6 values), and 9 kernel values (three for each waveband, see 4.6.1) are projected to the MODIS sinusoidal grid[29] and 'binned'; resampling using a nearest neighbour approach. If multiple samples for a particular day/sensor exist for any one grid cell, multiple spatial datasets are created so that all available samples are accounted for. This processing step is covered in GlobAlbedo_BBDR_ATBD_V3.0 (2011), although the methods used are standard BEAM implementation methods.

33.4 Optimal Estimation

The details of and justification for the optimal estimation framework are presented in GlobAlbedo_Albedo_ATBD_V3.0 (2011) and illustrated in Figure 33-4.

33.5 Post-Processing

A post-processing stage after the optimal estimation involves a merging of the 'snow' and 'no snow' data streams and the calculation of ancillary output parameters (such as fAPAR). This is described in GlobAlbedo_Albedo_ATBD_V3.0 (2011).

[29] http://remotesensing.unh.edu/modis/modis.shtml

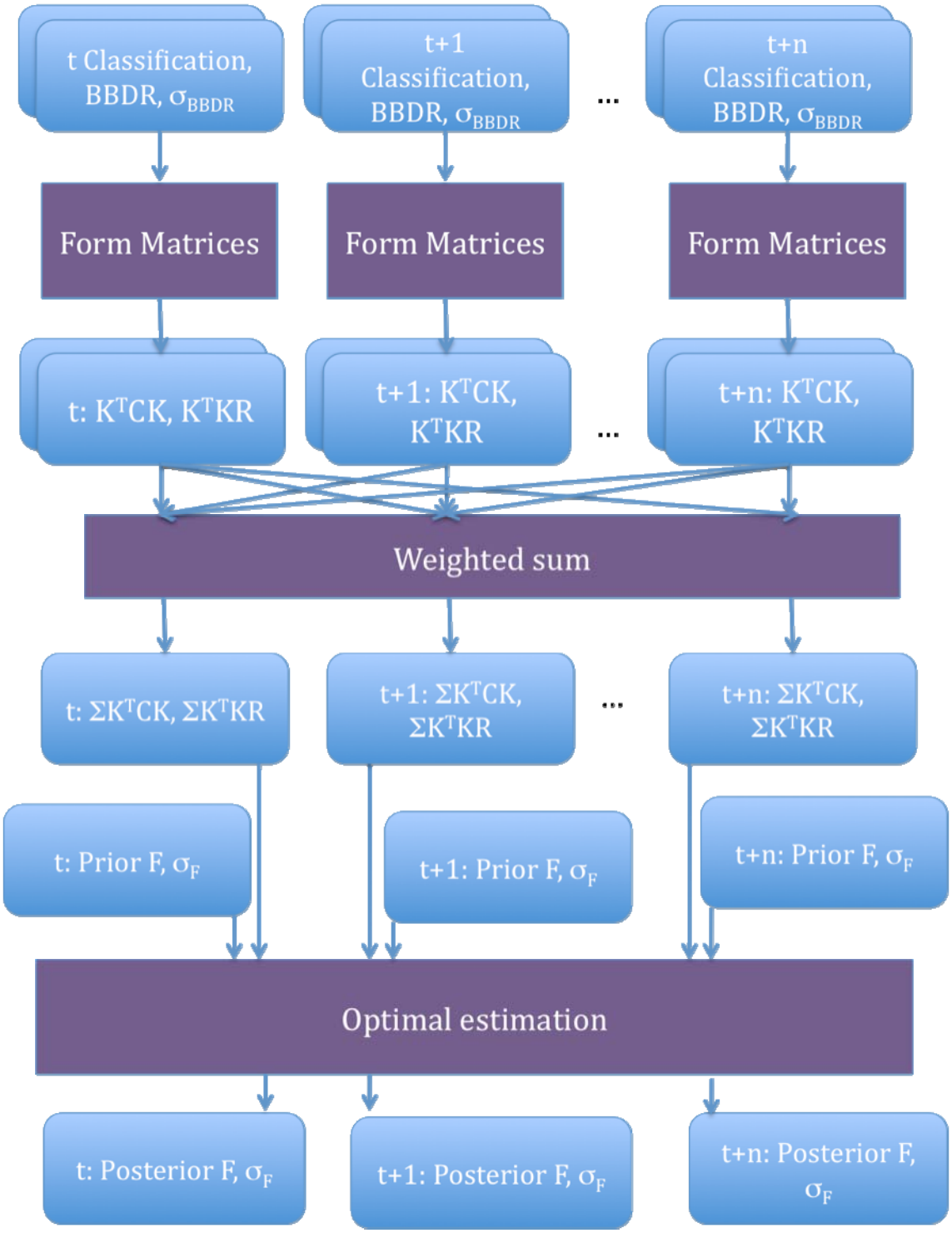

Figure 33-4. Optimal estimation

33.6 Projections and gridding

Given the significant user experience with the MODIS BRDF/Albedo product (Schaaf et al. 2002), now known as MCD43, and the availability of that product for the past decade, we aim to maintain a good degree of compatibility with MCD43 as required in the SoW and as detailed in the Technical Specification. This will facilitate users to switch between products with relative ease.

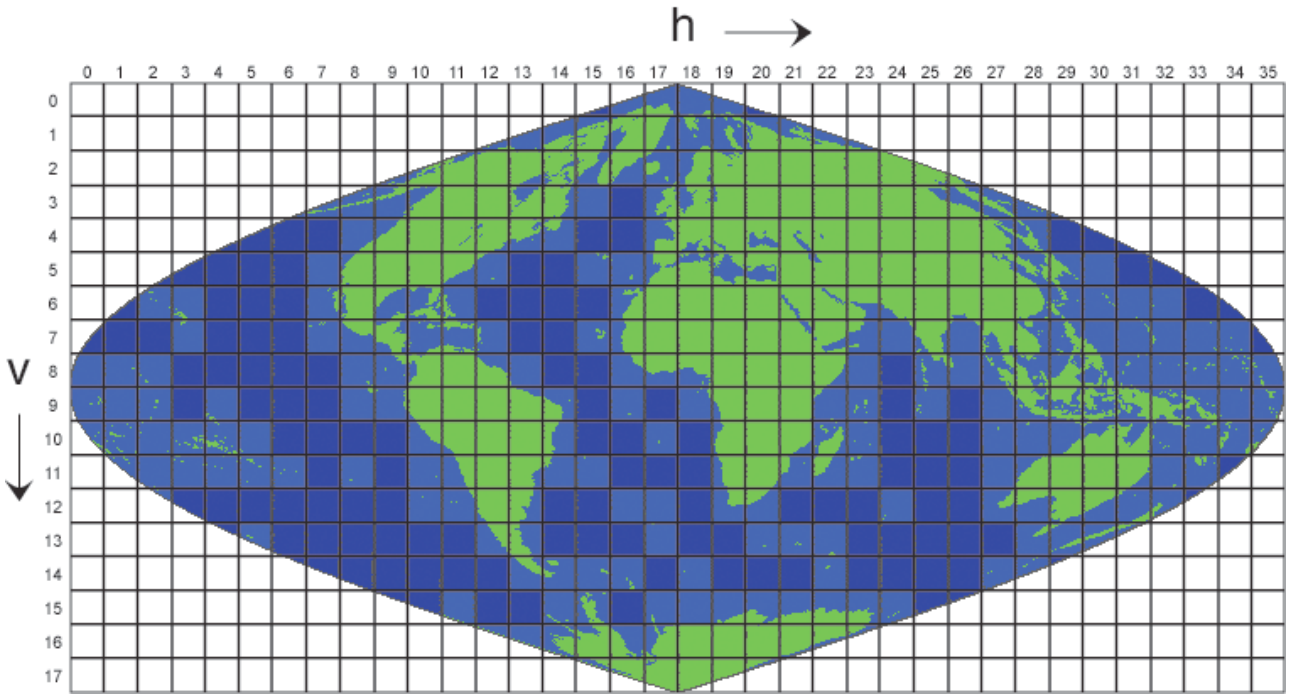

34 Practical considerations

Global datasets of the type being generated here are driven by very large amounts of data and can generate large amounts of output.

At present, we are only able to provide rough estimates of expected processing times and data file sizes. The reasoning behind these estimates is given below.

34.1 Processing time estimates

34.1.1 Pre-processing

The estimate for the pre-processing stages of the complete archive of AATSR and VEGETATION assumes 326 tiles to be processed globally, for 15 years, at around 4 core days per tile and year. This gives 19,560 core days for the whole data set of VGT and AATSR. On the SU supercomputer, with 80x8 cores, this can be achieved in 30.6 days (minimum estimate). With a safety factor of 2, the maximum estimate would be around 60 processing days.

For MERIS, we have about 41,000 orbits to process (over the complete L1b archive). Current tests indicate processing time of around 10min/orbit including AOT/BBDR retrieval and reprojection, giving 285 core days for the archive. On 10 cores, this could be achieved in 30 days.

We currently have no estimates for the processing time for the pixel classification, but might suppose a 10% increase in the above figures. This gives a total of 21,830 core days for pre-processing. It is clear that this is *only* achievable using a very large number of processing cores, the main overhead being AATSR and VEGETATION processing.

It is very likely that we will be able to reduce these numbers once code efficiencies are implemented.

34.1.2 Optimal estimation

The processing cost for the optimal estimation is currently not well known. A current prototype of the code takes around 4 core hours per tile, per 8-day date. Assuming 326 tiles to be processed globally, for 15 years (45 samples per year) gives 36,675 core days, or around twice the cost of the pre-processing. However, a large part of this is the currently inefficient algorithm: it reads data for periods of 64 days (which are then weighted), and forms and sums matrices per pixel. An efficient form of the algorithm is described in GlobAlbedo_Albedo_ATBD_V2.0, (2010) that operates on large spatial arrays simultaneously and uses the result for time *t* as input to the following time step. This sequential approach should introduce processing savings of at least a factor of 10. That would still require around 120 cores to process the archive in 30 days however. The impact of the simultaneous large spatial arrays is currently unknown, but should speed the code up several times at least.

34.1.3 Post-processing

The only significant processing step in post-processing other than data merging is the fAPAR estimate. This is achieved through LUTs and so the main limiting factor is data input/output.

34.2 Data volume and timing estimates

34.2.1 Input data

The data volume for the full archive is given in the statement of work for the project and is repeated below for ease of reference.

Satellite	*Sensor*	*Data Type*	*Period*	*Compressed data volume per day*	*Source*
ERS-2	ATSR-2	ATS_TOA_1P	1995-2002	3 Gbyte	ESA
Envisat	AATSR	ATS_TOA_1P	2002-2010	4 Gbyte	ESA
Envisat	MERIS	MER_RR__1P	2002-2010	5 Gbyte	ESA
SPOT-4	VEGETATION-1	P product	1998-2003	1.6 Gbyte	CTIV
SPOT-5	VEGETATION-2	P product	2003-2010	1.6 Gbyte	CTIV

Figure 3. Typical dataset sizes for the input data streams in GlobAlbedo

34.2.2 BBDR data

Each BBDR dataset currently contains 35 channels of information, amounting to about 2Gb/orbit (uncompressed) for MERIS, or a total of 80 Tb for the MERIS archive. For archiving, the data (in their current form) should compress by a factor of around 10, giving around 8 TB (compressed) for MERIS. Based on a joint AOT-BBDR processing scheme on a tile basis for the prototype processing the average time per tile is around 38 minutes. For a single year (2005 prototype) a conservative estimate (95 island tiles and 231 continental tiles, assuming the same processing time for both) is around 191 hours per year. This results in a conservative estimate of 55 processing days for the 7-year dataset for MERIS.

The total number of VGT tiles to be processed is 244253, with a total data volume of 1.5 TB (compressed). The processing time for BBDR (based on average processing times for prototype processing of 40 annual tiles/dat) for 12 years of VGT data (1998-2010) for the 235 majority land tiles is around 70 processing days for VGT.

Based on a separate AOT processing on an orbital basis (for the prototype 2005 processing) (11525 files) gives an average time of 4.3 minutes per file, so with 60 processing nodes available, this is around 15 hours of processing. The processing from AOT to BBDR is around the same, giving a processing time from VGT L1b to BBDR or around 30 hours per year, or 15 days for the 12 year dataset. For this way of processing, there would need to be an additional processing step to split the orbit tiles into MODIS tile equivalents, but this still would place the total processing significantly under the 70 processing days following the current scheme. 70 processing days then should be considered the upper estimate of processing time for the VGT archive to BBDR.

Estimates for (A)ATSR are a data volume of 6GB per tile and year (compressed) or around 20 TB of data (compressed) for the 15 year archive. The processing time required to BBDR is around 100 processing days for (A)ATSR, which should be a conservative estimate. Going to an orbit-based approach should provide similar speedups to those indicated for VGT (around a factor of 4.7) giving around 22 processing days.

It may be possible to reduce the number of channels of information associated with the BBDR dataset, which will clearly reduce the data volume proportionally.

34.2.3 Model parameter data

Here, we have a global gridded product 45 times per year for 15 years. Assuming the Earth land surface to be around 150 x 10^6 km^2, that equates to a data volume (ignoring non-land pixels completely) of 0.101 x 10^{12} times the number of bytes per pixel. The minimum information to be stored is: 9 parameter values, 45 uncertainty terms, plus several QA layers (e.g. 4 bytes). If we assume 2 bytes sufficient resolution for the parameter values and uncertainties, we have 140 bytes per pixel (minimum). This gives a minimum data volume of 13.16 TB. If we assume another ~10% of data for the snow product, the lower bound estimate is around15TB, with an upper bound estimate of 30TB.

For reference, the (intermediate) accumulator file sizes are: Daily accumulator files 500 MB x 540 days for 1 year processing (prototype) = 270 GB. 8 day full accumulator files reduces this to around 23 GB per tile, per year for all sensors (no matter how many sensors). There are two versions of these files (snow and no snow) so the total size for intermediate products of 586 GB per tile/year.

The BRDF merged (snow/no snow) product has 59 channels of information per tile/8 day period, giving 325MB per tile/8 day. This equates to (326 tiles, 46 samples per year, 15 years) 69.7TB (uncompressed).

The processing time from BBDR to BRDF is on average 15 processing hours on a single machine (Sun Blade) for 1.5 years of data, giving 1.6 tiles processed per day per machine, or 16 tiles per day using the current capacity of 10 machines. 326 tiles (1 year) are then processed in 20.3 days, so 15 year in 203 days. Increasing the number of machines to 12 then brings the total down to 169 days.

34.2.4 Final product data

The total number of pixels to serve is the same as for the model parameter data, giving 0.101 x 10^{12} times the number of bytes per pixel. The total number of data planes is reduced to 18 from 54 however.

The output 1 km 8 day product is a single 18-channel file of 99MB per tile, or 4.4GB for one year, for a single tile. This corresponds to 1.4TB per year (326 tiles) (uncompressed), so the 15 year 1 km dataset is 21TB.

The 0.05 degrees product is around 0.99MB per year or around 15 MB for the total dataset. One year of data for the12 monthly-global product is around 1.15GB so 17.25 GB for the total dataset.

The product merging and albedo estimation (final product) is processed at a rate of around 24 tiles per machine per day, or 240 tiles using 10 blades or 1.4 days for 326 tiles (21 days for all data).

35 Error budget estimates

We do not have enough reliable information on this yet.

36 Assumptions and Limitations

The assumptions made in developing the product are detailed in the various ATBD chapters. The product uses an optimal estimation framework that considers and tracks the uncertainty of the various data sources. This is the first time that such a product has been generated, and it is worth mentioning that such a method is reliant on reasonable estimates of the uncertainties (at least as relative uncertainties) and their structure.

Assuming that the models used are capable of describing the underlying functions they are supposed to represent, and that extraneous influences in the observational dataset can be filtered out (e.g. clouds etc.) the main limitations to the product then relate to information content of the data. This is a function of the particular spectral and angular sampling regimes available from the sensors used here and not a feature that we have any direct control of. Thus, for example, if a user wishes to know the directional-hemispherical reflectance of some particular area at a particular solar zenith angle, and the dataset does not contain samples around that part of the angular sampling space, the estimate will be relatively poor. A very positive feature of this product is that the user will be informed of this, since the uncertainty associated with that request is likely high.